

**15th International Workshop on
Physical Processes in Natural Waters:
*Fluids and Environments***



Burlington, Canada, 11-14 July, 2011

Conference Proceedings

Editors: Yerubandi R. Rao, J.D. Ackerman



**Environnement
Canada**

**Environnement
Canada**

**UNIVERSITY
of GUELPH**

**Proceeding of the
International Workshop on
Physical Processes in Natural Waters:
Fluids and Environments**

**Canada Centre for Inland Waters
Burlington, ON, Canada
11-14 July, 2011**

Editors: Yerubandi R. Rao¹ & Josef D. Ackerman²

¹ National Water Research Institute
Canada Centre for Inland Waters
867 Lakeshore Road, Burlington, ON

² Department of Integrative Biology
University of Guelph, Guelph, ON

15th International Workshop on
Physical Processes in Natural Waters: Fluids and Environments
Burlington, Ontario, Canada, July 11-14, 2011

Editors: Y.R. Rao and J.D. Ackerman

Copyright © 2011 Contributing authors
All rights reserved

National Water Research Institute
Canada Centre for Inland Waters
867 Lakeshore Road, Burlington, ON

Department of Integrative Biology
University of Guelph, Guelph, ON

Bibliographic information: Rao, Y.R. and Ackerman, J.D. (Eds.), Proceedings of the 15th
International Workshop on Physical Processes in Natural Waters, 11-14 July 2011,
Burlington, Canada, pp. 200.

ISBN 978-0-88955-591-4

Library and Archives Canada
Cataloguing in Publication

Rao, Yerubandi Ram and Ackerman, Josef Daniel
Proceeding of the International Workshop on Physical Processes in
Natural Waters: Fluids and Environments / Yerubandi R. Rao and Josef
Daniel Ackerman.

Issued also on CD-ROM
ISBN 978-0-88955-591-4

1. Limnology--Congresses. 2. Water quality--Congresses.
Environment Canada and University of Guelph Title

GB1601.2.I58 2011 551.48'2 C2011-905117-6

Preface

Water quality issues have been at the forefront of scientific enquiry since the 1960s. Legislation such as the Clean Water Act and Canada Water Act in North America has seen to many improvements in water quality as has the Great Lakes Charter, a good faith agreement among US and Canadian states and provinces, regionally. Despite the fact that much positive progress has been made, water quality and water quantity remain significant issues in the 21st century. Indeed, scientists, government bodies and NGOs believe that water quality and quantity will become even more important in the not-so-distant future.

Much of the problem related to water quality and quantity lies in the fact that water does not follow artificial boundaries created by humanity – i.e., disciplinary, jurisdictional, or isolation/compartmentalization. Problems or issues related to water have proven to be insoluble without the efforts and input of different stakeholders. Scientific inquiry has changed over this same period, from single discipline to multi- and interdisciplinary approaches and much progress has also been made in conceptualizing the nature of natural waters in mathematical and computer models.

This 15th International Workshop on Physical Processes in Natural Waters: Fluids and Environments will capture much of this interesting research related to water quality and quantity from an international perspective. We would like to thank all the authors for providing their manuscripts and enthusiastically participating in the workshop. We sincerely hope that it will prove timely and stimulate much interest and collaboration and cooperation in the future.

Ram Yerubandi and Josef Daniel Ackerman

Burlington and Guelph, Ontario

Introduction

The *Physical Processes in Natural Waters* workshops were originally conceived in Europe ~15 years ago to facilitate a dialogue between physical limnologists and modelers with colleagues in other disciplines, such as biologists, chemists and engineers. It is organized by scientists in local research institutes and universities and overseen by an international committee comprised of well-respected researchers who were involved in the PPNW activities.

This summer workshop will be the 15th in this series and organized for the first time in Canada and the second time in North America. It is being jointly organized by Environment Canada and the University of Guelph, and is endorsed and assisted by the Canadian Association on Water Quality and International Water Association. Although, the workshop is managed by individual registrations, we have also received support from ASLO's new journal, *Limnology and Oceanography: Fluids and Environment*, and industrial partners including Nortek, RBR, PME, Rockland Scientific and Hoskins Scientific.

It is well known to oceanographic and limnological communities that physical processes such as transport and mixing mediate biogeochemical processes, and that the observed temporal and spatial variability in water quality parameters is in part the result of physical processes in the lakes and oceans. Recognizing this, the focus of the 15th PPNW will be on understanding these physical processes in inland and coastal waters and their interactions with the biogeochemical processes that control water quality, ecosystem functions and ecosystem services such systems provide.

Whereas PPNW is an open workshop, we restrict participation to ~70 delegates and to a small number of invited speakers. We encourage student participation and provide a reduced rate for their registration. Importantly, this workshop is conducted in single session and there is a comfortable time frame for each presentation along with opportunity for discussion. This provides for a friendly and interactive atmosphere where formal and informal discussion is encouraged and has led to new collaborations and partnerships in the past workshops. The workshop presentations are synthesized and published in this conference proceedings, and will be made widely available to the public. Moreover, some of the workshop presentations will be included in a special issue of a peer-reviewed journal published by Canadian Association on Water Quality.

The workshop is truly international in character with nearly 50% of the participants coming from Europe, the U.S. and other countries. The water bodies to be discussed are also very diverse, ranging from laboratory scales to the scales of the Great Lakes and coastal oceans. Four internationally renowned researchers from Canada and the USA will provide keynote addresses on the main themes of the workshop. During the four days of the workshop, several presentations will deal with physical and biological processes in the water column (pelagos) and within the bottom boundary layers

(benthos) of lakes. Papers on internal waves in lakes and coastal water bodies and coupling of physical processes to ecological and water quality in large lakes are also scheduled. The workshop also features state of the art papers on the modeling of large lakes, water quality, and climate impacts on the aquatic ecosystems.

Sponsoring Organizations: NWRI and University of Guelph

National Water Research Institute of Environment Canada conducts research for management and protection of aquatic environments. NWRI is the centre of scientific expertise for advising government on management and policy decisions involving the international waters of the Great Lakes and other inland waters.

The University of Guelph is ranked as one of Canada's top comprehensive universities because of its commitment to student learning and innovative research. It has a vibrant research community who are actively conducting research in several water bodies in Canada.

NWRI and U of Guelph have successful collaborations on several mutually interesting scientific endeavors.

Local organizing committee:

- Ram Yerubandi, Ram.Yerubandi@ec.gc.ca
- Josef Ackerman, ackerman@uoguelph.ca
- Leon Boegman, Leon.Boegman@civil.queensu.ca

International steering committee:

- Adolf Stips, adolf.stips@jrc.it
- Andrew Folkard, a.folkard@lancaster.ac.uk
- Alfred Wüest, wüest@eawag.ch
- Arkady Terzhevik, ark@nwpi.krc.karelia.ru
- Bertram Boehrer, bertram.boehrer@ufz.de
- Francisco Rueda, fjrueda@ugr.es
- Geoffrey Schladow, gschladow@ucdavis.edu
- Guiseppe Ciralo, giuseppe.ciralo@unipa.it
- Hrund Ó. Andradóttir, mhrund@hi.is
- Lars Bengtsson, Lars.Bengtsson@tvrl.lth.se
- Lars Umlauf, lars.umlauf@io-warnemuende.de
- Madis-Jaak Lilover, madis@phys.sea.ee
- Nikolai Filatov, nfilatov@nwpi.krc.karelia.ru
- Xavier Castamitjana, xavier.casamitjana@udg.es

Table of Contents

Year-round Lake Water Quality Model and Simulations in Minnesota Lakes under Future Climate Scenarios : Shoeb R. Alam, Xing Fang, Heinz G. Stefan, Liping Jiang, Peter C. Jacobson, and Donald L. Pereira	1
Models of damping in layered models of lake dynamics: the effects of nonlinear steepening and wave formation : A. Baglaenko, M.Stastna, D. Steinmoeller	9
Calculating electrical conductance at low pH : Bertram Boehrer and Sophie Charlotte Diesing	12
Impact of small scale physical processes on the oxygen depletion in central Lake Erie : D. Bouffard, L. Boegman, Y. R. Rao and J.D. Ackerman	14
Determination of Phosphorus Loading to Lake Erie from the Detroit River : Jacob Bruxer, Aaron Thompson, Robert McCrea, Paul Klawunn, Rosanne Elison and Debbie Burniston	16
Modeling of October 2010 Storm Surge in Lake Winnipeg : Padala Chittibabu, Y. R. Rao	29
Temperature variability above three sites with different slopes in the near shore benthic region of Lake Opeongo, Canada : M.A. Coman and M.G. Wells	37
Experimental Observations of Flow Structures in Submarine Channels under the Influence of Coriolis Forces : R. Cossu, M.G. Wells	39
Horizontal exchange across the thermal bar front: laboratory and numerical modeling : N. Demchenko, I.Chubarenko	41
Flow Dynamics in a Free-Floating Macrophyte Root Canopy: M.A. Downing-Kunz and M.T. Stacey	43
A NEMO-based modelling system for the Great Lakes : Frederic Dupont, Padala Chittibabu, Anning Huang, Y. R. Rao, Vincent Fortin, Youyu Lu	46
Along-shore currents as a potential mechanism for invasive species transport in Lake Tahoe, CA-NV USA: A.L. Forrest, K.E. Reardon, M.E. Wittmann, B.E. Laval, S.G. Schladow	53
Physical interactions between suspended particles and biological collectors : M.Ghisalberti, A. Espinosa, G.Ivey, N.Jones and A. Purich	55
Hydrothermal and water quality model calibration and application to the evaluation of land use change and watershed management programs : Y. T. Huang, D. Pierson, A. Frei, N. Samal, E. Schneiderman, M. Zion, S. M. Pradhanang, A. H. Matonse, E. Owens	57
Chaotic advection in wind-induced shallow basin flows: a 3D approach János Józsa, Sándor Szanyi, Tamás Krámer, Enrico Napoli, Tamás Tél	66
Lake surface temperature of large northern lakes: A comparison between 1-D model simulations and MODIS satellite retrievals : H. Kheyrollah Pour, C.R. Duguay, A. Martynov, L.C. Brown	67
Some new methods for estimating hydraulic residence time from passive tracer release studies : A.T. King and E.A. Cowen	70
The influence of flooding events of the river Rhine on the anoxic hypolimnion of a river-connected lake : J. Kreling, A. Mäck, W. Heimann and A. Lorke	72
Wave attenuation by the eelgrass <i>Zostera marina</i> : J. R. Lacy and A.W. Stevens	75

Internal Solitary-like Waves in Oceans and Lakes: Theory, Modelling and Observations : K. G. Lamb	77
Occasional Enhanced Loss of Nutrient Material Through Water Supply Reservoir Overflows : C. Lemckert, P. Campbell, B. R. Gibbes	85
Summary of Hydrodynamic and Thermal Modelling in the Laurentian and Polar Great Lakes : Leon, L.F. , Lam, D.C. , Schertzer, W, McCrimmon, C, Antenucci, J.	87
The role of ice season in the physical and ecological conditions in Lake Vanajavesi, southern Finland : Matti Leppäranta and Lauri Arvola	89
Estimates of tidal currents from direct current measurements in the Gulf of Finland of the non-tidal Baltic Sea : M.-J. Lilover	90
Kelvin Wave Propagation around Point Pelee in Lake Erie : W. Liu and K.G. Lamb	93
Effects of lock operation and ship traffic on sediment oxygen uptake in impounded rivers : A. Lorke, D.F. McGinnis, A. Mäck, & H. Fischer	95
Layered weak mixing in central Yellow Sea in later summer : Youyu Lu, Jianing Wang and Hao Wei	97
Oxygen and Heat Flux in the Benthic Boundary Layer of a Shallow Lake : Lueck, R., F. Wolk, P.D. Stern, & J.D. Ackerman	99
Mixing Dynamics in Lakes across Latitudes : Sally MacIntyre	100
Methane emissions from rivers – Results from sampling a 93-km longitudinal transect of the river Saar, Germany : A. Mäck, S. Flury, T. DelSontro, M. Schmidt, D. F. McGinnis, H. Fischer and A. Lorke	101
Empirically-based parameterization of water mixing in 1D lake models - case study of Great Lakes : A. Martynov, D. Beletsky, L. Sushama, R. Laprise	103
Flows and Turbulence in a Tropical Lake : Stephen Monismith, Zikun Xing, Edmond Lo, Derek Fong, and James Hensch	105
Correlating electrical conductivity and density in limnic water: a practical lake specific approach to density from CTD data : Santiago Moreira and Bertram Boehrer	106
Sediment resuspension and transport in a large, shallow estuary: Pamlico Sound, NC : R.P. Mulligan, J.P. Walsh, R.L. Miller, D.R. Corbett	110
Mixing of stratified waters by <i>Daphnia magna</i> : C. Noß and A. Lorke	112
Three-dimensional modeling of nutrient transport in the Bay of Quinte : A. Oveisy, L. Boegman, Yerubandi, R. Rao	120
Modelling the transport of municipal, industrial and tributary discharges in eastern Lake Ontario and upper St. Lawrence River : Shastri Paturi, Leon Boegman, Sean Watt, Yerubandi R. Rao	122
Chemical composition and conductivity/temperature/salinity/density relationships in freshwaters and seawaters : R. Pawlowicz	123
Internal wave activity and the distribution of plankton in the epilimnion Lake Opeongo, Canada : P. Pernica, M.G.Wells, W.G.Sprules	125
A simplified model for deep water renewal in Lake Baikal : S. Piccolroaz, M. Toffolon	127
Plunging inflows and the summer photic zone, Kinbasket and Revelstoke	136

reservoirs : Roger Pieters, and Greg Lawrence	
Seasonal variation of solitary wave properties : M. Preusse, H.Freistuehler and F. Peeters	144
Relevance of inflow temperature variations over the daily cycle on tropical reservoirs physical limnology : Ricardo Román-Botero, Andrés Gómez-Giraldo, Mauricio Toro Botero	146
Impact of climate change on Cannonsville reservoir thermal structure in the New York City Water Supply : Nihar R. Samal, Don Pierson, Yongtai Huang, Jordan S. Read, Aavudai Anandhi, and Emmet M. Owens	147
A study of sedimentary oxygen demand with large eddy simulation: From large scale hydrodynamics to small scale mixing processes : Carlo Scalò, Ugo Piomelli and Leon Boegman	152
Some Applications of Lagrangian (Particle Tracking) Methods in Hydrodynamic Modeling : David J. Schwab	153
Application of a multi-nested ocean circulation model for investigating circulation, flushing time and dispersion in Halifax Harbour and adjacent waters : Shiliang Shan and Jinyu Sheng	154
Investigating Storm-Induced Circulation and Hydrodynamic Connectivity in the Pearl River Estuary of China using a Nested- Grid Coastal Circulation Model : Jinyu Sheng and Liqun Tang	158
Integration of Bayesian inference techniques with mathematical Modeling : Yuko Shimoda, Yerubandi R. Rao, and George B. Arhonditsis	163
Sensitivity of the simulated Kingston-Basin Lake Ontario summer temperature profile from a finite volume model : Jennifer A. Shore and Yerubandi R. Rao	165
Flow in porous sediments induced by steady and unsteady internal waves : M. Stastna, J. Olsthoorn	167
The impact of numerical method choice on solutions to a dispersive shallow water model : D. Steinmoeller, M. Stastna, K. Lamb	169
Climate Change, does it happen as abrupt transition or as steady linear process? : A. K. Stips, M-J. Lilover	173
Shear instabilities in internal solitary waves : C. Subich and K. Lamb	177
Study on the Physical Mixing Patterns in the St. Clair River by Dye Release : Y. Sun, M. Wells, S. Bailey, E.J. Anderson and D.J. Schwab	180
Near Inertial Poincare Waves in Lake Michigan : C. Troy, S. Ahmed, T.C. Hsieh, J. Chen, and N. Hawley	181
Poincaré Waves in the Central Basin of Lake Erie : Reza Valipour, Leon Boegman, Damien Bouffard, and Yerubandi R. Rao	185
Thermal Variability within a Complex Branching Estuarine System : R.W. Wagner and M. Stacey	187
Internal wave driven transport of fluid away from the boundary of a lake : D.J. Wain, M.S. Kohn, J.A. Scanlon, and C.R. Rehmann	189
Great Lakes Climate and Ice Research: Diagnosis and Modeling : Jia Wang	192
The dilution and dispersion of ballast water discharged into harbours of the Great Lakes : M. Wells, S.A. Bailey, and B. Ruddick	193

Particle- and temperature-related effects by a possible extension of the Grimsel pumpstorage scheme on downstream Lake Brienz : Alfred Wüest, Stefan Hunziker, Matteo Bonalumi, Martin Schmid	195
Numerical Study of Dispersion and Hydrodynamic Connectivity of Near-Surface Waters in Lake Huron : J. Zhao, Y.R. Rao, and J. Sheng	196

Year-round Lake Water Quality Model and Simulations in Minnesota Lakes under Future Climate Scenarios

Shoeb R. Alam¹, Xing Fang^{2*}, Heinz G. Stefan³, Liping Jiang², Peter C. Jacobson⁴, and Donald L. Pereira⁵

¹ *Department of Civil Engineering, Lamar University, Beaumont, Texas 77710-0024, USA, e-mail: shoeb1969@yahoo.com*

² *Department of Civil Engineering, Auburn University, Auburn, Alabama 36849-5337, USA, e-mail: xing.fang@auburn.edu (* corresponding author)*

³ *St. Anthony Falls Laboratory, Department of Civil Engineering, University of Minnesota, Minneapolis, Minnesota 55414, USA, e-mail: stef001@umn.edu*

⁴ *Minnesota Department of Natural Resources, 14583 County Road 19, Detroit Lakes, Minnesota 56501, USA, e-mail: Peter.Jacobson@state.mn.us*

⁵ *Minnesota Department of Natural Resources, 500 Lafayette Road, St. Paul, Minnesota 55155, USA, e-mail: Don.Pereira@state.mn.us*

ABSTRACT

A deterministic, process-oriented, dynamic and one-dimensional (vertical) year-round lake water quality model, MINLAKE2010, was enhanced and calibrated for water temperature and dissolved oxygen (DO) simulations to study impacts of climate warming on lake water quality and cisco fish habitat. The model can be run in a continuous mode in daily time steps over many simulation years for both open-water seasons and ice-cover periods. The DO model solves the one-dimensional, unsteady transport equation including oxygen sources (surface reaeration and photosynthesis) and oxygen sinks (sedimentary oxygen demand, biochemical oxygen demand, and plant respiration). The DO model is able to simulate metalimnetic oxygen maxima in vertical DO profiles of oligotrophic lakes. The model was calibrated with profile data from 28 study lakes in Minnesota; most of them are deep mesotrophic/oligotrophic lakes that support valuable coldwater fish species. The average standard error of estimate against measured data was 1.47 °C for water temperature and 1.50 mg/L for DO. Generalized calibration parameters were developed. The model was applied to simulate water temperature and DO profiles under past and two future climate scenarios, and projected profiles were used to identify future cisco fish habitat in Minnesota lakes.

KEYWORDS

Climate change; dissolved oxygen; fish habitat; lakes; simulation model; water quality; water temperature.

INTRODUCTION

Water quality is a critical issue because of its direct influence on public health and biological integrity of natural resources. Water resources managers and professionals are concerned for the potential significance and impacts of climate change on inland aquatic ecosystems, i.e., streams, lakes, and reservoirs. To make projections of water quality and fish habitat in lakes under future climate scenarios, numerical simulation models are very useful if not indispensable. To project potential effects of climate change on water quality and ecology of fresh water systems, deterministic simulation models have been developed and applied to the

Laurentian Great Lakes (Blumberg and Di Toro 1990); single reservoirs and lakes in north-temperate regions, and lakes in the contiguous U.S. (Fang and Stefan 2009).

The study described herein was aimed at the simulation of daily water temperature and DO profiles in cisco lakes in Minnesota, and then to identify cisco refuge lakes in Minnesota under projected future climate warming. The Minnesota Department of Natural Resources (MN DNR) has sampled cisco from 648 lakes in netting assessments since 1946 (Minnesota DNR files). The lakes are scattered throughout much of the central and northern portions of the state and cross several ecoregions (boreal forest, hardwood forest, and prairie) and land uses (agricultural, urban, and forested). It was found that, on average, Minnesota cisco lakes are deeper, more transparent and less productive than other lakes. A deterministic, process-oriented, unsteady, one-dimensional (vertical) year-round lake water quality model (Stefan et al. 1998), which has been successfully applied over a period of years to simulate hydrothermal and DO processes in individual lakes and regional lakes, was especially adapted for deep oligotrophic lakes in Minnesota as will be shown.

METHODS

A year-round lake water quality model, MINLAKE2010, was modified and enhanced from the MINLAKE96 model (Fang and Stefan 1996) that was developed for and applied to small lakes (up to 10 km²) at different longitudes, latitudes and altitudes in the contiguous U.S. under original model framework of Minnesota Lake Water Quality Management Model – MINLAKE (Riley and Stefan 1988). The model can be run in daily time steps in a continuous mode over many simulation years for both open-water seasons and ice-cover periods. The model uses a stacked layer system, the layers consisting of water and lake sediments during the summer open-water season and additional ice cover and snow cover layers for the winter ice-cover period.

Year-round water temperature model

The one-dimensional, unsteady heat transfer equation (1) in a lake was solved for daily vertical water temperature profiles.

$$\frac{\partial T}{\partial t} = \frac{1}{A} \frac{\partial}{\partial z} \left(K_z A \frac{\partial T}{\partial z} \right) + \frac{H}{\rho C_p} \quad (1)$$

where $T(z, t)$ (°C) is the water temperature in different well-mixed horizontal layers, t (days) is the time, A (m²) is the horizontal area as function of depth z (m) based on bathymetry, K_z (m²/day) is the vertical turbulent heat diffusion coefficient, ρC_p (J/(m³ °C)) represents heat capacity per unit volume of water and is the density of water (ρ) times heat capacity of water (C_p), and H [J/(m³ day)] is the internal heat source strength per unit volume of water. Solar radiation absorption in the water column is the main contributor to the heat source term during the open-water season. Heat exchange between the lake and the atmosphere (climate conditions) is treated as a source/sink term for the topmost water layer of a lake during the open-water season and for snow or ice covers during ice-cover period. It includes incoming heat flux from net shortwave solar and long-wave radiation and outgoing heat fluxes from back radiation, evaporation, and convection related to wind speed. The heat budget components are directly linked to climate parameters that are related to future climate changes.

MINLAKE96 conjunctively uses a vertical eddy diffusion expression, mechanical energy balance (turbulent kinetic energy from wind and potential energy due to density difference),

and a convection algorithm for natural cooling, to distribute heat energy and predict well-mixed epilimnetic thickness and water temperature profiles. The model uses previous calibration parameters and initial conditions linked to lake geometry and/or geographic location (Hondzo and Stefan 1993; Fang and Stefan 1998). The eddy diffusion coefficient below the mixed layer (K_z in cm^2/s) is a function of lake surface area (A_s in km^2) and stability frequency [$N^2 = -(\partial\rho/\partial z)(g/\rho)$ in sec^{-2} , where g is acceleration of gravity] (Hondzo and Stefan 1993):

$$K_z = 8.17 \times 10^{-4} (A_s)^{0.56} (N^2)^{-0.43} \quad (2)$$

The maximum vertical hypolimnetic eddy diffusivity, $K_{z\text{max}}$, occurs when temperature profiles are under weakly stratified conditions that were defined as $N^2 = 7.0 \times 10^{-5} \text{ sec}^{-2}$ (Riley and Stefan 1988). The model is the bulk mixed-layer model, and the wind sheltering coefficient adjusts the wind speed for fetch over the lake in the direction of wind and is used to compute turbulent kinetic energy from a wind speed that is typically measured at an off-site weather station at 10-m elevation. The wind sheltering coefficient (W_{str}) is set as a function of lake surface area based on model calibrations of various Minnesota lakes (Hondzo and Stefan 1993).

To make projections of ice cover characteristics for lakes over many years in a continuous mode, a physics-based algorithm was developed (Fang et al. 1996); it uses a full heat budget equation to estimate surface cooling, quantifies the effect of forced convective (wind) mixing, and includes the latent heat removed by ice formation. The algorithm has a fine (0.02 m) spatial resolution near the water surface where temperature gradients before freeze-over are the greatest. Snow thickness is determined from snow accumulation, followed by compaction and melting of snow by surface heat input (convection, rainfall, solar radiation) and melting within the snow layer due to internal absorption of short wave radiation, and transformation of wetted snow to ice when cracks in the ice cover allow water to spill onto the ice surface. In the model, ice growth occurs from the ice-water interface downward and from the ice surface upward. Ice decay occurs at the snow-ice interface, ice-water interface, and within the ice layer.

Heat exchange between lake sediment and water is calculated separately for all horizontal layers and then included as a source/sink term in the lake water temperature model. To determine heat flux between water and sediment, the one-dimensional (vertical), dynamic heat conduction equation is solved to simulate sediment temperature distribution up to 10 meters below the lake bottom (Fang and Stefan 1998).

Year-round dissolved oxygen model

The numerical simulation model for daily DO profiles in a lake solves the one-dimensional, unsteady transport equation including a balance between oxygen sources (surface reaeration and photosynthesis of phytoplankton) and oxygen sinks [sedimentary oxygen demand (SOD), biochemical oxygen demand (BOD), and algal respiration]:

$$\frac{\partial C}{\partial t} = \frac{1}{A} \frac{\partial}{\partial z} (AK_z \frac{\partial C}{\partial z}) + P_{\text{MAX}} \theta_p^{T-20} \text{MIN}[L] \text{Chla} - \frac{S_b}{A} \frac{\partial A}{\partial z} \theta_s^{T-20} - k_b \theta_b^{T-20} \text{BOD} - Y_{\text{O}_2\text{CH}} k_r \theta_r^{T-20} \text{Chla} \quad (3)$$

where $C(z, t)$ is the DO concentration in mg/L as a function of depth and time, $K_z(z, t)$ is the vertical turbulent diffusion coefficient for DO in m^2/day , S_b is the coefficient for SOD at 20°C in $\text{mg O}_2/(\text{m}^2 \text{ day})$, P_{MAX} is the maximum specific oxygen production rate by photosynthesis at 20°C under saturating light conditions = $9.6 \text{ mg O}_2/(\text{mg Chla day})$, $\text{Min}[L]$ is the light limitation

determined by Haldane kinetics, Chl a is the chlorophyll a concentration in mg/L, Y_{O_2CH} is the yield coefficient that equals 120 mg O $_2$ /(mg Chl a), k_b and k_r are the first order decay rate coefficient for BOD and algal respiration, respectively, and equal to 0.1 per day. $\theta_s = 1.065$, $\theta_p = 1.036$, $\theta_b = 1.047$ and $\theta_r = 1.047$ are the temperature adjustment coefficients for SOD, photosynthesis, BOD, and algal respiration, respectively. BOD is related to primary productivity represented as chlorophyll a , therefore, BOD is set as 1.0 mg/L, 0.5 mg/L, and 0.2 mg/L for eutrophic, mesotrophic, and oligotrophic lake in MINLAKE96 (Stefan and Fang 1994), respectively. SOD varies with trophic status and maximum depth (Stefan and Fang 1994), e.g., 0.2 g/(m 2 day) in deep oligotrophic lake and 2.0 g/(m 2 day) in shallow eutrophic lake. In the model chlorophyll a is specified by a mean annual value and a function that calculates typical seasonal chlorophyll cycles (Stefan and Fang 1994) based on observation data from 56 lakes or reservoirs in Europe and North America (Marshall and Peters 1989). In the model, the oxygen transfers through the water surface (reaeration) during the open water season is used as an oxygen source or sink term in the topmost water (surface) layer of the lake, and surface oxygen transfer coefficient is calculated as a function of wind speed. For the DO simulations in a lake during the winter ice cover period, modifications were made to account for the presence of an ice cover and low temperatures, e.g., reaeration is zero because the lake ice cover prevents any significant gas exchange between the atmosphere and the water body. DO concentrations were simulated after water temperature and snow and ice covers had been simulated.

MINLAKE96 was developed to study impacts of climate warming on lake water quality and fish habitat in regional lakes with maximum depth up to 24 meters. Water temperature and DO models of MINLAKE96 were previously calibrated and validated against 5,378 daily measurements for 48 'lake years' in 9 Minnesota lakes (their maximum depths ranged from 4.7 to 20.7 m; 6 eutrophic lakes, 3 mesotrophic or oligotrophic lakes). Winter ice and snow cover models were calibrated against 128 ice/snow measurements over 8 years in Thrush Lake in Minnesota and Little Rock Lake in Wisconsin, and 198 observed freeze-over dates in another 9 Minnesota lakes (Fang et al. 1996). Model parameters or coefficients were set either to depend on surface area (e.g., equation 2) or to be a function of lake trophic status and maximum depth, for example, BOD and SOD (Stefan and Fang 1994).

Several modifications and refinements were made to develop MINLAKE2010 from MINLAKE96. (1) The maximum number of horizontal layers in MINLAKE2010 was increased to 80, so that the model can handle much deeper lakes. (2) Several calibration parameters were activated or introduced in the program. Use of these parameters enhances the performance of the model significantly for the deep oligotrophic lakes as will be shown in the next section. (3) The model was coded to perform an error analysis between simulated and measured mixed-layer depths, and between simulated and measured temperature and DO in the mixed layers. (4) The model was expanded to read the output from two most-recent climate projection models. (5) The model was coded so that at the end of the winter ice-cover period when simulated water temperature increases to greater than 4°C within two days, complete lake mixing (overturn) is enforced. (6) Various modifications were made in the program to make the input data files to be user-friendly.

RESULTS AND DISCUSSION

In this study, twenty-one cisco lakes and seven non-cisco lakes (Table 1) were selected for model calibration based on multi-year data availability. About 70% of 28 lakes have a lake maximum depth (H_{max}) greater than 23.0 m, and 23 of the 28 lakes are either mesotrophic or oligotrophic lakes. Five model parameters were calibrated for these deep and oligotrophic lakes. Basic lake

parameters and quantitative measures of the success of the water temperature ($^{\circ}\text{C}$) and DO (mg/L) simulations in the 28 study lakes are listed in Table 1. Four hundred thirty nine (439) lake-days with measured water temperature and DO profiles (7,384 data pairs) were used for model calibration. After calibration the average standard error (S.E. in Table 1) of estimate against measured data for all 28 lakes was 1.47°C for water temperature (range from 0.8 to 2.06°C) and 1.50 mg/L for DO (range from 0.88 to 2.76 mg/L).

Figure 1 shows examples of observed and simulated temperature and DO profiles in Little Trout Lake that has a maximum depth of 29 m (Table 1) and mean summer Secchi depth of 6.3 m (oligotrophic lake). Temperature profiles in the summers of 1997 and 2008 show very strong stratification, e.g., a temperature difference between lake surface and lake bottom was 19°C on August 6, 1997. Both measurements and simulation results show metalimnetic oxygen maxima in the DO profiles (Fig. 1). DO concentration in the metalimnion was up to 12.6 mg/L but only 8.6 mg/L in the surface mixed layer on July 13, 2008. This creates favorable habitat conditions for coldwater fish species such as cisco. Figure 2 illustrates the seasonal change of water temperature and DO in the epilimnion (1.0 m) and hypolimnion (45.0 m) in Ten Mile Lake that has a maximum depth of 63 m (Table 1) and mean summer Secchi depth of 5.5 m (oligotrophic lake). Measured and simulated water temperatures near the lake surface respond to variations of weather with season every year; a strong thermal stratification develops in Ten Mile Lake every summer (simulation and data for one year are shown in Figure 2). Measured and simulated water temperatures near the lake bottom vary from 4°C in winter to about 7°C in summer; they have much smaller variations with season (Fig. 2) than surface waters because of the attenuation of solar radiation with water depth and lack of vertical mixing.

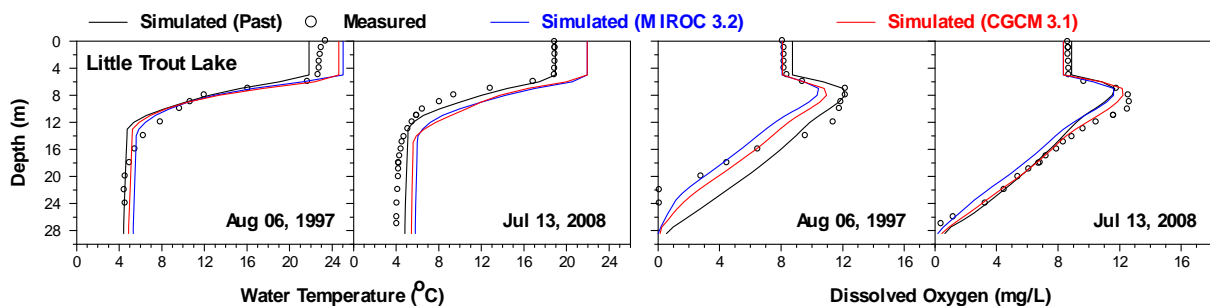


Figure 1. Examples of simulated water temperature and DO profiles in Little Trout Lake for past climate and two future climate scenarios (solid lines). Circles show measurements.

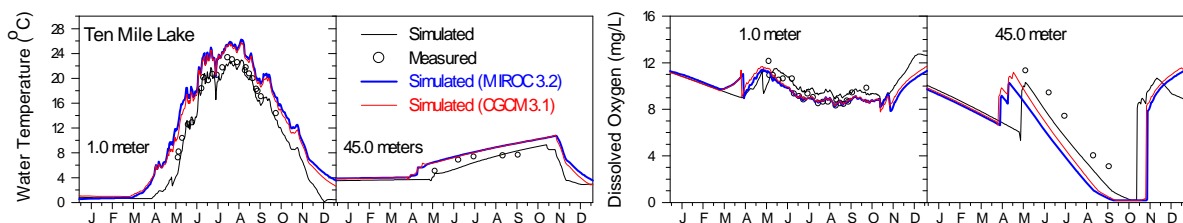


Figure 2. Examples of simulated water temperature and DO time series at 1.0 and 45 m depth in Ten Mile Lake for past (2008) climate and two future climate scenarios. Circles show measurements.

Individual model calibration parameter values were analyzed, and generalized model calibration parameter values were developed for cisco lakes without data. The model performance using generalized calibration parameter values was only marginally lower than with calibration

parameter values based on data (Fang et al. 2010). A general multiplier for the diffusion coefficient in the metalimnion was determined by calibration to be 0.5 for deep lakes and 1.0 for medium-deep and shallow lakes. For the hypolimnion the multiplier of the diffusion coefficient was determined by calibration to be 1.0 for all lakes regardless of maximum depth. This means that the eddy diffusion coefficient (equation 2) is valid for shallow and medium-deep lakes but too large for deep lakes.

Table 1. Lake characteristics and standard errors (S.E.) of water temperature ($^{\circ}\text{C}$) and DO (mg/L) simulations in 28 Minnesota lakes.

Lake name	A_s (km^2)	H_{\max} (m)	Secchi Depth (m)	Data (days /data pairs)	S.E. for Temp ($^{\circ}\text{C}$)	S.E. for DO (mg/L)
Big Trout	5.43	39.01	4.78	46/916	1.65	1.52
Blue	0.71	14.63	6.76	13/205	1.70	1.80
Burntside	28.90	38.40	5.80	14/274	1.72	1.37
Carlos	10.20	50.00	3.27	16/366	1.70	1.32
Cedar	0.98	26.80	3.56	22/410	1.34	1.40
Elk	1.10	28.00	2.57	17/312	1.47	1.03
Fish Hook	6.61	23.16	3.44	4/61	2.06	1.10
Greenwood	8.18	34.14	5.46	14/222	1.76	1.36
Grindstone	2.13	46.63	2.88	5/98	1.67	1.83
Kabekona	9.12	41.00	4.03	5/104	1.37	0.89
Little Sand	1.56	24.38	5.22	7/102	1.76	1.28
Little Trout	0.97	28.95	6.33	11/281	1.46	1.44
Mukooda	3.05	23.77	5.12	7/141	1.13	1.56
Siseebakwet	5.29	32.00	3.89	6/122	1.66	1.47
Six	0.76	42.67	3.94	4/70	1.72	2.38
Snowbank	17.30	45.72	5.28	4/67	0.92	0.88
South Twin	4.52	8.80	2.78	15/126	1.42	1.33
Ten Mile	18.90	63.00	5.54	30/828	1.68	1.04
Trout (Cook)	1.04	23.00	5.40	23/349	1.24	1.63
Trout (St. Louis)	30.94	29.87	4.71	5/89	0.80	0.95
White Iron	13.88	14.30	1.44	21/342	1.43	1.63
Bear Head ¹	2.73	14.00	3.28	16/193	0.97	1.06
Carrie ¹	0.37	7.90	1.44	15/121	1.22	1.57
Elephant ¹	2.93	9.10	3.29	13/135	1.24	1.62
Hill ¹	2.66	14.60	3.99	21/267	1.41	1.83
Madison ¹	4.50	18.00	0.88	34/456	1.72	2.76
South Center ¹	3.38	32.20	1.45	19/413	1.47	1.77
St. Olaf ¹	0.37	10.10	1.41	32/314	1.34	2.05
Total measured data and average standard errors:				439/7,384 ²	1.47 ³	1.50 ³

¹ – Non-cisco lakes, ² – Total days or pairs of measurements, and ³ – Average standard error (S.E.).

Chlorophyll *a* concentrations were available as model input for all 28 lakes from measurements near the lake surface (epilimnion), but not in the metalimnion and hypolimnion. The multiplier for chlorophyll-*a* below the mixed layer was determined by calibration to be 1.5 for oligotrophic lakes (mean summer Secchi depth greater than 4.5 m) and 1.0 for mesotrophic and eutrophic lakes. Higher chlorophyll-*a* concentrations in the metalimnion matched observations in Thrush Lake (Stefan et al. 1996), and are a key input for simulations of

metalimnetic oxygen maxima occurring in oligotrophic lakes, such as Little Trout Lake (Fig. 1). BOD is the sum of carbonaceous biochemical oxygen demand and nitrogenous biochemical demand. BOD is from the aerobic microbial decomposition of particulate and dissolved organic matter in the lake (MINLAKE2010 does not consider inflow). Generalized BOD values for MINLAKE2010 determined by calibration were set at 1.5 mg/L, 0.75 mg/L, and 0.5 mg/L for eutrophic, mesotrophic, and oligotrophic lake, respectively. Sedimentary oxygen demand SOD below the mixed layer depends on both maximum depth and trophic status (Table 3). The recommended S_{b20} values, SOD at 20°C ($\text{g O}_2/(\text{m}^2 \text{ day})$), were adopted from the regional DO model (Stefan and Fang 1994). The proposed multiplier EMCOE(2) for SOD was found by calibration to be typically greater than 1.0, which means that sedimentary oxygen demand is larger than the values used for the regional lake model, especially for oligotrophic and mesotrophic lakes. Long-term accumulation on the lake bottom of organic matter from the death of phytoplankton and from the surrounding watershed is the source of sedimentary oxygen demand below the mixed layer.

Table 2. Generalized (calibrated) values of the multiplier EMCOE(2) for SOD below the mixed layer.

	Lake maximum depth	Eutrophic	Mesotrophic	Oligotrophic
Average of values used in input files	Deep (all lakes)	1.00 (1) ¹	1.30(7)	0.99(11)
	Deep (cisco lakes)	- (0)	1.30 (7)	0.99 (11)
EMCOE (2) × S_{b20} [$\text{g O}_2/(\text{m}^2 \text{ day})$]	Medium (all lakes)	1.98(4)	2.05(4)	0.96 (1) ²
	Medium (cisco lakes)	1.80 (1)	1.13 (1)	0.96 (1)
Proposed values of EMCOE (2) × S_{b20} [$\text{g O}_2/(\text{m}^2 \text{ day})$]	Deep	1.50	1.25	1.00
	Medium	1.95	1.75	1.20
	Shallow	2.20	1.90	1.25
Proposed EMCOE (2) values	Deep	1.5	2.5	5.0
	Medium	1.3	2.3	3.0
	Shallow	1.1	1.9	2.5
Recommended S_{b20} [$\text{g O}_2/(\text{m}^2 \text{ day})$]	Deep	1.0	0.5	0.2
	Medium	1.5	0.75	0.4
	Shallow	2.0	1.0	0.5

¹ – only one deep eutrophic lake used, ² – only one medium-depth oligotrophic lake used

Simulation for future climate scenarios

Besides lake bathymetry, meteorological conditions control water temperature and DO distribution in a lake. Weather data are inputs to model simulations of lake water temperature and DO concentrations, which in turn impact cisco fish habitat in lakes. Weather data consist of daily air temperature, dew point temperature, wind speed, solar radiation, percent sunshine, and precipitation (both rainfall and snowfall). Projected future climate scenarios were based on the output of the Coupled Global Climate Model (CGCM), CCCma CGCM 3.1 from the Canadian Climate Centre for Climate Modeling and Analysis (CCCma), and the Model for Interdisciplinary Research on Climate, MIROC 3.2 developed in Japan. Monthly climate parameter increments from the closest GCM grid center point were applied to measured daily climate conditions (1961-2008) to generate the projected daily future climate scenario. Monthly changes of air temperature at International Falls were projected by CGCM 3.1 to be from 2.89 to 6.89°C and by MIROC 3.2 from 3.53 to 5.15°C. The highest change of air temperature was projected by CGCM 3.1 to be 8.09°C in February at Duluth. Figures 1 and 2 give examples of

projected temperature and DO profiles and time series under two future climate scenarios. Surface temperatures were projected to increase by about 3°C and hypolimnetic temperature less than 1°C (Fig. 1). Surface DO concentrations were projected to decrease by about 0.5 mg/L and hypolimnetic DO concentrations by more than 1~2 mg/L (Fig. 1), largely because of the increase of water temperature and the earlier onset of stratification (see time series at 45.0 m in Fig. 2). The model projects ice-out to be on April 14 under the MIROC 3.2 future climate scenario in Ten Mile Lake (Fig. 2). The model predicts ice cover formation on December 15, 2008, but projects no ice formation by December 30 under the MIROC 3.2 future climate scenario in Ten Mile Lake (Fig. 2). Lakes are projected to freeze up later and melt out earlier, under the future climate scenarios, i.e. ice cover periods are projected to be shorter.

CONCLUSIONS

A one-dimensional year-round lake water quality model, MINLAKE2010, was developed and calibrated with more than 7,000 measurements for water temperature and DO simulations in order to study impact of climate warming on lake water quality and cisco fish habitat in relative deep and mesotrophic/oligotrophic lakes in Minnesota. It is projected that lake surface water temperature will increase by about 3 °C and hypolimnetic DO will decrease by about 1~2 mg/L. These potential changes due to climate warming would be expected to have a significant effect on coldwater fish species that require low water temperatures and well oxygenated water.

REFERENCES

- Blumberg, A. F., and Di Toro, D. M. (1990). "Effects of climate warming on dissolved oxygen concentrations in Lake Erie." *Trans. Am. Fish. Soc.*, 119(2), 210-223.
- Fang, X., Ellis, C. R., and Stefan, H. G. (1996). "Simulation and observation of ice formation (freeze-over) in a lake." *Cold Regions Science and Technology*, 24(2), 129-145.
- Fang, X., and Stefan, H. G. (1996). "Development and validation of the water quality model MINLAKE96 with winter data." Project Report 390, St. Anthony Falls Laboratory, University of Minnesota, Minneapolis, MN 55414.
- Fang, X., and Stefan, H. G. (1998). "Temperature variability in the lake sediments." *Water Resources Research*, 34(4), 717-729.
- Fang, X., and Stefan, H. G. (2009). "Simulations of climate effects on water temperature, dissolved oxygen, and ice and snow covers in lakes of the contiguous United States under past and future climate scenarios." *Limnol Oceanogr*, 54(6), 2359-2370.
- Fang, X., Alam, S. R., Jacobson, P., Pereira, D., and Stefan, H. G. (2010). "Simulations of Water Quality in Cisco Lakes in Minnesota." Project Report No. 533, St. Anthony Falls laboratory, University of Minnesota, Minneapolis.
- Hondzo, M., and Stefan, H. G. (1993). "Lake water temperature simulation model." *Journal of Hydraulic Engineering*, 119(11), 1251-1273.
- Marshall, C. T., and Peters, R. H. (1989). "General patterns in the seasonal development of chlorophyll a for temperate lakes." *Limnology Oceanography*, 34(5), 856-867.
- Riley, M. J., and Stefan, H. G. (1988). "Minlake: A dynamic lake water quality simulation model." *Ecological Modelling*, 43(3-4), 155-182.
- Stefan, H. G., and Fang, X. (1994). "Dissolved oxygen model for regional lake analysis." *Ecological Modelling*, 71(1-3), 37-68.
- Stefan, H. G., Fang, X., and Hondzo, M. (1998). "Simulated climate changes effects on year-round water temperatures in temperate zone lakes." *Climatic Change*, 40, 547-576.

Models of damping in layered models of lake dynamics: the effects of nonlinear steepening and wave formation

A. Baglaenko*¹, M. Stastna¹, D. Steinmoeller¹

¹ *Department of Applied Mathematics, University of Waterloo, 200 University Avenue West, Waterloo, ON, Canada, N2L 3G1.*

**Corresponding author, e-mail abaglaen@uwaterloo.ca*

Keywords

internal waves; nonlinear wave trains; shallow water equations; weakly nondispersive models; bottom drag.

EXTENDED Abstract

Introduction

Lake scale numerical models, along with field observations, laboratory work and fundamental theory, play a key role in understanding and predicting characteristics of lake dynamics. While lake dynamics models have improved vastly in the past decade (Marshall, 1997) there is still a great deal of numerical dissipation in currently employed models. This dissipation can vary widely based on flow parameters such as the Reynolds number, the boundary conditions as well as the shape of the domain. While the numerical dissipation is crucial for maintaining stability of models, it is often justified physically as an approximation of turbulent interactions which cannot be accurately resolved for any reasonably sized lake basin. It is certainly true that a variety of dissipative processes, including boundary layer turbulence, internal wave breaking, Langmuir cells and many others profoundly influence the biogeochemical cycles (e.g. nutrient sources due to re-suspension) and food webs in a lake. However these should be understood through accurate, well-resolved simulations and physical parametrizations and not in an ad hoc manner.

We have focused on the manner in which bottom drag is commonly parametrized in lake scale models. Bottom drag itself is a key part of lake models since it links lake dynamics and the behavior of the bottom boundary layer. This can in turn effect sediment dynamics, the interaction with a porous medium, as well as sediment resuspension and the kick-up and redistribution of nutrients. Bottom drag is usually modeled as a quadratic friction applied to the bottom-most layer (in layered models). It thus dissipates energy and affects the dynamics of wave train formation. We have found that in some cases quadratic bottom drag can decrease the amplitude of the nonlinear wave train that forms from an initial standing wave by as much as 20 percent. Moreover, due to the nonlinearity of the drag, the drag itself induces a cascade in spectral space, one that has nothing to do with the classical turbulent cascade.

Methods

Using spectral methods we consider weakly nonhydrostatic, weakly nonlinear models of a layered lake. For modelling real lake systems a multi-layered approach is needed; however, in the interests of brevity we will present only a single-layer (i.e. barotropic) system here. The model used is a simple dispersive shallow water model as presented by de la Fuente et al. (2008) in their study of internal waves:

$$h_t + \nabla \cdot (h\mathbf{u}) = 0, \quad (1)$$

$$(h\mathbf{u})_t + \nabla \cdot ((h\mathbf{u})\mathbf{u}) = -g h \eta_x + f v h + (H^2/6) (\nabla \cdot (h\mathbf{u}))_x, \quad (2)$$

$$(h\mathbf{v})_t + \nabla \cdot ((h\mathbf{v})\mathbf{u}) = -g h \eta_y - f u h + (H^2/6) (\nabla \cdot (h\mathbf{u}))_y, \quad (3)$$

where $h(x,y,t) = H(x,y) + \eta(x,y,t)$ is the total depth of the fluid column, g is the acceleration due to gravity, f is the Coriolis frequency, H is the mean depth, η is the free surface elevation, and $\mathbf{u} = (u,v)$ represents the depth-averaged horizontal velocity vector.

The last terms in equations (2) and (3) are the effects of a weakly non-hydrostatic correction to the standard shallow water model.

The spectral methods used result in relatively little numerical dissipation and this allows us to focus on the effect of commonly prescribed bottom drag parametrization. While more complex formulations that cover general domains are possible (Steinmoeller, 2011), the results presented use a leapfrog discretization in time and the built in fast Fourier transform, or FFT, in Matlab. The quadratic bottom drag is thus easy to implement as part of the explicit step. For the periodic domains we consider, the spectra are easy to calculate and do not require windowing.

Results and Discussion

Figure 1 (left) shows the effects of a quadratic bottom drag on the breakdown of a standing wave (the period of the wave corresponds roughly to the depth of the layer as $10,000/\sqrt{gH}$, in this case approximately 68 seconds) into wavetrains. It is clear that the wave with drag (black solid line) exhibits decreased wave-induced currents compared to the simulations without drag. Also it is obvious that the wave train forming near what would be the shock in the absence of dispersive effects has also been significantly damped by the bottom drag. Examining the spectrum (figure 1 (right)) we notice immediately that the simulations with drag display more evenly distributed spectra, as seen by the lack of deep troughs in the red line in figures (b) and (c). It is also of note that removing the nonlinear terms results in a more condensed spectrum. This, along with the detailed energetics of the test cases, will be discussed further in the poster.

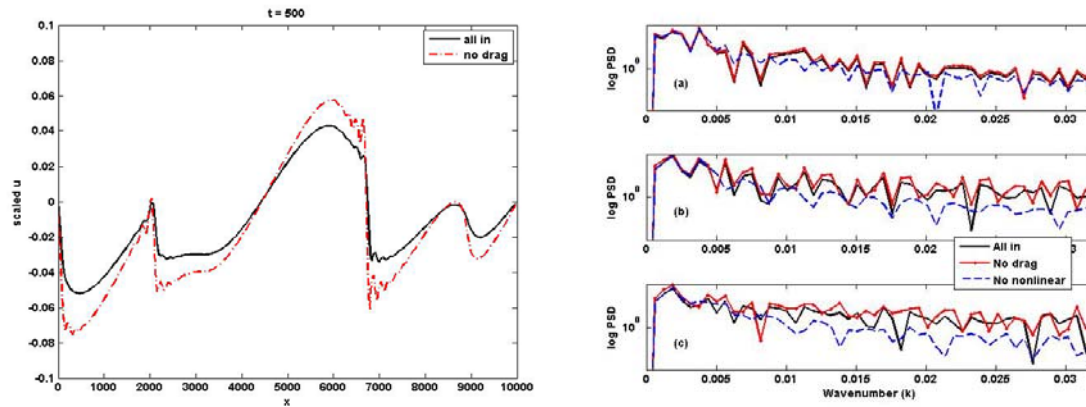


Figure 1. Results of a 1D one-layer simulation showing the effects of bottom drag compared to a simulation with no drag whatsoever. These figures show wave velocities at time $t=500$ seconds (left) and the spectra of the same wave (right) at (a) 250 seconds, (b) 500 seconds, and (c) 750 seconds.

References

- Marshall, J., Hill, C., Perelman, L. and Adcroft, A. (1997). Hydrostatic, quasi-hydrostatic and nonhydrostatic ocean modeling. *J. Geophys. Res.*, 102, 5733-5752.
- de la Fuente, A., Shimizu, K., Imberger, J. & Nino, Y. (2008). The evolution of internal waves in a rotating, stratified, circular basin and the influence of weakly nonlinear and nonhydrostatic accelerations. *Limnol. Oceanogr.*, **53**(6), 2738-2748.
- D.T. Steinmoeller, M. Stastna, K.G. Lamb, Fourier pseudospectral methods for 2D boussinesq-type equations, *in preparation*, 2011.

Calculating electrical conductance at low pH

Bertram Boehrer^{1*}, Sophie Charlotte Diesing^{1,2}

¹ Helmholtz Centre for Environmental Research – UFZ, Brueckstrasse 3a, D-39114
Magdeburg, Germany

² University of Bayreuth, Bayreuth, Germany

*Corresponding author, e-mail bertram.boehrer@ufz.de

KEYWORDS

Electrical conductivity, pH, physical limnology, physical chemistry

INTRODUCTION

Electrical conductivity of water depends on dissolved substances and temperature. Using electrical conductivity as a tracer, for indication of gradients, evaporation or similar, its temperature dependence must be compensated. We searched for an easy to implement approach for CTD profiles (C for electrical conductivity, T for temperature, D for depth) to calculate electrical conductivity at the reference temperature of 25°C, i.e. “electrical conductance” κ_{25} . Especially for lake waters of unusual composition the standard approach ISO-standard 7888 (1985)

$$\kappa_{25} = \frac{C(T)}{\alpha_{25}(T - 25) + 1} \quad (1)$$

is not viable. Acidic waters pose a problem. In lakes of low pH but only little gradient of chemical composition, the coefficient α_{25} can be evaluated in a purely empirical approach from lab measurements of the temperature dependence of electrical conductivity (see e.g. Boehrer and Schultze 2008). For Mining Lake 111 of pH=2.6, Karakas et al. (2003) found a coefficient $\alpha_{25} = 0.0166$ in contrast to the commonly used $\alpha_{25} = 0.02$ for pH neutral lakes. If such lab experiments cannot be done, or if gradients in the water composition require different adjustments for α_{25} in different layers, e.g. mixolimnion and monimolimnion, an alternative approach including pH gradients must be found.

In this contribution, we show that a good approximation can be proposed, if in addition to the CTD profile, a pH profile is available. From tables of physical chemistry, we produce a numerical approximation based on pH measurements, and we finally test this approach in a lake with a pH gradient from 3 to 7. We find a good agreement with the purely empirical approach for each layer in separate.

APPROACH

Temperature dependence of electrical conductivity is specific. Each solute shows a characteristic of its own. From the composition of the solutes, the electrical conductivity can be calculated at any temperature as the sum of the components under dilute conditions (e.g. Sorensen and Glass 1987):

$$C(T) = \sum_i C_i(T) = \sum_i \lambda_i c_i \left(\frac{\eta(T)}{\eta_{25}} \right)^{K_i} = \sum_i \lambda_i c_i E^{K_i} \quad (2)$$

λ_i and K_i are specific constants c_i is the concentration of solute i , and finally $\eta(T)$ is the viscosity at given temperature, while η_{25} at 25°C. Hence, temperature dependence and conductance can be evaluated, in principle. However, the implementation of coefficients of

physical chemistry requires information about the chemical composition. In most cases, this information is not readily available. In other cases, gradients between layers oppose a straight forward use. In all cases, the implementation of coefficients from physical chemistry is a tedious exercise, and as a consequence, has rarely been done.

In general, common ions in natural waters show a similar temperature dependence of conductivity. Only H^+ , shows a clearly different behaviour. If a pH profile is available, concentrations of H^+ and OH^- are known, and so are their contributions to conductivity at given temperature. The remainder is contributed to other substances. The conductivity due to H^+ and OH^- ions can be calculated for $25^\circ C$ using coefficients from physical chemistry, see Table 1. The remainder is converted to $25^\circ C$ using an average value for common ions. Again assuming dilute conditions, the three groups can be added to yield conductance now referred to as C_{25} .

coeff.	λ_i	K_i
unit	[mS l/(cm mol)]	[-]
H^+	349.65	0.615
OH^-	198	0.841
else	irrelevant	0.9

$$C_{25} = C_{else} E^{-K_{else}} + \lambda_{H^+} 10^{-pH} + \lambda_{OH^-} 10^{pH-14} \quad (3)$$

RESULTS AND DISCUSSION

We implemented this approach in a lake with a pronounced pH gradient (Moritzteich). This lake shows a pronounced pH gradient between mixolimnion and monimolimnion. A purely empirical approach for mixolimnion and monimolimnion in separate shows a good agreement with the results for the respective layer (Figure 1).

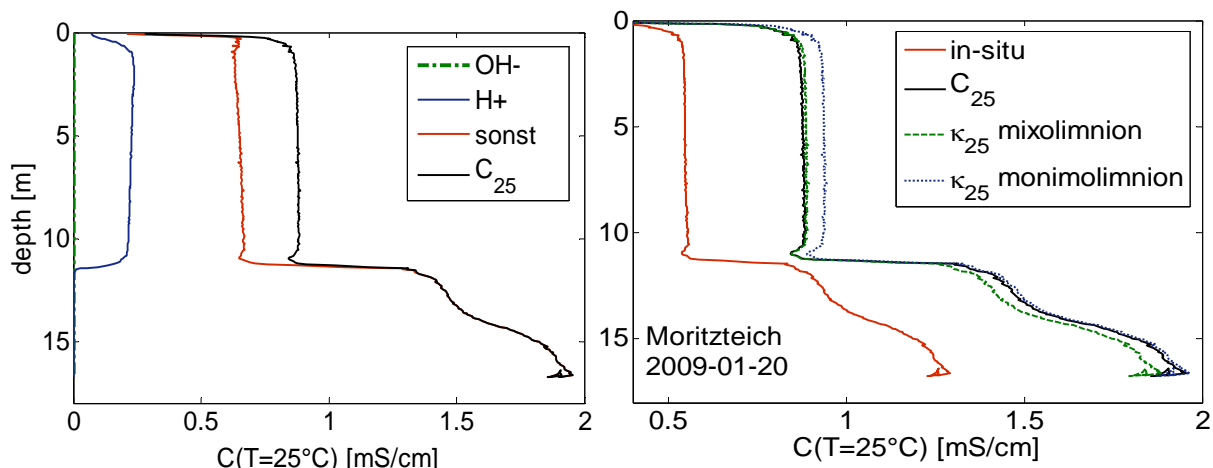


Figure 1. left panel: decomposition of the electrical conductivity profile into contributions of H^+ , OH^- and other ions (OH^- contribution hardly visible at left margin); right panel: in-situ conductance on 20th Jan 2009 and calculated profiles of conductance

REFERENCES

- Boehrer, B., and M. Schultze (2008), Stratification of lakes, *Rev. Geophys.*, 46, RG2005, <http://dx.doi.org/10.1029/2006RG000210>
- ISO standard 7888 (1985), *Water quality: Determination of electrical Conductivity*, International Organization for Standardization, www.iso.org.
- Karakas, G., Brookland, I., Boehrer, B. (2003): Physical characteristics of Acidic Mining Lake 111. *Aquatic Sciences* 65: 297-307, doi:10.1007/s00027-003-0651-z.
- Sorenson, J.A., and G.E. Glass (1987), Ion and temperature dependence of electrical conductance for natural waters. *Analytical Chemistry* 59(13), 1594-1597, doi: 10.1021/ac00140a003.

Impact of small scale physical processes on the oxygen depletion in central Lake Erie

D. Bouffard^{1*}, L. Boegman¹, Yerubandi R. Rao² and J.D. Ackerman³

¹ *Department of Civil Engineering, Queen's University, K7L 3N6, Kingston, Ontario, Canada*

² *Environment Canada, Water Science and Technology, National Water Research Institute, 867 Lakeshore Road, L7R 4A6, Burlington, Ontario, Canada.*

³ *Department of Integrative Biology and Faculty of Environmental Sciences, University of Guelph, Guelph, Ontario N1G 2W1, Canada*

*Corresponding author, e-mail damien.bouffard@queensu.ca

Keywords

Oxygen depletion, vertical mixing

EXTENDED ABSTRACT

The problem of hypoxia (dissolved oxygen less than 2 mg/L) in the hypolimnion of central Lake Erie has been historically studied by focussing on assessing (i) the spatial and temporal extent of the hypoxia and (ii) linking the rate of oxygen depletion to the hypolimnion thickness. While the former has shown that hypoxia typically occurs between mid July and mid October in the central basin and can extend over 10 000 square kilometers, the latter has only shown that a thin hypolimnion is necessary to sustain low oxygen conditions. Research gaps remain in assessing physical-biogeochemical processes that regulate inter-annual variability, and in determining the effects of these processes on small-scale temporal and spatial patchiness, where oxygen depletion rates change rapidly over -2 mg/L/d to +1 mg/L/d. These high-frequency changes may have a cumulative effect on hypoxia formation.

The goal of the present study is to focus on the short term oxygen depletion variability and to link it to the rate of vertical mixing. Results are presented through a vertical oxygen budget (e.g., Edwards et al. 2005, Rao et al. 2008),

$$\frac{dO_h}{dt} = \frac{K_z}{H_h} \frac{\Delta O}{\Delta Z} - SOD + P - R,$$

where O_h is the dissolved oxygen in the hypolimnion, $\Delta O / \Delta Z$ the oxygen gradient through the thermocline, H_h the hypolimnion thickness, SOD the sediment oxygen demand and P and R the oxygen production and respiration in the hypolimnion, respectively. Such methodology enables us to quantify how much the oxygen variability

is controlled by physical processes relative to biological respiration and the sediment oxygen demand (SOD).

The data presented here comes from two intensive measuring campaigns in the summers of 2008 and 2009 in Lake Erie (Fig. 1). The data includes that from 13 moorings with high-frequency temperature loggers, acoustic Doppler current profilers (ADCP), dissolved oxygen loggers, chlorophyll and turbidity loggers, YSI biogeochemistry profiles and more than 600 SCAMP microstructure profiles. This diversified fast sampling field tool gives us a unique opportunity to investigate the dynamics of the oxygen depletion.

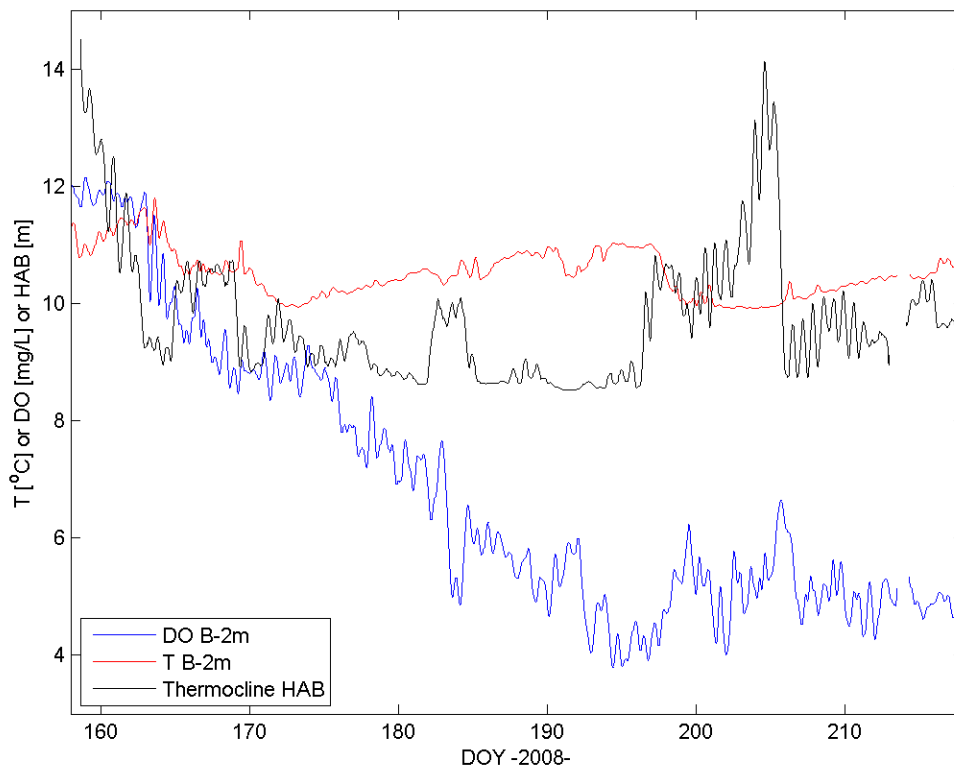


Figure 1: Dissolved Oxygen and temperature recorded 2 m above the bottom in the western part of the central basin (Station 341) in 2008. Thermocline height above the bottom is estimated using the 1-m spacing temperature mooring chain.

REFERENCES

- Edwards, W. J., J. D. Conroy, and D. A. Culver. 2005. Hypolimnetic oxygen depletion dynamics in the central basin of Lake Erie. *J. Great Lakes Res.* 31, pp 262–271.
- Rao, Y. R., N. Hawley, M. N. Charlton, and W. M. Schertzer. 2008. Physical processes and hypoxia in the central basin of Lake Erie. *Limnol. Oceanogr.* 53(5), pp 2007–2020.

Determination of Phosphorus Loading to Lake Erie from the Detroit River

Jacob Bruxer¹, Aaron Thompson¹ (presenter), Robert McCrea², Paul Klawunn³,
Rosanne Elison⁴ and Debbie Burniston³

¹*Environment Canada, Boundary Waters Issues Unit, Canada Centre for Inland Waters,
867 Lakeshore Rd. Burlington, Ontario, L7R 4A6*

²*Environment Canada-Retired*

³*Environment Canada, Water Quality Monitoring and Surveillance Office, Canada Centre for Inland
Waters, 867 Lakeshore Rd. Burlington, Ontario, L7R 4A6*

⁴*United States Environment Protection Agency-Great Lakes National Program Office, 9311 Groh Road,
Grosse Ile, Michigan 48138*

Introduction

The Lake Erie LaMP (Lakewide Management Plan) was created to preserve, restore and protect the beneficial uses of Lake Erie. The LaMP aims to identify water quality problems, identify the key causes and identify what the desired state of the lake is, once the water quality issues have been addressed. Environment Canada serves as the federal lead for Canada on the LaMP. In response to requests from the Lake Erie LaMP, Environment Canada undertook a nutrient study in the Detroit River. One component of the study was to quantify phosphorus loading to Lake Erie via the Detroit River. Phosphorus loading has been a key water quality problem in Lake Erie causing excessive algal growth and eutrophic conditions. The work presented in this paper describes an effort to estimate phosphorus loading for April to November 2007 through a combination of field monitoring and hydrodynamic modelling.

Study Area

The Detroit River connects Lake St. Clair and Lake Erie in the Great Lakes Basin, and forms part of the international boundary between Canada and the United States (Figure 1). The Detroit River is approximately 51 km long and has a mean flow of approximately 5,270 m³/s. Nearly 98% of the Detroit River flow enters from Lake Huron via Lake St Clair with 2% entering through a number of additional tributaries, the most significant of which being the Rouge River, located in Michigan, USA. Much of the Detroit River shoreline is highly urbanized and is one of the world's most heavily industrialized areas (UGLCCS, 1988). The average flushing time for the Detroit River is 19 hours (UGLCCS 2). The flow in the Detroit River is complicated by the many branches around islands and through navigation channels, particularly in the lower Detroit River near Lake Erie (Figure 2). The river has two distinct reaches, the upper and lower reaches, with the divide occurring at Fighting Island. The upper reach contains two large islands, Belle Isle and Peche Isle, followed by a single channel that is generally uniform in width. The lower reach contains several large islands including Fighting

Island and Grosse Ile in addition to many smaller islands, man-made berms and dykes. As a result, there are many separate passage ways for the flow to move through the river.

Previous Monitoring Studies

Environment Canada conducted preliminary nutrient studies in 2004 in the Detroit River, noting there were no significant changes in total phosphorus (TP) concentration from water exiting the St. Clair River and water entering the Detroit River even though high concentrations of TP entered Lake St. Clair from major tributaries during the study period. There were also no significant changes in total phosphorus concentrations from water entering the Detroit River and the concentration found in the middle channels of the lower Detroit River, but there were significant increases found in the water in both the Amherstburg and Trenton channels. In 2006, unpublished studies were made to determine the spatial and temporal variation in TP in the numerous channels in the lower Detroit River. The key findings from those studies were that there was a large temporal variation in the Trenton channel; there were large horizontal variations across the Trenton and Amherstburg channels; there was minimal vertical variation in TP at all sites for all times investigated; and the Trenton channel had the highest TP concentrations, greatest cross-channel (horizontal) variation and the greatest temporal variation.

These results helped shape the strategy for the 2007 Detroit River corridor nutrient monitoring program. Because a fairly consistent spatial pattern was observed, it was hypothesized that this pattern may allow for effective monitoring from a single near-shore site if a relationship could be established with samples collected from across the channel. Also, since variability in the discharge regime of the sewage treatment plants (which function as point sources of TP to the Detroit River) may increase the temporal variations of TP concentrations in the river, it was determined that future sampling efforts need to include time-integrated sampling to incorporate variability within the day. Collection of daily time-integrated samples would mitigate the need to interpolate data between surveys.

Therefore, the objectives of the 2007 monitoring study were to: characterize the Detroit River TP concentrations across the river in all major channels and downstream of all major inputs and across the river inlet; characterize the mean daily concentrations in Amherstburg and Trenton Channels for the duration of the study period; characterize the temporal variation in TP concentrations over two day sampling periods; and to estimate the daily TP loading into Lake Erie for open water conditions. These objectives were accomplished through monitoring, applying empirical regression models and a physical hydrodynamic model.

Monitoring Methods

The 2007 sampling program involved two types of sample collection methods: Teledyne ISCO © continuous automatic water samplers (ISCO) and discrete grab samples. The ISCO samplers automatically collected a water sample every two hours

over 24-hours. Discrete grab samples were collected manually during 14 two-day surveys performed biweekly from July 30th to November 1st, 2007. For each survey, single grab samples were collected at a number of locations spaced across the channels in the lower river to spatially measure the flow before it entered Lake Erie (Figure 3). Samples from the ISCO in the Trenton channel were retrieved by the U.S. Environmental Protection Agency staff. The ISCO samples in the Amherstburg channel were collected by the Town of Amherstburg Water Filtration Plant staff. The samples were later sub-sampled and combined to form a single integrated sample; the combined sub-samples represented a 24-hour (daily) composite sample for TP. Further analysis of the samples was done at the National Laboratory for Environmental Testing in Burlington, Ontario.

Development of Relationships between Grab and ISCO Samples

After the monitoring, attempts were made to develop relationships between the grab samples collected at the various locations in the lower Detroit River and the grab samples collected at the ISCO stations. If successful, these relationships could then be used to estimate continuous phosphorus loading to Lake Erie from August to November, 2007, based on the 24-hour (daily) composite samples collected at the ISCO stations.

The locations of the five Trenton Channel (TC) grab sample locations (TC1 to TC5) and the Trenton Channel ISCO station (TCISCO) are shown in (Figure 4). The mean daily TP concentrations for grab samples taken at TCISCO were used to build the TP relationships between sites. The TCISCO grab sample concentrations showed fairly strong linear relationships with each of the other TC grab samples. The correlation coefficients are greater than 0.82 at all locations, indicating that the linear relationships in the Trenton Channel were generally strong (Figure 5).

The Amherstburg Channel grab sample locations (AC2 to AC5) and the Amherstburg Channel ISCO (ACISCO) station are shown in (Figure 6). The grab samples as the ACISCO site displayed a wide variability detected through collecting multiple samples at that location. Samples taken from the other Amherstburg Channel locations did not demonstrate as much variability. The variability with the ACISCO grab sample data may be a result of transient effects in the river, or with the ACISCO site location. The ACISCO site may have been influenced by nearby point sources or it may also be influenced by variable current due to the irregular shoreline directly upstream of the site. Another possible factor is the periodic discharge from the upstream Amherstburg sewage treatment plant. In light of these factors, developing a relationship between the ACISCO location and the other (AC2-AC5) grab sample locations was not successful (Figure 7).

The grab sample locations in the middle channels of the Detroit River, which included East Sugar Island (ES), West Sugar Island (WS), Livingstone Channel (LC) and the Boise Blanc Channel (BB), are shown in (Figure 3). Past monitoring and the results from this monitoring indicated little change in the TP concentration between the upstream sites near Lake St. Clair and these middle channel sites. This implies that a relationship between the mid-channel and ISCO site grab samples is unlikely. The middle channels

show less temporal variation than the outer channels, and hence display poor relationships between the middle channels and the ACISCO and TCISCO stations' TP grab sample data. Given that the TP concentrations in the mid-channels had less variability, the daily phosphorus load could therefore be established with less temporal and spatial monitoring than the other channels.

Lower Detroit River Hydrodynamic Model Overview

Given that grab sample data collected varied in TP concentration across the lower Detroit River and having developed acceptable relationships between grab sample data in the Trenton Channel, an estimate of the variation in discharge in the individual lower Detroit River channels was needed to calculate the TP load entering Lake Erie. A hydrodynamic model of the lower Detroit River was used for this purpose.

The hydrodynamic model used in this application was derived from the RMA2 model of the full St. Clair-Detroit River system developed by the U.S. Geological Survey and U.S. Army Corps of Engineers (Holtschlag and Koschik, 2002a). The original full-system model covers the connecting channel system between Lakes Huron and Erie in its entirety, including the St. Clair River, Lake St. Clair, and the Detroit River. The model used in this application characterizes only the lower portion of the Detroit River, from approximately Fort Wayne, Michigan, to Bar Point, Ontario, which is at the downstream boundary of the Detroit River and the western end of Lake Erie (Figure 9). The total length of the modelled reach is approximately 27.8 kilometers (17.3 miles). In addition to shortening the original model domain, the model mesh density was increased by a factor of four. This was done to improve model convergence and flow continuity in the various channels making up the lower Detroit River.

The original USGS model was extensively calibrated and validated during development using measured water levels, flows and flow distributions. The finite element grid adapted for this study was substantially different than the original model and therefore required validation to ensure it maintained adequate estimates of water levels and flows in the Detroit River. The model's roughness and viscosity parameters, specified as Manning's roughness coefficients and Peclet number respectively, were retained from the original model. Two validation scenarios were examined; first a simulation under steady-state boundary conditions using a subset of twelve mean daily discharge and water level sets from 2007; and second, a series of unsteady-state boundary conditions on a 24-hour time step for the period from April 1st to October 31st 2006. Daily means were used to negate wind effects, which can have a significant influence on water levels in the lower Detroit River, especially at shorter time steps. The adapted model's performance was validated by comparing computed versus actual measured water levels and discharge. For the first validation scenario, i.e. steady-state simulations, the simulated daily mean water levels at gauges located at Gibraltar, Amherstburg, Wyandotte and Fort Wayne were compared to the observed daily mean water levels at these locations as well as the computed values from the full system model and in both cases were found to agree well (RMSE 5 cm and 1 cm respectively). For the second validation analysis, i.e. unsteady-state simulations, simulated results were again

compared to the observed daily mean water levels at gauge stations located throughout the lower Detroit River. Similar to the steady-state simulation results, the model performed well during the unsteady simulation.

Channel Flow Factors

The hydrodynamic model adapted for this study was used to develop flow factors for each grab sample location since TP concentrations varied horizontally across each channel as did channel velocity and water depth. The flow factors are estimates of the proportion of the total discharge in the Detroit River occurring in a 24-hour period that passes through a specific part of a cross-section in each channel. More specifically, the flow factors indicate the proportion of the total flow to be applied to the TP concentration to calculate the loading at each grab sample location.

The flow factors were estimated from the simulated results of the twelve steady-state scenarios from 2007. Continuity check lines were used in the RMA2 model to determine the flow distribution across each channel. Figure 10 shows an example of the continuity check lines located at the approximate locations of the grab samples for the Trenton Channel. The flow passing through each continuity check line was calculated using the RMA2 model and then divided by the total flow in the lower Detroit River to determine the proportion of the total flow passing each location for each scenario. The flow factors were then related to the mean calculated flow from all scenarios at each location to estimate the TP load to Lake Erie.

Phosphorus Loading Estimates to Lake Erie

The flow factors were used with the TP concentrations from the grab samples to estimate the TP load by mass to Lake Erie. Two methods were employed, each specific to the channel investigated.

Since relationships between the grab samples taken at the ISCO stations and the grab sample locations could be developed for only the Trenton Channel, the mean grab sample TP concentrations for all other channels were first used to estimate the TP load to Lake Erie. Due to the temporal variability of the TP concentrations measured in both the Trenton and Amherstburg Channels, the TP load to Lake Erie as determined from this method is likely underestimated. The flow factors developed for each grab sample location were multiplied by the mean 24-hour total flow in the lower Detroit River to estimate the mean daily flow passing each grab sample location as given by Equation 1:

$$Q_n = FF_n \cdot Q_{LowerDetroit} \quad (Eq. 1)$$

Where Q_n = the discharge (m^3/s) passing through each location, n ; FF_n = the flow factor calculated for each location; $Q_{LowerDetroit}$ = the total discharge (m^3/s) in the lower Detroit

River. The discharge estimates were then used to estimate the total volume passing each location.

The grab sample mean TP concentrations were multiplied by the total volume passing each location from August to November, 2007. The TP load (kg) at each location was then calculated and summed to estimate the TP load to Lake Erie from each channel using equation 2:

$$TP_{channel} = \sum_{n=1}^k V_n \cdot tp_n \quad (Eq. 2)$$

Where $TP_{channel}$ = the 24-hour total phosphorus loading (kg) for a given channel; V_n = the volume (m^3) of water flowing through each location, n , over a 24-hour period; tp_n = the grab sample mean total phosphorus concentration (mg/L); n = specific grab sample site; k = the total number of locations in the channel.

The results showed that the TP load for each channel ranged from approximately 24.2 metric tonnes for the BB channel to 312.9 metric tonnes for the AC. The total TP load to Lake Erie from the lower Detroit River was approximately 852.4 tonnes over the four-month period from August to November, 2007, or approximately 2557 mta. This is similar to the 2135 mta estimated from the 2004 data. With the TP load estimate from the upper river approximately 1850 mta, the 2007 results using this method indicate an estimated increase of 707 mta between the head and mouth of the Detroit River.

However, TP concentrations measured in the lower Detroit River channels vary over time. The ISCO station data collected in 2007 for this study showed greater range of TP concentrations than did the grab sample data. Therefore, it is possible that the TP load as calculated above from the mean grab sample data underestimates the TP loading to Lake Erie, and that a more continuous measure of TP concentrations is needed to obtain an accurate estimate. Strong linear relationships existed between the grab samples taken at the Trenton Channel grab sample (TC1-TC5) and TCISCO station locations. Since the TP concentration in the Trenton and other channels varied both spatially and temporally the relationships developed between the grab sample data collected for the Trenton Channel were used to give a time-varying estimate of TP concentration. These concentrations were used with the flow factors to produce a more continuous estimate of TP load to Lake Erie from the Trenton Channel.

The discharge passing by each grab sample location was used to calculate the total volume passing through each location over a 24-hour period, which was multiplied by the 24-hour (daily) composite TP concentration at each location as determined from the linear fitted model developed from the grab sample data. These sub-loadings were then summed to provide an estimate for the TP load for the entire Trenton Channel over a 24-hour period as given by Equation 3:

$$TP_{TC} = \sum_{n=1}^{k=5} V_n \cdot tp'_n \quad (\text{Eq. 3})$$

Where TP_{TC} = the 24-hour total phosphorus loading (kg) from the Trenton Channel; V_n = the volume (m^3) of water flowing through each location in the Trenton Channel over a 24-hour period; tp'_n = the estimated 24-hour total phosphorus concentration (mg/L) at each location in the Trenton Channel as derived from the model-fitted relationships. In this case $k = 5$ as there are five grab sample locations in the Trenton Channel. Using this method the total load of phosphorus to Lake Erie from the Trenton Channel was estimated from a number of relationships to be between approximately 540,200 and 918,400 kg for the period of August to November 2007 or between 1621 and 2755 mta. In comparison, using the mean grab sample data the estimated TP load from the Trenton channel was between 836 and 913 mta.

Given the temporal variability observed in the TP concentrations as measured in the Trenton Channel, the TP load estimated above using the 24-hour (daily) composite data from the Trenton Channel ISCO station should be considered a more accurate estimate than that obtained from the grab sample data. Overall the use of continuous ISCO samplers provided a more robust estimate of the TP loads for the Detroit River compared to grab sampling alone. This study demonstrated that the temporal variability in TP concentrations necessitates a continuous sampling approach.

Conclusions

The flow factors determined from the adapted flow model were used to estimate the total flow to be applied to each grab sample location over the study period. This total flow was used with the measured TP concentrations to estimate the TP load to Lake Erie. Using the mean grab sample concentrations with the calculated flows resulted in a TP load of approximately 2557 mta for the entire lower Detroit River, with 836 to 913 mta coming from the Trenton Channel alone. This TP load estimate for the lower Detroit River was close to the 2135 mta estimated in 2004.

However, the study results also indicate that there is temporal variability of TP loading, and show that the TP loads to Lake Erie can be underestimated if spatial variability is not accounted for. Using the current best estimates (Table 1) of between 2000 and 2500 mta for the Trenton channel based on the ISCO results, and grab sample data for the remaining channels, the estimates for TP to Lake Erie via the Detroit River range from roughly 3500 mta to 4300 mta, a significant increase from previous estimates. Additional time varying sampling and analysis could improve these estimates further.

Table 1 – Loading Estimate to Lake Erie

Channel	Data Used For Estimate	Current Best Estimate Range (mta)	
		Low	High
Trenton Ch. (TC)	grab sample relationships and ISCO 24 hour (daily) composite data	2000	2500
West Sugar Is. (WS)	grab sample data	225.3	271.2
East Sugar Is. (ES)	grab sample data	76.8	99.6
Livingstone Ch. (LC)	grab sample data	314.4	354.9
Bois Blanc Ch. (BB)	grab sample data	60.0	84.9
Amherstburg Ch. (AC)*	grab sample data	870.9	1006.2
Total Load	--	3547	4317

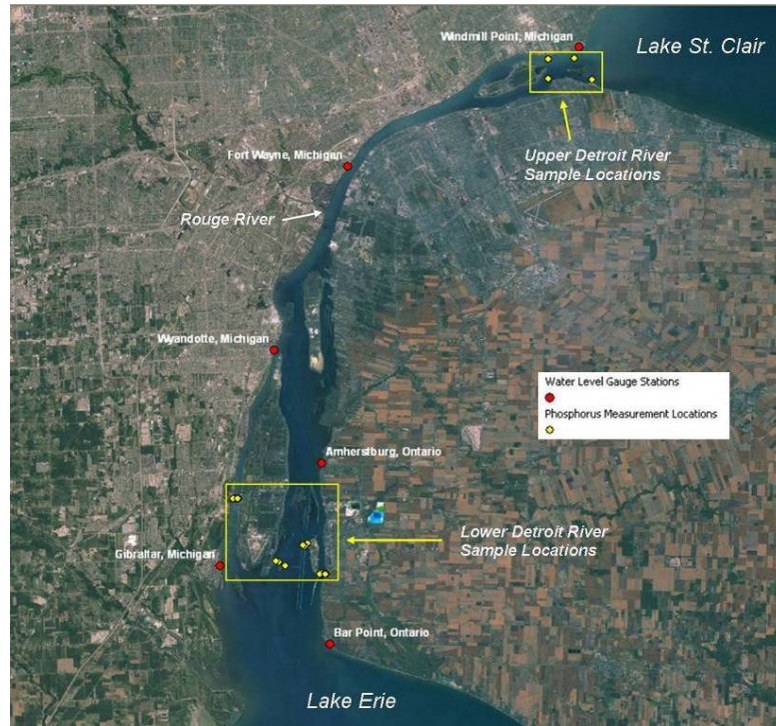


Figure 1: Detroit River study area.

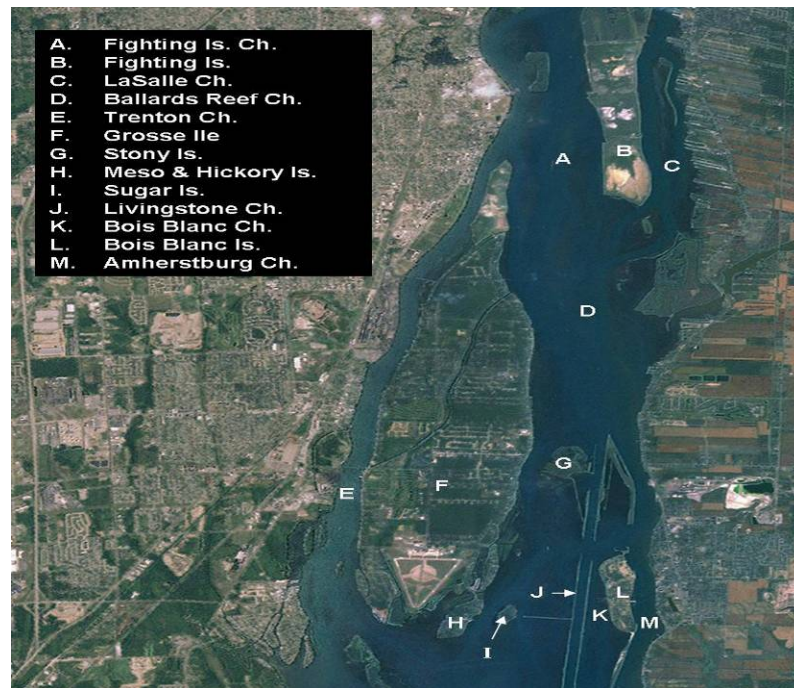


Figure 2: Lower Detroit River features and channels.

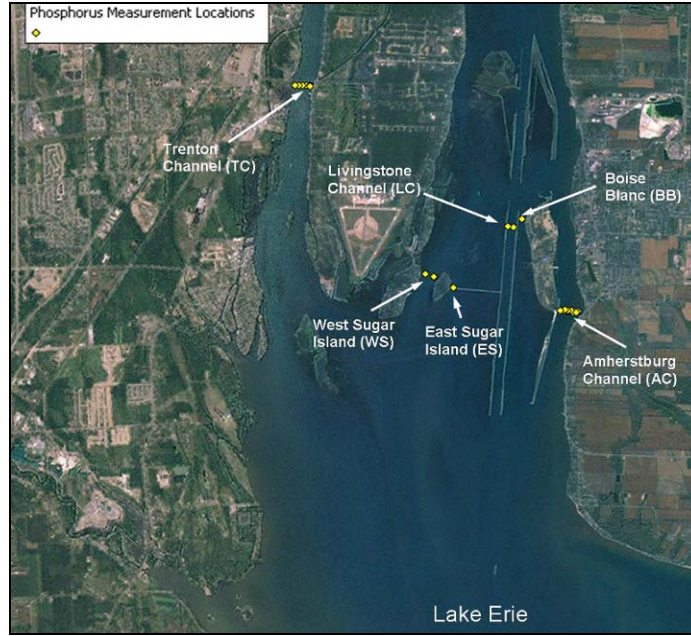


Figure 3 – Sample locations in lower Detroit River



Figure 4 – Sample locations in Trenton Channel

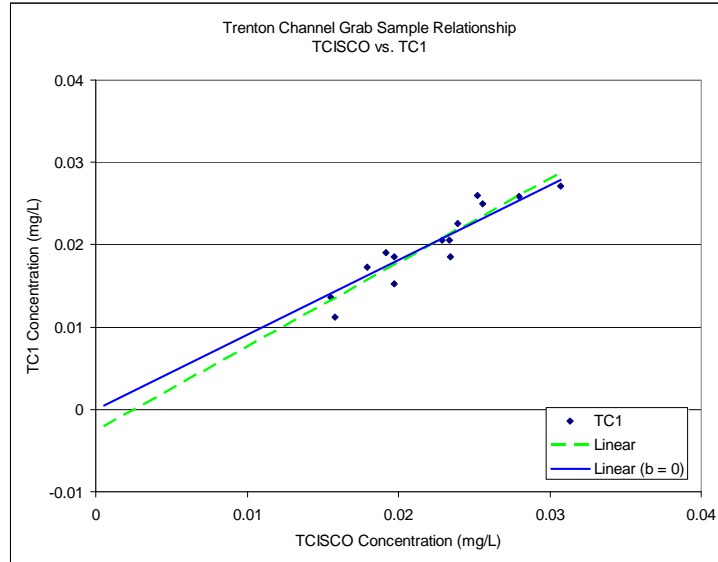


Figure 5 – Correlation between grab samples at TC1 and TCISCO sampling locations

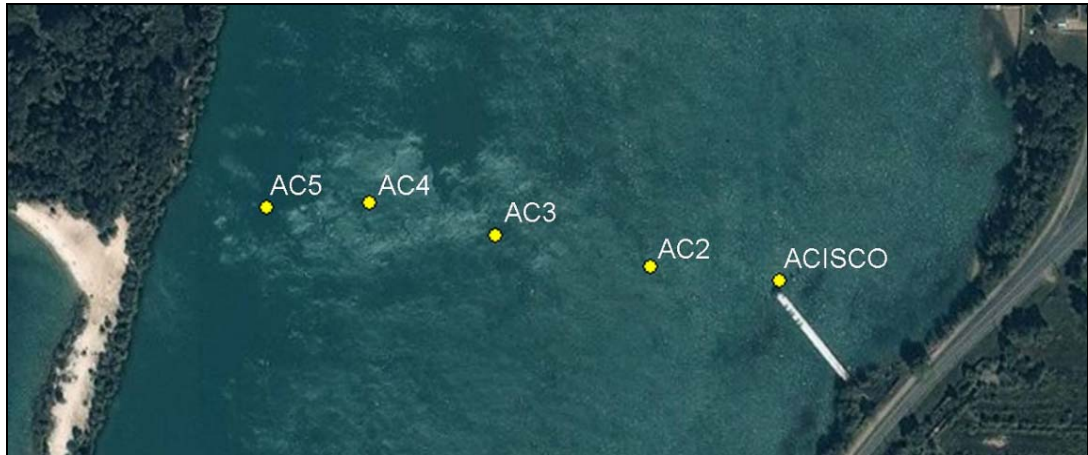


Figure 6 – Sample locations in the Amherstburg Channel

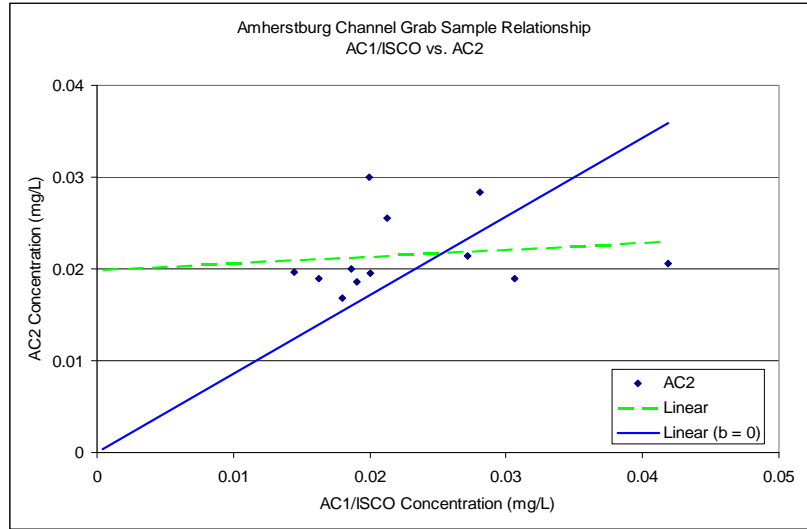


Figure 7 – Correlation between grab samples at TC1 and TCISCO sampling locations

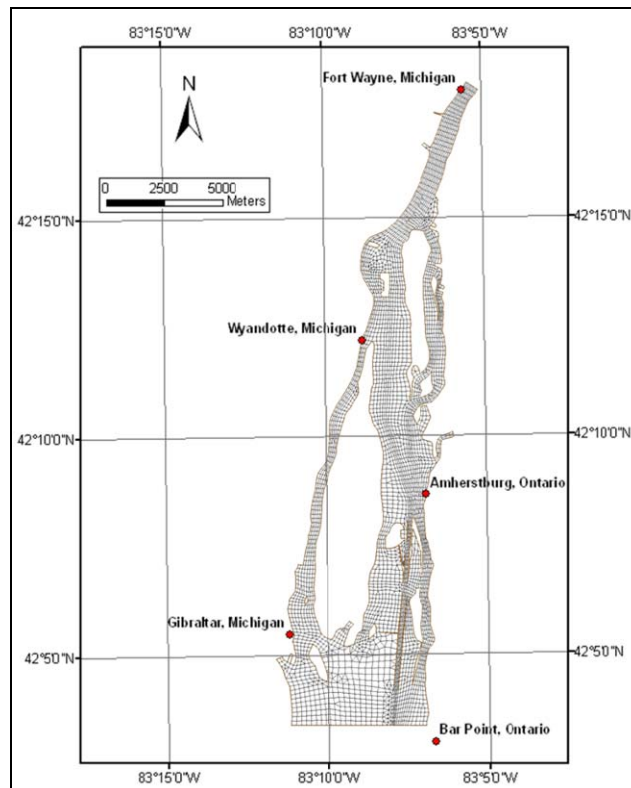


Figure 8 - Lower Detroit River RMA2 model mesh extent, boundaries and water level gauge locations.

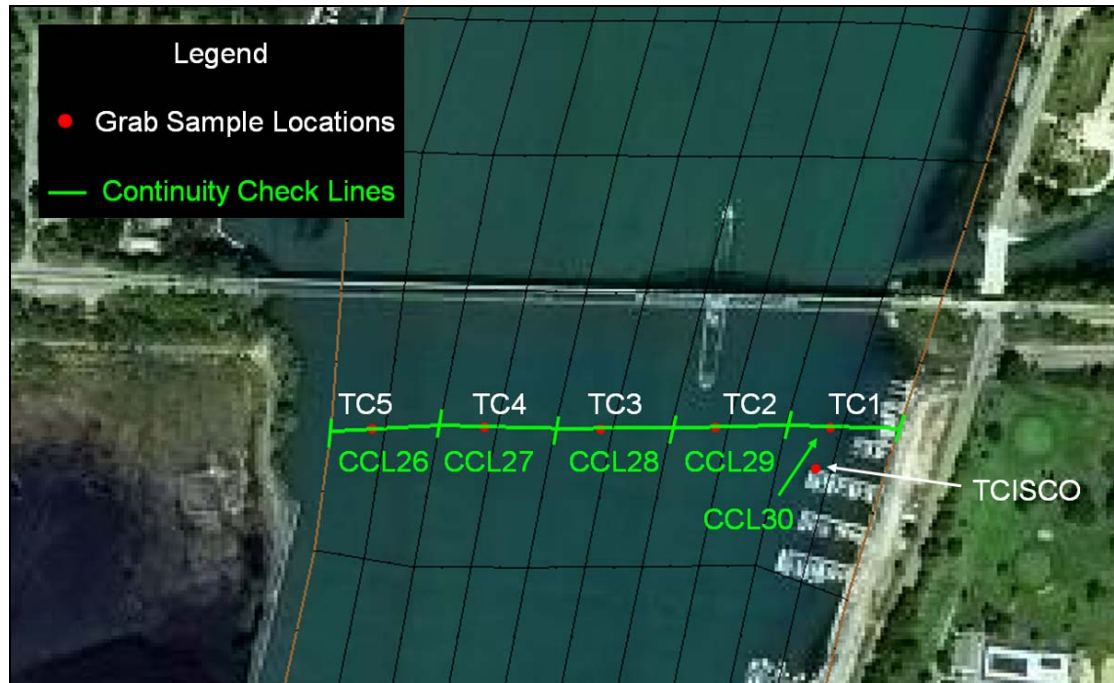


Figure 9 - Example of continuity check lines (CCL) located at Trenton Channel grab sample locations.

References

Holtschlag, D. J. and Koschik, J. A. (2002a). *A two-dimensional hydrodynamic model of the St. Clair and Detroit Rivers within the Great Lakes Basin*: U.S. Geological Survey Water Resources Investigations Report 01-4236.

<http://mi.water.usgs.gov/pubs/WRIR/WRIR01-4236/>

Holtschlag, D. J. and Koschik, J. A. (2002b). *Flow distribution of selected branches of St. Clair and Detroit Rivers*. *Journal of Great Lakes Research*. 28(3), pp. 379-395.

Ontario Ministry of Environment Data source:

<http://www.ene.gov.on.ca/en/publications/dataproducts/index.php#PartWater>.

Upper Great Lakes Connecting Channels Study 1984 - 1988. Final Report of the Upper Great Lakes Connecting Channels Study Volume II. December 1988. 626 pp.

Burniston et al., *Detroit River Phosphorus Loading Determination*. Environment Canada Internal Publication #WQMS09-006. 2010.

Modeling of October 2010 Storm Surge in Lake Winnipeg

Padala Chittibabu¹, Yerubandi R. Rao¹

¹National Water Research Institute, Water Science and Technology Directorate, Environment Canada,
867 Lakeshore Rd., Burlington, ON, Canada L7R 4A6
Corresponding author email : padala.chittibabu@ec.gc.ca

Abstract

The wind and pressure fields from two high resolution weather forecast models were used to drive a high resolution unstructured grid two-dimensional finite element model to simulate the storm surge associated with the October, 2010 extra tropical storm in Lake Winnipeg. The model results were compared with the observed water levels at several stations during the storm event. The model predicted storm surge in the range of 0.6 to 1.5 m is comparable to observations in the southern basin of Lake Winnipeg. Model results are further analyzed to assess the transport of water between north and south basins of Lake Winnipeg during the event. Computed water surface elevations at specific locations at the outlet of the rivers and embayments indicate that the model needs some improvements in terms of grid resolution in those areas.

Introduction

Lake Winnipeg is the 10th largest freshwater lake in the world and the 5th largest in Canada (LWSB 2006). It has two distinct basins, the north basin (100 km wide) and the south basin (40 km wide), which are separated by the Narrows, a 2.5 km wide channel. The dual-basin lake is elongated in shape, extends 436 km from north to south, and is relatively shallow with a mean depth of 9 m and 12 m in south and north basins, respectively. Due to the Lake Winnipeg's orientation, shape and shallow bathymetry, the Lake Winnipeg generally experiences higher amplitudes of surge in comparison to some other large lakes. Its elongated shape from north to south allows a long fetch of about 440 km for wind to cause higher setup over the southern basin whenever there is a predominant northerly wind. The recent extra-tropical storm on 27 October, 2010 over Lake Winnipeg produced considerable damage along the southern shores of Lake Winnipeg. Storm surges more than a meter are observed at several recording stations. Since accurate shore line representation is important to calculate inundation due to storm surge flooding, we use a unstructured grid finite element model, A Parallel Advanced Circulation model for Oceanic, Coastal and Estuarine Waters (ADCIRC) to simulate the storm surge associated with the October 27th storm.

2.0 Hydrodynamic Model and Grid

Storm surge simulations are performed using the two dimensional form of ADCIRC (Luettich et al. 1992) model. A high-resolution grid was generated for the ADCIRC

model using the grid generator from Surface Modeling System (AQVEO, 2010). The bathymetry of Lake Winnipeg (Figure 1) is obtained from Canadian Hydrographic Service Charts. The mean lake level (MLL) of 217.44 m was derived from Environment Canada's long term level average. Bathymetry depths in the model were adjusted to the October 23 level. The model domain covers from 96.20° W to 99.27° W and 50.24° N to 54.45° N (Fig. 1). The total number of horizontal grid elements is 109,169 and the total number of nodes is 56,976. The spatial grid resolution varies from 85m in the shallow waters and along the shoreline to 500m in the deeper offshore waters. The configuration of the grid used in this study is shown in Fig. 2.

We used wind and pressure fields from two numerical atmospheric model forecasts which are available at good spatial resolution. The first atmospheric model forcing used in this study is from the regional version of the GEM (Global Environmental multi-scale Model). The second numerical forecast model is North American Mesoscale Model (NAM) run by National Environmental Prediction centre (Rogers et al., 2009). Wind speeds from the models are corrected for over-water values before using those in the hydrodynamic model. The method used to spatially interpolate the winds from the 15-km GEM grid and 12-km NAM grid to the model grid is carried internally by ADCIRC model.

3.0 Results and Discussion

The model results are validated with water levels recorded from six water level gauges located in both southern and northern basins of the lake. Since the flow from the north basin would influence the water levels in the south basin, we will also examine the exchange flow between the basins during the storm period.

Figures 3(a to h) show the comparison of hourly time series of observed and modelled water levels at eight water level gauge locations using GEM and NAM forcings. On the west coast of the north basin at Mission Point, where the surges are negative (-0.82) GEM forcing resulted in better predictions than the NAM forcing. However, at an interior station (Play Green Lake) both models over-estimated the negative surges. This could be due to lack resolution in this bay or due to other factors such as outflow controls at this location. Farther south near the George Island, both model forcings predicted similar negative surges, with early arrival of negative surge at this location. It could be due to the representation of topography or due to the location of the gauge itself. Although observations at this location show several small scale oscillations due to seiches, model results are not able to predict those fluctuations. The positive storm surges from the Narrows to the southern shoreline are well-predicted by both model forcings. At most of these locations the results from GEM compare slightly better than the results from the NAM model. The surge values at Victoria Beach and Gimili are 1.39 and 1.21 respectively, which are close to the observations. The highest surge of 1.9 m simulated by the GEM model at Breezi Point inside the Red river is 0.5 m higher than the observed surge. The representation of shoreline as a solid boundary may not have allowed the passage of higher surges into the Red River, and could be the main reason for

amplification of surge at this location. In general the ADCIRC model is able to simulate the timing of peak surge that occurred at 2:00 AM on 28 October, 2010.

Figures 4 show the simulated water surface elevations and depth-averaged currents produced by the model with GEM and NAM forcings at the peak surge occurrence. Although both models produce negative surges in the northern portion of the north basin, there are some subtle differences. The negative surge area from the NAM forcing is large and the magnitude is slightly smaller. Further, NAM also shows significantly higher surges in the embayment of the western shoreline. Because of these differences the simulated circulation is also slightly different under these forcings. The current speeds varied from 0.2 to 2.0 m/s, with strongest currents occurring near the south-western corner of the north basin of Lake Winnipeg. The cyclonic gyre in the north basin is confined to the southern portion of the north basin with the GEM forcing, whereas it extended to much larger area with the NAM forcing. Several other gyres, particularly along the western shoreline are produced with the GEM forcing. In the southern basin and north of the Narrows, surge levels are positive in both models, which is consistent with observations. The peak surges produced by GEM forcing along the southern shoreline is consistent with observations. In general both model forcings produced similar circulation patterns in the south basin, which is consistent with the expected coastal dynamics. Figure 5 shows the net transport between two basins as simulated by NAM and GEM model forcings. During the storm between 26 and 28 October, a net volume of 4.6 km³ water flowed into the south basin. The volume of the south basin at the MLL is 27 km³ for a mean depth of 9.7 m (Brunskill et al. 1980). Therefore, during the storm the net transport from the north basin increased the water levels in the south basin by 11.4 cm.

6. Conclusions

A two dimensional, finite element model, ADCIRC, has been used to simulate storm surge and depth averaged currents in Lake Winnipeg associated with October 2010 storm. The wind and pressure fields from two operational forecast models were used to drive the model. The sensitivity experiments suggest that the barometric pressure effect is not significant for storm surge generation in the lake. The model results are verified with observed water surface elevations at several gauge locations. Comparisons of the model results with the observed water levels demonstrate that the model can simulate storm surges reasonably well.

The model developed in this study can be useful to lake modelers and for planning the coastal protection works. Although, surface waves during the storms can be a potential hazard, we have not considered its effect in this study. Studies are underway to couple a shallow water wave model with ADCIRC model for Lake Winnipeg. Further, the influence of major tributaries and associated flood waters during the storms need to be assessed.

References

AQUAVEO. 2010. Surface modelling system user guide. 22pp. Utah. United States

Brunskill, G.J., Elliott, S.E.M., Campbell, P. 1980. Morphometry, hydrology, and watershed data pertinent to the limnology of Lake Winnipeg. Canadian manuscript report of fisheries and aquatic sciences, no. 1556

Lake Winnipeg Stewardship Board, 2006. Nutrient Literature Review.
http://www.lakewinnipeg.org/web/downloads/Nutrient_Literature_Review_LakeWinnipeg_FinalMay_2006.pdf.

Luetlich, R. A., Jr., Westerink, J. J., and Scheffner, N. W. 1992. ADCIRC: An advanced three-dimensional circulation model for shelves, coasts and estuaries. Report 1: Theory and methodology of ADCIRC- 2DDI and ADCIRC-3DL. Technical Rep. DRP-92-6, U.S. Army Corps of Engineers, Waterways Experiment Station, Vicksburg, Miss.

Schwab, D.J., and Morton, J.A. 1984. Estimation of overlake wind speed from overland wind speed: A comparison of three methods. *Journal of Great Lakes Research*. **10**(1):68-72.

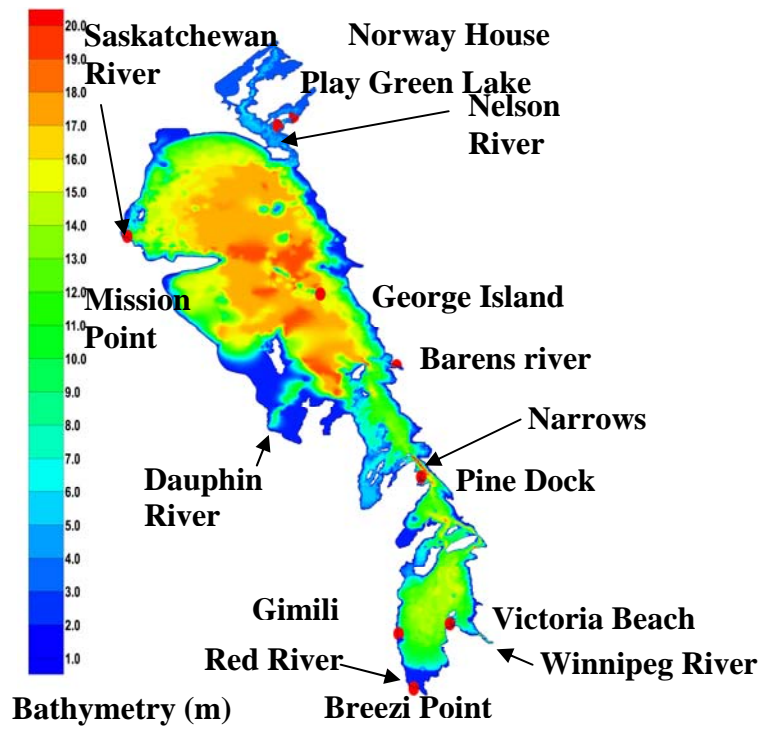


Figure 1 Bathymetry of Lake Winnipeg with water level gauge locations



Figure 2 Unstructured model mesh of Lake Winnipeg

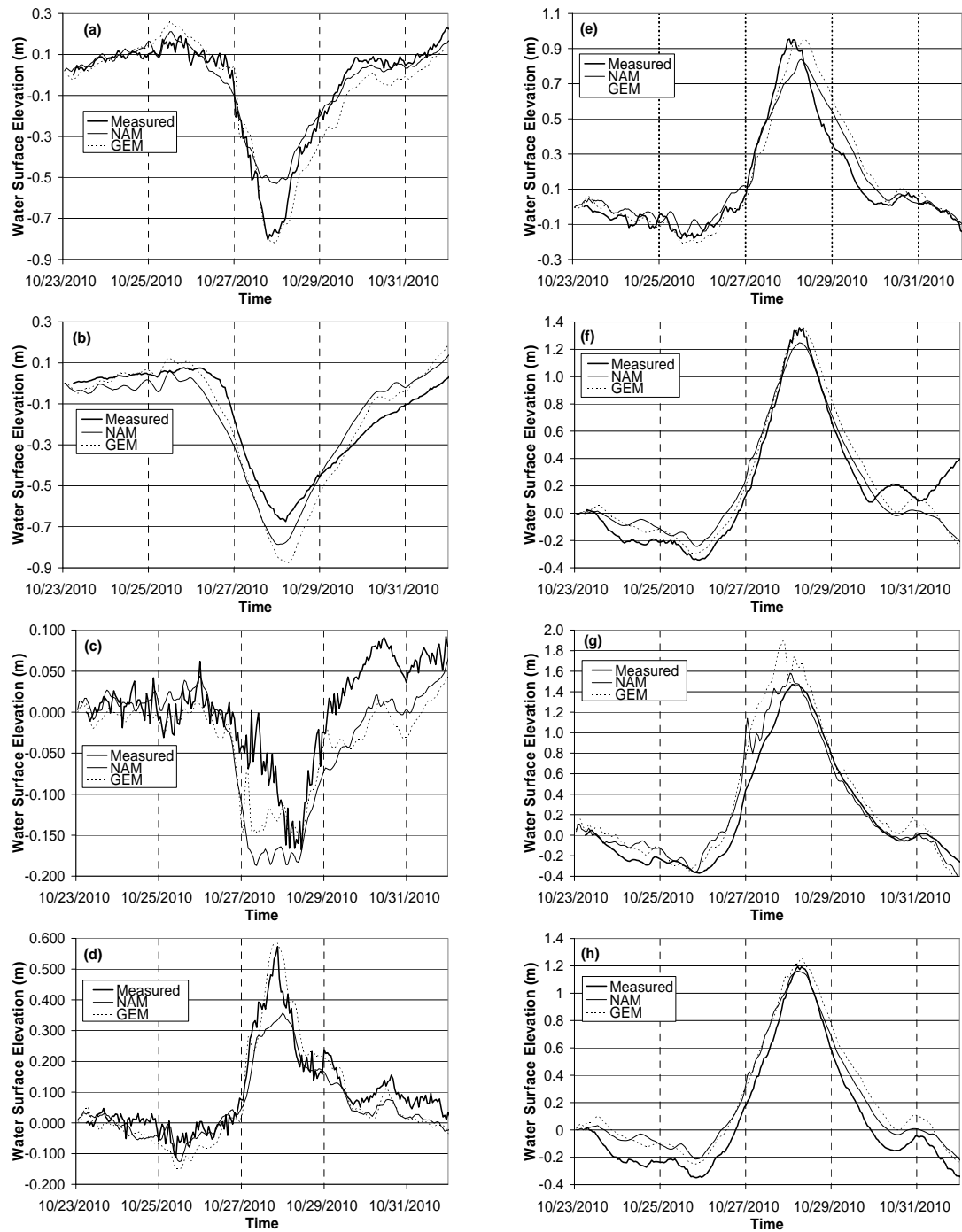


Figure 3 Time series of observed and modelled water level deviations from 23 October level at (a) Mission Point (b) Play Green Lake (c) George Island (d) Berens River (e) Pine Dock (f) Victoria Beach (g) Breezi Point (h) Gimli.

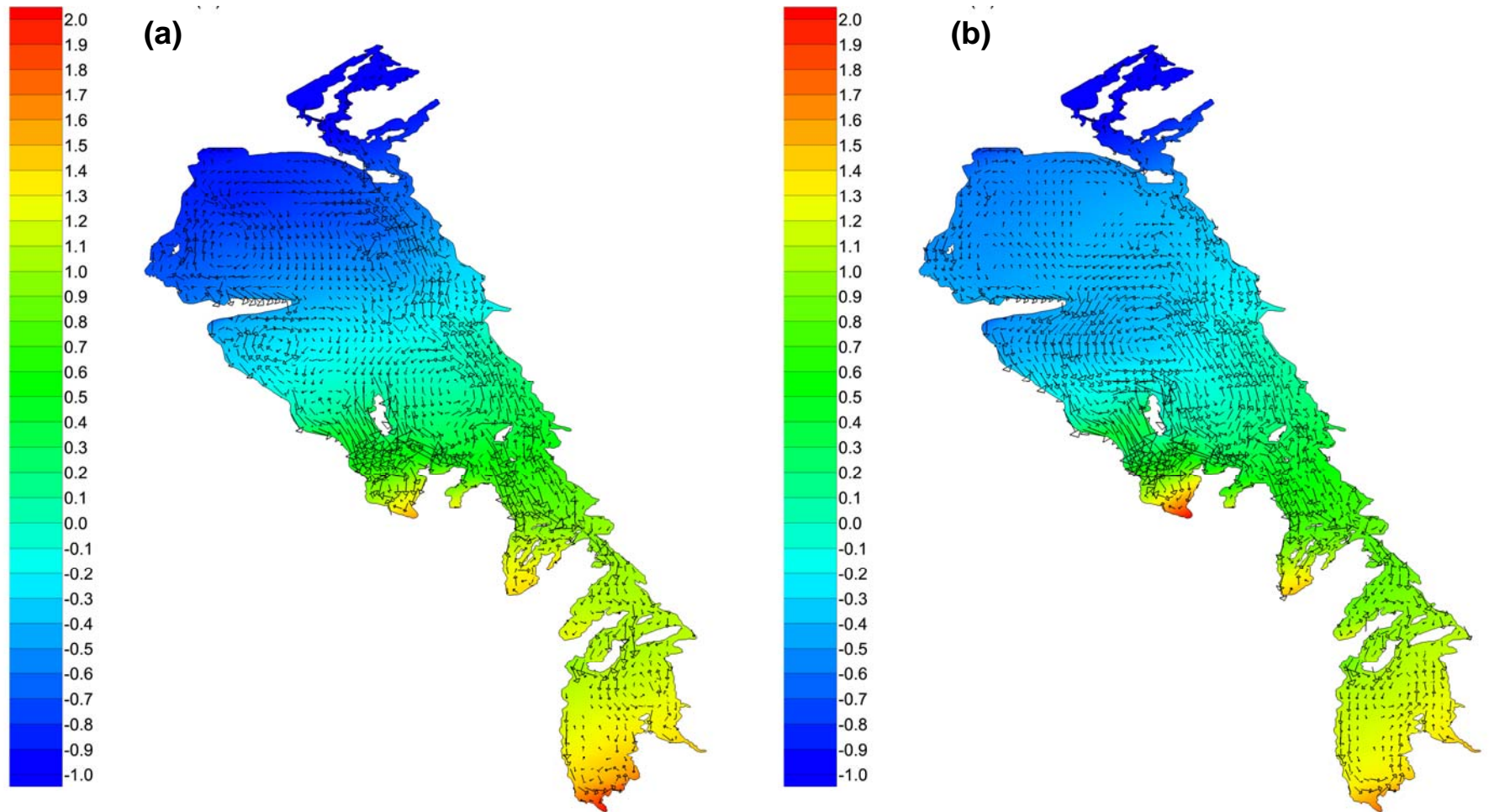


Figure 4 Modelled water level deviations and depth-averaged currents at the time of peak surge occurrence- (a) GEM (b) NAM.

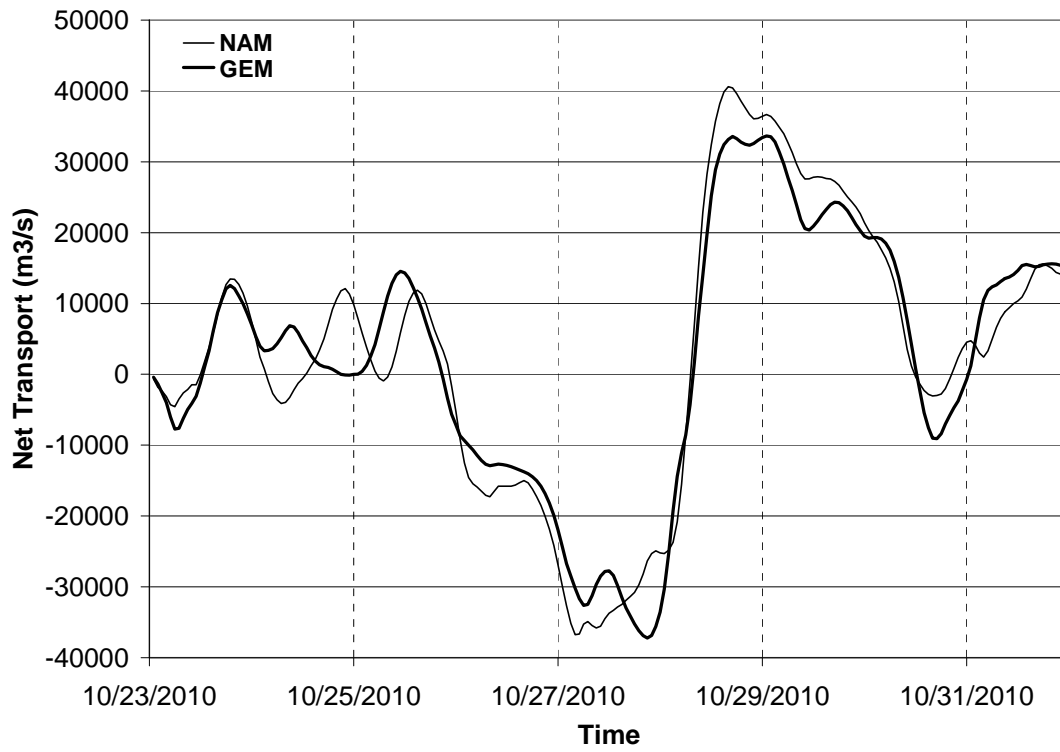


Figure 5. Modelled net transport between North and South basins. Here -ve indicates flow to the south basin.

Temperature variability above three sites with different slopes in the near shore benthic region of Lake Opeongo, Canada.

M.A. Coman^{1*} and M.G. Wells¹

¹ Department of Physical and Environmental Sciences, University of Toronto Scarborough, 1265 Military Trail, Toronto, ON, Canada, M1C 1A4

*Corresponding author, e-mail melissa.coman@utoronto.ca

KEYWORDS

Temperature variability; thermocline tilt; near shore benthic; sloping bottom; Lake number.

EXTENDED ABSTRACT

The wind driven basin scale seiche is the primary cause of daily and smaller scale temperature variability in medium sized, stratified lakes. This seiche causes vertical displacement of isotherms, resulting in localized fluctuations of temperature and we investigate whether internal waves or convective instability is the most important mechanism at the depth where the thermocline intersects the lake bed (near shore benthic region). Fluctuations of a few degrees over a few hours can arise due to these motions, which will directly impact the food web as the temperature fluctuations affect species morbidity and lake productivity. Previous studies on Lake Opeongo have shown a strong correlation between environmental variability (temperature, wind) and biological growth, diversity and spatial location. Finlay *et al.* (2001) found that wind played an important role in driving temperature variability in the littoral zone. They found that upwind sites showed more variability than downwind sites, which they concluded would cause variations in the productivity of different regions of the littoral zone, such as the locations of bass nests during spring. In a field experiment in the South Arm basin of Lake Opeongo McCabe and Cyr (2006) found the diversity of benthic algal communities increased with increasing temperature variability in the littoral zones. Specifically they measured larger temperature variability in the west end of South Arm, which was both upwind and located on a shallow slope, compared to the east end, which had less temperature variability in the downwind, steeper sloped environment. Of critical interest to limnologists is understanding the location, frequency and magnitude of near shore benthic temperature variability. In this paper we will discover whether the presence of temperature variability in the near shore benthic region is predicted by Lake number, L_N , and if basin slope is a factor. The research was conducted in Lake Opeongo, Canada between May and September 2009. It is a low nutrient, medium sized lake typical of many Canadian Shield lakes. We instrumented the east-west orientated South Arm basin with 3 inshore fast response thermistor strings. The sites were situated above bottom slopes of 1% (site I1) and 8% (site I2) in the west end of the basin and of 4% (site I3) in the east. The daily wind mostly blew from the west and the thermocline was at 5–9 m during this study. We define an overturn (temperature inversion) to occur when the temperature difference between two vertically separated thermistors exceeds the threshold: $T(z_1) - T(z_2) \leq -0.03^\circ\text{C}$, where the height of the thermistors are such that $z_1 > z_2$.

The number of overturns at each depth for each inshore site is shown as a contour plot of overturns/12 hours in Figure 1a. Most of the overturns exist in the bottom 2 m of the lake at all sites, however the number and frequency of overturns is quite different. Site I1 has the

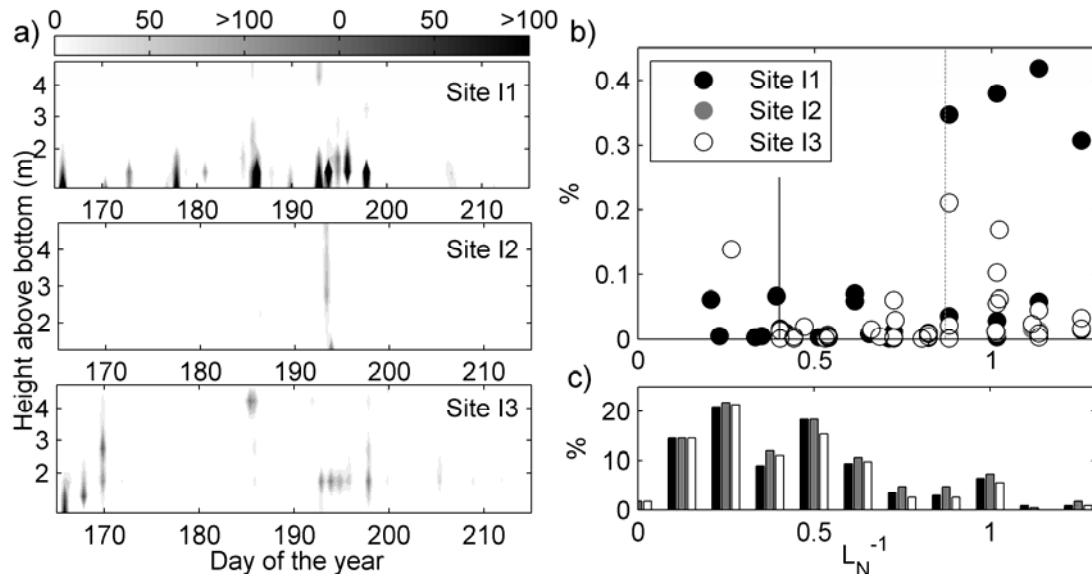


Figure 1. a) Contour plot of overturns/12 hours for the 3 inshore sites at a depth of 10 m b) histogram of the % of time in 3 hrs that the water column contained overturns and c) histogram of the % of the entire time that the water column is stable (i.e. no overturns).

largest amount of overturns and also the greatest frequency. In contrast site I2 has only one major occurrence of overturn activity. Site I3 has a moderate number of overturns, with a frequency slightly less than site I1. On the one occasion in the overturn record when an easterly is blowing at more than 4 m/s (day 169) the response at site I3 is stronger compared to site I1. The number of overturns at sites I1 and I3 suggest that the benthic near shore region at the upwind end of a basin will have a larger amount of temperature inversions compared to the downwind end, consistent with previous work. The exception is the response at site I2. Although one may expect a similar response from sites I1 and I2 due to their location in the west basin, two important differences exist. I2 is situated above a relatively steep slope of 8% and secondly, site I1 is aligned with the major along lake axis whereas I2 is slightly south of the main axis. Considering the small response from site I2 we suggest that the number of overturns in the water column for any near shore location will also be a factor of bottom slope and location relative to the major lake axis and prevailing wind direction. To help understand when to expect overturns in the water column we compare L_N to a measure of overturn magnitude. Specifically in Figure 1b we compare L_N to the percentage of time in 3 hours that the water column at each site contains at least one overturn. We do not include data for which no overturn was measured; this is presented in Figure 1c. Figure 1b shows that the largest L_N for which we measure overturns in the near shore region is about $L_N \sim 5$, and that on the steep slope L_N had to drop below 1.2 before overturns occurred there. Figure 1c shows a histogram of the percentage of the entire time that the water column contained no overturns. We see that about 50% of this no-overturn data occurs for $L_N > 2.5$ and that if $L_N \leq 1$ there is a 90% chance that there will be overturns in the near shore region. Therefore from Figure 1b and c we learn that $L_N < 2.5$ before there is a 50% chance that overturns will be measured at site I1 and site I3 and that $L_N < 1.15$ for overturns to be found at site I2. Based on these results we expect that the greatest number of overturns may occur in near shore benthic regions that are upwind, have bottom slopes below 4% and are aligned with the main axis of the wind. We expect the frequency of overturns to be dependent on L_N being below a critical value, $L_N < 2.5$ for shallow or moderate slopes and $L_N < 1.15$ for steep slopes.

Finlay, K., Cyr, H. and Shuter, B.J. (2001). Spatial and temporal variability in water temperatures in the littoral zone of a multibasin lake. *Can. J. Fish. Aquat. Sci.*, 58, 609 - 619.

McCabe, S.K. and Cyr, H. (2006). Environmental variability influences the structure of benthic algal communities in an oligotrophic lake. *Oikos.*, 115(2), 197-206.

Experimental Observations of Flow Structures in Submarine Channels under the Influence of Coriolis Forces

R. Cossu^{1*}, M.G. Wells²

¹ *Department of Geology, University of Toronto 22 Russell Street, Toronto, Ontario, M5S 3B1, Canada*

² *Department of Physical & Environmental Sciences, University of Toronto, 1265 Military Trail, Toronto, Ontario M1C 1A4, Canada*

* remo.cossu@utoronto.ca

KEYWORDS

gravity currents; Coriolis forces; submarine channels

EXTENDED ABSTRACT

Submarine channels are the main conduits for turbidity currents to transport sediments from the continental shelf over thousands of kilometers to deep ocean basins. Coriolis forces can become important at higher latitudes and influence the processes by which submarine channels evolve. Channels systems at low latitudes often show sinuous planform geometries similar to meandering rivers, whilst at high latitudes they are less sinuous [Peakall *et al.*, 2011]. We present results from experimental gravity currents to show that the density interface and position of the downstream velocity core shift when Coriolis forces dominate the internal flow structure of channelized turbidity currents. We combine our new observations of the velocity structure with an existing conceptual model [Amos *et al.*, 2010] for sedimentation and erosion in sinuous submarine channels to elucidate potentially different sedimentation patterns at different latitudes.

The experiments were conducted in a channel model placed in a tank that was rotated at various rates (reflected by the Coriolis parameters f) ranging from $f = 0$ to $\pm 0.5 \text{ rad s}^{-1}$. The channel consisted of a 0.64 m long straight section, joined to a 0.9 m long single left turning channel bend with a mean radius of $r = 0.36 \text{ m}$. We used saline gravity currents as a surrogate for fine mud turbidity currents. Downstream and cross stream velocity data in the channel bend were recorded using a Metflow Ultrasonic Doppler Velocity Profiler (UDVP) and additional downstream data were taken along the channel with a Nortek Acoustic Doppler Velocimeter (ADV).

Some of the main experimental results are shown in Figure 1. The strong dependence of the slope of the density interface on rotation is shown in a series of photographs in Figure 1. For $f = 0 \text{ rad s}^{-1}$ the density interface slopes up towards the outer bend due to the centrifugal acceleration. For a positive Coriolis parameter $f = +0.25 \text{ rad s}^{-1}$ the tilt of the interface towards the outer bend increases as now the Coriolis and centrifugal forces act in the same direction. In contrast, for a larger negative Coriolis parameter $f = -0.5 \text{ rad s}^{-1}$ the current ramps up towards the inner bend and is completely reversed. The changes in the position of the density interface clearly correspond to changes in the position of the location of downstream velocity core (u_{max} , Figure 1b). For $f = 0 \text{ rad s}^{-1}$ the velocity core is predominantly close to the centre

line whilst for $f = -0.5 \text{ rad s}^{-1}$ a significant deflection of the velocity core towards the inner bend can be seen. For $f = +0.25 \text{ rad s}^{-1}$ the velocity core is shifted towards the outer bank while there is almost no downstream flow near the inner bend.

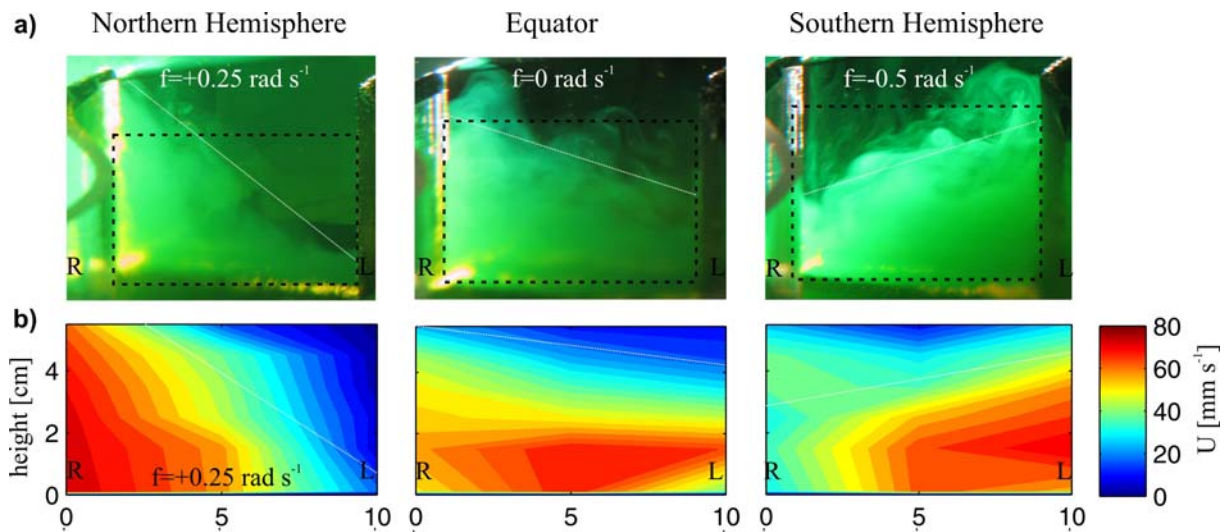


Figure 1. a) Photos of the density interface for various rotation rates f . b) Position of the downstream velocity core for various f . The perspective is upstream.

Based upon the locations of the downstream velocity maxima and the dependence of erosion and deposition on the velocity structure we hypothesize that Coriolis forces will introduce a shift at high latitudes. In bed-load dominated flows at high latitudes we predict that lateral accretion packages (LAP) are built only on one side, thus inhibiting the growth of channel bends. In suspension fall-out regimes sediment will mainly be deposited on the side to which the high velocity core is shifted resulting in significant levee asymmetries due to overbanking. In both sedimentation regimes, the shift of the velocity core to either the left- or right-hand-side of the channel should lead to a gradual decrease in sinuosity in mid- and high latitude systems and a lateral migration of the entire channel pathway. The relation of the Rossby number $Ro_w = U/fW$ (where U is the mean downstream velocity and W the channel width) to R/W (with R being the radius of curvature) can be used to determine whether a submarine channel system is influenced by Coriolis forces (Cossu and Wells, 2011). In channel systems at high-latitudes in the Northern Hemisphere we predict $|Ro_w| < |R/W|$, so that channels exhibit a low sinuosity, have a distinct higher right levee system and migrate predominantly to the left side. In channel systems at low latitudes we usually find $|Ro_w| > |R/W|$ implying that Coriolis forces are negligible. LAPs are then formed on the inside of bends enabling an increase in sinuosity. Therefore equatorial channel systems can become very sinuous, show a distinct lateral migration to both sides and alternating levee asymmetry in subsequent channel bends.

REFERENCES

- Amos, K. J., Peakall, J., Bradbury, P. W., Roberts, M., Keevil, G., and Gupta, S. (2010). The influence of bend amplitude and planform morphology on flow and sedimentation in submarine channels. *Mar. Petrol. Geol.*, **27**, 1431-1447.
- Cossu, R., and Wells, M.G. (2011). Flow Structures and Sedimentation Processes in Submarine Channels under the Influence of Coriolis Forces: Experimental Observations in Rotating Gravity Currents. Submitted to *Geology*.
- Peakall, J., Kane, I.A., Masson, D.G., Keevil, G., McCaffrey, W. and Corney, R. (2011). Global (Latitudinal) variation in submarine channel sinuosity. Submitted to *Geology*.

Horizontal exchange across the thermal bar front: laboratory and numerical modelling

N. Demchenko*, I.Chubarenko

*P.P.Shirshov Institute of Oceanology RAS, Atlantic branch, Prospect Mira, 1, 236022,
Kaliningrad, Russia*

**Corresponding author, e-mail ndemchenko@mail.ru*

KEYWORDS

Buoyancy flux; flow-rate; horizontal exchange; onshore flow; passive tracers; thermal bar.

INTRODUCTION

The ‘thermal bar’ is a remarkable phenomenon, seasonally arising at mid latitudes in large lakes and in coastal regions, when water temperature gradually increases in spring (or decreases in autumn) and then crosses the temperature of maximum density (hereafter referred to as T_m ; for fresh water, $T_m \approx 4^\circ\text{C}$). Under both spring heating and autumn cooling conditions, crossing over the T_m leads to principal change of type of vertical mixing regime: vertical convection is replaced by the establishing of a direct summer (or inverse winter) stratification. For simplicity, we shall speak further for the conditions of the “spring” thermal bar. Field studies in many large lakes, including, e.g., Lake Ladoga (Rymiantsev and Drabkova 2002), Lake Baikal (Wüest et al. 2005), and Lake Michigan (Mortimer 2004), have demonstrated its significance for the basin-wide water circulation, transport and biological processes. The point addressed in the present study is a nature of the thermal bar permeability for horizontal mixing. We present the results of laboratory experiments in 2-m-long basin with sloping bottom, heated from the free surface, starting from water temperature $T < T_m$, what reproduces the development of the spring thermal bar in a lake. The PIV method was used in order to obtain a detailed structure of the flow field, especially, to reveal onshore flow in intermediate layers. The process was also reproduced numerically.

METHODS

The experiments were performed in 2-m long water channel with a sloping bottom, the slope being defined by the aspect ratio of the maximum water depth D to the tank length L , with $A = D/L \sim 0.1$. The tank was filled with tap water, which was cooled down to a temperature of 1°C by using a cooling machine (ULTRA KRYOMAT TK-30D) and by putting melting ice cubes on the free surface. Subsequently, the water temperature gradually increased due to heat-exchange through the free surface with the warmer ambient air ($T_{\text{air}} \sim 22^\circ\text{C}$). The sidewalls and the bottom were thermally protected by insulating material. For the optical flow measurement, the middle part of the tank was used only. The fluid there was seeded Pliolite particles, initially sieved to have a maximum diameters of $250 \mu\text{m}$, soaked in the water and injected in some specific studied part of the tank. The particles were illuminated by an argon ion laser. The motion of the particles was recorded by the CCD camera; the video

window being 50 cm wide and 40 cm height. The DigiFlow software (see www.dalzielresearch.com) was used to track the particles and calculate the velocity fields. Numerical modelling of the spring thermal bar was performed using 3D non-hydrostatic MIKE3-FlowModel (<http://www.dhi.dk/>) at the scales of the laboratory flume and lake. One of the simulated flow domains was taken to be similar to the laboratory configuration; 80 x 20 cells (i.e., with mesh size 0.04 m) was used. Another domain was reproduced the dimensions of the natural lake: 50 m depth, 5000 m long, 2400 from which occupied slope with aspect ratio 0.02. Modelling was performed on the numerical grid 100 x 30 cells (50 m x 50 m) in horizontal, 50 layers (1 m each) in vertical time step of integration 2 s.

CONCLUSIONS

Laboratory and numerical experiments showed, that during the entire process of the thermal bar propagation, the compensating onshore flow is present at intermediate depths. Its intensity depends on the phase of the thermal bar development: in the ‘slow’ stage the onshore flow is very weak due to the very low buoyancy flux values, in the ‘fast’ stage, it is more intense due to larger buoyancy fluxes and stronger advection from the shallows. Thus, the thermal bar propagation in the ‘fast’ stage of its development supports horizontal transport.

The analysis of the passive tracers concentration distribution presented a clear description of the flow field and showed, that the compensating flow in the intermediate layers is observed during the thermal bar development and propagates onshore though the water area with the temperature very close the T_m .

The flow rate of horizontal transport during the thermal bar propagation is very important characteristic of the flow field. We attempted to link the flow rate to the spatial scale and horizontal density differences; this resulted in the relation $Q \sim [\Delta\rho/\rho_0]^{1/2} H^{3/2}]^{1.0}$ with high correlation coefficient. This law provides an opportunity to estimate value of flow rate, which may help to solve water pollution problems, appearing during the evolution of the ‘spring’ thermal bar in the nearshore zone of large freshwater lakes.

ACKNOWLEDGEMENTS

The investigations are supported by grants RFBR-10-05-00472a, 10-05-00540, 11-05-90743-mob_st. The authors would like to express great thanks to Prof GertJan van Heijst for the possibility to perform the laboratory experiments at the Fluid Dynamics Laboratory, TU/e, the Netherlands.

REFERENCES

- Mortimer J. (2004). Lake Michigan in motion. University of Wisconsin Press, USA.
- Rymiantsev VA, Drabkova VG. (2002). Ladoga Lake: past, present and future. Nauka, Saint-Petersburg.
- Wüest AJ, Ravens TM, Granin NG, Kocsis O, Schurter M, Sturm M. (2005). Cold intrusions in Lake Baikal: Direct observational evidence for deep-water renewal. *Limnol. Oceanogr.*, **50**, 184-196.
- For information about the numerical simulation code of the MIKE3-FlowModel, see: <http://www.dhi.dk/>
- For information about the DigiFlow software, see: <http://www.dalzielresearch.com>

Flow Dynamics in a Free-Floating Macrophyte Root Canopy

M.A. Downing-Kunz* and M.T. Stacey

Department of Civil & Environmental Engineering, University of California, Berkeley, CA USA

*Corresponding author, e-mail mokunz@berkeley.edu

KEYWORDS

Macrophyte; canopy; vegetated flow; mixing layer, turbulence.

EXTENDED ABSTRACT

Macrophytes, macroscopic aquatic plants, modify the hydrodynamics of their environment by extracting fluid momentum. Macrophyte assemblages form canopies comprising the structural elements extending into the flow (i.e., leaves, stems, and/or roots). Studies of both submerged and emergent macrophyte canopies have found that a region of high velocity shear develops at the canopy-water interface, forming a mixing layer (Ghisalberti and Nepf, 2004; White and Nepf, 2007). A mixing layer is characterized by an inflection in the mean velocity profile, giving rise to coherent vortices that transport momentum and scalars across the canopy-water interface at greater rates than for conventional boundary layers (Raupach *et al.*, 1996). This increased transport causes macrophytes to strongly affect environmental processes such as nutrient and metals uptake, dissolved oxygen content, and sediment transport.

Unlike submerged and emergent macrophyte canopies, the hydrodynamics of root canopies in free-floating macrophytes are less studied. However, since the root canopy structure of free-floating macrophytes is fundamentally similar to that of submerged macrophytes, one can infer that the hydrodynamics are likewise analogous, and that a mixing layer should develop. Several species of free-floating macrophytes reduce water quality by lowering dissolved oxygen content, pH, and alkalinity; on the other hand these species can also improve water quality by removing nutrients (e.g., nitrogen and phosphorus) and heavy metals in wastewater treatment applications (Gopal, 1987). Despite these varied water quality impacts, little is known of the hydrodynamic interactions that control them.

The objective of this study was to characterize the hydrodynamics of flow through and around the root canopy of a finite patch of live, free-floating macrophytes. In this laboratory study, we observed spatial development of mean and turbulent flow structure using high-frequency velocity measurements.

This research was conducted using the tropical macrophyte *Eichhornia crassipes* (Martius) Solms, also known as common water hyacinth. *E. crassipes* floats at the water surface and has fibrous, unbranched roots with numerous feathery, densely-spaced laterals along the length. To study flow dynamics in *E. crassipes* root canopies, we constructed a canopy of dimensions $55 \times 55 \times 12.5$ cm (length, $L \times$ width \times height, h_c) comprising 35 individual plants (leaf density: 500 m^{-2}). Water velocity measurements were obtained using an acoustic Doppler velocimeter (ADV) in the recirculating laboratory flume previously described by Downing-Kunz and Stacey (2011). The ADV was deployed in downwards-looking mode and the sampling volume was aligned with the centerline of both flume and raft. Mean and turbulent flow fields were constructed from 81 point measurements of velocity taken as vertical profiles

at 15 streamwise (x) positions. In addition to these flow fields, a high-resolution vertical profile of velocity was measured near the downstream end of the canopy at $x=43$ cm ($x/L=0.7$), centered laterally. Velocity was sampled at 42 vertical locations separated by 0.3-1.0 cm. All velocity records were collected for five minutes at a sampling frequency of 25 Hz.

The presence of the root canopy in the flume altered both the mean and turbulent velocity structures by diverting flow around the root canopy and by generating turbulence at the canopy-water interface. Mean velocity magnitude was decreased within the canopy and increased in the open water below. The streamwise velocity profile, $U(z)$, approached fully-

developed conditions $\left(\frac{dU}{dz} \sim 0\right)$ at 70% of the canopy length. Turbulence generation was evidenced as an increase in Reynolds stress $\left(\overline{u'w'}\right)$ beginning halfway along the canopy, culminating in a high stress wake region downstream of the canopy.

Despite the relatively short length of the root canopy, there is evidence for mixing layer development. The vertical profile of $U(z)$ is reasonably described by the theoretical hyperbolic tangent shape of a mixing layer (Figure 1a). The Reynolds stress within the root canopy ($z/h_c < 1$) is uniformly low, increasing only within the last 2 cm of the canopy (Figure 1b). This suggests a small exchange zone, likely caused by the high density of the root canopy. Previous studies of mixing layer development in vegetation considered canopies comprising stems and leaves, rather than roots as in this study.

Two unique results of this study are the double, coincident peaks in both velocity shear and Reynolds stress profiles (Figure 1b). The peaks in velocity shear are of similar magnitude while those of Reynolds stress are not. Other studies of terrestrial and aquatic leaf canopies demonstrate a single peak in Reynolds stress near the canopy edge and subsequent decrease outside the canopy (e.g., Raupach *et al.*, 1996; Ghisalberti and Nepf, 2004); here we found a peak in Reynolds stress near the canopy edge ($z/h_c = 1.03$) followed by a second peak of higher magnitude ($z/h_c = 1.3$). Peaks in Reynolds stress suggest the presence of coherent vortices, as expected in a mixing layer. We expect that the first, smaller peak in stress is the one typical of mixing layers, caused by the discontinuity of drag from the canopy. Given the somewhat confined flow conditions in this experiment, we attribute the second, larger peak in Reynolds stress to the external pressure gradient forcing flow underneath the root canopy.

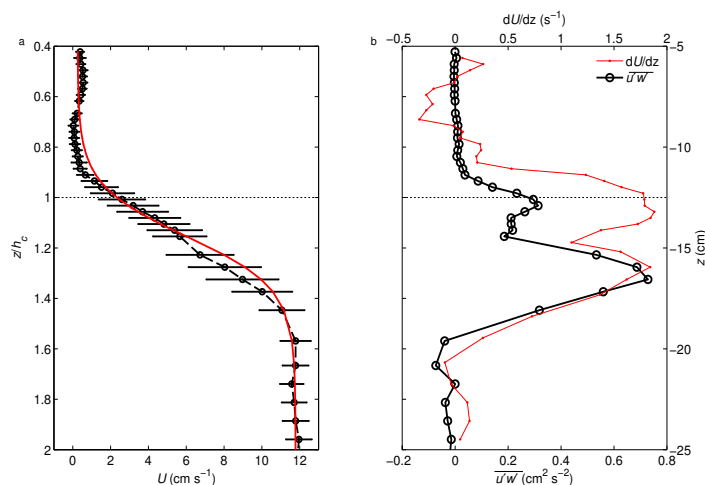


Figure 1. a) Vertical profile of streamwise (x) velocity at $x/L=0.7$ for an approach velocity of 8 cm s^{-1} . Error bars represent one standard deviation. Red line denotes the hyperbolic tangent profile typical of a mixing layer. b) Vertical profiles of velocity shear (dU/dz) and Reynolds stress $\left(\overline{u'w'}\right)$. Root canopy extends from water

surface ($z=0$) to canopy depth, h_c , denoted by horizontal lines at depth $z=-12.5$ cm and at normalized depth $z/h_c=1$.

REFERENCES

- Downing-Kunz, M.A. and Stacey, M.T. (2011). Flow-induced forces on free-floating macrophytes. *Hydrobiologia*. DOI 10.1007/s10750-011-0709-1
- Ghisalberti, M. and Nepf, H. (2004). The limited growth of vegetated shear layers. *Water Resources Res.*, **40**.
- Gopal, B. (1987). *Aquatic Plant Studies 1: Water Hyacinth*. Elsevier, New York.
- Raupach, M.R., Finnigan, J.J. and Brunet, Y. (1996). Coherent eddies and turbulence in vegetation canopies: The mixing-layer analogy. *Boundary-Layer Met.*, **78**: 351-382.
- White, B. and Nepf, H. (2007). Shear instability and coherent structures in shallow flow adjacent to a porous layer. *J. of Fluid Mech.*, **593**.

A NEMO-based modelling system for the Great Lakes

Frederic Dupont¹, Padala Chittibabu², Anning Huang³, Ram Yerubandi², Vincent Fortin¹, Youyu Lu⁴

¹*Canadian Meteorological Centre, Montreal*

²*National Water Research Institute, CCIW, Burlington, L7R4A6, Canada.*

³*School of Atmospheric Sciences, Nanjing University, Nanjing, China*

⁴*Bedford Institute of Oceanography, Department of Fisheries and Oceans, Dartmouth, NS, Canada*

**Corresponding author, e-mail Frederic.Dupont@ec.gc.ca*

KEYWORDS:

Hydrodynamic model, hydrological system, Great Lakes.

1. Introduction

Environment Canada is actively pursuing the development of a complete environmental forecasting system for the Great Lakes, including the weather, hydrology and water quality conditions. In this perspective, an hydrological system for the Great Lakes is under development. The hydrological system will be able to predict lake levels and flood risks. Upcoming developments include two-way coupling with the atmosphere, the downstream Saint-Lawrence river/upper estuary and to a river router (and river regulations rules). A full coupling is expected to be beneficial to weather forecasting downstream of the Great Lake region as well as other environmental conditions. For instance, the need for a flood forecasting system has been recently highlighted in the Quebec province where recent floods due to high lake levels and storm surge were witnessed in the Lake Champlain region.

2. The hydrological modelling system

2.1 The hydrodynamic lake model

The NEMO model (Nucleus for European Modelling of the Ocean; <http://www.nemo-ocean.eu>) is implemented over the Great Lakes at 2 km horizontal resolution (Fig.1). The vertical discretization is based on 35 fixed z-levels with a close to constant 1m resolution in the first 10 layers and allows for a good representation of the surface and mixed layer processes. The model advances in time, temperature, salinity, lake surface height, currents and ice properties. A compact grid of 355x435x35 allows the integration of one year per clock day on a 16 cpu machine with a timestep of 600s.

2.2 The hydrological components

The hydrodynamic model is forced by winds and atmospheric variables from the Canadian operational weather model (GEM) and by river flows provided by a component described below. Coupled to the hydrodynamic model is a regulation river model (Tolson, 2009) which computes allowable flows in the connecting channels of the Great Lakes system. Hence, the modelling system can predict absolute lake level.

A river router WATFLOOD (Kouwen, 1988; Bingeman et al, 2006) at 1/6 degree resolution coupled to an offline version of Canadian operational weather model (GEM) and a land-surface model --which estimates evaporation and other turbulent fluxes-- provides the river forcing to the hydrodynamic model. This component, named MESH (Pietroniro et al., 2006), is also able to estimate independently lake level thanks to simple discharge parametrizations. MESH was validated in terms of net basin supply against GLERL estimates and lake level

residual data (manuscript in preparation).

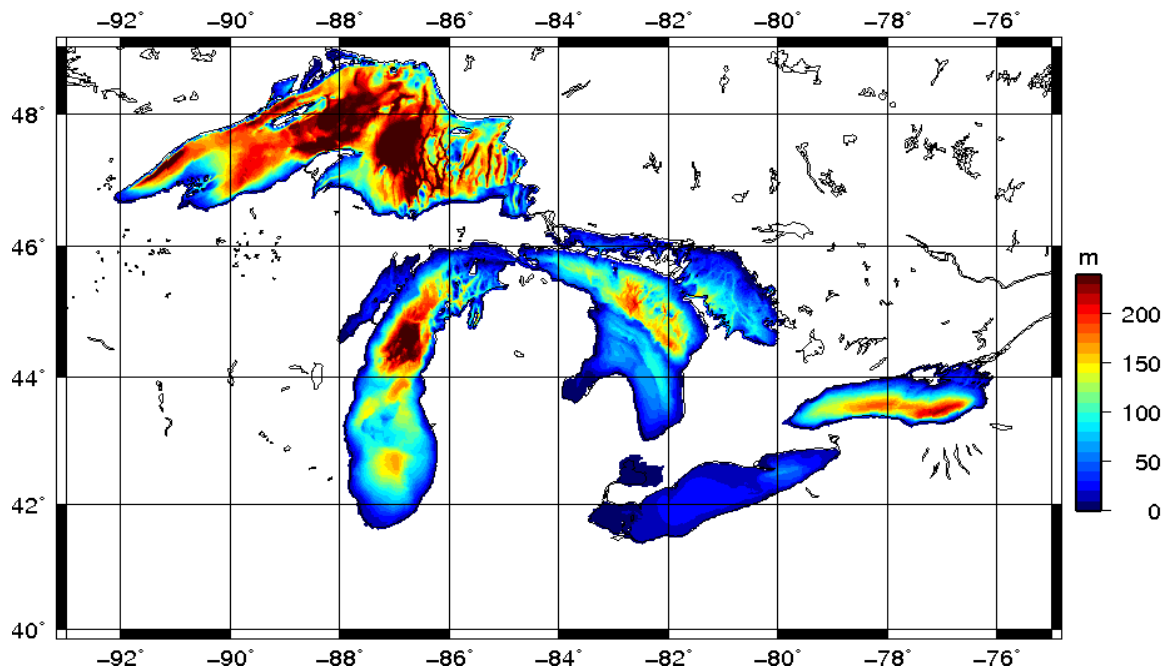


Illustration 1: Bathymetry of the hydrodynamic model over the Great lakes

3. Results

3.1 Validation of the hydrodynamic model in Lake Erie and Ontario

NEMO was compared to the POM (Mellor and Blumberg, 1985) and CANDIE (Sheng et al, 1998) models for 2 lake configuration (Lake Erie and Ontario). A similar intercomparison was done over Lake Ontario and for the POM, CANDIE and ELCOM models (Huang et al, 2010). All three models uses the same bathymetry. NEMO has the same vertical axis as mentioned above. CANDIE uses a 60 z-level grid which has more resolution in the bottom layers (however, a test of the 60 z-level vertical grid in NEMO did not show significant improvement in scores). POM has a 31 sigma-levels vertical grid with a minimum spacing of 0.001(sigma) in the first layer. The three models use the same bulk formulae (here for consistency, the bulk formulae of Schertzer et al, 2006). The atmospheric forcing is in all cases the GEM 40m (last prognostic level). In Lake Ontario, the three models are compared against data obtained during the 2006 measurement campaign from thermistor chains and ADCPs. Overall, NEMO obtains the best scores (temperature, Table 1 and currents, Table 2), although representation of the thermocline transition is not optimal. The high frequency signal present in currents was difficult to represent in all models. For both lake Erie and Ontario, lake surface temperature from satellite (NOAA) was compared to all 3 models and again NEMO did a little better than the other 2 models (Table 3). The bias and RMS scores shows transient events that the models do not necessarily resolve correctly.

Table 1: comparisons of RMS errors in temperature (degC) at different stations (mean over the upper 50m of each profile) over lake Ontario during a 2006 measurement campaign.

Stations	CANDIE	POM	NEMO
CCIW	2.49	2.21	1.72
403	2.16	2.05	1.96
586	2.61	2.84	2.52
1263	2.43	2.46	2.58
1266	2.49	2.21	1.72

1269	2.80	2.49	2.48
1270	2.40	2.70	2.20
752	2.69	2.42	1.85
Mean	2.51	2.42	2.13

Table 2: comparisons of RMS errors in velocity (m/s) at different stations over lake Ontario during a 2006 measurement campaign.

Stations	CANDIE	POM	NEMO
1266	0.049	0.052	0.044
1269	0.069	0.087	0.057
1270	0.041	0.039	0.036
Mean	0.053	0.059	0.046

Table3: comparisons of bias and RMS error for the three models in terms of surface lake temperature against satellite observations (NOAA).

Years	CANDIE	POM	NEMO
2005 bias	1.12	0.48	0.19
2005 rmse	1.20	1.05	1.18
2006 bias	1.32	0.61	-0.19
2006 rmse	1.29	1.22	1.20

3.2 Preliminary results of the hydrological system

An hindcast of 2004-2009 for the lake levels is shown in Figure 2. The system can predict upwelling/downwelling events, the formation of a seasonal thermocline and the extent of the winter ice-covered waters. The surface water temperature in Lake Ontario and Erie is reasonably predicted. However, that of the Lake Superior shows a 2 degree Celsius bias (model too warm, not shown). Also, representation of sharp thermocline present in shallow lakes, such as in Lake Erie, is a weak point of the model. Although in general the lake levels are reasonably well predicted, the evaporation predicted in NEMO using the CORE bulk formulae is somewhat too strong in the upper lakes and leads to weaker than observed connecting flows. Corrections currently being implemented and tested in GEM bulk formulae to fix the same problem will also be ported to NEMO. The overall goal being to achieve a 2-way flux-coupling instead of a variable-coupling approach between the lake and the atmosphere.

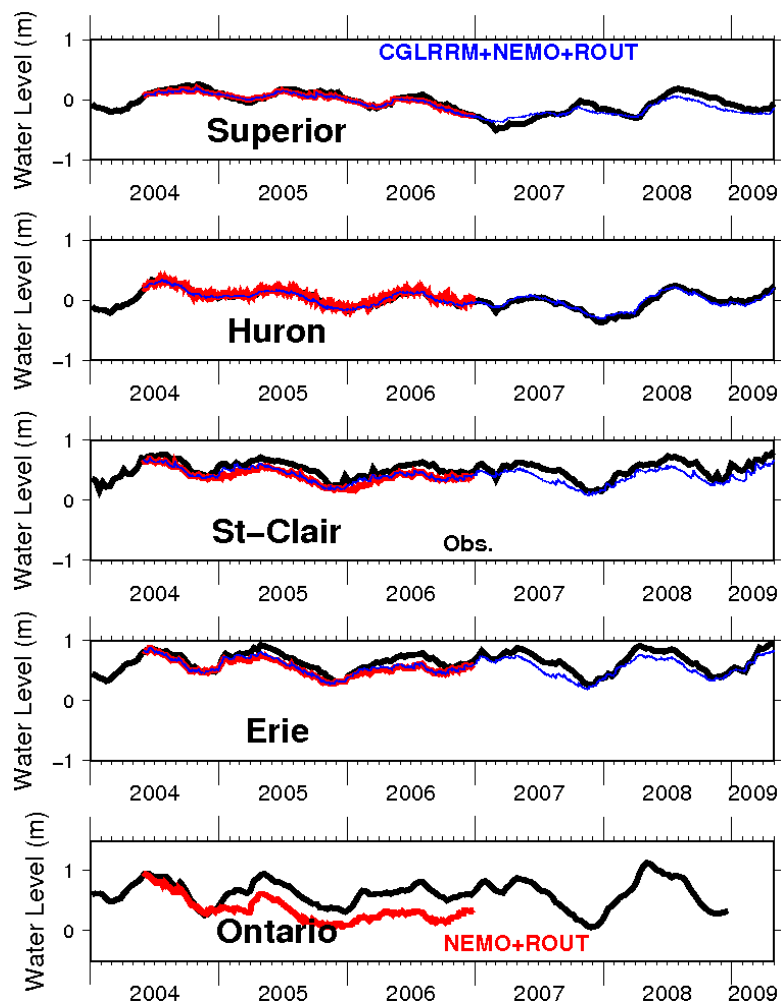


Illustration 2: Validation of NEMO-regulation model against offline calculation. Black: observation, blue: expected levels based on NEMO evaporation and river routing, red modelled by NEMO. There are no defined regulation rules for Lake Ontario, so an adhoc equation for the outflow is used there instead.

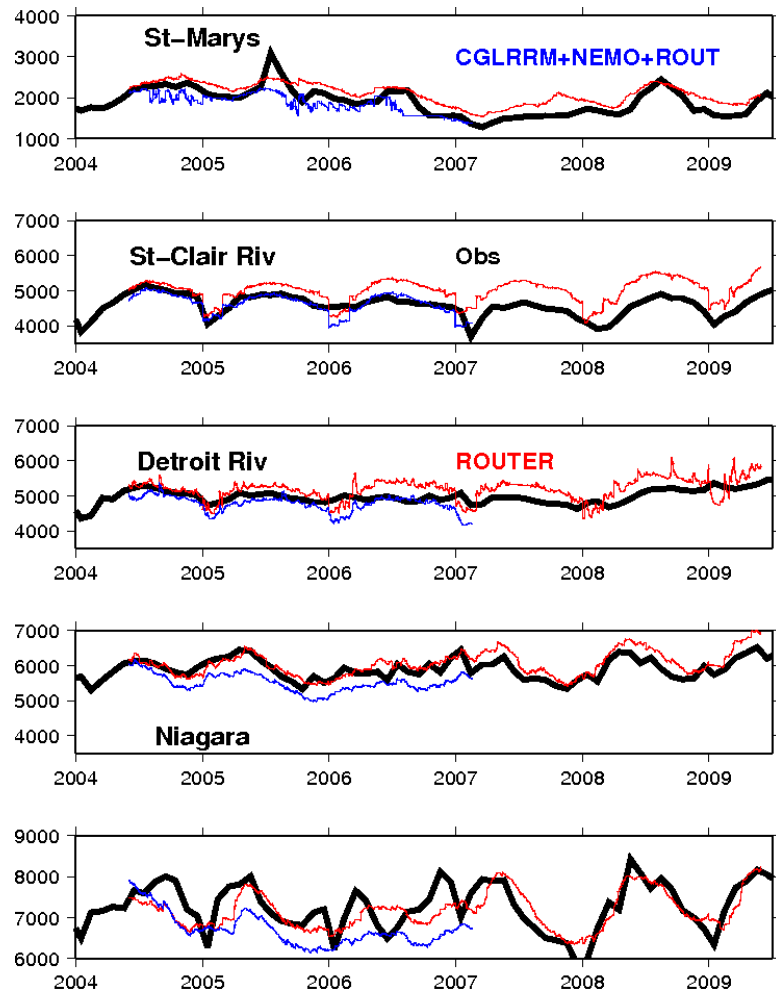


Illustration 3: river flow through the connecting channels. In black observations, in blue the model, in red what the river router (no regulation) is led to believe due to an independent estimated evaporation from the atmospheric model.

3.3 Ice validation

The 2004-2009 ice seasons were used for validation. The mean ice concentration was computed for each lake and compared with that analyzed by the Canadian Ice Service (CIS) in Fig.4. The comparison shows that the model is usually close to observations with slight underestimation in Lake Huron and Erie.

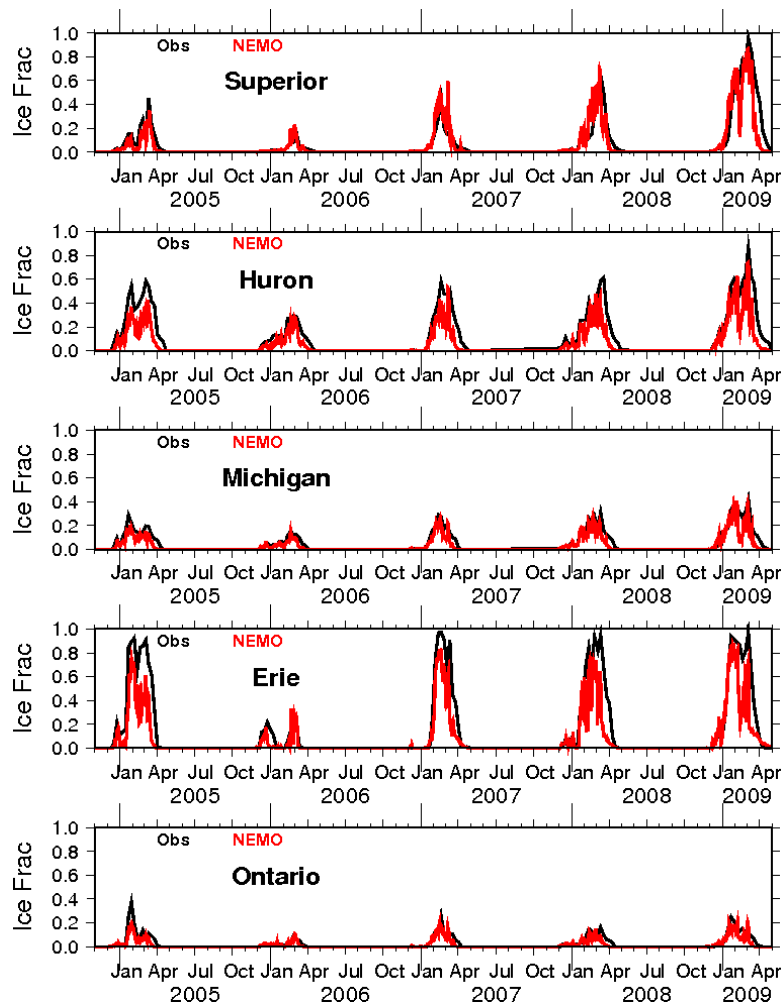


Illustration 4: Comparison of mean ice concentration in each lake from observations (black) and model (red)

4. Conclusions

The Environment Canada hydrological modelling system for the Great Lakes was represented. The hydrodynamic model (NEMO) performed a little better than POM and CANDIE models for both temperature and currents, although the erosion of the thermocline remains an issue in shallow lakes such as in Lake Erie. Choice of a vertical coordinate that is near-neutral to the passage of internal seiches and waves seem to be crucial. The ice concentration over all lakes over the 2005-2009 period was very encouraging despite the relative simplicity of the ice component (LIM2) in NEMO.

The present system under development is expected to be two-way coupled in the very near future to the Canadian operational atmospheric model GEM (where the river router WATROUTE would be an integrated component) and to a downstream finite element model covering the Saint Lawrence river and upper estuary. Extension to the lake Champlain watershed is also under discussion which will allow more accurate flood risk forecasting for the Quebec region. We finally envisioned extension to the whole Saint-Lawrence watershed, including the Gulf of Saint-Lawrence, where NEMO will cover all inland and coastal waters.

References

Tolson, B. (2009), "Rationalizing the Decline in Lake Michigan-Huron Water Levels Using the Coordinated Great Lakes Routing & Regulation Model", Final report to St. Clair Task Team Hydroclimate TWG, Nov 7, 2009.

http://pub.iugls.org/en/St_Clair_Reports/Hydroclimatic/Hydroclimate-06.pdf

Bingeman, A.K, N. Kouwen, M. ASCE and E. D. Soulis, (2006), "Validation of the hydrological processes in a hydrological model." *Journal of Hydrologic Engineering*, ASCE. 11 (5),451-463.

Kouwen, N., (1988). "WATFLOOD: A Micro-Computer based Flood Forecasting System based on Real-Time Weather Radar," *Canadian Water Resources Journal*, 13(1):62-77

Mellor, G. L. and A. F. Blumbrg (1985), Modeling vertical and horizontal diffusivities with the sigma coordinate system. *Mon. Wea. Rev.*, 113, 1380-1383.

Huang, A., Y. R. Rao, Y. Lu, and J. Zhao (2010), Hydrodynamic modeling of Lake Ontario: An intercomparison of three models, *J. Geophys. Res.*, 115, C12076, doi:10.1029/2010JC006269.

Pietroniro, A., V. Fortin, N. Kouwen, C. Neal, R. Turcotte, B. Davison, D. Versegny, E. D. Soulis, R. Caldwell, N. Evora and P. Pellerin (2006), "Using the MESH Modelling System for Hydrological Ensemble Forecasting of the Laurentian Great Lakes at the Regional Scale". *Hydrology and Earth System Sciences Discussions*. 3: 2473-2521.

Schertzer WM, Rouse WR, Blanken PD, Walker AE (2003) Over-lake meteorology and estimated bulk heat exchange of Great Slave Lake in 1998 and 1999, *J. Hydrometeor* 4:649-659.

Sheng, J., D. Wright, R. Greatbatch and D. Dietrich (1998), [CANDIE: A new version of the DieCAST Ocean Circulation Model](#), *J. Atm. and Oceanic Tech.*, 15, 1414-1432.

Along-shore currents as a potential mechanism for invasive species transport in Lake Tahoe, CA-NV USA

A.L. Forrest^{1*}, K.E. Reardon¹, M.E. Wittmann², B.E. Laval³, S.G. Schladow¹

¹University of California Davis Tahoe Environmental Research Center, Incline Village, NV 89451, USA

²University of Notre Dame, Notre Dame, IN 46556-0369, USA

³University of British Columbia, Department of Civil Engineering, Vancouver, BC V6T 1Z4, Canada

*Corresponding author, e-mail alforrest@ucdavis.edu

KEYWORDS

Invasive species dispersal, currents, Lake Tahoe, surface forcing, Asian clam

EXTENDED ABSTRACT

The establishment of an invasive bivalve Asian clam (*Corbicula fluminea*) has impacted water quality, native species diversity, and ecosystem use value in Lake Tahoe, CA-NV. The observation of *C. fluminea* adult individuals at water depths down to 70 m, and unsuitable for reproduction due to temperature limitation), suggests that along-shore currents are a potential physical transport mechanism for juvenile or adult *C. fluminea*.

To understand the potential formation of colder density currents in a region of high density (up to 6400 clams m⁻²) *C. fluminea* populations, two thermistor chains (1 m intervals to a maximum 15 m height above the lakebed) were installed in southern Lake Tahoe at 25 and 50 m depths. A 1200 kHz Acoustic Doppler Current Profilers (ADCP) unit was also deployed at the same site at 25 m.

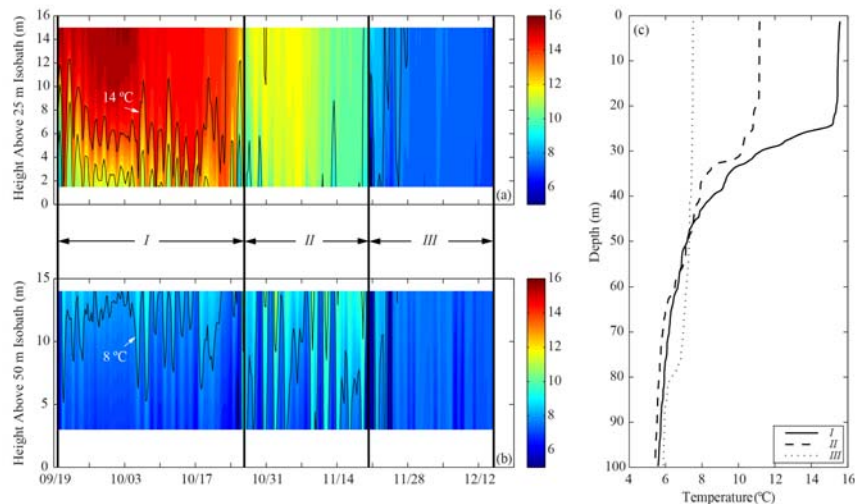


Figure 1. Water column response during period of autumnal cooling from 19 Sept – 15 Dec 2010: (a) 6 hr bin average temperature record from 1.5 – 15 m above the 25 m isobath; (b) 6 hr bin average temperature record from 3 – 14 m above the 50 m isobath; (c) 0.5 m bin averaged vertical profiles collected at the northeast side of the lake.

Temperatures at the 25 m isobath (Figure 1a) show three distinct periods: (I) stratified from 12 – 16 °C; (II) weakly-stratified from 10 – 12 °C; and, (III) well mixed at ~ 6 °C. Temperature from the thermistor chain at the 50 m isobath (Figure 1b) are weakly stratified from 6 – 8 °C during periods I and II with mixing to the lakebed occurring to greater frequency during period II. Similar to the shallower temperature record, period III is relatively well-mixed at ~ 6 °C. Vertical profiles were collected during each of the periods on 27 Sept, 9

Nov and 12 Dec 2010 (Figure 1c). Between the three profiles, the epilimnion is shown to deepen by 50 m and cool by ~ 8 °C. This deepening will potentially result in increased vertical transport relative to the summer months.

Period transitions were defined as a > 1 °C decrease in temperature in the thermistor located closest to the 25 m isobath. These transitions were observed at 15:00 hours, 26 Oct 2010 and 07:30 hours, 20 Nov 2010 (Figure 1a and 1b). Figures 2a and 2b show the wind speed and direction measured during the entire sampling time with a mean wind speed of 3.5 m s^{-1} for the entire sampling period and peak wind speeds reaching 10 m s^{-1} just prior to the period transitions. Wind directions associated with wind speeds greater than the mean are circled (Figure 2a).

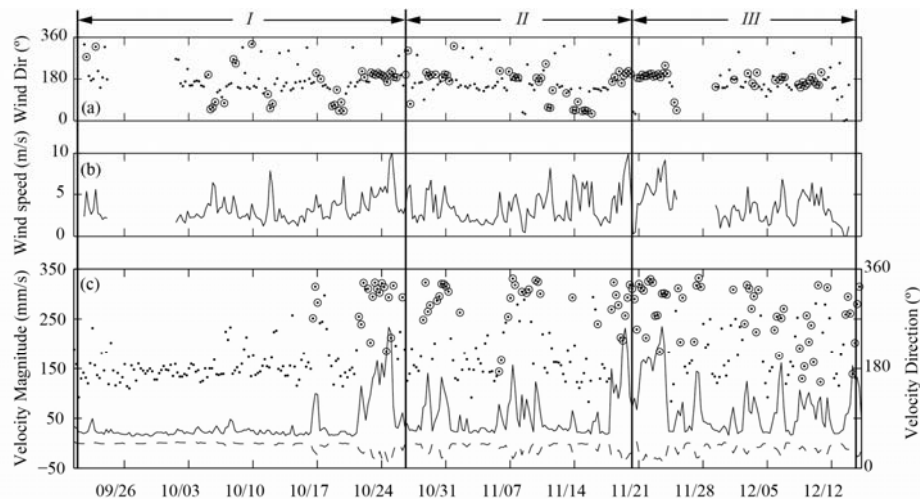


Figure 2. 6 hr bin time averaged surface forcing and water column response from 19 Sept – 15 Dec 2010: (a) wind direction (filled points) with values associated with wind speeds $> 3.5 \text{ m s}^{-1}$ circled (0° and 360° represent north); (b) wind speed (m s^{-1}); and, (c) depth averaged velocity magnitude (solid line), depth averaged vertical velocity magnitude (dashed line), 1 – 3 m height above bottom mean direction (filled points) with values associated with velocity magnitudes $> 50 \text{ mm s}^{-1}$ circled. Gaps in wind speed and direction result from missing data.

The mean velocity magnitude of the entire water column was 50 mm s^{-1} for the entire period with a maximum of 230 mm s^{-1} (Figure 2c). Peak horizontal velocity values are qualitatively associated with downward vertical velocities of 10 mm s^{-1} (Figure 2c – dashed line). The average direction of the water column within 1 – 3 m of the lakebed (Figure 2c – filled points) is generally from the southwest and is qualitatively correlated with winds blowing from that direction. Using 50 mm s^{-1} of the velocity magnitude as a threshold, directions associated with greater flows (Figure 2 – circled points) are associated with a northerly direction during periods I and II. Although this correlation is still evident in period III, the relationship appears to becoming less pronounced indicative of transport no longer being directly along-shore.

Direct transport of *C. fluminea* have been observed in lotic environments as a means of downstream dispersal (Prezant and Chalermwat 1984). Potential entrainment of juvenile or adult *C. fluminea* associated with flows observed in this study along the benthic layer may result in advective transport of individuals downslope to record water depths. Ongoing work is currently investigating entrainment of different size classes of *C. fluminea* in a laboratory setting at the range of velocities observed in this study.

References

Prezant, R.S. and K. Chalermwat. 1984. Science 225: 1491-1493

Physical interactions between suspended particles and biological collectors

M.Ghisalberti^{1*}, A. Espinosa¹, G.Ivey^{1,2}, N.Jones^{1,2} and A. Purich¹

¹ *School of Environmental Systems Engineering, University of Western Australia, Crawley, WA, Australia.*

² *UWA Oceans Institute, University of Western Australia, Crawley, WA, Australia.*

*Corresponding author, e-mail ghisalbe@sese.uwa.edu.au

KEYWORDS

computational fluid dynamics; corals; particle capture; seagrass pollen; suspended sediment.

EXTENDED ABSTRACT

Introduction

The term *particle capture* refers to the physical process by which suspended particles come into contact with biological structures ('collectors') and adhere to the collector's surface, thereby being removed from suspension. Particle capture is of significant ecological importance; in particular, it can control the efficiencies of (1) seagrass pollination, (2) turbidity reduction by wetland vegetation, (3) coral feeding, and (4) larval settlement.

Despite its fundamental ecological importance, particle capture in aquatic systems remains poorly understood. Previous research has typically been motivated by a desire to understand aerosol behaviour, where the Stokes number (St , a measure of the importance of particle inertia) is high. Particle capture in aquatic systems is, however, characterised by low St ($O(1)$ or less). Furthermore, all existing studies investigate the particle capture of an isolated collector. In aquatic systems, biological collectors typically form part of an array, where the hydrodynamic impact of neighbouring collectors cannot be ignored.

The aims of this study are, through numerical and experimental modelling, to (1) develop predictive capability for particle capture rates by biological collectors at low St , and (2) understand the impact of neighbouring collectors on particle capture in an array.

Methods

The open-source CFD code OpenFOAM was used to determine the fluid flow and the motion of suspended particles around a single cylindrical collector. In addition, experiments with cylinder arrays were performed in a laboratory flume. Test cylinders in the arrays were coated with an adhesive grease and placed in a particle-laden flow. The number of particles captured by each adhesive cylinder was counted to determine the particle capture rate.

Results and Discussion

Single collector: Particle capture rates in the numerical simulations agree very well (to within approximately 15%) with the experimental results of Palmer *et al.* (2004). The vast majority (>99%) of particles are captured on the front of the collector, within $\pm 50^\circ$ of centre. Vortex

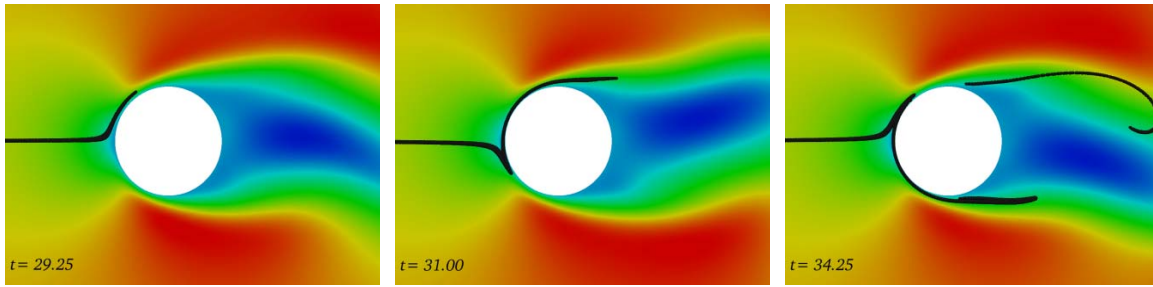


Figure 1. Model snapshots showing particles being forced around alternating sides of the collector due to vortex shedding. The background colour represents streamwise velocity.

shedding behind the collector generates small pressure oscillations upstream of the collector. These oscillations force particles around alternating sides of the collector (Figure 1). The net result is that captured particles come from a much broader lateral area than previously thought. Also, particles immediately upstream of the cylinder *are not* the most likely to be captured.

Multiple collectors: Particle capture in an array differs significantly from that of an isolated collector. Firstly, adjacent collectors cause a reduction in particle capture efficiency and a *decreasing* trend with the Reynolds number of the collector, Re_c (Figure 2). Furthermore, particles are captured on all parts of the collector, with particles captured uniformly around the cylinder at high Re_c . Preliminary numerical simulations suggest that capture in arrays is dominated by turbulent transport of the particles, rather than by direct interception.

Future work: Our current research focuses upon the impact of collector shape, roughness and motion on particle capture. Particle capture under oscillatory flow is also being investigated.

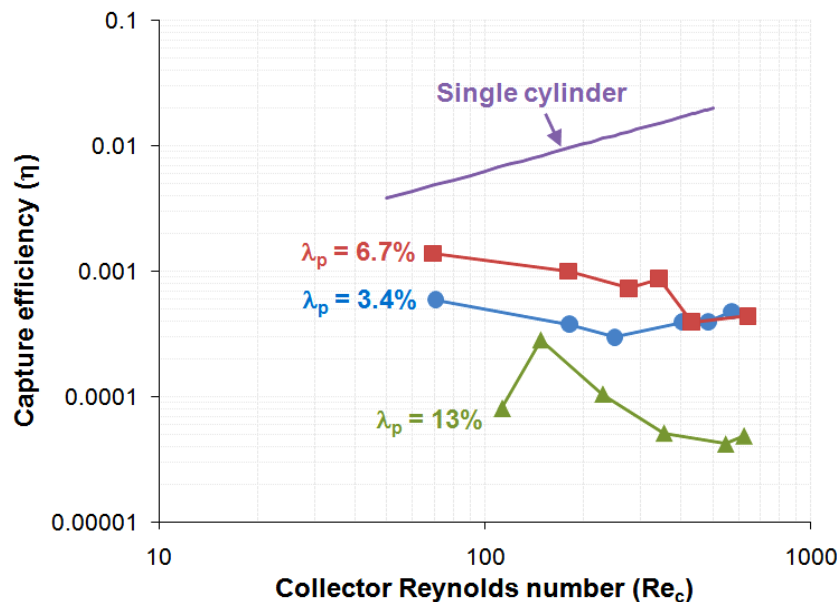


Figure 2. Particle capture efficiencies of collectors in arrays of various areal densities (λ_p).

REFERENCES

- Palmer, M., Nepf, H.M., Pettersson, T.J.R. and Ackerman, J.D. (2004). Observations of particle capture on a cylindrical collector: Implications for particle accumulation and removal in aquatic systems. *Limnol. Oceanogr.*, **49**(1), 76-85.

Hydrothermal and water quality model calibration and application to the evaluation of land use change and watershed management programs

Y. T. Huang^{1*}, D. Pierson², A. Frei¹, N. Samal¹, E. Schneiderman², M. Zion², S. M. Pradhanang¹, A. H. Matonse¹, E. Owens³

¹*CUNY Institute for Sustainable Cities, Hunter College, The City University of New York*

²*New York City Department of Environmental Protection, Kingston, NY*

³*Upstate Freshwater Institute, Syracuse, NY*

**Corresponding author, e-mail:hyongtai@dep.nyc.gov*

ABSTRACT

Located in Delaware County, New York, Cannonsville Reservoir was constructed to provide water supply for New York City. A one-dimensional hydrothermal and water quality model has been set up to simulate the thermal stratification, nutrient levels and phytoplankton biomass in the reservoir. This study aims to improve the model performance through automated calibration using a long-term record of measured reservoir water quality data and apply the model to the evaluation of the effects of land use change and watershed management programs on the water quality in the reservoir. To implement automated model calibration, a hybrid genetic algorithm (HGA) consisting of a real-encoded genetic algorithm and the Nelder-Mead simplex (NMS) algorithm is developed as an optimization algorithm, and an overall objective function is designed to measure the degree of fitness between the measurements and the predicted values of the selected variables including temperature, dissolved oxygen, total phosphorus and chlorophyll *a*. The HGA and the objective function are used to calibrate the hydrothermal and water quality model by comparison with long-term measured reservoir water quality data. The output of the calibrated model matches the measured values reasonably well. The calibrated model is then used in conjunction with a watershed model to evaluate the effects of land use change and watershed management programs. The watershed model is used to simulate the changes in nutrient loading caused by land use change and watershed management programs. The calibrated reservoir model is used to evaluate the effects of the changes in nutrient loading on reservoir water quality and it predicts the significant improvement of reservoir water quality.

KEYWORDS

Automated calibration; Cannonsville Reservoir; Reservoir model; Watershed model

INTRODUCTION

Located in Delaware County, New York, Cannonsville Reservoir was constructed to provide water supply for New York City. The Cannonsville watershed had a relatively high portion of agricultural land use, and there were also a number of small sewage works and other point sources contributing to the rivers entering the reservoir. These factors in the past led to high point and non-point nutrient loading to the reservoir, high average chlorophyll concentrations and frequent phytoplankton blooms. Starting in 1992, the implementation of sewage treatment upgrades, and an aggressive program of agricultural, storm water and other best management

practices (BMPs), have reduced nutrient inputs, improved trophic status and reduced the occurrence of phytoplankton blooms (NYCDEP, 2006).

A one-dimensional hydrothermal and water quality model has been set up to simulate the thermal stratification, nutrients and phytoplankton in the reservoir (Owens 1998; Doerr, 1998; UFI, 2001). The objective of the study is to improve the performance of the reservoir model through automated calibration using long-term measurement data and use the calibrated model to evaluate the effects of land use change and watershed management programs on reservoir water quality.

STUDY AREA

The Cannonsville watershed has a drainage area of 1178 km². Before the occurrence of land use change and the implementation of watershed management programs, the land use was composed of agriculture (14%), urban areas (3%), non-agricultural grass areas (7%), undeveloped forested and brushland areas (73%), and water and wetland areas (3%) (NYCDEP, 2006).

The reservoir's capacity is 362 million m³. The surface area of the reservoir is 19.2 km², about 24 kilometers long and 0.8 kilometers wide on average (see Figure 1). Its maximum depth is about 42.7 meters with an average depth of 18.6 meters.

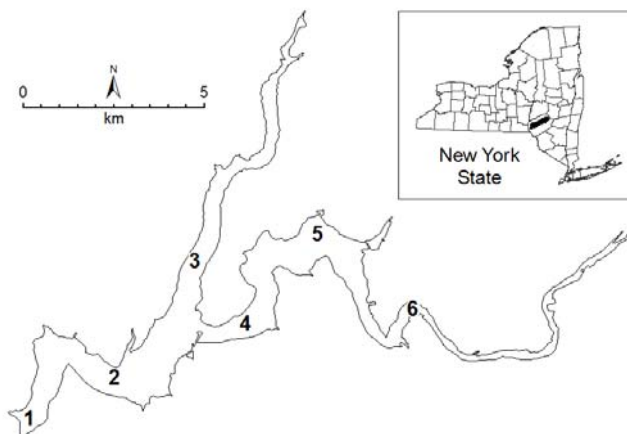


Figure 1. Cannonsville reservoir and sampling stations 1-6.

WATERSHED MODEL

In this study, the generalized watershed loading function (GWLF) model is used to simulate the flow and loads of the watershed, as well as evaluate the load variation due to the land use change and watershed management programs. The original GWLF was developed by Haith and Shoemaker (1987). It is a lumped-parameter model that simulates daily water, nutrients, and sediment loads from non-point and point sources. GWLF treats the watershed as a system of different land areas (hydrologic response units or HRUs) that produce runoff, and a single groundwater reservoir that supplies baseflow. Dissolved and suspended substances (e.g. nutrients and sediment) in streamflow are estimated at the watershed outlet by loading functions that empirically relate substance concentrations in runoff and baseflow to watershed and HRU-specific characteristics.

The modified version of GWLF model (i.e. GWLF-VSA model) was set up to simulate the streamflow, and nutrient loads produced in the watershed. The model is described in detail in Schneiderman *et al.* (2002).

RESERVOIR MODEL

A one dimensional reservoir model has been developed to simulate the hydrothermal and water quality conditions in Cannonsville reservoir. The model consists of three components: (1) a hydrothermal sub-model, (2) nutrient sub-models, and (3) a phytoplankton sub-model.

The hydrothermal sub-model simulates the vertical dynamics of reservoir thermal stratification and related transport regimes, based on changes in such critical (state) variables as meteorological, hydrological and operational conditions.

The nutrient sub model describes the transformation and fate of the nutrient loads in the reservoir. The reservoir model distributes nutrients vertically through the water column based on vertical mixing coefficients derived from the hydrothermal sub-model, and the nutrient inputs are partitioned into different forms based on model coefficients.

The PROTBAS (PROtech Based Algal Simulations) (Markensten and Pierson, 2007) which is based on PROTECH (Reynolds *et al.*, 2001) is used to simulate phytoplankton biomass. In the model, phytoplankton biomass is predicted in terms of algal carbon and is a balance between growth (photosynthesis), and losses due to respiration, grazing, sedimentation and outflow. Chlorophyll *a* is calculated from the algal carbon based on system-specific stoichiometric relationships.

RESERVOIR MODEL CONFIGURATION AND PARAMETERS

To set up the one-dimensional model to simulate the hydrothermal and water quality conditions, the reservoir is discretized vertically into 35 layers with an average thickness of 1.5 meters per layer. The model is fed with daily meteorological data (such as air temperature) and data related to the water balance (water elevation, discharge, dam spill and tunnel outflow). The time series data, such as dissolved phosphorus and nitrogen from non-point and point sources, (which are generated by the GWLF model) are taken as input of the model. The model can be configured to output daily simulated values for a large number of variables, such as dissolved oxygen in the epilimnion and hypolimnion layers.

According to the model description (UFI, 2001), 116 hydrothermal and kinetic parameters (also called coefficients) are used in the model. Among them, 52 can be adjusted during model calibration. The Morris method (Morris, 1991; Saltelli *et al.*, 2004) is employed to identify the sensitive parameters in the model. See Huang and Liu (2008) for a detailed description of the method if necessary. It was found that 18 parameters were of great importance in determining in the simulated values of the variables including temperature (Temp), dissolved oxygen (DO), total phosphorus (TP) and chlorophyll *a* (Chla). These parameters were the focus in model calibration and only their values were adjusted in model calibration. The names and definitions of the 18 parameters, as well as their lower and upper bounds are presented in Table 1. These bounds were determined according to the recommendations provided by the model developer (UFI, 2001), and adjustments were made to ensure the numerical stability of the model.

RESERVOIR MODEL CALIBRATION AND VALIDATION

In this study, a hybrid genetic algorithm (HGA) consisting of a real-encoded genetic algorithm (a global search method) (Haupt and Haupt, 2004) and the Nelder-Mead simplex (NMS) algorithm (a local search method) (Nelder and Mead, 1965) is used as an optimization algorithm to vary the values of the 18 sensitive parameters. An overall objective function is designed to measure the degree of fitness between the measurements and the predicted values of the selected variables including Temp, DO, TP and Chla. A more detailed description of the HGA and the overall objective function is given by Huang and Liu (2010).

The model is calibrated against the measured data over the time period of 1986-1999, while model validation was performed using 2000-2004 data. The calibrated parameter values are presented in Table 1. Figure 2 depicts (for example) the time series of simulated daily Temp, DO, TP and Chla in the epilimnion layer. It can be observed that the simulated values match the measurements reasonably well for the calibration period.

Figure 3 shows the validation results, i.e. simulated and measured Temp, DO, TP and Chla in epilimnion and hypolimnion layers over the validation period. It can also be observed that the simulated values match the measurements reasonably well.

Table 1. Reservoir model parameters

	Name	Calibrated value	Lower Bound	Upper Bound	Definition
1	aC2CHL	53.000	50.600	100.000	Ratio carbon to chlorophyll (ugC/ugChl)
2	aC2P	150.00	80.00	150.00	Ratio carbon to phosphorus (ugC/ugP)
3	betaw	0.3570	0.3500	0.5000	Surface adsorption fraction
4	emisi	0.9413	0.9000	0.9900	Ice emissivity
5	eta	1.3655	1.0000	1.5000	Wind mixing
6	fardl	0.9923	0.5000	0.9950	Fraction of algal respiration as dissolved labile
7	farpl	0.0077	0.0045	0.0100	Fraction of algal respiration as particle labile
8	htcwi	0.0609	0.0100	0.1000	Ice transfer
9	kc	0.0500	0.0100	0.0500	Chlorophyll multiplier (L/ugChl/m)
10	kldoc	0.0116	0.0100	0.0150	Oxidation of labile DOC (1/d)
11	kldop	0.0173	0.0100	0.1000	Decay of labile DOP (1/d)
12	klpop	0.0600	0.0500	0.0900	Hydrolysis of labile POP (1/d)
13	phir	0.1500	0.0100	0.1500	Respiration multiplier - growth
14	PPvel	1.1589	0.2640	1.4960	Settling organic PP (m/d)
15	rz	0.2973	0.2000	0.6000	Diffusion exponent
16	sod	0.4800	0.3200	0.4800	Sediment oxygen demand (g/m ² /d)
17	trncon	0.0022	0.0020	0.0030	Evaporation multiplier
18	turb	2.2963	2.0000	2.5000	Atmospheric turbidity

MODEL APPLICATION

Land use change and watershed management programs

NYCDEP has implemented a number of aggressive programs to protect and enhance the quality in the Cannonsville reservoir since the early 1990s (NYCDEP, 2006). These programs can be classified into three categories: land use change, point source and non-point source management programs. The baseline condition and the programs are described briefly as follows:

- *Baseline scenario* represents the watershed conditions without the land use change and watershed management programs.
- *Land use change* scenario differs from the Baseline scenario with less active farmland, lower farm animal density, and increased census population.
- *Point source management program* refers to the upgrades of the wastewater treatment plants (WWTP) which were implemented to reduce the amount of phosphorous entering the reservoir.
- *Non-point source management program* includes an agricultural program and urban stormwater management program, as well as septic system rehabilitation and remediation programs.

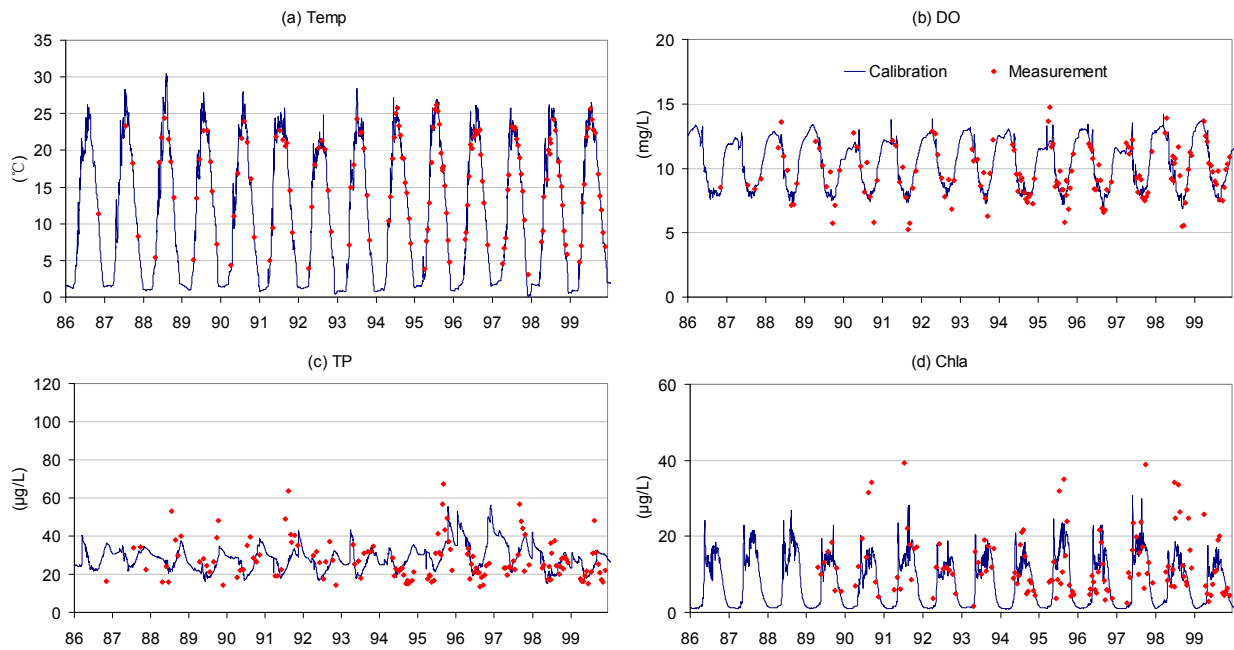


Figure 2. Model calibration: Simulated and measured daily Temp and concentrations of DO, TP and Chla in the epilimnion layer, 1986-1999.

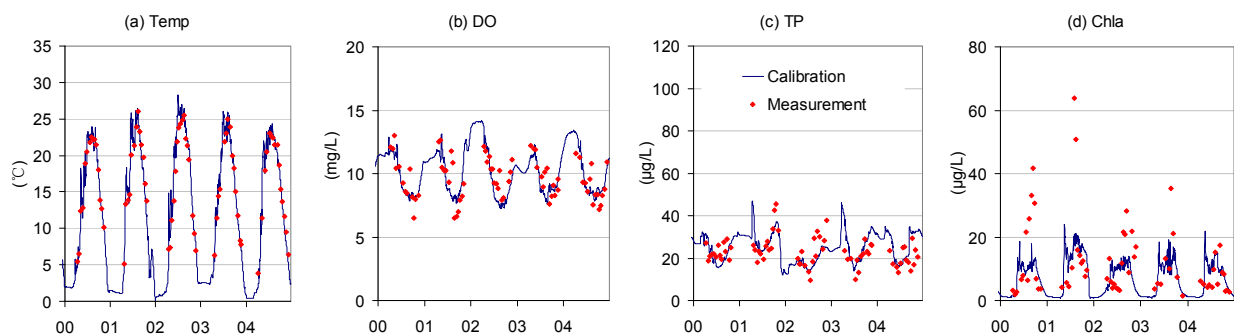


Figure 3. Model validation: Simulated and measured daily Temp and concentrations of DO, TP and Chla in the epilimnion layer, 2000-2004.

Effects on watershed loadings

In order to evaluate the effect of the land use change and watershed management programs described above, five scenarios are developed with different combinations of land use change, non-point source management, and point source management programs. The effects of land use change and non-point source management on nutrient loads (phosphorus loads including

total dissolved phosphorus or TDP and total particulate phosphorus or TPP in this study) are simulated in the GWLF model using land use-specific BMP reduction factors in the GWLF model. Loading reductions due to point-source management (WWTP upgrades) are implemented in GWLF by revising the daily WWTP effluent loading estimates that are inputted to the model. Loading reductions due to septic system upgrades are implemented in GWLF by revising the percentages of failing systems and size of un-sewered population.

Assuming land use change and watershed management programs took effect from 2000, the 2000-2004 meteorological records were used to drive all scenario simulations. The watershed model outputted time series of (daily) simulated streamflow, particulate phosphorus, and dissolved phosphorus loads to the reservoir. Based on GWLF output, the annual TDP and TPP loads for the five scenarios were calculated and presented in Figure 4. The differences between the scenarios represent the effects of changes in land use and the cumulative effects of land use change coupled with differing combinations of management programs on watershed loads. These results indicate that TDP reduction is mainly caused by land use change and point source management program, while TPP reduction is caused by land use change and non-point management program.

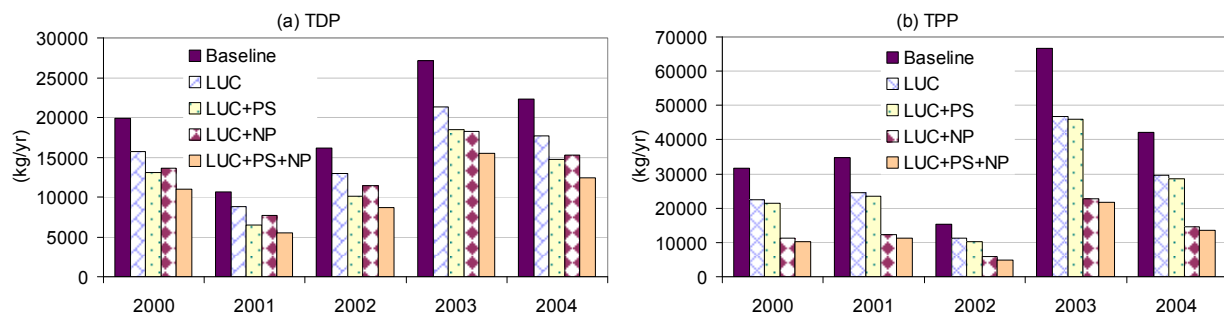


Figure 4. Annual TDP and TPP loads for five scenarios, i.e. combinations of land use change (LUC) with point source (PS) and non-point (NP) source management programs.

Effects on reservoir water quality

The effects of land use change and watershed management programs on TP and Chla in Cannonsville reservoir were evaluated by driving the reservoir model with the different nutrient loading scenarios simulated using GWLF. Based on daily simulated mean TP and Chla concentrations for the epilimnion and hypolimnion layers, annually average TP and Chla were calculated and presented in Figure 5 and Figure 6. Differences between the scenarios represent the effects of land use change and the cumulative effects of land use change coupled with differing combinations of management programs. It can be observed that the combination of land use change and point and non-point source management programs reduce the TP concentrations in both epilimnion and hypolimnion layers significantly. In addition, although their effect on the Chla in the hypolimnion layer is small (because the concentration of Chla is very low), their effect on the Chla in the epilimnion layer is noticeable.

Figure 7 and Figure 8 show the effect of land use change and watershed management programs on monthly average TP and Chla for the period of 2000-2004 in epilimnion and hypolimnion layers. It can be observed that land use change, point source, non-point source management programs have effects on TP throughout the year, but mainly affect Chla from April through November during the period of maximum phytoplankton growth.

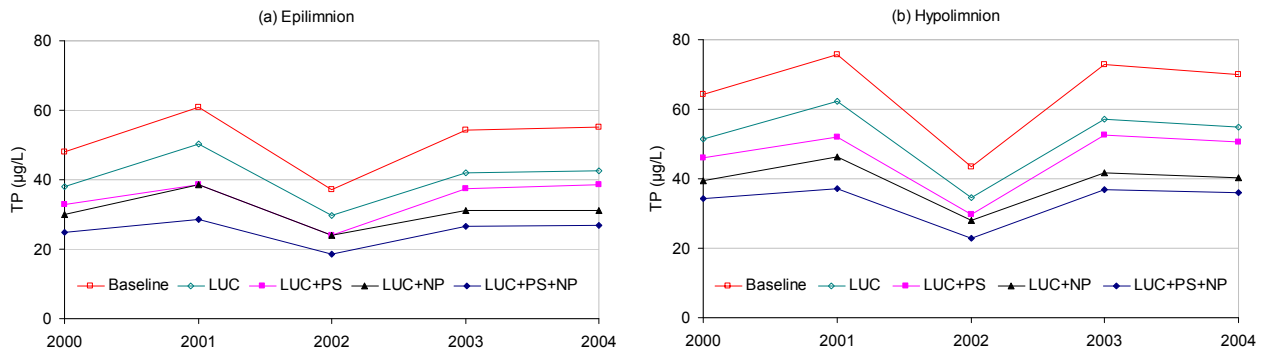


Figure 5. The effect of landuse change (LUC) as well as point source (PS) and non-point (NP) source management programs on annual average TP.

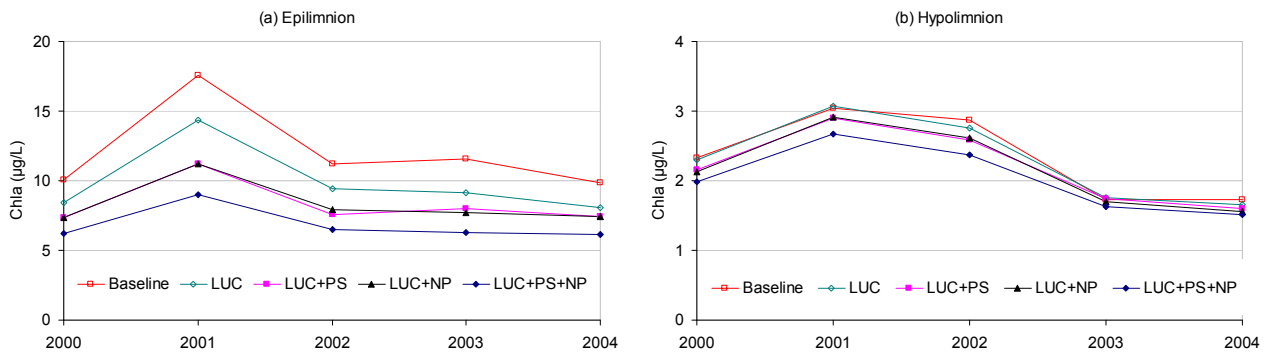


Figure 6. The effect of landuse change (LUC) as well as point source (PS) and non-point (NP) source management programs on annual average Chla.

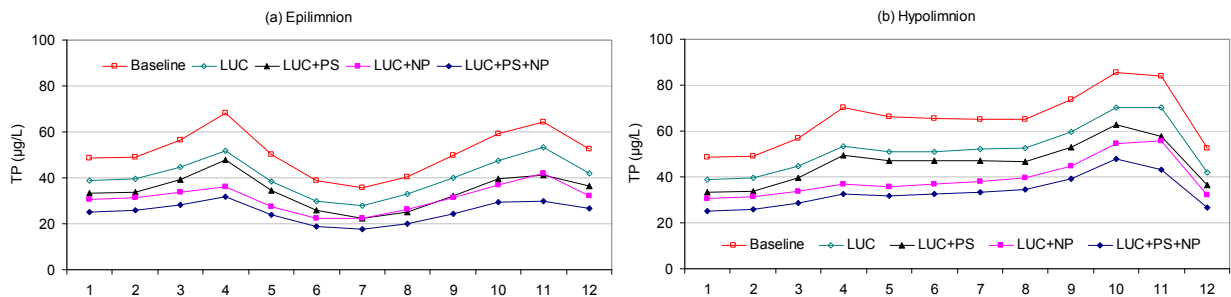


Figure 7. The effect of land use change (LUC) as well as point source (PS) and non-point (NP) source management programs on monthly average TP.

SUMMARY AND CONCLUSIONS

In this study, an automated procedure is implemented to calibrate a one-dimensional reservoir model which is set up to simulate the hydrothermal structure and water quality of Cannonsville reservoir. The calibrated model produces simulated values that match the observed data reasonably well for calibration and validation time periods.

The calibrated model was used to evaluate the effects of land use change and watershed management programs on reservoir water quality. Model simulations confirmed that these

programs reduce the TP and Chla concentrations in both epilimnion and hypolimnion layers, and thereby improve reservoir water quality.

The changes in water quality simulated in this study are specific to the land use change and watershed management programs occurred in the Cannonsville watershed. However, the results still have implications for water quality management and land use planning in other regions facing similar situations.

ACKNOWLEDGEMENTS

The views expressed in this paper are those of the authors and do not reflect the official policy or position of New York City Department of Environment Protection. The authors would like to thank David Lounsbury for preparing the map of Cannonsville Reservoir.

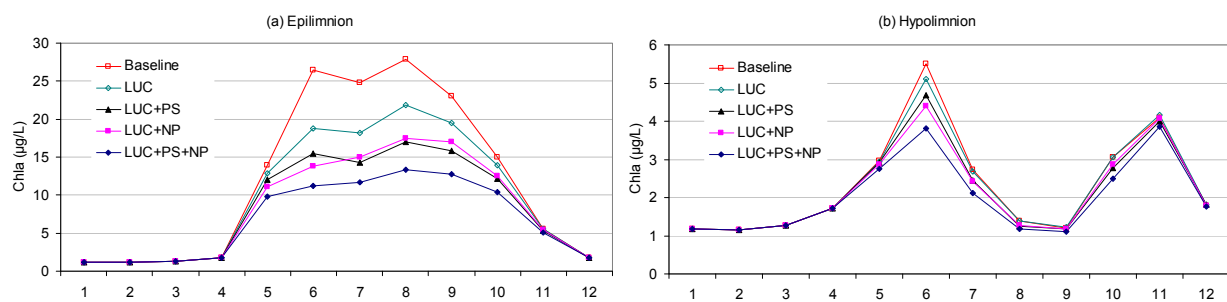


Figure 8. The effect of land use change (LUC) as well as point source (PS) and non-point (NP) source management programs on monthly average Chla.

REFERENCES

- Doerr, S.M., Owens, E.M., Gelda, R.K., Auer, M.T. and Effler, S.W. (1998). Development and testing of a nutrient-phytoplankton model for Cannonsville Reservoir. *Lake and Reservoir Management* 14, 301-321.
- Haith, D.A. and Shoemaker, L.L. (1987). Generalized Watershed Loading Functions for Stream Flow Nutrients. *Water Resources Bulletin* 23(3), 471-478.
- Haupt, R.L., and Haupt, S.E. (2004). *Practical Genetic Algorithms*. John Wiley & Sons, Inc.
- Huang, Y.T. and Liu L. (2010). Multiobjective water quality model calibration using a hybrid genetic algorithm and neural network-based approach. *Journal of Environmental Engineering* 136(10), 1020-1031.
- Huang, Y.T. and Liu, L. (2008). A hybrid perturbation and Morris approach for identifying sensitive parameters in surface water quality models. *Journal of Environmental Informatics* 12(2), 150-159.
- Markensten, H. and Pierson, D. (2007). Weather driven influences on phytoplankton succession in a shallow lake during contrasting years: application of PROTBAS. *Ecological Modelling* 207, 128-136.
- Morris, M.D. (1991). Factorial sampling plans for preliminary computational experiments. *Technometrics* 33(2), 161-74.
- Nelder, J.A. and Mead, R. (1965). A simplex method for function minimization. *The Computer Journal* 7, 308-313.
- NYCDEP (New York City Department of Environmental Protection) (2006). *Watershed Protection Program Summary and Assessment*.
- Owens, E.M. (1998). Development and testing of a one-dimensional hydrothermal models of Cannonsville reservoir. *Lake and Reservoir Management* 14, 172-185.
- Reynolds, C.S., Irish, A.E. and Elliott, J.A. (2001). The ecological basis for simulating phytoplankton responses to environmental change (PROTECH). *Ecological Modelling* 140, 271-291.
- Saltelli, A., Tarantola, S., Campolongo, F. and Ratto, R. (2004). *Sensitivity Analysis in Practice: a Guide to Assessing Scientific Models*. John Wiley & Sons Ltd, Chichester, UK.
- Schneiderman, E.M., Pierson, D.C., Lounsbury, D.G. and Zion, M.S. (2002). Modeling the hydrochemistry of the Cannonsville watershed with GWLF. *Journal of the American Water Resources Association* 38(5), 1323-1347.

Huang et al.

UFI (Upstate Freshwater Institute) (2001). *Calibration, Verification of a One-Dimensional Hydrothermal and Eutrophication Model for Catskill/Delaware Reservoirs*. Internal report NYCDEP, Vahalla N.Y.

Chaotic advection in wind-induced shallow basin flows: a 3D approach

János Józsa¹, Sándor Szanyi¹, Tamás Krámer¹, Enrico Napoli², Tamás Tél³

¹*Budapest University of Technology and Economics, Hungary*

²*University of Palermo, Italy*

³*Eötvös University, Budapest, Hungary*

Corresponding author: Prof. János Józsa, jozsa@vit.bme.hu

As important environmental features, mixing properties of water bodies in closed shallow basins are investigated. Time dependent motion, often resulting in chaotic behavior, requires the Lagrangian description of the transport. Pattantyús-Ábrahám et al. (2008) and Károlyi et al. (2010) considered unsteady hydrodynamics driven by periodical wind forcing in simplified shallow lake geometry to explore chaotic advection properties in a depth-averaged manner. With methods originating in chaos theory it was possible to locate spatial structures which govern the flow and areas where the most effective mixing occurs. Such structures as hyperbolic points (the Lagrangian analogs of Eulerian instantaneous or steady-state stagnation points) and manifolds have long been used for classifying the evolution of trajectories in abstract dynamical systems but their application in the context of fluid dynamics offers a novel tool with clear physical meaning: identifying vortex boundaries, barriers and avenues of transport, or lines of strong stretching. In the sample lake mixing was found typically strong at complex intersection of stretching and contracting manifolds around the hyperbolic points, where trajectories of initially close particles quickly separated from each other along the stretching directions. In fact, near hyperbolic points, the rate of separation of nearby particles is exponential in time, leading to the finite size Lyapunov-exponent (FSLE) as a key parameter for chaos analysis, by which coherent structures as stable and unstable manifolds were also identified.

Using the same simple lake geometry, the complete 3D flow pattern driven by realistic wind shear stress field modeled by proper CFD tool is looked at to identify and analyze chaotic advection features. Instead of one Eulerian stagnation point in 2D steady-state, a tilted inner stagnation line can be found, the impact of which on 3D particle advection and spreading is investigated. Next, periodic wind forcing is applied and particle advection is analyzed primarily by means of Lyapunov-exponent distributions to identify hyperbolic points and chaos behavior. Such hydrodynamic aspects are important to reveal for applied sciences, e.g. for estimating water exchange mechanisms, interpreting plankton movement or planning and operating pollutant outfalls, at last all contributing to the water resources management in shallow lake environments.

References

- Pattantyús-Ábrahám, M., Tél, T., Krámer, T., Józsa, J. (2008): Mixing properties of a shallow basin due to wind-induced chaotic flow. *Advances in Water Resources* 31: pp. 525-534.
- Károlyi, G., Pattantyús-Ábrahám, M., Krámer, T., Józsa, J., Tél, T. (2010): Finite-size Lyapunov exponents: a new tool for lake dynamics. *Proc. Institution of Civil Engineers, Engineering and Computational Mechanics* 163, Issue EM4: pp. 251–259.

Lake surface temperature of large northern lakes:

A comparison between 1-D model simulations and MODIS satellite retrievals

H. Kheyrollah Pour*¹, C.R. Duguay¹, A. Martynov², L.C. Brown¹

¹Interdisciplinary Centre on Climate Change and Department of Geography & Environmental Management, University of Waterloo, Canada

²Centre ESCER, Département des sciences de la Terre et de l'atmosphère, Université du Québec à Montréal, Montreal, Canada

*Email: h2kheyro@uwaterloo.ca

KEYWORDS

Great Bear Lake; Great Slave Lake; Lake Ice; Lake Modeling; Lake Surface Temperature; MODIS.

EXTENDED ABSTRACT

Large lakes are known to have a considerable influence on local and regional climates and circulation of the atmosphere. The impact of lakes on local temperature can be important for regions in which lakes are abundant. The presence or absence of ice cover on lakes during the winter months is also known to affect both regional climate and weather events (Rouse *et al.*, 2007a). If lakes are frozen, the physical properties of the lake surface such as surface temperature, albedo, and roughness are very different. Lake surface properties and the amount of surface lake area are major issues of interest when dealing with the lake-atmosphere interactions (Ljungemyr *et al.*, 1996). Understanding the process of the lake ice/temperature interactions with climate allows for better climate modeling and weather forecasting. In most numerical weather prediction (NWP) and climate models, however, the effect of lakes is often ignored or parameterized very roughly (Brown and Duguay, 2010). Improvement in numerical weather forecasting can be achieved by interactive coupling of NWP and regional climate models with lake models (Mironov *et al.*, 2010).

In this study, we assess the performance of the Canadian Lake Ice Model (CLIMo) and Freshwater Lake (FLake) model in simulating LST and ice cover for two large, deep, lakes of northern Canada and identify the uncertainties in the 1-D lake models and satellite data products. In particular, LSTs simulated with the lake models are compared with those derived from Moderate Resolution Imaging Spectroradiometer (MODIS) on a daily basis annually and seasonally (open water and ice cover seasons) for the period 2002-2010. Simulated ice thickness and freeze-up/break-up dates are compared to *in situ* observations for the periods 1961-1996 and 2002-2008.

The simulations conducted for a nine-year period have shown that both models are capable of reproducing the seasonal and inter-annual evolution of surface temperatures of the lakes as well

as the inter-annual variations in ice thickness and freeze-up/ break-up dates. LST over both lakes changes in different seasons during summer and winter seasons with the higher temperature in summer and colder temperature in winter. Both lakes are located at high latitude and are frozen for a considerable part of the year, so that the atmosphere does not always directly interact with the lake water. Lake-atmosphere interactions occur for several months through the air-ice interface or, if snow is present, at the air-snow interface.

CLIMo demonstrated a generally better performance than FLake in the case of GSL and GBL, especially for ice cover season, when compared to MODIS and *in situ* measurements. The absence of snow in the FLake model had a large effect on ice growth and decay rates and thus, by extension, ice break-up dates. Figure 1 shows the simulated ice thickness from both models in comparison with *in situ* measurements at the Back Bay site. Results indicate a strong agreement between *in situ* measurements and CLIMo ($I_a = 0.943$, MBE = 9 cm, RMSE = 17 cm), and a lower agreement with FLake ($I_a = 0.765$, MBE = 26 cm, RMSE = 39 cm). As indicated earlier, FLake does not consider snow depth over lake ice. The accumulation of snow influences ice growth and thaw rates by adding an insulation layer.

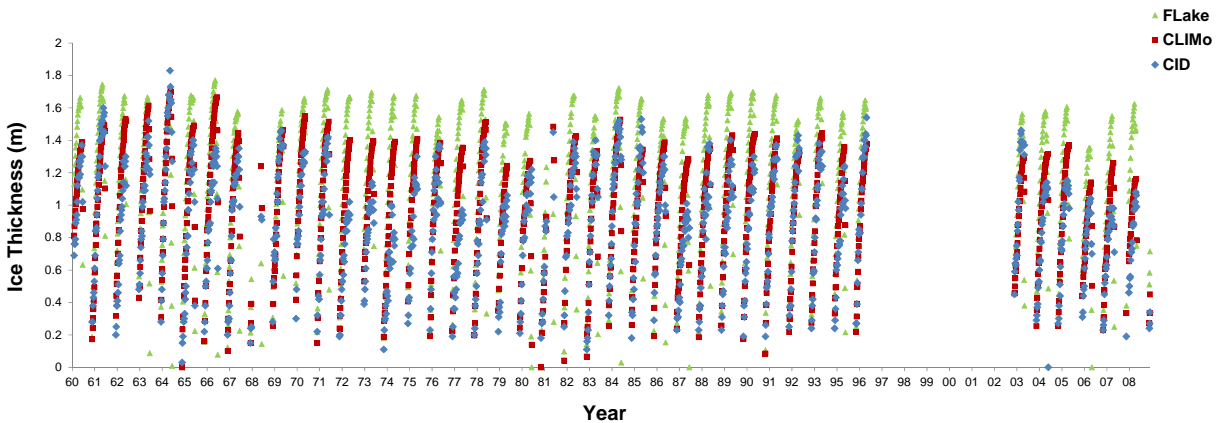


Figure 1: Comparison of observed (CID) and simulated (CLIMo and FLake) ice thickness for Back Bay (1961-2008).

As the FLake model is based on a two-layered structure, it does not allow for the formation of the hypolimnion layer in deep lakes. As a result, open water temperature for the deepest lake sites (40 m) tended to be underestimated. MODIS data showed generally colder temperatures compared to models, which could be explained to some extent by undetected clouds (erroneous measurements during cloudy conditions) and the time differences of the MODIS LSTs used to calculate clear-sky daily averages, compared to the daily air temperatures from weather stations used as forcing data in models. Cloud contamination has been identified as a source of occasional (low temperature) errors in MODIS products. To minimize this problem, averaging of LSTs over longer time periods (weekly or monthly) merits to be further examined. Overall, MODIS showed a very good agreement with the models when calculating statistics over a full annual cycle. Although biases were larger when years were broken down into the open water and ice cover seasons, results indicate that LST data from MODIS or other thermal infrared satellite sensors such as AATSR are a promising data source for calibrating/evaluating lake models, as well as for data assimilation into NWP models. Evaluation of the accuracy of satellite-derived LSTs is also needed for northern lakes as previous investigations have tended to focus on mid-latitude lakes during the open water season only.

References

- Brown, L.C., and Duguay, C.R. 2010. The response and role of ice cover in lake-climate interactions. *Progress in Physical Geography*, 1-34.
- Ljungemyr, P., Gustafsson, N., and Omstedt, A. 1996. Parameterization of lake thermodynamics in a high-resolution weather forecasting model. *Tellus*, **48A**, 608-621.
- Mironov, D., Heise, E., Kourzeneva, E., Ritter, B., Schneider, N., and Terzhevik, A. 2010. Implementation of the lake parameterisation scheme FLake into the numerical weather prediction model, COSMO. *Boreal Environment Research*, **15**, 218-230.
- Rouse, W.R., Binyamin, J., Blanken, P.D., Bussi eres, N., Duguay, C.R., Oswald, C.J., Schertzer, W.M., and Spence, C. 2007a. The Influence of lakes on the regional heat and water balance of the central Mackenzie River Basin. Chapter 18 in *Cold Region Atmospheric and Hydrologic Studies: The Mackenzie GEWEX Experience*, Volume 1: Atmospheric Dynamics. Springer-Verlag, 309-325.

Some new methods for estimating hydraulic residence time from passive tracer release studies

A.T. King* and E.A. Cowen

DeFrees Hydraulics Laboratory, School of Civil & Environmental Engineering, Cornell University, 220 Hollister Hall, Ithaca, NY 14853, USA

*Corresponding author, e-mail atk6@cornell.edu

KEYWORDS

Residence time; tracer study; continuously stirred tank reactor.

EXTENDED ABSTRACT

Hydraulic residence time (HRT), the time that a water parcel remains in a system, is a key variable influencing chemical and biological processes in estuaries, lakes, and wetlands. A standard method for measuring HRT is the passive tracer release study, in which a known mass of neutrally buoyant tracer is released all at once into an aquatic system, and the flux of that tracer out of the system is continuously monitored at one or more outlets. If the tracer leaves the system through a single outlet and the tracer is fully mixed across that outlet, the fraction of tracer leaving the system per unit time, $r(t)$, is given by

$$r(t) = \frac{Q(t)C(t)}{M_0} \quad (1)$$

where t is time, $Q(t)$ is the volume flow rate through the outlet (positive out), $C(t)$ is the tracer concentration at the outlet (mass per unit volume), and M_0 is the mass of tracer released. Provided that all of the initial mass is observed leaving the system, the first temporal moment of $r(t)$ is equal to the mean HRT, T_R .

However, calculation of T_R is seldom as straightforward as taking the first moment of the measured $r(t)$ curve. Non-conservative effects, such as tracer decay with exposure to sunlight (photolytic decay) and sorption of tracer onto sediment and vegetation, may be significant, and $r(t)$ must be corrected for these effects. Furthermore, due to limitations in time or other resources, field experiments are typically terminated before all of the tracer mass is observed leaving the system, in which case $r(t)$ must be extrapolated, either by analytical or numerical methods, to obtain an estimate of T_R . Traditional analytical methods for extrapolating $r(t)$ often violate the principle of mass conservation, predicting that greater or less than 100% of the tracer mass exits the system after infinite time. Extrapolation by the most common analytical method is difficult when there is oscillatory flow, especially if $Q(t)$ is negative for some portion of time. In this extended abstract, we outline a new method for extrapolating $r(t)$ that does not violate conservation of mass and that is robust in the case of highly unsteady and reversing flow. This work is part of a larger project that also includes development of a new method for correcting for photolytic decay of common tracers and some progress on the problem of sorption.

Extrapolation requires a model predicting $r(t)$. Often, the system is assumed to behave as a continuously stirred tank reactor (CSTR) after some initial mixing period. For a CSTR,

$$r(t) = r_0 \exp(-k_0 t) \quad (2)$$

where r_0 and k_0 are constants. Let us assume that our system is fully mixed after time $t = t_0$. It is common practice for $r(t)$ to be extrapolated by taking the natural log of the measured $r(t)$ curve for $t > t_0$ and finding the best fit to the natural log of Equation 2 using r_0 and k_0 as free variables. However, this method does not guarantee that mass is conserved. In order to specify conservation of mass, let us define the moving zero'th moment of $r(t)$:

$$R(t) \equiv \int_0^t r(\tau) d\tau. \quad (3)$$

In our new notation, the conservation of mass condition is $R(t) \rightarrow 1$ as $t \rightarrow \infty$. For a CSTR, the conservation of mass constraint requires that r_0 and k_0 satisfy the following equation:

$$r_0 = k_0 \exp(k_0 t_0) (1 - R(t_0)), \quad (4)$$

reducing the number of free variables to one.

If $Q(t)$ is negative for part of a tracer study, the natural log of $r(t)$ will be imaginary at those times when $Q(t)$ is negative, and it will be difficult to fit an exponential tail to $r(t)$. We propose that a better general approach is to find the best fit of the CSTR model to a quantity that approaches what we are looking for: T_R , which is the first moment of $r(t)$. Let us define the running first moment of $r(t)$ as follows:

$$\Theta(t) \equiv \int_0^t r(\tau) \tau d\tau. \quad (5)$$

By definition, $\Theta(t) \rightarrow T_R$ as $t \rightarrow \infty$. For a CSTR, we may plug Equation 2 into Equation 5, finding

$$\Theta(t) \equiv \Theta(t_0) + \frac{r_0}{k_0^2} [\exp(-k_0 t_0) (k_0 t_0 + 1) - \exp(-k_0 t) (k_0 t + 1)]. \quad (6)$$

While the measured $r(t)$ curve may be highly oscillatory and even become negative in many tracer studies, deviating strongly from Equation 2, the measured $\Theta(t)$ curve tends to more closely resemble Equation 6, even in the case of highly unsteady flow, provided that the time scale of flow unsteadiness is much less than T_R . Hence, we recommend for systems that exhibit CSTR behavior after some time t_0 that instead of extrapolating the measured values of $r(t)$, investigators should extrapolate the measured values of $\Theta(t)$ by finding the best fit to Equation 6 under the conservation of mass constraint given by Equation 4. In our presentation, we will demonstrate the application of this method in a surface water system with highly oscillatory flow, and we will also discuss the application of this method using a transient storage model (sometimes referred to as a dead zone model) as an alternative to the CSTR model. We may also discuss correction for photolytic decay and the problem of sorption of rhodamine WT, a popular fluorescent water tracing dye.

The influence of flooding events of the river Rhine on the anoxic hypolimnion of a river-connected lake

J. Kreling^{1*}, A. Mäck¹, W. Heimann¹ and A. Lorke¹

¹ *Institute for Environmental Sciences, University of Koblenz-Landau, Fortstrasse 7, 76829 Landau, Germany*

** Corresponding author, e-mail kreling@uni-landau.de*

KEYWORDS

flood; inflow; mixing; redoxcline; oxygen loss; reduced substances.

EXTENDED ABSTRACT

In the Upper Rhine Valley, many backwaters and lakes exist reflecting the historic straightening of the river Rhine. Especially the waters connected to the main channel provide important ecosystem functions to the riverine communities. For example they serve as spawning and nursery grounds for many fish species (Staas and Neumann, 1994). Today many of these water bodies suffer from severe oxygen depletion in the hypolimnion during summer stratification. We tested the hypothesis that the inflow of river water during rising water levels might enter the hypolimnion and therefore oxygenate this anoxic part of a river-connected lake.

In summer 2010, we conducted a four month field survey at a gravel pit lake which is connected to the Rhine via a backwater. During this survey near Leimersheim, Germany, we sampled weekly depth profiles of temperature and dissolved oxygen with a multiparameter probe. Additional profiles were measured at the peak of flooding events. Continuous profile measurements were obtained from an automatic profiling buoy with a measurement interval of 4 hours for a period of 9 weeks. From the profiles of the multiparameter probe and the bathymetry of the lake we derived heat and mass balances for oxygen. Furthermore, we calculated surface net-heat fluxes based on meteorological data from a nearby weather station.

We observed seven flooding events which all could not lead to water import into the hypolimnion, even though the river water cooled down during flooding. However, six flooding events were accompanied by a decreased surface net-heat flux and resulted in mixing of the epilimnion (Figure 1). The inflowing water merged into the epilimnion within the first 150 m of the lake. During four of the flooding events the mixing affected more than 90 % of the lake's volume and the redoxcline was forced downwards between 1 and 2.5 m. Thereby the anoxic volume was greatly reduced to between 8 and 34 % of its previous extent. At the same time, a considerable undersaturation of oxygen was observed in the mixed layer. Mass balances revealed that the deepening of the oxic layer was accompanied by a loss of oxygen, which could not be explained completely by mixing, as shown in

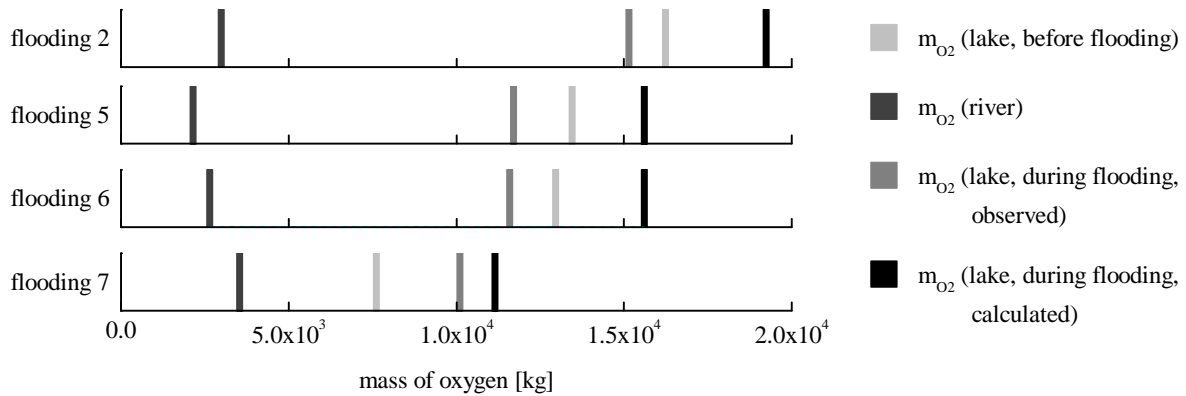


Figure 2. We assume that the upwelling of anoxic water into the oxic layer and thereby especially the oxidation of reduced substances contribute to the observed oxygen deficit in large part. Such processes are usually known to deplete oxygen in lakes during fall overturn (Effler *et al.*, 1988).

Although we found the anoxic volume to be reduced during flooding, three flooding events even resulted in a decrease in the lake’s total oxygen content. This may compromise the lake’s biocenosis and can be expected to become more important as climate change will make flooding events more frequent in future.

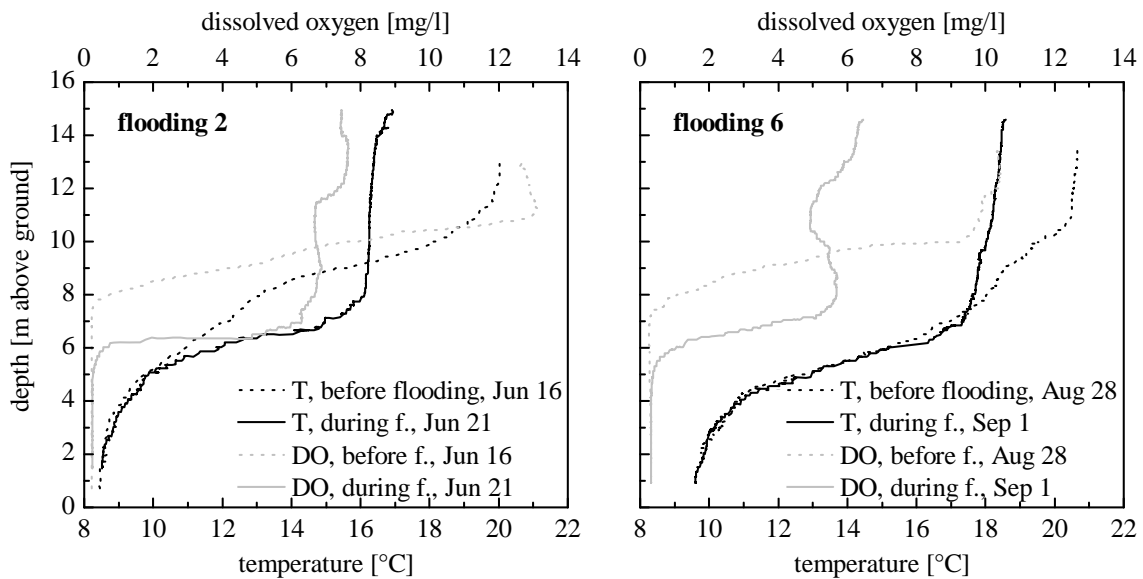


Figure 1. Depth profiles of temperature (black) and dissolved oxygen (grey) measured at the deepest point of the lake before (dotted line) and during (solid) two exemplary flooding events.

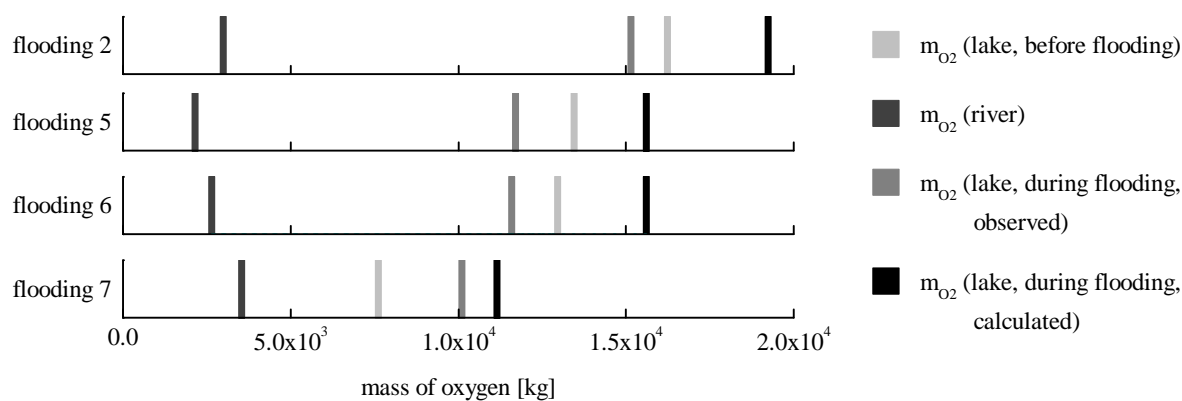


Figure 2. Mass of oxygen in the lake before the flooding event (light grey), in the inflowing river water (dark grey) and in the lake after mixing of river and lake water as it was observed (grey) and calculated based on mass balances (black).

REFERENCES

- Effler S.W., Hassett J.P., Auer M.T. and Johnson N. (1988). Depletion of epilimnetic oxygen and accumulation of hydrogen sulfide in the hypolimnion of Onondaga Lake, NY, U.S.A. *Water, Air, and Soil Pollution* 39 (1-2), 59-74.
- Staas S. and Neumann D. (1994). Reproduction of fish in the Lower River Rhine and connected gravel-pit lakes. *Water Science and Technology* 29 (3), 311-313.

Wave attenuation by the eelgrass *Zostera marina*

J. R. Lacy* and A.W. Stevens

US Geological Survey, Pacific Coastal and Marine Science Center, 400 Natural Bridges Drive,
Santa Cruz CA 95060, USA

*Corresponding author, e-mail jlacy@usgs.gov

KEYWORDS

Wave attenuation, eelgrass, submerged vegetation.

EXTENDED ABSTRACT

Prevention or reduction of coastal erosion through wave damping is often cited as an ecological benefit of submerged aquatic vegetation such as eelgrass. However, there are few field measurements quantifying the effect of eelgrass on waves, or the dependence of such an effect on water depth, wave period, or wave height. We investigated wave attenuation by the eelgrass *Zostera marina* on a high-energy shoreline in Puget Sound, Washington USA, just north of Possession Point on Whidbey Island.

Prior to the wave measurements, bathymetry and eelgrass percent cover at the study site were mapped acoustically (Figure 1) (Stevens et al., 2008). The eelgrass meadow extended about

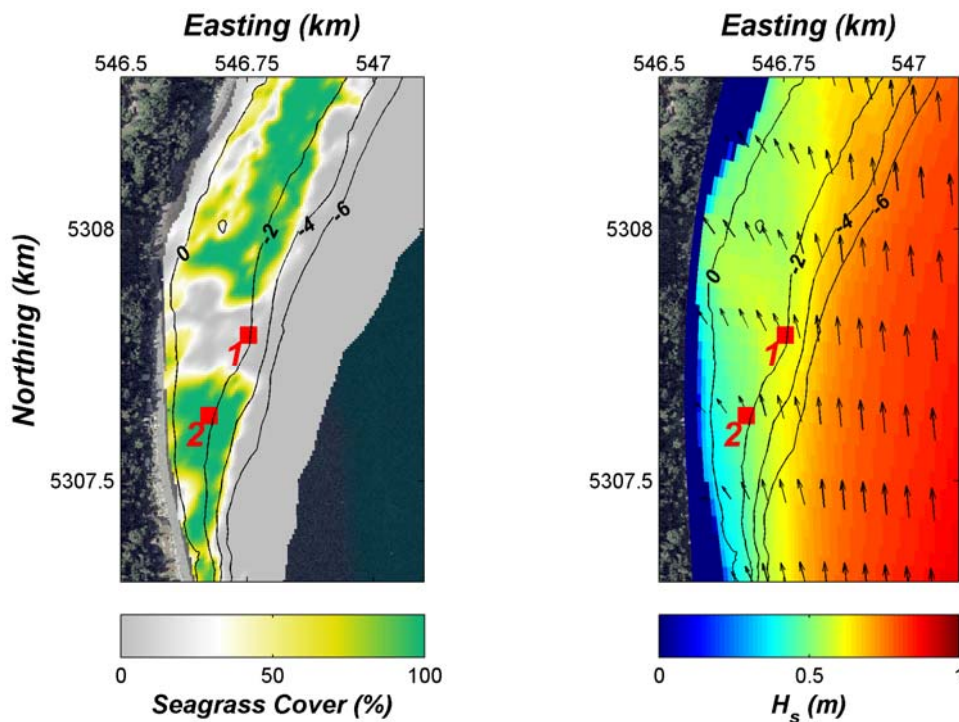


Figure 1: Eelgrass percent cover from acoustic mapping (left), and modeled significant wave height and direction (right), with station locations and bathymetric contours in m MLLW.

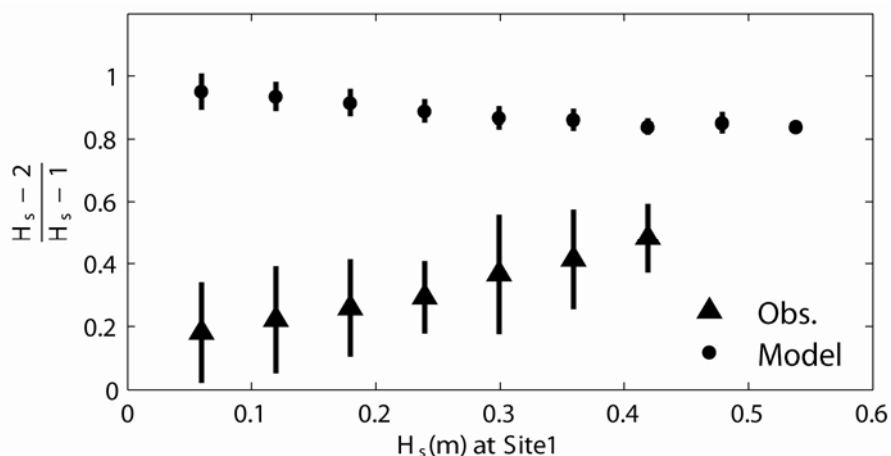


Figure 2. Means and standard deviations of ratio of H_s at site 2 to H_s at site 1 vs. H_s at site 1.

150 m cross-shore, from 0 to -4 m MLLW, except for a naturally-occurring break in vegetation approximately 150 m wide. Eelgrass blade length averaged 0.55 m. We measured wave properties within the canopy (site 2) and in the bare patch (site 1). Significant wave height (H_s) and wave orbital velocities (u_b) were calculated from six-minute bursts of 4-Hz pressure and velocity data collected at 30 minute intervals. Maximum H_s during the study period (February 28 to March 21, 2007) exceeded 0.6 m outside the meadow, and during three events H_s exceeded 0.3 m for more than 6 hours. Representative wave periods were 2-4 s.

We used a numerical model to identify the influence of factors other than vegetation (such as bathymetry) on differences in wave heights between the two sites. Wave heights for the study period were simulated with the hydrodynamic model Delft3D (in depth-averaged mode) coupled with the SWAN wave model. The model did not account for the effects of vegetation on currents or waves. The model domain encompassed all of Puget Sound, with increased grid resolution for Possession Sound. Wind-wave development was driven with a spatially uniform, time varying wind field. Model accuracy was assessed by comparison to observations at site 1: RMS error for H_s was 0.11 m.

The ratio of measured H_s at site 2 to H_s at site 1 was 0.32 ± 0.17 ("mean \pm s.d.") during wavy periods (defined as $H_s > 0.15$ m at site 1). In contrast, the same ratio with model results was 0.87 ± 0.045 . The results indicate that the eelgrass reduced wave height by approximately 50%, less than 100 m (in the direction of wave propagation) into the meadow. Larger waves were attenuated less than smaller waves (Figure 2). In addition, attenuation varied with wave frequency, with greatest attenuation at periods of 3-4 s. These variations of attenuation with wave height and frequency are consistent with the findings of Bradley and Hauser (2009) at a lower-energy site, where maximum H_s was less than 0.1 m. We also observed a reduction in wave orbital velocity u_b within the meadow, but the effect was less than for wave height.

REFERENCES

- Stevens, A.W., Lacy, J.R., Finlayson, D.P., and Gelfenbaum, G.. (2008). Evaluation of a single-beam sonar system to map seagrass at two sites in northern Puget Sound, Washington. U.S. Geological Survey Scientific Investigations Report 2008-5009, 45 p.
- Bradley, K. and Houser, C. (2009). Relative velocity of seagrass blades: Implications for wave attenuation in low-energy environments. *Journal of Geophysical Research* **114** (F01004), doi:10.1029/2007JF000951.

Internal Solitary-like Waves in Oceans and Lakes: Theory, Modelling and Observations

K. G. Lamb
Department of Applied Mathematics
University of Waterloo

June 7, 2011

1 Introduction

Internal solitary waves (ISWs) are localized, finite-amplitude internal waves with a single extremum which propagate horizontally without changing shape. They exist in an inviscid, horizontally homogeneous stratified fluid of constant depth with a rigid lid and in the absence of rotation. Such waves do not exist in the ocean for a number of reasons, including the effects of rotation, which produce long-wave dispersion, free-surface effects, variable bathymetry, and horizontally varying stratification and currents which also modify the propagation of internal solitary-like waves (Helfrich and Grimshaw, 2008). Never-the-less, the concept of a solitary wave has proven to be a very useful model of many observed solitary-like waves. In the ocean they are typically hundreds of meters long and tens of meters high. ISWs often appear as a group and are ubiquitous in the stratified coastal ocean.

Numerous observations and numerical simulations make it clear that the most important generation mechanism for ISW in the ocean is the nonlinear evolution of the internal tide generated by tide-topography interaction (Hibiya, 1986; Lamb, 1994; Gerkema, 2001). There are other generation mechanisms, including the adjustment of river plumes, resonant flow over topography, and possible via the interaction of Kelvin waves with variable bathymetry (Hosegood and van Haren, 2004). In long narrow lakes ISWs are formed by the nonlinear evolution of basin-scale internal seiches.

ISWs can be the source of large stresses suffered by off-shore oil-drilling rigs (Osborne and Burch, 1980). They can transport fluid (Lamb, 1997) and energy large distances. As they propagate they can trigger instabilities in the bottom boundary layer beneath the waves and as they shoal into shallow water they can break. Mixing related to the breaking waves can result in a vertical flux of nutrients from the bottom to the ocean interior, making the local region fertile for fishery. ISWs are believed to be an important source of vertical mixing in coastal oceans and play an important role in nutrient dispersion and sediment transport (Huthnance, 1989).

Shoaling ISWs have been the subject of much recent interest, including both laboratory investigations (Helfrich, 1992; Michallet and Ivey, 1999; Boegman and Ivey, 2005) and numerical simulations (Bourgault and Kelley, 2007; Lamb and Nguyen, 2009; Aghsaee et al., 2010). In another set of laboratory experiments (Sveen et al., 2002; Guo et al., 2004) the evolution of ISWs passing over a ridge was considered.

In this talk I will give an overview of observations, experiments, theory and numerical simulations relevant to shoaling internal waves and internal wave energetics including the effects of background sheared currents.

2 Theory

2.1 Governing equations

The governing equations we use are the incompressible Navier-Stokes equations. The equations are solved numerically by first splitting the density and pressure into two parts via

$$\begin{aligned}\tilde{\rho} &= \rho_0(1 + \rho), \\ \tilde{p} &= -\rho_0gz + \rho_0p,\end{aligned}\tag{1}$$

where ρ_0 is a reference density. In the following the scaled non-dimensional density ρ will be referred to simply as the density. The governing equations can then be written as

$$(1 + \epsilon\rho)(\vec{u}_t + \vec{u} \cdot \vec{\nabla}\vec{u} + f\hat{k} \times \vec{u}) = -\vec{\nabla}p - \rho g\hat{k} + \nu\nabla^2\vec{u},\tag{2a}$$

$$\rho_t + \vec{u} \cdot \vec{\nabla}\rho = \kappa\nabla^2\rho,\tag{2b}$$

$$\vec{\nabla} \cdot \vec{u} = 0.\tag{2c}$$

Here $\vec{u} = (u, w)$ is the velocity in the vertical xz -plane, ν the kinematic viscosity, κ the diffusivity and the parameter ϵ is zero if the Boussinesq approximation is made and one otherwise.

Exact mode-one internal solitary wave solutions of the above equations exist provided (i) viscosity and diffusion are ignored, (ii) rotation is ignored ($f = 0$), (iii) the water depth and fluid properties are horizontally homogeneous; and (iv) the fluid has a rigid lid. Under the Boussinesq approximation ISWs are obtained by solving the Dureuil-Jacotin-Long (DJL) equation. The extension to include a background current $\bar{U}(z)$ (Stastna and Lamb, 2002; Lamb, 2003) leads to the following nonlinear, elliptic eigenvalue problem:

$$\nabla^2\eta + \frac{\bar{U}'(z - \eta)}{c - \bar{U}(z - \eta)}(\eta_x^2 + (1 - \eta_z)^2 - 1) + \frac{N^2(z - \eta)}{(c - \bar{U}(c - \eta))^2}\eta = 0,\tag{3}$$

together with the boundary conditions $\eta = 0$ at $z = 0, -H$ and $\eta = 0$ (or $\rightarrow 0$ as $x \rightarrow \pm\infty$) at the lateral boundaries. Here η is the vertical displacement of the streamline passing through (x, z) relative to its far-upstream height. The propagation speed of the solitary wave, c , is an eigenvalue which is found as part of the solution.

2.2 Weakly-nonlinear models

The KdV equation and extensions are often used to model ISWs. Including third-order nonlinearity and the effects of slowly varying bathymetry gives the variable coefficient Gardner equation

$$\frac{\partial\eta}{\partial t} + c(x)\frac{\partial\eta}{\partial x} + \epsilon\alpha(x)\eta\frac{\partial\eta}{\partial x} + \epsilon^2\alpha_1(x)\eta^2\frac{\partial\eta}{\partial x} + \mu\gamma(x)\frac{\partial^3\eta}{\partial x^3} + \delta\frac{c}{2S}\frac{\partial S}{\partial x} = 0,\tag{4}$$

(Small, 2001). ϵ , μ and δ are small parameters for weak-nonlinearity, weak dispersion and weak shoaling effects respectively. Here $\eta(x, t)$ is the wave amplitude (maximum isopycnal displacement), x is the horizontal coordinate, t is time, and $c(x)$ is the linear long-wave propagation speed determined by solving the linear long-wave eigenvalue problem

$$\phi_{zz}(x, z) + \frac{N^2(z)}{c^2} \phi(x, z) = 0, \quad (5)$$

with boundary conditions

$$\phi(x, 0) = \phi(x, -H(x)) = 0. \quad (6)$$

Here x appears parametrically. ϕ is normalized to have a maximum value of one and the leading-order expression for the isopycnal displacement is

$$\zeta(x, z, t) = \eta(x, t)\phi(z, x). \quad (7)$$

The remaining parameters in (4) are the quadratic nonlinear coefficient $\alpha(x)$, the cubic nonlinear coefficient $\alpha_1(x)$, and the dispersion parameter $\gamma(x)$. These are all given in terms of ϕ and c and, in the case of the cubic coefficient, in terms of the first-order correction to the eigenmode ϕ (Lamb and Yan, 1996). The last term in (4) is called the shoaling term.

When the water depth is constant, the coefficients of (4) are constant and the shoaling term drops out. The resulting equation has solitary wave solutions of the form (Lamb, 1998)

$$\eta(x, t) = \frac{\eta_0}{b + (1 - b)\cosh^2\theta} = \frac{\eta_0 \operatorname{sech}^2\theta}{1 - b + b\operatorname{sech}^2\theta}, \quad (8)$$

where

$$\theta = \frac{x - Vt}{\lambda}, \quad (9a)$$

$$V - c = \frac{4\gamma}{\lambda^2} = \frac{\eta_0}{3} \left(\alpha + \frac{1}{2} \alpha_1 \eta_0 \right), \quad (9b)$$

$$b = -\frac{\alpha_1 \eta_0}{2\alpha + \alpha_1 \eta_0}. \quad (9c)$$

If $\alpha_1 < 0$ the wave amplitude is limited by

$$\eta_{lim} = -\frac{\alpha}{\alpha_1}. \quad (10)$$

As the wave amplitude approaches the limiting amplitude waves become very broad and horizontally uniform in the centre. When $\alpha_1 > 0$ waves of either polarity exist. In this case waves with $\alpha\eta_0 > 0$ can have any amplitude while waves with $\alpha\eta_0 < 0$ have a minimum amplitude

$$\eta_{min} = -2\frac{\alpha}{\alpha_1}. \quad (11)$$

Figure 1 summarizes the types of solitary wave solutions for different signs of α and α_1 following Grimshaw et al. (1999). The amplitude limitation and the possibility of ISWs of either polarity for certain stratifications require the cubic-nonlinear term and this qualitative behaviour is exhibited by exact ISWs.

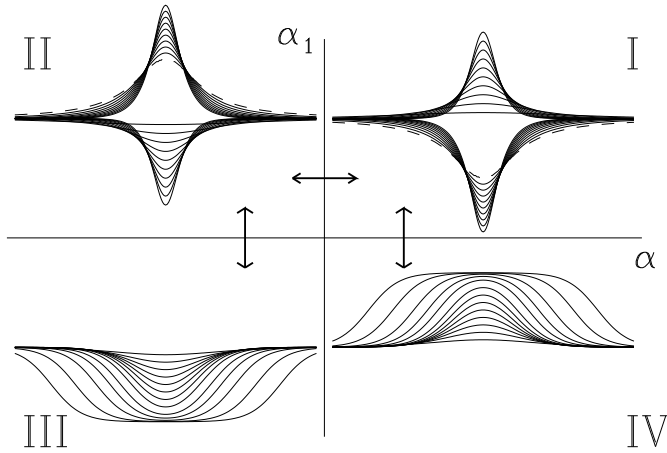


Figure 1: A schematic illustration of the shapes of internal solitary wave solutions of the Gardner equation following (Grimshaw et al., 1999). α and α_1 are the quadratic and cubic nonlinear coefficients. When $\alpha_1 > 0$ waves of either polarity exist with no maximum amplitude. Minimum wave amplitudes exist for waves of elevation/depression for negative/positive quadratic coefficients. When $\alpha_1 < 0$ the polarity of the waves is determined by the sign of the quadratic coefficient. There is no minimum amplitude but now a maximum amplitude exists. Arrows between adjacent quadrants indicate possible transformations of the signs of the nonlinear coefficients that will not destroy internal solitary waves, as long as waves of the given polarity exist in both regions.

An alternative weakly-nonlinear evolution equation is

$$\frac{\partial \xi}{\partial x} + \frac{\alpha(x)}{c^2(x)\sqrt{S}}\xi \frac{\partial \xi}{\partial s} + \frac{\alpha_1(x)}{c^2(x)S}\xi^2 \frac{\partial \xi}{\partial s} + \frac{\gamma(x)}{c^4(x)}\frac{\partial^3 \xi}{\partial s^3} = 0, \quad (12)$$

(Zhou and Grimshaw, 1989; Grimshaw et al., 2004). Here

$$\xi(x, t) = \eta(x, t)\sqrt{S(x)}, \quad (13)$$

and

$$s = \int^x \frac{dl}{c(l)} - t, \quad (14)$$

is a characteristic variable which measures time relative to the leading-order motion along the characteristic curves. Under the transformation $(x, t) \rightarrow (x, s)$ (4) transforms to (12) modulo higher-order terms. x becomes the time-like variable and s the space-like variable.

These weakly-nonlinear models can be extended to include weak rotational and dissipative effects. Weakly-nonlinear models by their nature can not give a complete description of internal solitary waves due to the restrictions they have. Firstly, they always have an amplitude limit due to the fact that the theory assumes the waves are weakly nonlinear. Secondly, most weakly-nonlinear

models are unidirectional, therefore wave reflection cannot be modelled (Boussinesq-type models (ref) are bi-directional). Thirdly, most weakly-nonlinear models are uni-modal. Therefore, they cannot describe the transfer of energy to other wave modes as an ISW shoals.

3 Energy Conservation and Energy Flux

In many instances internal solitary-like waves can be expected to be propagating in an environment with a background sheared current. In the ocean this can be due to large scale ocean currents, however even in their absence most ISWs are riding on an internal tide and hence experience temporally varying vertically sheared background currents. In lakes ISWs are often superimposed on an internal seiche which also induce background sheared currents that will affect the ISWs.

Let $\bar{U}(z)$ be the background current and set $u = \bar{U}(z) + u'$. Neglecting rotation and viscous and diffusive effects the pseudo-energy equation is

$$\frac{\partial}{\partial t} (E_{kp} + E_a) + \vec{\nabla} \cdot (\vec{u}(E_k + E_a + p_d)) = 0, \quad (15)$$

where p_d is the pressure disturbance from the hydrostatic pressure of the undisturbed flow $\bar{p}(z)$,

$$E_k = \frac{1}{2} \rho_0 (1 + \epsilon \rho) (u^2 + w^2), \quad (16)$$

be the kinetic energy density,

$$E_{kp} = E_k - \frac{\rho_0 (1 + \epsilon \bar{\rho})}{2} \bar{U}^2. \quad (17)$$

is the perturbation kinetic energy density, and

$$E_a(x, z, t) = \rho_0 g \int_z^{z^*(x, z, t)} (\bar{\rho}(s) - \rho(x, z, t)) ds, \quad (18)$$

is the available potential energy density. Here $\bar{\rho}(z)$ is the reference density and $z^*(x, z, t)$ is the height of the fluid particle at (x, z, t) in the reference stratification (Scotti et al., 2006; Lamb, 2007, 2008; Lamb and Nguyen, 2009).

Integrating (15) over \mathcal{D} gives the energy balance equation

$$\frac{d}{dt} (\bar{E}_{kp} + \bar{E}_a) = (K_f + APE_f + W) \Big|_{x_r}^{x_\ell}, \quad (19)$$

where $E_{pseudo} = E_a + E_{kp}$ is the total pseudo-energy density,

$$\begin{aligned} K_f &= \int_{-H(x)}^0 u E_k dz, \\ APE_f &= \int_{-H(x)}^0 u E_a dz, \end{aligned} \quad (20)$$

are the vertically integrated kinetic and available potential energy flux densities, and

$$W = \int_{-H(x)}^0 u p_d dz, \quad (21)$$

is the rate work is done by the pressure perturbation. The total energy flux through a horizontal location x is $E_f = K_f + APE_f + W$.

A particularly simple version of the energy equation can be obtained if we assume an isolated disturbance in which no waves have reached the lateral boundaries in the time of interest. In this case it can be shown that

$$\frac{d}{dt}(\bar{E}_{kp} + \bar{E}_a) = -\Delta p_s M, \quad (22)$$

where

$$M = \int_{-H}^0 \bar{U}(z) dz, \quad (23)$$

is the volume flux associated with the background current entering the left boundary and $\Delta p_s = p_s(x_r) - p_s(x_l)$ is the change in the surface pressure across the domain. If the water depth is constant $\Delta p_x = 0$ however it can be non-zero if the water depth varies. Under these conditions the energy may change in time due to work done by the cross-domain pressure difference. The pressure change is a consequence of the use of a rigid lid. With a free surface surface waves are generated. The energy change associated with the internal waves is now balanced by a compensating energy flux associated with surface waves.

For barotropic tidal flow over isolated topography (same water depth to each side) it is appropriate to consider the energy equation in a reference frame moving with the far-field barotropic tide $\bar{U}_b(t)$. This results in the energy balance

$$\frac{d}{dt} \bar{E}_{pseudo} = (K_f + APE_f + W) \Big|_{x_r}^{x_\ell} + G. \quad (24)$$

where the conversion term is

$$G = \int_{x_l}^{x_r} (E_k + E_a + p_d) \Big|_{z=-H+\bar{h}} \bar{U}_b h_{\bar{x}} dx = \bar{U}_b(t) \int_{x_l}^{x_r} (E_k + E_a + p_d) \Big|_{z=-H+\bar{h}} h_{\bar{x}} dx. \quad (25)$$

The rate of change of wave energy is balanced by the flux of energy through the lateral boundaries plus the rate energy is injected into the system through the conversion term.

Acknowledgments This work is supported by a grant from the Natural Sciences and Engineering Research Council of Canada. Part of this work was supported by a Project Grant from the Canadian Foundation for Climate and Atmospheric Science (CFCAS).

References

- Aghsaee, P., Boegman, L., Lamb, K. G., 2010. Breaking of shoaling internal solitary waves. *J. Fluid Mech.* 659, 289–317.
- Boegman, L., Ivey, G. N., 2005. Flow separation and resuspension beneath shoaling nonlinear internal waves. *J. Geophys. Res.* 114, c02018, doi:10.1029/2007JC004411.
- Bourgault, D., Kelley, D., 2007. On the reflectance of uniform slopes for normally incident interfacial solitary waves. *J. Phys. Ocean.* 37, 1156–1162.
- Gerkema, T., 2001. Internal and interfacial tides: beam scattering and local generation of solitary waves. *J. Marine Res.* 59, 227–255.

- Grimshaw, R., Pelinovsky, E., Talipova, T., 1999. Solitary wave transformation in a medium with sign-variable quadratic nonlinear and cubic nonlinearity. *Physica D* 132, 40–62.
- Grimshaw, R., Pelinovsky, E. N., Talipova, T. G., Kurkin, A., 2004. Simulations of the transformation of internal solitary waves on oceanic shelves. *J. Phys. Oceanogr.* 34, 2774–2791.
- Guo, Y., Sveen, J. K., Davies, P. A., Grue, J., Dong, P., 2004. Modelling the motion of an internal solitary wave over a bottom ridge in a stratified fluid. *Env. Fluid Mech.* 4, 415–441.
- Helfrich, K. R., 1992. Internal solitary wave breaking and run-up on a uniform slope. *J. Fluid Mech.* 243, 133–154.
- Helfrich, K. R., Grimshaw, R., 2008. Nonlinear disintegration of the internal tide. *J. Phys. Oceanogr.* 38, 686–701.
- Hibiya, T., 1986. The generation of internal wave by tidal flow over a sill. *J. Geophys. Res.* 91, 533–542.
- Hosegood, P., van Haren, H., 2004. Near-bed solibores over the continental slope in the faeroeshetland channel. *Deep-Sea Research II* 51, 2943–2971.
- Huthnance, J. M., 1989. Internal tides and waves near the continental shelf edge. *Geophys. Astrophys. Fluid Dyn.* 48, 81–105.
- Lamb, K. G., 1994. Numerical experiments of internal wave generation by strong tidal flow across a finite amplitude bank edge. *J. Geophys. Res.* 99, 843–864.
- Lamb, K. G., 1997. Particle transport by nonbreaking, solitary internal waves. *J. Geophys. Res.* 102, 18641–18660.
- Lamb, K. G., 2003. Shoaling solitary internal waves: on a criterion for the formation of waves with trapped cores. *J. Fluid Mech.* 478, 81–100.
- Lamb, K. G., 2007. Energy and pseudoenergy flux in the internal wave field generated by tidal flow over topography. *Cont. Shelf Res.* 27, 1208–1232.
- Lamb, K. G., 2008. On the calculation of the available potential energy of an isolated perturbation in a density stratified fluid. *J. Fluid Mech.* 597, 415–427, doi:10.1017/S0022112007009743.
- Lamb, K. G., Nguyen, V. T., 2009. Calculating energy flux in internal solitary waves with an application to reflectance. *J. Phys. Oceanogr.* 39, 559–580, doi: 10.1175/2008JPO3882.1.
- Lamb, K. G., Yan, L., 1996. The evolution of internal wave undular bores: comparisons of a fully nonlinear numerical model with weakly nonlinear theory. *J. Phys. Oceanography* 26, 2712–2734.
- Michallet, H., Ivey, G. N., 1999. Experiments on mixing due to internal solitary waves breaking on uniform slopes. *J. Geophys. Res.* 104, 13,467–13,477.
- Osborne, A. R., Burch, T. L., 1980. Internal solitons in the andaman sea. *Science* 208, 451–460.
- Scotti, A., Beardsley, R., Butman, B., 2006. On the interpretation of energy and energy fluxes of nonlinear internal waves: an example from massachusetts bay. *J. Fluid Mech.* 561, 103–112.

- Small, J., 2001. A nonlinear model of the shoaling and refraction of interfacial solitary waves in the ocean. part I: Development of the model and investigations of the shoaling effect. *J. Phys. Oceanogr.* 31, 755–772.
- Stastna, M., Lamb, K. G., 2002. Large fully nonlinear internal solitary waves: the effect of background current. *Phys. Fluids* 14, 2987–2999, doi: 10.1063/1.1496510.
- Sveen, J. K., Guo, Y., Davies, P. A., Grue, J., 2002. On the breaking of internal solitary waves at a ridge. *J. Fluid Mech.* 469, 161–188.
- Zhou, X., Grimshaw, R., 1989. The effect of variable currents on internal solitary waves. *Dyn. Atmos. Oceans* 14, 17–39.

Occasional Enhanced Loss of Nutrient Material Through Water Supply Reservoir Overflows

C. Lemckert^{1*}, P. Campbell¹, B. R. Gibbes²

¹ Griffith School of Engineering, Griffith University, Gold Coast, Queensland, Australia

² Centre for Water Studies, School of Civil Engineering, The University of Queensland, Brisbane, Queensland, Australia

*Corresponding author, e-mail c.lemckert@griffith.edu.au

KEYWORDS

Stratification; overflows; reservoir; zooplankton.

EXTENDED ABSTRACT

Introduction

The transfer of nutrients into and out of lakes and reservoirs depends upon a number of factors including, atmospheric conditions, terrestrial properties and inflow and outflow rates. How the nutrients are trapped, transferred through, produced, and recycled, within lakes or reservoirs are also a function of the internal reservoir dynamics. These internal dynamics cover chemical, biological and physical (such as internal wave mixing and selective withdrawal as a result of water extraction) processes.

In South East Queensland, Australia, recent field investigations have shown local reservoirs experience strong diurnal zooplankton cycling, whereby during daylight hours zooplankton remain on or near the sediment-water interface. As light intensity decreases (in the late afternoon) the zooplankton commence a migration to the surface layer where they stay during the night. As soon as an increase in light intensity occurs in the morning (even long before sunrise) the zooplankton begins its migration down towards to sediment-water interface. As the zooplankton is small in size ($O(5\text{mm})$), and their vertical migration rates are slow ($O(1\text{cm/s})$), their Reynolds number is also small ($O(50)$) and the direct physical mixing they induce may be small, but as yet not quantified. It is also possible they could enhance vertical nutrient mixing through natural biological processes (feeding etc).

Methodology

A detailed field study program aimed at quantifying the mixing dynamics within a small reservoir was conducted on Little Nerang Dam (LND), Queensland, Australia. LND is a small reservoir in South East Queensland (see Corke et al, 2010) with nearly pristine surrounds. It has a length of 5km and a maximum depth of 37 near the dam wall with a general prism type bathymetry. The reservoir experiences a strong stratification during the summer months with vertical overturning occurring in mid to late winter. LND is not used a general water supply reservoir and thus its water level remains approximately steady with levels changing predominately as the result of catchment rainfall and a low outflow required for environmental purposes.

Properties within the reservoir are being monitored with the use of five thermistor chains and two buoy mounted weather stations. Water velocities within the reservoir are being monitored with ADCPs (from 1-5 depending on instrument availability). Additionally, three intensive

field studies have been undertaken to examine various water properties including DO levels and turbulent mixing processes – with the focus being on night time processes..

Results and Discussion

At the commencement of a year-long study program the reservoir was near capacity. Shortly after the study commenced local heavy and persistent rain events resulted in the reservoir experiencing continual spillway overflows that lasted for over 6 months. Levels over the spillways averaged around the 6 cm level. That is, there was a continual flow through the reservoir with surface water being constantly removed from the system, with the replenishment coming from either direct surface overflows or groundwater inflows.

Figure 1 presents a contour plot of the return echo intensity as measured using a bed mounted ADCP located near the centre of LND. The magnitude of the echo intensity reveals that previously described zooplankton behaviour.

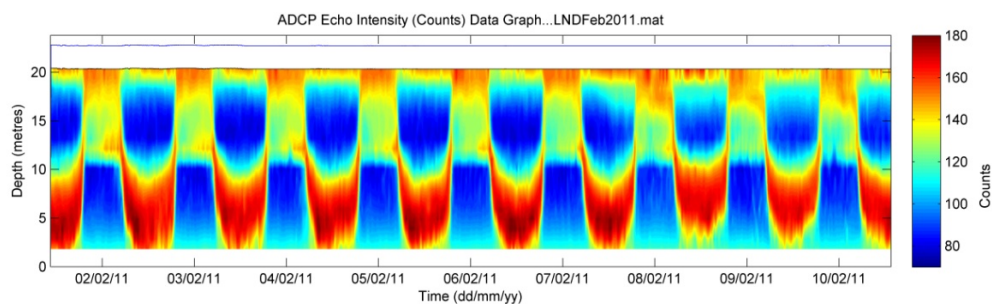


Figure 1. Plot acoustic echo intensity, using a 600 KHz ADCP, recorded from the bed looking upwards in Little Nerang Dam. The horizontal axis tick marks are midnight.

From the observed zooplankton behavior and the constant overflow of the reservoir the results revealed the overflow process was a significant mechanism for removing zooplankton from the system during the night as the zooplankton rich surface water flowed over the wall, but during the day the loss of zooplankton from such a process was substantially reduced. Such an outcome could be useful to reservoir managers as it might represent a potentially unrecognised nutrient removal mechanism. Furthermore, when combined with selective withdrawal (i.e., remove water from an appropriate depth where zooplankton concentrations are high) reservoir managers might more effectively control nutrient removal. Further study is required to quantify the zooplankton removal loadings.

References

Corke, P., Dunbabin, M. and Grinham, A. (2010) Autonomous Surface Vehicles & Aquatic Sensor Networks *International Conference on Intelligent Robots and Systems (IROS2010)*, Taipei, Taiwan, 22nd of October 2010.

Summary of Hydrodynamic and Thermal Modelling in the Laurentian and Polar Great Lakes

Leon, L.F.¹, Lam, D.C.¹, Schertzer, W.¹, McCrimmon, C.¹, Antenucci, J.²

¹ National Water Research Institute, Environment Canada, Burlington, Ont, L7R 4A6, Canada

² University of Western Australia, Center for Water Research, Crawley, WA, 6009, Australia.

*Corresponding author, e-mail luis.leon@ec.gc.ca

KEYWORDS

Great Lakes; hydrodynamic model; thermal modelling

EXTENDED ABSTRACT

Introduction

Ecological modelling in lakes is increasingly being driven by 3D hydrodynamic models. The complex ecological dynamic processes rely on the use of sophisticated models to simulate water quality in lakes. As well, climate modelling is also tapping into the capability of such models to resolve the spatial distribution of the thermal behaviour in lakes. As temperature dependent bio-chemical processes mostly happen in epilimnetic waters and the coupling with climate models is achieved basically within the exchanges at the air-water surface, is important to properly simulate the temperature structure and dynamics in lakes.

Methods

In this study, ELCOM (3D Estuary and Lake Computer Model; Hodges and Dallimore, 2006) acts as the hydrodynamic driver that provides temperature, salinity, and the transport forces that, if coupled with CAEDYM (Computational Aquatic Ecosystem Dynamics Model; Hipsey et al., 2006), simulates nutrients, phytoplankton, zooplankton, fish, and benthic habitat. Here we present a summary of the performance of ELCOM and its ability to reproduce thermal structure and circulation patterns (Fig. 1); gathering results from studies developed over the last few years in two Laurentian Great Lakes (Erie and Ontario) and two Polar Great Lakes (Grt. Bear Lake and Grt. Slave Lake).

Results

Table 1. Summary – Temperature (model/observed statistics)

Lake (output)	Site (total depth)	Mod:avg [min-max]	Obs:avg [min-max]	R2	NS
ERIE 2002 (semi-daily) ^{1a}	W-T05*	20.7 [15.0-26.6]	23.4 [14.7-26.7]	0.83	0.77
	C-T07	19.7 [7.6-26.5]	20.2 [6.5-26.7]	0.94	0.83
	E-T12	17.7 [4.4-25.1]	18.3 [3.4-25.4]	0.96	0.85
ONTARIO 2007 (semi-daily) ^{1b}	TC2	13.4 [4.3-22.5]	15.1 [5.6-24.0]	0.67	0.55
	TC4	14.6 [6.4-24.1]	14.7 [5.9-22.8]	0.71	0.73
	TC6	15.6 [6.5-25.3]	15.3 [5.3-23.8]	0.73	0.69
GSLAVE 2003 (semi-daily) ²	T06A	13.1 [3.1-19.7]	12.9 [6.3-19.1]	0.83	0.59
	T01A	7.3 [2.4-12.2]	7.9 [2.2-14.9]	0.87	0.76
	T10A	9.4 [2.3-15.5]	9.8 [2.0-16.9]	0.93	0.89

¹Leon et al., 2011a and 2009b; ²Schertzer et al.

The results presented in Table 1 were compiled for the different lakes and periods, but selecting only the 2 km grid resolution and 45 vertical layers setting. Simulations in the various systems, with very complex dynamics, appeared to perform quite well. R^2 values ranged from [0.67-0.96]. As correlations tend to give good fit for time series that shadow each other and produce decent regressions anyway, the Nash-Sutcliffe coefficient (NS ; Nash and Sutcliffe, 1970) was used as an additional performance test. For the same sites NS values ranged from [0.55-0.89]; $NS > 0.4$ are considered to be satisfactory (good above 0.75 and 1.0 indicating a perfect fit).

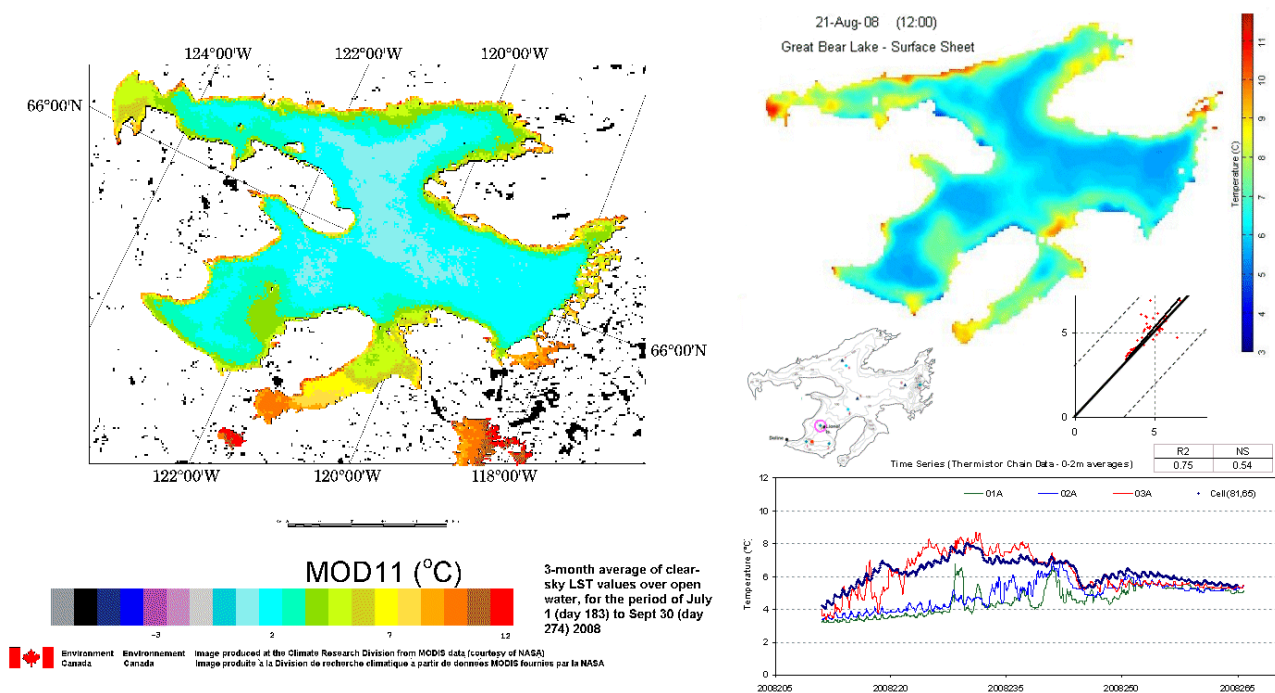


Figure 1. ELCOM temperature simulation in Great Bear Lake in 2008 (MODIS imagery by N. Bussi eres – W. Schertzer; Environment Canada’s Science and Technology Branch).

REFERENCES

- Hipsey, M.R., J. Romero, J. Antenucci, D. Hamilton. (2006) Computational Aquatic Ecosystem Dynamics Model CAEDYM Science Manual, Centre for Water Research, University of Western Australia.
- Hodges, B.R., C. Dallimore. (2006) Estuary and Lake Computer Model Science Manual, Centre for Water Research, University of Western Australia.
- Leon, L.F., Smith, R.E.H., Hipsey, M.R., Bocainov, S.A., Higgins, S.N., Hecky, R.E., Antenucci, J.P. and Guildford, S.J. (2011) Application of a 3D hydrodynamic-biological model for seasonal and spatial dynamics of water quality and phytoplankton in Lake Erie, *J. Great Lakes Res* 37-1, Mar 2011, pp. 41-53 (doi: 10.1016/j.jglr.2010.12.007)
- Leon, L.F., Smith R.E., Malkin, S., Depew, D. and Hecky, R.E. (2009) Modelling and analysis of Cladophora dynamics and their relationship to local nutrient sources in a nearshore segment of Lake Ontario, RA#4253501, Final Report for the OPG, (Oct 2009), University of Waterloo, Waterloo, On., 64p.
- Nash, J. E. and J. V. Sutcliffe (1970), River flow forecasting through conceptual models part I — A discussion of principles, *Journal of Hydrology*, 10 (3), 282–290.
- Schertzer, W.M., Rouse, W.R., Blanken, P.D., Walker, A.E., Lam, D.C.L. and Leon, L. (2008), Chapter 11, Interannual Variability of the Thermal Components and Bulk Heat Exchange of Great Slave Lake, In: M.K. Woo (ed.) *Cold Region Atmospheric and Hydrologic Studies: The Mackenzie GEWEX Experience*, Vol. 2: Hydrologic Processes, Springer, NY, 507 p.

The role of ice season in the physical and ecological conditions in Lake Vanajavesi, southern Finland

Matti Leppäranta¹ and Lauri Arvola²

¹*Department of Physics, University of Helsinki, Box 48 (Erik Palménin aukio 1)
Fi-00014 Helsinki, Finland*

Email matti.lepparanta@helsinki.fi

²*Lammi Biological Station, University of Helsinki, 320 Pääjärventie, 16900 Lammi, Finland
Email lauri.arvola@helsinki.fi*

A three-year research program has been performed on the physics, water quality and ecosystem in Lake Vanajavesi, southern Finland in 2009–2011. The lake is eutrophic, mean depth is 8 m and area is 150 km², and the lake is ice-covered on average through December–April. Ice sheet is stable, 30–80 cm thick, consisting of snow-ice and congelation ice. Attenuation (e-folding) depth of light level is 50–70 cm for congelation ice and 10–20 cm for snow-ice and snow. Ice and snow cover in mid-winter reduce dramatically light penetration, and as a result, phytoplankton production is typically low or very low. Therefore heterotrophic and mixotrophic species often dominate over autotrophic ones in winter, and phytoplankton communities are also sparse. However, in absence of snow, especially later in spring, photosynthesis can be high beneath ice due to improved light conditions. Water temperature is low under ice and the water column is inversely stratified. Due to low water temperature biotic activity is generally low. Ice-cover isolates lake water body from atmosphere and hence oxygen concentration decreases in winter, especially close to the bottom sediments. At the same time carbon dioxide concentration in lake water increases due to the respiration activity. Mixing processes are usually very limited under ice that affects on physical and chemical conditions and the biota. Conditions during fall cooling are crucial, because the temperature of the water body at freeze-over depends on them and may reach anything within 1–4°C. If ice season is long enough and water temperature was relatively high at freezing, the risk for oxygen depletion increases. Oxygen depletion may have serious chemical and ecological consequences such as release of phosphorus from bottom sediments and fish kills with subsequent food web impacts.

Estimates of tidal currents from direct current measurements in the Gulf of Finland of the non-tidal Baltic Sea

M.-J. Lilover

Marine Systems Institute at Tallinn University of Technology, Akadeemia 15a, 12618 Tallinn, Estonia

e-mail madis@phys.sea.ee

KEYWORDS

Baltic Sea; Gulf of Finland; ADCP measurements; tidal currents.

EXTENDED ABSTRACT

Recent relevant handbooks on the physical oceanography state that the tides are either weak in the Baltic Sea or even that the Baltic Sea is virtually tideless (Leppäranda and Myrberg, 2009; Feistel *et al.*, 2008). The statement is motivated by the landlocked intracontinental location of the sea connected to the ocean (North Sea) via narrow and shallow Danish Straits (Belt Sea). Due to the narrow cross section of the Belt Sea compared with the area of the Baltic Sea, the tidal wave is heavily damped out in the Baltic Sea. For most of the non-south-western Baltic Sea the tidal amplitude of the sea level is less than 10 cm except in the eastern Gulf of Finland (GoF) where the amplitudes greater than 10 cm have been reported. In the connection areas Skagerrak and Kattegat the tides are dominantly semidiurnal, though in the Baltic Sea both diurnal and semidiurnal partial tides have been observed in sea level spectra. The data collected at sea level stations in our study area, GoF, have shown the most pronounced spectral peaks at the diurnal periods K1 and O1 (Jönsson *et al.*, 2008). Theoretically the semidiurnal M2 and S2 tides are subjected to stronger astronomical forcing than the diurnal components, but on the other hand the K1 and O1 tides are in an approximate resonance with the gulf seiche. Wübbler and Krauss (1979) have estimated the Western Baltic – Gulf of Finland mode of 2 seiche period to be 23.8 hours and the entire Baltic mode of 2 seiche period 26.4 hours. From sea-level measurements for the GoF an oscillation period of 26.2 hours has been estimated. It is worth to mention that the spectral amplitude estimated from the sea-level data increases toward the east end of the Gulf of Finland (Jönsson *et al.*, 2008). At the same time the basin-wide seiche periods have not been discernible from these spectra calculations.

While the water level oscillations caused by tides have been thoroughly studied then the knowledge about the horizontal motion of water associated with the water level oscillations (tidal currents) has been insufficient except the study reported by Evdokimov *et al.* (1974). They have found that the diurnal and semi-diurnal tidal currents in the eastern GoF can reach the values as high as 8 cm/s and 4 cm/s, respectively.

In this paper we use the current velocity measurements which originate from three locations (denoted by W, M and E in Fig. 1) along the southern coast of the GoF performed in the years 2009, 2008 and 2010 using a bottom-mounted ADCP. As our current series were relatively long (about 100 days at the stations W and E) and because of the need to reach a sufficiently high spectral resolution in order to separate seiche and tides we used hourly averaged time

series with the length of 4096 data values (adding zeros to the measured series to fulfil this requirement) for the spectral calculations. The rotary spectra of the current velocity revealed significant energetic peaks with periods of dominating seiches, tides and inertial oscillation (13.9 h). However, the spectral resolution was not sufficient to resolve the K1 tide from the Western Baltic – Gulf of Finland mode 2 seiche of the period 23.8 hours. Still, the semi-diurnal tides M₂, S₂ as well as the diurnal tides K₁, O₁ were well resolved. In the bottom layer (at about 5 m above the seafloor) at all three measurement stations the tidal currents of the diurnal tide constituents (O₁ and K₁) dominated over the semi-diurnal (M₂ and S₂) constituents with roughly twice larger current velocity amplitudes (about 9, 3 and 5 cm/s at stations W, M and E respectively for the diurnal tides and 4, 1 and 2 cm/s respectively for the semi-diurnal tides). At station W the remarkable (13 cm/s) inertial currents were observed and at stations M and E the inertial current velocities remained below 1 cm/s. In the upper layer the both, diurnal and semi-diurnal, tidal amplitudes were similar – about 6 cm/s. Remarkable inertial currents (20 cm/s) were observed at station W and at station E the inertial currents had value (~5 cm/s) similar to the tidal currents. Applying the band-pass filtering we found that at station M the relatively large diurnal currents (4 cm/s) were visible during 3 or 4 days after each 14 day period pointing to their generation only during the spring tide.

Considering that the long-term mean currents in the GoF are as weak as some 5 cm/s and that the meso-scale currents of different origin are of about 10-15 cm/s, then the tidal currents cannot be ignored in the bottom layer (in the upper layer the wind-induced Ekman currents and the inertial currents reach the values of 20 cm/s and even more). Some 3D simulations of the Baltic Sea salinity in the deep layer below the halocline by a model with the effect of tides included have shown the salinity values smaller than the outcome of the model with the tides excluded. The latter result probably implies the importance of tidal currents on the vertical mixing of bottom layer salt and nutrients.

In conclusion, in contrast to the intermittent wind and density-driven currents in the bottom layer the tidal currents are always present and can substantially contribute to the vertical mixing and in this way have an effect on the eutrophication - the most discussed ecological problem of the Baltic Sea.

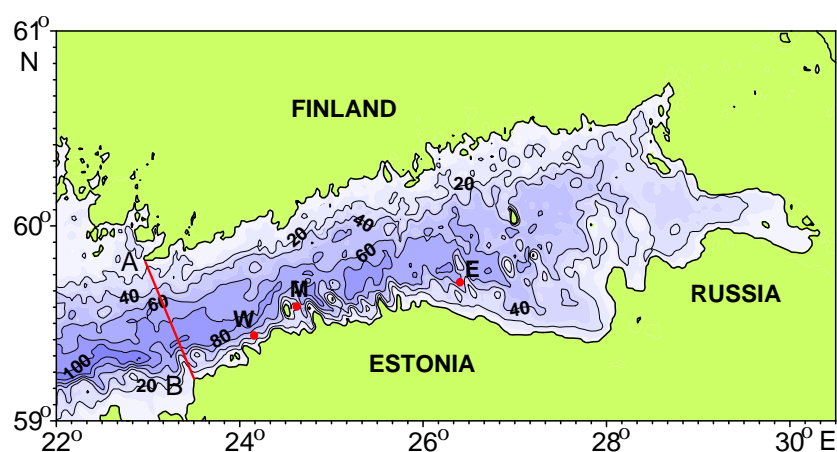


Figure 1. Map of the Gulf of Finland with bathymetry. The locations of the bottom-mounted ADCP are indicated by dots.

REFERENCES

- Alenius P., Myrberg K. and Nekrassov A. (1998). Physical oceanography of the Gulf of Finland: a review. *Boreal Env. Res.* **3**(2), 97-125.
- Feistel R., Nausch G. and Wasmund N. (2008). State and Evolution of the Baltic Sea, 1952-2005: A Detailed 50-year Survey of Meteorology and Climate. Physics, Chemistry, Biology, and Marine Environment. John Wiley & Sons, Hoboken.
- Evdokimov S.N., Klevantsov Y.P. and Sustavov Y.V. (1974). Analysis of dynamics of waters in the Gulf of Finland. *Collected works of the Leningrad Hydrometeorological Observatory.* **8**, 155–164. [In Russian]
- Jönsson B., Döös K., Nycander J. and Lundberg P. (2008). Standing waves in the Gulf of Finland and their relationship to the basin-wide Baltic seiches. *J. Geophys. Res.* **113**, C03004, doi:10.1029/2006JC003862.
- Leppäranta M. and Myrberg K. (2009). Physical Oceanography of the Baltic Sea. Springer-Praxis, Berlin-Chichester.
- Wübber C. and Krauss W. (1979). The two-dimensional seiches of the Baltic Sea. *Oceanol. Acta*, **2**, 435–446.

Kelvin Wave Propagation around Point Pelee in Lake Erie

W. Liu* and K.G. Lamb

*Department of Applied Mathematics, University of Waterloo, 200 University Avenue West,
Waterloo, Ontario, Canada*

**Corresponding author, e-mail w13liu@math.uwaterloo.ca*

KEYWORDS

Hydrodynamical modeling; internal waves; Kelvin wave; Lake Erie; MITgcm.

EXTENDED ABSTRACT

Introduction

The Great Lakes are a collection of freshwater lakes located in eastern North America which form the largest group of their kind on Earth. Lake Erie is the fourth largest by surface area. Of great concern in recent years about Lake Erie is hypoxia in the deep water of the central basin, which is generally defined as oxygen concentrations less than 2 mg/l. A three-year interdisciplinary project funded by an NSERC Strategic Grant is directed to the coupling between physical-hydrodynamic and biogeochemical processes in Lake Erie with particular emphasis on hypoxia.

Understanding the internal wave field and associated mixing in the lake using field observations and numerical simulations plays a crucial role in investigating the hypoxia issue. Past work in Lake Erie has focused on large spatial and temporal scales. In light of the recent realization that high frequency internal waves can play important roles in biogeochemical processes in lakes, both large-scale and small-scale hydrodynamic processes will be considered through a combination of modeling and field work. These approaches will provide valuable insight into other important biogeochemical processes in Lake Erie. One type of these internal waves is Kelvin wave, which is a traveling wave that requires the support of a lateral boundary, with the amplitude decaying away from the boundary. A series of numerical simulations are performed to investigate the internal Kelvin waves in an idealized Erie-like lake using the MIT General Circulation Model (MITgcm).

Model Setup

Preliminary simulations have been done in an idealized lake with a dimension of 160 km length, 20 km width, and 20 m depth, and a sharp corner with a similar size of Point Pelee in Lake Erie. The temperature field is initialized with a partially tilted thermocline (Fig. 1),

$$T = T_b + \frac{T_s - T_b}{2} \left(1 + \tanh \left(\frac{z - z_0 - \alpha y}{d} \right) \right),$$

where T is the water temperature, z and y denote the vertical and meridional coordinates, the temperature at the surface T_s is 10°C, at the bottom T_b is 3°C, the position of the thermocline at $y=0$, $z_0 = -14$ m, the thickness of the thermocline d is 2 m, and the slope of the tilted thermocline α is 2×10^{-4} .

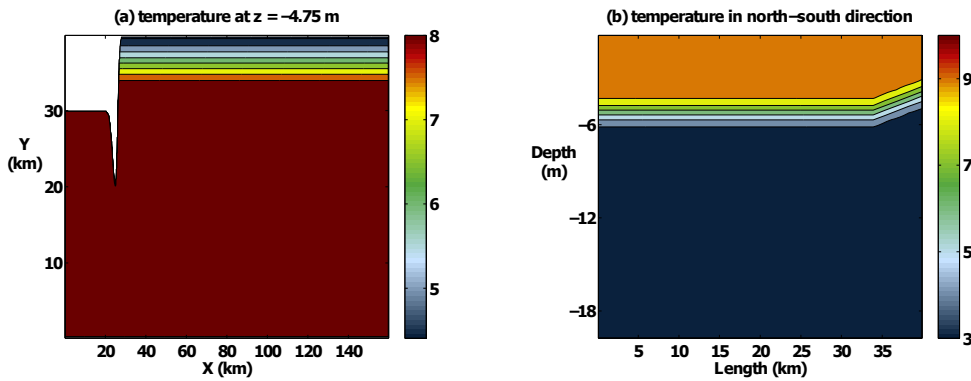


Figure 1: Initial temperature profile in (a) horizontal and (b) vertical.

The MITgcm is a 3D numerical model designed for the study of the atmosphere, ocean, and climate (Marshall *et al.* 1997). The simulations are run with 200 m, 50 m, and 25 m horizontal grid size and 40 layers vertically with a uniform thickness. The highest resolution with 25 m grid size took about 4-5 days to finish a 20-day run using 256 Intel Xeon 2.6 GHz processors on SciNet, which is a high performance computing system from University of Toronto.

Results and Discussion

After the release of the tilted thermocline, the wave elevation travels along the northern boundary to the corner. An interesting result of these simulations is that an eddy with a diameter of several kilometres is formed near the sharp corner. Fig. 2a shows a horizontal temperature profile at -4.75 m deep near the corner. Around $t = 9$ day, the eddy is fully developed near the east side of corner, as it is seen from the velocity field in Fig. 2b. The existence of the eddy depends on the horizontal eddy viscosity (A_h), as the eddy will not form when A_h is greater than $10 \text{ m}^2/\text{s}$, but seems not sensitive to the vertical eddy viscosity. More sensitivity tests of the dependence on the characteristics of the thermocline, horizontal grid size, boundary conditions, bathymetry, and turbulence schemes will be presented in the conference. In future study adding idealized or observed wind is the next step of our simulations in order to test the formation, longevity, and robustness of these eddies.

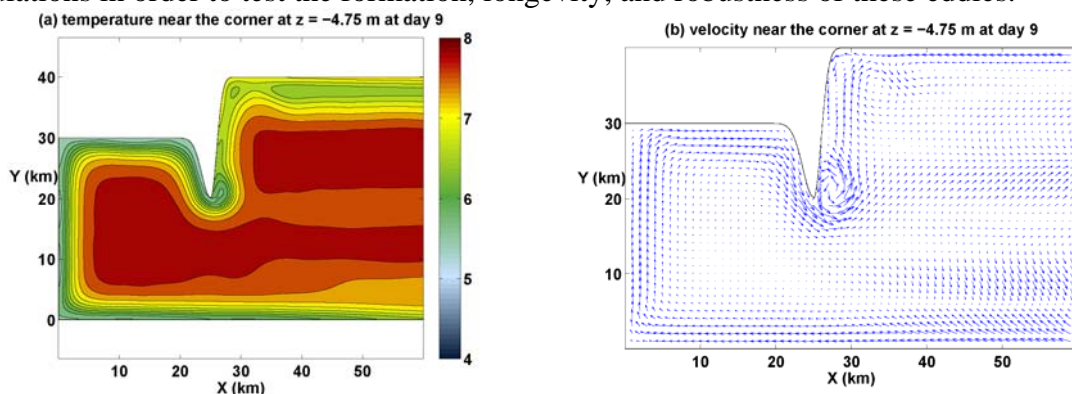


Figure 2: (a) temperature at $z = -4.75$ m at day 9; (b) velocity field at $z = -4.75$ m at day 9.

REFERENCES

Marshall J., Hill C., Perelman L., and Adcroft A. (1997). Hydrostatic, quasi-hydrostatic, and nonhydrostatic ocean modeling. *J. Geophys. Res.*, **102**(C3), 5733-5752.

Effects of lock operation and ship traffic on sediment oxygen uptake in impounded rivers

A. Lorke^{1*}, D.F. McGinnis^{2,3}, A. Mäck¹, & H. Fischer⁴

¹ *Institute for Environmental Science, University of Koblenz-Landau, Fortstrasse 7, D-76829 Landau, Germany*

² *IFM-GEOMAR, Leibniz Institute of Marine Sciences, RD2 Marine Biogeochemistry, Kiel, Germany D-24148*

³ *Southern Danish University, Institute of Biology and Nordic Center for Earth Evolution (NordCee), Odense M, Denmark*

⁴ *Federal Institute of Hydrology, Am Mainzer Tor 1, D-56068 Koblenz, Germany*

* *Corresponding author, e-mail lorke@uni-landau.de*

KEYWORDS

impoundments; dissolved oxygen; sediment-water flux; eddy-correlation; ship navigation

EXTENDED ABSTRACT

INTRODCUTION

Many rivers in densely populated areas are impounded and used for hydropower generation and transportation. This causes a strong reduction of flow velocity, which, in combination with increased organic carbon and nutrient loading, can lead to dissolved oxygen deficits and associated degradation of water quality. Mitigation and management strategies aimed at restoring or maintaining sufficient oxygen concentrations in impounded rivers require knowledge of the magnitude as well as the spatial and temporal dynamics of sediment oxygen uptake. Here we present high-resolution measurements of the sediment oxygen fluxes in the River Saar (Germany) and discuss the observed oxygen uptake with respect to lock operation and cargo ship traffic.

MEASUREMENTS

A benthic lander system measuring the three-dimensional current velocity and oxygen concentration was deployed from 8 to 12 Sept. 2010 in the river Saar, Germany. The river is heavily impounded for hydropower generation and ship navigation purposes. It features a minimum depth of 4 m, strongly reduced flow velocities and exhibits temporal thermal stratification and severe depletion of dissolved oxygen during summer (Becker et al. 2009). The sampling site was located approximately 1.3 km downstream of the impoundment Serrig. The lander was equipped with an acoustic Doppler velocimeter (ADV) and two oxygen microelectrodes positioned in close proximity of the ADV sampling volume, which was located 0.32 m above the sediment surface. The benthic lander system was additionally equipped with an oxygen optode and a temperature and depth logger.

The measured three-dimensional velocity vectors were rotated using the planar fit method in order to obtain a vertical velocity component which is normal to the local stream line. Vertical oxygen fluxes were estimated from cross-correlation of vertical velocity and oxygen concentration fluctuations for time intervals of 512 s, respectively.

RESULTS AND DISCUSSION

Mean current speed and standard deviation was $4\pm 2 \text{ cm}\cdot\text{s}^{-1}$. The observed current velocities, however, are predominantly influenced by up- and downstream lock operation. Solitary-like waves of depression and elevation with amplitudes exceeding 0.2 m are generated as the result of down- and up-stream ship locking, respectively. The waves are reflected back and forth within the impoundment and superposition of these waves result in a series of distinct periods of flow variation between 12 and 68 minutes at the sampling site. Enhanced locking activities during daytime further impose a diel pattern on flow variability. Upstream travelling waves frequently cause reversals of the longitudinal flow velocity. Similar patterns of temporal variability were observed for oxygen concentration, which, on top of this, decreased during the sampling period from 7 to $5.5 \text{ mg}\cdot\text{L}^{-1}$, corresponding to 70 to 55 % saturation (Fig. 1).

The lock-induced diurnal pattern observed in fluctuations of water level and current velocity was also observed in sediment-water oxygen fluxes (Fig. 1). While the mean flux during time periods of lock operation was $1.1\pm 0.5 \text{ g}\cdot\text{m}^{-2}\cdot\text{day}^{-1}$, it was reduced by about a factor of two to $0.5\pm 0.1 \text{ g}\cdot\text{m}^{-2}\cdot\text{day}^{-1}$ during nighttime, when no ship locking was performed. The driving force for the increased fluxes is enhanced bottom-boundary layer turbulence associated with the passage of lock-induced waves, as indicated by the correlation observed oxygen fluxes and dissipation rates of turbulent kinetic energy estimated from the velocity fluctuation spectra.

It can be concluded that strong locking-induced velocity and discharge variations during daytime increase the sediment oxygen flux in comparison to nighttime even though the mean flow velocities are not significantly different. Up to a certain extent, the magnitude of the sediment oxygen uptake is thus controlled by the timing and frequency of lock operation and ship traffic.

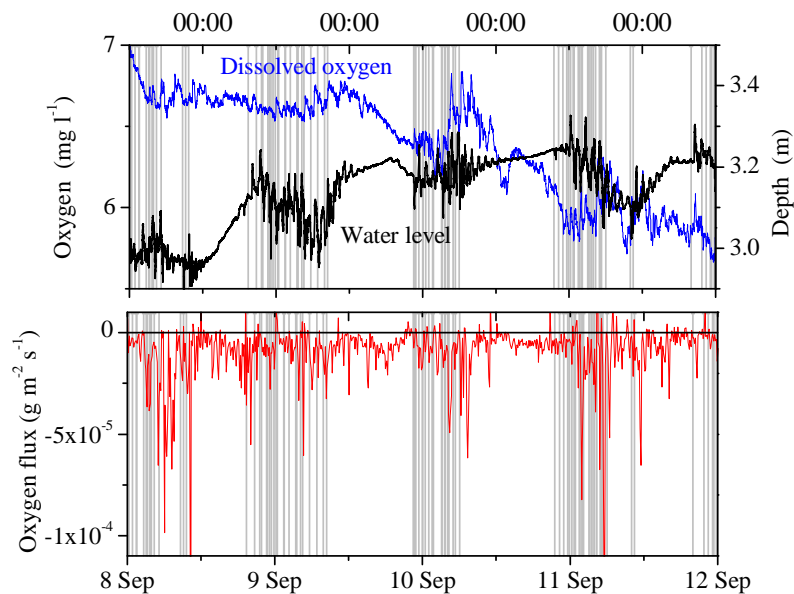


Fig. 1: Dissolved oxygen concentration and water level fluctuations (upper panel) and sediment-water oxygen fluxes (lower panel) during the observation period. Grey vertical lines correspond to times of up- or downstream lock operation. The data clearly reveal the water level fluctuations resulting from daytime locking and the corresponding increase in sediment-water oxygen flux.

REFERENCES

- Becker, A., V. Kirchesch, H. Baumert, H. Fischer, and A. Schöl. (2009). Modelling the effects of thermal stratification on the oxygen budget in an impounded river. *River Research and Applications* **26**, 572-588.

Layered weak mixing in central Yellow Sea in later summer

Youyu Lu^{1*}, Jianing Wang² and Hao Wei³

¹ Ocean Sciences Division, Bedford Institute of Oceanography, Fisheries and Oceans Canada, Dartmouth, NS, B2Y 4A2, Canada

² Laboratory of Physical Oceanography, Ocean University of China, Qingdao 266100, China

³ College of Marine Science and Engineering, Tianjin University of Science and Technology, TEDA, Tianjin 300457, China

*Corresponding author, e-mail Youyu.Lu@dfo-mpo.gc.ca

KEYWORDS

Shear spectrum; stratification; turbulence microstructure; turbulence mixing; Yellow Sea.

EXTENDED ABSTRACT

Introduction

Based on field observations in September 2006, Liu et al. (2009) derived well defined layered structure in density, rate of turbulent kinetic energy dissipation (ϵ), and vertical eddy diffusivity (K_N) in the central YS with water depth of 73 m. Low values of ϵ around 10^{-9} W Kg⁻¹ and K_N around 10^{-7} m² s⁻¹ were obtained. The estimates of ϵ were derived by integrating the measured shear spectra over the wavenumber range between 2 cpm and the Kolmogorov wavenumber (k_K). However, quantitative comparison between the measured and fitted spectra was not provided. According to the well accepted universal spectra, the spectral ranges shift to lower wavenumbers as ϵ decreases, and vice versa (e.g., Greg 1999). The purpose of this study is to re-process the shear profiles, quantitatively compare the observed and universal spectra, and derive estimates of ϵ using a spectral fitting technique.

Analysis method

The measurements were made at 35.01°N, 123.00°E using a free-fall microstructure profiler MSS-60 packed with two parallel airfoil sensors (PNS98), a fast-response temperature sensor (FP07), three standard CTD sensors and an accelerometer. The sampling rate of all the sensors was 1024 Hz. Each shear profile is first broken into 1 m segments. For each segment, an initial estimate of ϵ is obtained by integrating the spectrum from 2 cpm to the highest wavenumber resolved; this provides an initial estimate of k_K . Then by integrating the spectrum from 2 cpm to the first estimate of k_K , the second estimates of ϵ and k_K are obtained. This procedure is repeated until the difference in k_K between the two adjacent steps is less than 2 cpm; and the resulting estimates are denoted as ϵ^* and k_K^* . Next, we try to improve an estimate of ϵ by finding a “best fit” of the universal spectrum to the observed spectrum. For each measured spectrum we examine the universal spectra with the corresponding dissipation rates of $\epsilon^f = 1.1^m \epsilon^*$. The discrepancy between the universal and observed spectra is measured by

$$D = \int_{k_i}^{k_K} |P - P^f| dk / \int_{k_i}^{k_K} P^f dk, \quad (1)$$

where $k_i = 6$ cpm is the lower-bound wavenumber for this evaluation, P and P^f are the power densities of the measured and empirical spectra, respectively. The universal spectrum with the minimal value of D is regarded as the best fit to the observed spectrum; and the corresponding ϵ^f is regarded as the final estimate of ϵ .

Results

The vertical eddy diffusivity K_N was calculated using the Osborn (1980) formula with the value of the mixing efficiency being empirically set to a constant value of 0.2. Figure 1 shows the scatter and medians of the squared buoyancy frequency N^2 , ε , K_N and the buoyancy Reynolds number $\varepsilon/(\nu N^2)$ (where ν is the molecular viscosity) for each 1 m segment as a function of depth. The layered structure of these quantities is similar to that reported by Liu et al. (2009), but quantitative differences are noticeable. At 5-6 m below the pycnocline there lies a layer of elevated ε with values between 10^{-8} and 10^{-7} W Kg⁻¹ according to this estimate, smaller than those obtained by Liu et al. (2009). The lowest values of K_N are found in the narrow pycnocline, where both the present and previous analyses obtain values around 10^{-7} m² s⁻¹. There are considerable amounts of values of $\varepsilon/(\nu N^2)$ less than 20. In particular, the medians of $\varepsilon/(\nu N^2)$ are less than 20 in the depth ranges of 17-22 m and 26-58 m, associated with low turbulent levels and relatively strong stratification. Under such conditions, the dissipative motions are strongly affected by buoyancy effects, and the assumption of isotropic turbulence and the universal shapes of the spectra become questionable (Yamazaki and Osborn, 1990). Hence, the estimated small dissipation rates in these depth ranges are subject to uncertainties due to this complication.

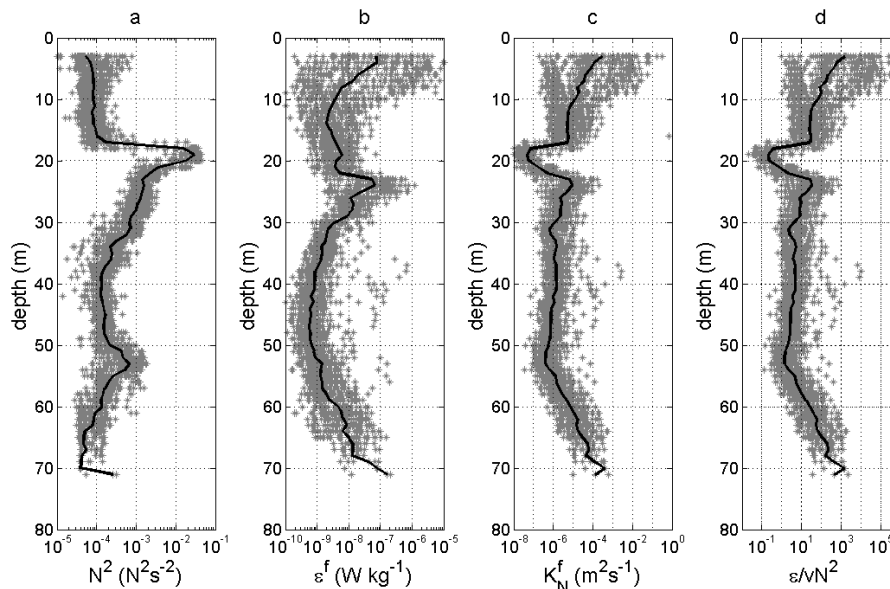


Figure 1. Vertical distribution of the estimates of (a) N^2 , (b) ε^f , and (c) K_N^f (d) $\varepsilon/(\nu N^2)$ (all in grey asterisks) and their medians (black curves).

REFERENCES

- Gregg M.C., 1999: Uncertainties and Limitations in Measuring ε and χ_T . *J. Atmos. Oceanic Technol.*, **16**, 1483-1490.
- Liu, Z., H. Wei, I.D. Lozovatsky, and H.J.S. Fernando, 2009: Late summer stratification, internal waves, and turbulence in the Yellow Sea. *J. Mar. Syst.*, **77**, 459-472.
- Osborn, T., 1980: Estimates of the local rate of diffusion from dissipation measurements. *J. Phys. Oceanogr.*, **10**, 83-89.
- Yamazaki, H., and T. Osborn, 1990: Dissipation estimates for stratified turbulence. *J. Geophys. Res.*, **95**, 9739-9744.

Oxygen and Heat Flux in the Benthic Boundary Layer of a Shallow Lake

Lueck¹, R., F. Wolk¹, P.D. Stern¹, & J.D. Ackerman²

¹*Rockland Scientific Inc., Victoria, BC Canada V8Z 1C1, fabian@rocklandscientific.com*

²*Integrative Biology, University of Guelph, Guelph, ON Canada, N1G 2W1*

We collected simultaneous measurements of oxygen, temperature, and three components of velocity to derive the vertical flux of oxygen (DO) and heat, using the eddy correlation technique. The sensors were 95 mm above the silty bottom in 1 m of water near the outflow of Beaver Lake, Saanich, British Columbia.

We collected data at 64 Hz with an eddy correlation system, consisting of a 6 MHz acoustic Doppler velocimeter (Vector, Nortek AS) and a 2-channel scalar sensor signal conditioning unit (MicroSquid, Rockland Scientific Inc.).

We compared – for 1 to 2 hours – a polarographic oxygen sensor (OX-10 Unisense A/S) against a galvanic oxygen sensor (AMT GmbH) and a temperature sensor (FP07-38-1 RSI). A multi-parameter instrument (AAQ JFE Advantech) sampled ambient conditions (oxygen, temperature, turbidity, PAR) 0.65 m away from the sampling volume. A 19-hour deployment with the galvanic oxygen-temperature sensor pair was used to examine diurnal changes beginning at ~17:00 hr.

Whereas both oxygen sensors agreed on time scales longer than 10 seconds, the galvanic sensor had a much lower noise level than the polarographic sensor. The galvanic DO sensor record tracked closely with the DO record from the multi-parameter instrument, which also used a galvanic DO sensor (Oxyguard, Ocean Probe).

A conspicuous algal bloom, which was observed during daylight hours, dissipated overnight. The lake was supersaturated with respect to DO until midnight and declined to ~ 70% saturation in the morning. Water temperature declined monotonically 20.5 °C to 19.7 °C over this period. The Reynolds stress derived from the velocity measurement, after editing to remove spurious data, was downward and significantly different from zero. The DO flux was also downward.

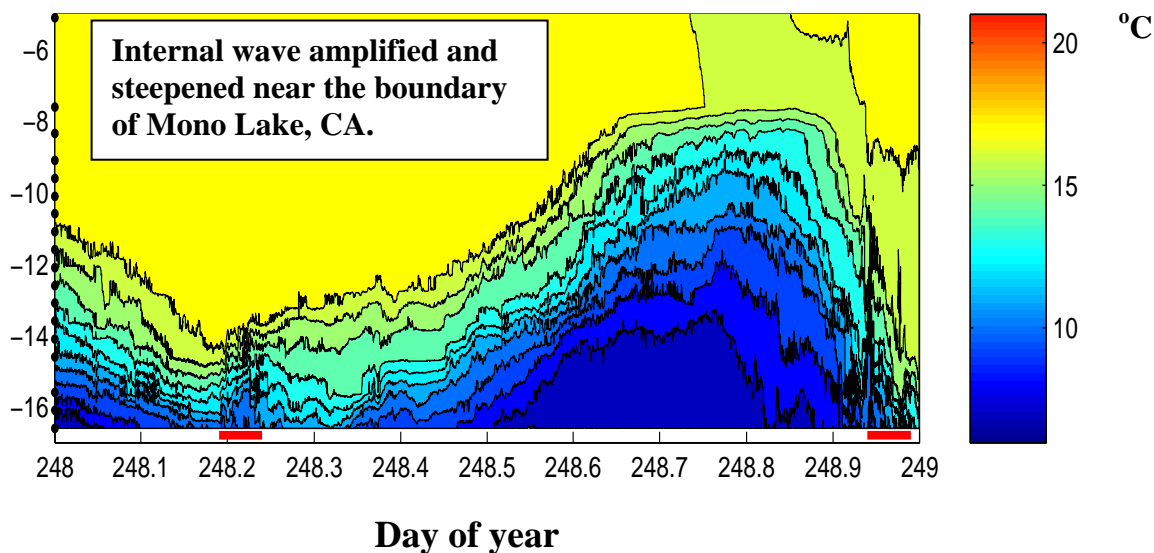
Mixing Dynamics in Lakes across Latitudes

Sally MacIntyre

University of California at Santa Barbara

sally@icess.ic.ucsb.edu

Turbulence, and the resulting mixing which affects rates of biogeochemical processes within lakes, is caused by wind and cooling. Development of accurate equations for the gas transfer coefficient, which mediates the flux of green house gases, and the coefficient of eddy diffusivity, which is needed to characterize within lake fluxes, requires consideration of the full range of processes which cause turbulence. Buoyancy flux, which has generally been neglected in modeling the flux of green house gases, reduces the gas transfer coefficient during heating and increases it at night during light winds relative to what would be predicted from wind alone. Below the mixed layer, turbulence is mediated by the internal wave field. The extent of non-linearity can be predicted from a phase space which incorporates dimensionless indices computed from basin morphometry, stratification, and wind forcing. Here I'll show examples of internal waves from lakes ranging in size from Lake Tanganyika, East Africa, to Lawrence Lake, MI, USA; relate their non-linearity, the magnitude of the resulting eddy diffusivities, and implications for biological processes to position in the phase space; and indicate how climate change may moderate the extent of non-linearity in an arctic and a tropical lake.



Methane emissions from rivers – Results from sampling a 93-km longitudinal transect of the river Saar, Germany

A. Mäck^{1*}, S. Flury², T. DelSontro³, M. Schmidt⁴, D. F. McGinnis^{4,5}, H. Fischer⁶ and A. Lorke¹

¹ *Institute for Environmental Science, University of Koblenz-Landau, Fortstrasse 7, 76829 Landau, Germany*

² *Center for Geomicrobiology, University of Aarhus, Ny Munkegade 114, 8000 Aarhus Denmark*

³ *Eawag, Swiss Federal Institute of Aquatic Science and Technology, Seestrasse 79, 6047 Kastanienbaum, Switzerland*

⁴ *IFM-GEOMAR, Leibniz Institute of Marine Sciences, RD2 Marine Biogeochemistry, Kiel, Germany D-24148*

⁵ *Southern Danish University, Institute of Biology and Nordic Center for Earth Evolution (NordCee), Odense M, Denmark*

⁶ *Federal Institute of Hydrology (BfG), Am Mainzer Tor 1, 56068 Koblenz, Germany*

*Corresponding author, e-mail maeck@uni.landau.de

KEYWORDS

impounded river, methane, diffusive flux, hydroacoustic, ebullition

EXTENDED ABSTRACT

INTRODUCTION

Latest estimates of global greenhouse gas emissions from freshwater systems indicate that the combined effects of limnic carbon dioxide and methane emissions have the potential to balance the terrestrial greenhouse gas sink. However, the evaluation of methane emissions from these aquatic systems remains challenging since the contribution of the different diffusive, advective and ebullition pathways from the sediment to the atmosphere is difficult to estimate because of its high temporal and spatial variability. In this work, we present an approach to quantify the methane emissions from the impounded River Saar, Germany, on a basin-scale dimension.

MEASUREMENTS

We sampled a 93 km long transect, which consists of a chain of seven impounded river sections, separated by dams with ship locks. We used various ship mounted instruments to continuously sample multiple parameters, including a sensor for dissolved methane, an echosounder, a multiparameter probe, and an acoustic Doppler current profiler. Water and sediment samples complimented the continuously measured set of data from the sensors.

RESULTS AND DISCUSSION

We observed that along the whole transect the river water was supersaturated with dissolved methane against atmospheric equilibrium concentrations. The methane levels ranged from 57 nM to 1780 nM (Fig. 1) which reflects an oversaturation by a factor of 19 to 613. This

leads to a mean diffusive emissions at the water-air interface of $1.41 \pm 0.46 \text{ mg CH}_4 \text{ m}^{-2} \text{ d}^{-1}$, calculated by using the thin-boundary-layer method.

In Addition, the measured ebullition rates, calculated from the free gas bubble record of the echosounder, increased significantly toward the forebay of the dams, especially in the two deepest basins. These high emission sites reflect the sedimentation regime; low flow velocities allow particles to settle resulting in the accumulation of organic-rich cohesive sediments. These sediments in turn facilitate high methane production rates and enable the subsequent formation of gas bubbles. Since the bubble emission pathway bypasses microbial oxidation in surface sediment and the water column, methane emissions to the atmosphere increase up to an order of magnitude in these regions compared to sites where no ebullition could be detected.

Our results highlight the importance of resolving the spatial distribution of methane emissions and indicate that especially impounded rivers in temperate regions could be an overlooked but significant source of methane to the atmosphere.

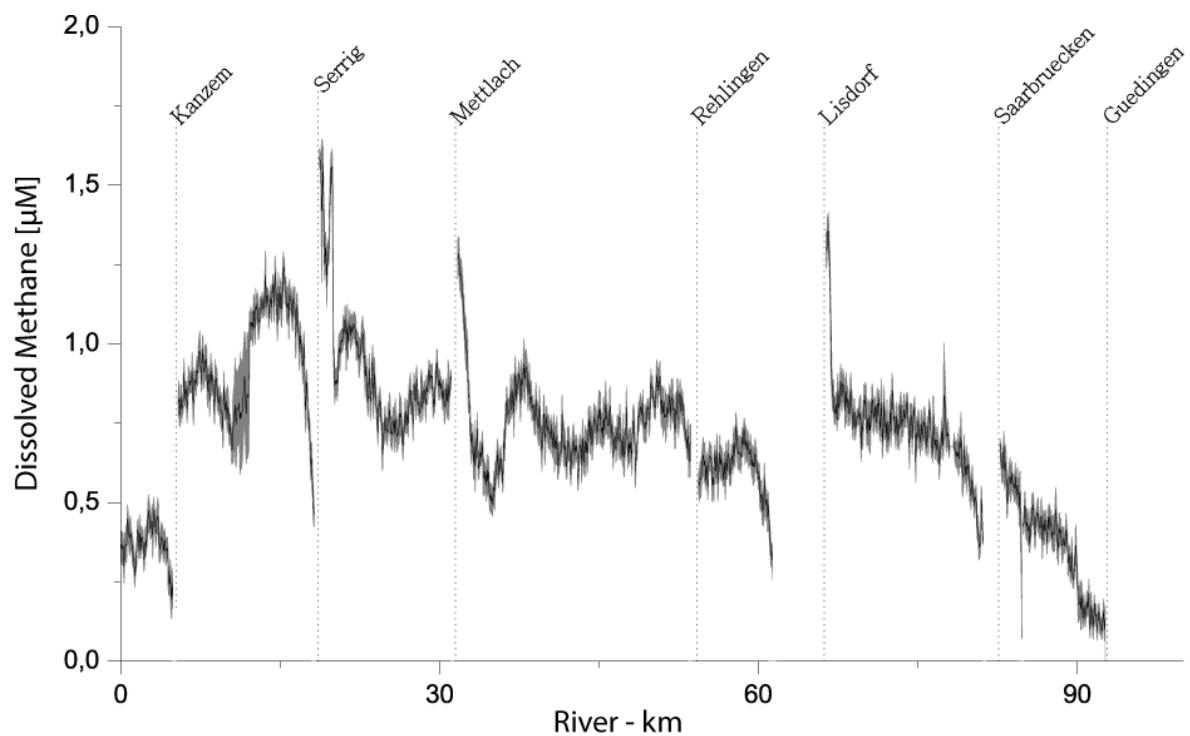


Fig. 1: Concentration of dissolved methane in 1 m depth along the river Saar starting below the dam Guedingen and ending at the confluence with the river Moselle at km 0. The solid line shows the mean averaged over a longitudinal distance of ± 50 m while the grey shaded area displays the standard deviation. Dotted lines denote the locations of dams. Especially in the first two to three kilometers upstream of the dams, the concentration shows a steep increase. The flow through the turbines and ship locks at the dams is responsible for a degassing of the water, so that concentrations behind the dams are lower than above.

Empirically-based parameterization of water mixing in 1D lake models - case study of Great Lakes.

A. Martynov*¹, D. Beletsky², L. Sushama¹, R. Laprise¹

¹ Centre ESCER, University of Quebec in Montreal, Montreal (Quebec), Canada
201 avenue Président-Kennedy, local PK-2315 Montréal (Québec) Canada H2X 3Y7.

² CILER - School of Natural Resources and the Environment (UM SNRE),
University of Michigan, 2205 Commonwealth Blvd Ann Arbor, MI 48105-2945, USA.

*Corresponding author, e-mail andrey.martynov@uqam.ca

KEYWORDS

Great Lakes; 1D lake model; regional climate model; empirical approach; water temperature profile; physical parameterization.

EXTENDED ABSTRACT

Lakes are abundant in many areas of North America and strongly influence the climate of these regions. It is therefore important to include lakes in Regional Climate Models (RCM), used in transient climate change experiments for these regions. The 1D lake models, integrated into modern RCMs, perform well for relatively shallow lakes (Martynov et al. 2010, 2011). These models run into problems, however, when applied to large and deep lakes, such as the Laurentian Great Lakes, as these models do not take into account important physical processes, characteristic of big lakes. Many of such processes are essentially three-dimensional, and can hardly be reproduced satisfactorily by 1D lake models. Though better results can be obtained by using much more complex 3D models (Beletsky, Schwab 2001), coarse horizontal resolution of RCMs (40-50 km) and computational power restrictions currently prevent the use of such complex 3D lake models. 1D lake models therefore are preferred in RCMs with integrated lakes and it becomes important to find ways of adequately simulating deep lakes with 1D lake models.

The rather poor performance of 1D lake models in large and deep freezing lakes can be addressed by adding parameterization of essential 3D processes, such as seiches, included in the DYRESM and SIMSTRAT 1D lake models, which notably improves their performance (Perroud et al. 2009). We propose a more empiric approach, based on estimation of differences between modeled (by 1D and 3D models) and observed thermal regime for Great Lakes. In this way, we can identify weak points of 1D lake models, applied to Great Lakes. The next step is modifying the physical parameterization of these 1D models, using empirically-based information in order to improve their performance in these conditions, aiming at reproducing the main features of the thermal regime of deep Great Lakes.

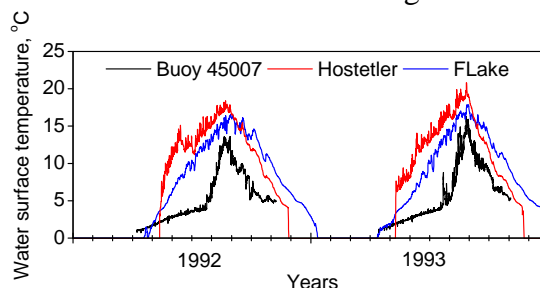


Figure 1. Off-line simulations of Lake Superior by 1D lake models (Martynov et al, 2010)

SST simulated by two 1D lake models compared to those observed for a large deep lake in Figure 1 clearly shows the limitations of these 1D models. It can be seen that most substantial differences between simulated and observed SST arise in spring, when the long warming period between the ice disappearance and crossing the maximum density temperature (4°C) is not adequately reproduced by 1D lake models. The most important reason of such underperformance is that these models do not reproduce correctly the thermal structure of water column in winter and spring seasons. In reality, in central regions of large lakes, even in the presence of ice cover deep and cold mixed layer is formed in wintertime and in spring a thick layer of cold water has to be warmed up before the surface temperature can cross the 4 degrees threshold. This process can be even more complex and three-dimensional with the development of the thermal bar phenomenon.

The Hostetler model (Hostetler *et al.* 1993) is based on the simple thermal regime parameterization, taking into account the wind-driven turbulence, free convection and background molecular thermal conductivity. Winter water temperatures simulated by this model are close to the maximum density temperature throughout the water column because the wind-driven turbulence is cut off by the ice cover. This approach, suitable for small quiet lakes, leads to very rapid overturning after ice disappearance, followed by rapid surface heating and rapidly developing positive stratification. Compared to the Hostetler model, the FLake model (www.lakemodel.net), based on the concept of self-similarity of water temperature profiles, produces, due to the specificity of its physical model, colder water below ice, which leads to slower spring warming. It is occurring, however, much faster than observed.

The Hostetler model, being relatively simple, is convenient for testing empirically-based corrections to the winter behavior of lake models. Several possible ways of adaptation of 1D lake models were proposed and tested. It was shown in an earlier study (Martynov *et al.* 2010) that the simple increase of the background thermal conductivity during the whole annual cycle does not improve the performance of the model. It is shown that wind-driven turbulence in presence of the ice cover improves slightly the performance of the model, but is not sufficient for reproducing the observed SST patterns. Introduction of complete vertical mixing in winter conditions, leading to the formation of a cold water column under the ice thereby improves the spring warming period; however this also extends the ice cover duration. Best results can be obtained by a combined approach.

List of references

- Beletsky D., D. J. Schwab (2001) Modeling circulation and thermal structure in Lake Michigan: Annual cycle and interannual variability. *J. Geophys. Res.*, **106**, 19745–71
- Hostetler, S.W., Bates, G.T. and F. Giorgi, (1993) Interactive nesting of a lake thermal model within a regional climate model for climate change studies. *J. Geophys. Res.*, **98**, 5045–57.
- Martynov A., L. Sushama, R. Laprise (2010) Simulation of temperate freezing lakes by one-dimensional lake models: performance assessment for interactive coupling with regional climate models. *Boreal Env. Res.*, **15**: 143–64
- Martynov A., L. Sushama, R. Laprise, K. Winger and B. Dugas (2011) Interactive Lakes in the Canadian Regional Climate Model, version 5: The Role of Lakes in the Regional Climate of North America. (*submitted to Tellus A*).
- Perroud, M., S. Goyette, A. Martynov, M. Beniston, O. Anneville, (2009) Simulation of multi-annual thermal profiles in deep Lake Geneva: a one-dimensional lake-model intercomparison study. *Limnol. Oceanogr.*, **54**: 1574–94.

Flows and Turbulence in a Tropical Lake

Stephen Monismith, Zikun Xing, Edmond Lo, Derek Fong, and James Hench

Department of Civil and Environmental Engineering, Stanford University, Stanford, CA 94305
monismith@stanford.edu

I will discuss a series of observations of currents, temperature variability and turbulence made in Kranji Reservoir, a shallow tropical reservoir in Singapore. I will highlight two important aspects of this system:

- (1) The lake stratifies and de-stratifies every day, with daily temperature variations comparable to what is observed for the lake over the course of a year. As a consequence, wind-generated baroclinic motions are not seiche-like, since since computed seiche periods are longer than the time over which the stratification forms and is destroyed;
- (2) Inflows tend to vary diurnally, also altering the stratification significantly.

Nonetheless, turbulence measurements made using a small microstructure profiler and combined ADCP/temperature data show that vertical mixing in the lake is strongly affected by the diurnal stratification. Most importantly, as a consequence of the rapid variability of the stratification, the standard conceptual models of lake dynamics derived from observations of temperate lakes, are generally inapplicable to the Kranji.

Correlating electrical conductivity and density in limnic water: a practical lake specific approach to density from CTD data

Santiago Moreira¹ and Bertram Boehrer²

¹*Institute of Hydrobiology, TU-Dresden.*

²*Helmholtz Centre for Environmental Research-UFZ, Magdeburg.*

Extended Abstract

Density calculations are crucial to study stratification, circulation patterns, wave formation and other relevant aspects of lake hydrodynamics. Density, i.e. potential density, of pure water (SMOW standard mean ocean water) ρ_w , can be calculated very accurately using e.g. Kell (1975). Specific contributions of solutes to volume and mass are known from tables of physical chemistry for the ocean (Millero 2001). More recently, Boehrer et al., (2011) implemented an algorithm, RHOMV, to calculate density with a second order approximation for temperature dependence and ionic strength dependence of cations anions and other solutes. This approach can be included in numerical stratification models for the simulation of chemically induced stratification (Moreira et al., 2011).

Most of the density equations applied in models for lakes and reservoirs are based only on temperature and salinity (not including the specific chemical composition) using general coefficients that are not specifically obtained for the study site, despite the fact that different solutes contribute in a different way to conductivity, salinity and density. Hydrodynamic models applied in lakes very often use the UNESCO equation (Fofonoff and Millard, 1983) which is designed for ocean purposes and hence not valid for salinities below 2 psu or in lakes where compositions is not dominated by NaCl. The approach by Chen and Millero (1986) allows to calculate density at low salinity (< 0.6 psu). However, the composition of many limnic waters differ remarkably from Chen and Millero's assumptions, that the density approach is not sufficiently accurate. For some lakes, specific density equations are developed by measuring the density at different temperatures and dilution conditions or compositions (Jellison et al. 1999, Bührer and Ambühl, 1974).

In this contribution, an approach is presented to include the effect of the solutes in limnic waters by calculating specific coefficients for a density conductance relation from coefficients of physical chemistry. These coefficients can be used to calculate density profiles from temperature and electrical conductance obtained from CTD profiles. Temperature and electrical conductivity can be measured in the CTD profiles at a high local and temporal resolution and even small changes can be detected, e.g. for microstructure measurements. This approach facilitates the inclusion of dissolved substances as long as changes in composition are not large.

Our approach calculates density in different lakes (water samples) as a function of the temperature T and the specific conductance κ_{25} at 25 °C. Specific coefficients for the density equation are

evaluated for each lake (or water sample) in spite of using general coefficients. The proposed equation is:

$$\rho(T, \kappa_{25}) = \sum a_i \cdot T^i + \kappa_{25} (\lambda_0 + \lambda_1 \cdot (T - 25))$$

where the first part $\sum a_i \cdot T^i$ is the equation for density of pure water (SMOW) presented by Kell (1975). The coefficient λ_0 relates density to measured electrical conductivity based on the lake specific composition. In addition, the introduction of λ_1 can reflect the temperature dependence; hence a shifting temperature of maximum density can be reflected with this approach. Only two coefficients need to be determined.

In the example presented here, density is calculated using the RHOMV algorithm (Boehrer et al., 2011) and the specific conductance at 25 °C using the numerical approach proposed in the PHREEQC code (Parkhurst and Appelo, 1999). The method is described in detail in the webpage of Dr C.A.J. Appelo: <http://www.xs4all.nl/~appt/exmpls/sc.html>. Once the values of $\rho_{(real)}$ and $\kappa_{25(real)}$ the values of λ_0 and λ_1 can be calculated as follows. First λ_0 is calculated using the measured or calculated density and specific conductance at T=25°C. Once λ_0 is calculated, λ_1 can be evaluated for any temperature T in which the density will be evaluated.

$$\lambda_0 = \frac{\rho_{25(real)} - \sum a_i \cdot T^i}{\kappa_{25(real)}} \quad \lambda_1(T) = \frac{\frac{\rho(T)_{real} - \sum a_i \cdot T_1^i}{\kappa_{25(real)}} - \lambda_0}{T_1 - 25}$$

For testing this new algorithm, some reference water samples are necessary. The density correlation for ocean water and two different approaches for lakes have been chosen for comparison using the known concentrations of the water in all the cases (Figure 1). The Fofonoff and Millard (1983) using the seawater composition at different dilution states, the equation developed by Jellison et al. (1999) using the composition of the water of Lake Mono and the equation developed by (Bührer and Ambühl, 1975) for Lake Constance.

The results (Figure 1) of the new approach were compared with the Fofonoff and Millard (1983) approach at four different salinities (S=3.0, 7.0, 17.5 and 35.0 psu), the density equation for Lake Mono by Jellison et al. (1999) for a diluted sample with conductivity equal to 42.68 mS cm⁻¹ at 25 °C and the Bührer and Ambühl (1985) approach for Lake Constance.

The absolute differences between the new approach and the “real” values are shown in Figure 2. In the case of the ocean water densities, the errors are lower than 0.2 kg/m³ for the complete range of temperatures for salinities equal to 3.0, 7.0 and 17.0 psu and for S=35.0 psu for temperatures from -3°C to 20 °C. In the case of fresh waters of Lake Constance, the absolute differences were around 0.1 kg/m³ for the complete range of temperatures and in the case of Lake Mono, the new approach provides good results for temperatures between 10 and 25°C.

According to the results, the new equation provides a good value of the water density even in lakes whose composition differs from natural freshwaters or oceanic conditions. Besides, the equation is

based only in a preliminary calculation to obtain the proper coefficients and in the usual values of temperature and specific conductance which makes possible to calculate density directly from the standard CTD profiles and it can be easily implemented in hydrodynamic and stratification models.

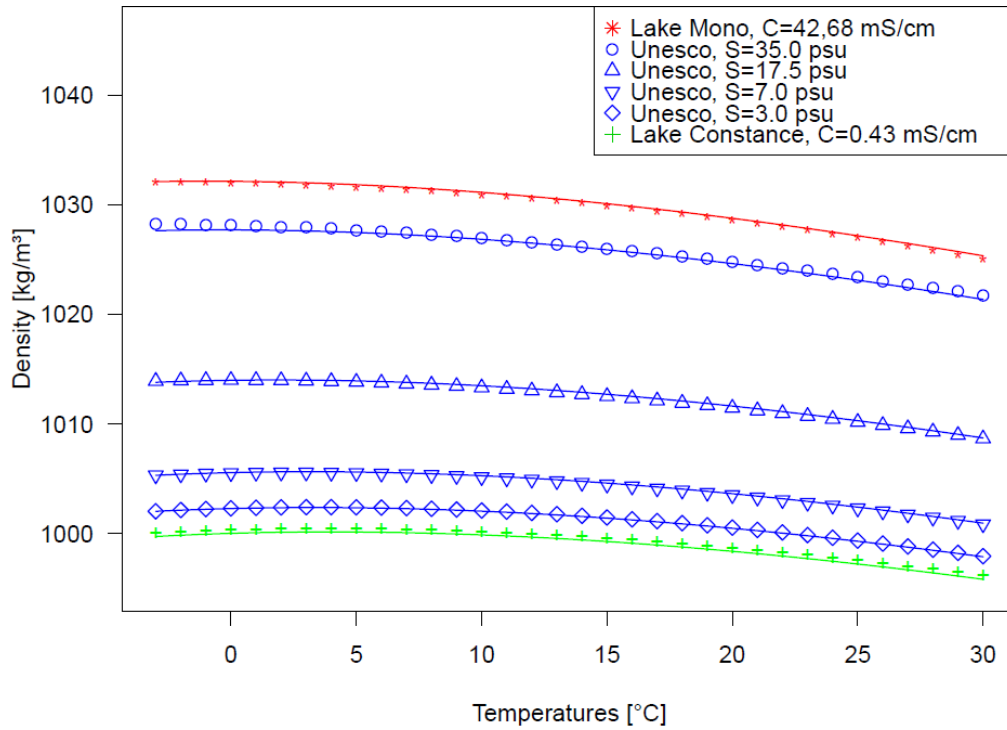


Figure 1. Comparison of the densities calculated for different salinities for water of ocean composition, Lake Mono and Lake Constance.

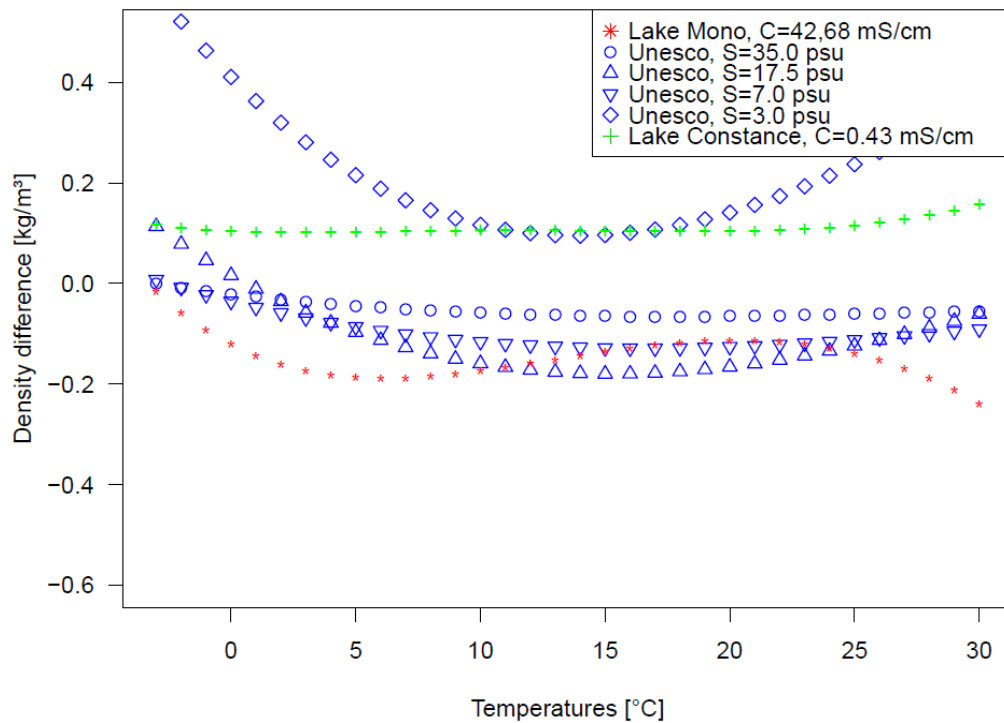


Figure 2. Density differences between the new approach and the density equations. Salinities in psu are provided for water of ocean composition (blue symbols), Lake Mono (red squares) and Lake Constance (green triangles).

References

- Boehrer, B.; Herzsprung, P.; Schultze, M.; Millero, F. J. (2010). Calculating density of water in geochemical lake stratification models. *Limnology and Oceanography Methods*, 8, 567-574.
- Bührer, H and Ambühl, H (1975). Die Einleitung von gereinigtem Abwasser in Seen. *Schweizerische Zeitschrift für Hydrologie*, 37:347-369.
- Chen, C.-T.A.; Millero F. J.. 1986. Precise thermodynamic properties for natural waters covering only the limnological range. *Limnol. Oceanogr.* 31, 657-662.
- Fofonoff, N.P.; Millard, R.C. Jr (1983). Algorithms for communication of fundamental properties of seawater, UNESCO technical papers in marine science, 44.
- Jellison, R; Macintyre, S.; Millero, F.J. (1999). Density and conductivity properties of Na-CO₃-Cl-SO₄ from Mono Lake, California, USA, *International Journal of Salt Lake Research*, 8: 41-53.
- Kell, G.S. (1975). Density, thermal expansivity, and compressibility of liquid water from 0° to 150°C: correlations and tables for atmospheric pressure and saturation reviewed and expressed on 1968 temperature scale. *J. Chem. Eng. Data* 20, 97-105.
- Moreira, S.; Boehrer, B.; Schultze, M.; Dietz, S.; Samper, J. (2011). Modelling geochemically caused permanent stratification in Lake Waldsee (Germany). *Aquatic Geochemistry*, 17(3): 265-280.
- Parkhurst D.L., Appelo C.A.J. (1999) Users guide to PHREEQC (version 2). A Computer program for speciation, batch-reaction, one-dimensional transport, and inverse geochemical calculations. Water-Resources Investigation Report 99-4259. U.S. Geological Survey.
- von Rohden, C.; Boehrer, B.; Ilmberger J. (2010) Evidence for double diffusion in temperate meromictic lakes. *Hydrology and Earth System Sciences*, 14:667-674.

Sediment resuspension and transport in a large, shallow estuary: Pamlico Sound, NC

R.P. Mulligan^{1,2*}, J.P. Walsh², R.L. Miller², D.R. Corbett²

¹ *Department of Civil Engineering, Queen's University, Kingston, Ontario, K7L 3N6, Canada*

² *Department of Geological Sciences and the Institute for Coastal Science and Policy,
East Carolina University, Greenville, North Carolina, 27858, USA*

*Corresponding author, e-mail mulliganr@civil.queensu.ca

KEYWORDS

Hydrodynamic modelling, satellite imagery, sediment resuspension, surface waves, winds.

EXTENDED ABSTRACT

Introduction

Pamlico Sound, North Carolina, is part of the second largest estuarine system in the United States. With limited connections to the Atlantic Ocean through tidal inlets, small astronomical tides, shallow bathymetry and a large surface area, wind-generated waves have been suggested to be critical to sediment redistribution (Wells, 1989). Portions of the sound are regularly impacted by water-quality issues (e.g., hypoxia) and are critical fish spawning and larval recruitment regions in which resuspension may play an important role. Hurricanes and extra-tropical storm wind events frequently impact the region and can have dramatic impacts on sediment transport. Previous modelling studies have not considered surface waves or sediment dynamics, but have shown that the hydrodynamics are driven by wind forcing. As an example, Luettich (2002) identified basin-scale seiching using the ADCIRC model. The present study examines the role of winds on both the surface waves that cause resuspension and the circulation responsible for transport of suspended materials.

Methods

The spatial extent of resuspension in this shallow estuary in response to a storm wind event is examined using 1) synoptic MODIS (Moderate Resolution Imaging Spectroradiometer) 250-m satellite data to estimate suspended sediment concentrations (SSC) following the method of Miller (2004); 2) near-bed *in situ* observations using acoustic velocimeters, pressure sensors and optical backscatter turbidity sensors at two sites in western Pamlico Sound; and 3) sediment transport modelling using coupled wave and hydrodynamic models, SWAN (Simulating Waves Nearshore, Booij, 1999) and Delft3D (Lesser, 2004). Delft3D is a finite-difference model that numerically solves the horizontal momentum equations. The sediment component includes parameterizations of hydrodynamic roughness in the bottom boundary layer, bedload and suspended-load transport, and deposition, erosion, and evolution of bed morphology. Waves are simulated by SWAN, a spectral wave model that contains the appropriate physics for predicting waves in shallow water.

Results and Discussion

We examine the hypothesis that wind-generated waves dominate sediment resuspension and dispersal within the Pamlico Sound. We test the hypothesis by prescribing the bottom sediment characteristics across the sound based on previous work (e.g., Wells, 1989),

applying wind forcing for a storm event and simulating wave-driven SSC across the estuary. *In-situ* data were collected at two field sites in winter 2008 (Figure 1) in the Tar-Pamlico (TP) and in Pamlico Sound (PS). During a northerly wind event (Fig. 1a), the model simulated the hydrodynamics accurately at the field sites, with significant wave heights up to 0.8 m at TP (Fig. 1b), a mean water level set-down of 0.6 m at TP (Fig. 1c), mean current magnitudes up to 0.2 m/s at TP and similar results at PS. Satellite-based estimates of the surface SSC were nearly uniformly 40 mg/l across Pamlico Sound, suggesting that persistent 10-15 m/s winds were sufficient to cause widespread resuspension of bottom material except near some coastlines and in narrow estuaries where wave growth was fetch-limited. Plumes of sediment following the event (Fig. 1d) suggest that finer material in the deeper (5-7m) basins of the sound remain in suspension for a timescale of 2-4 days upon relaxation of the winds. Model results (Fig. 1e) corroborate the hypothesis that wind-generated waves dominate sediment resuspension and also suggest strong correlation between surface SSC and bathymetry, indicating the source of finer material to be the deeper basins of the sound. Since wind events of this magnitude occur frequently (several times per month) and are often much stronger (e.g. hurricanes and nor'easters), the wave-driven resuspension of bottom material into the water column is likely the dominant mechanism affecting present-day sediment distributions across Pamlico Sound. Due to the large extent and regular frequency, these dynamics have important implications for biogeochemical cycling and ecosystem behavior.

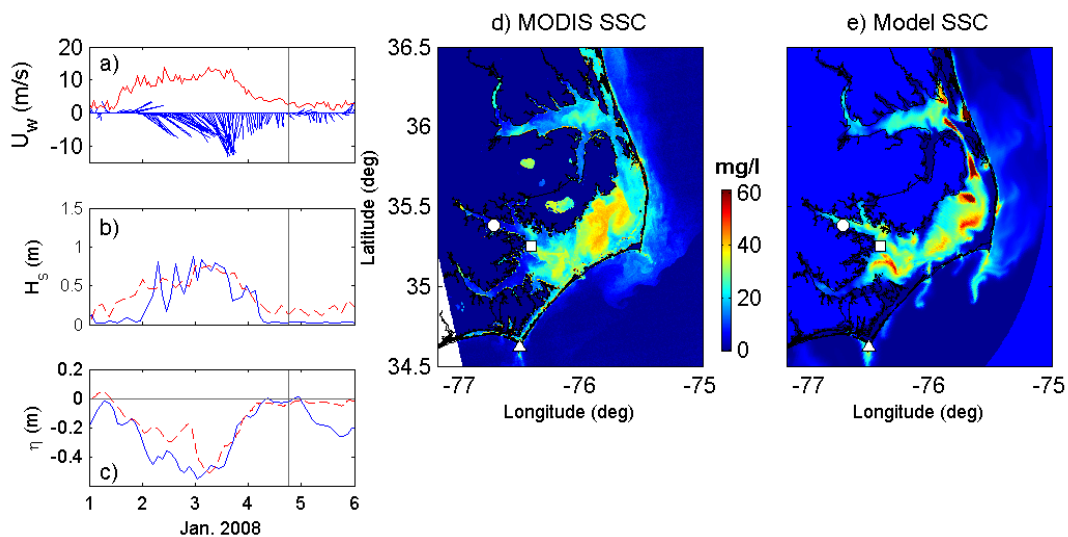


Figure 1. Observations and model results for a northerly wind event in January 2008: a) wind speed and stick vectors at Cape Lookout; b) significant wave height data (solid blue) and model results (dashed red) at site TP; c) water level observations (solid blue) and model results (dashed red) at site TP; d) surface SSC from MODIS on Jan. 4 at 18:15; e) model estimate of surface SSC on Jan. 4 at 18:00. Wind station at Cape Lookout (triangle) and field sites TP (circle) and PS (square) are indicated by white symbols.

REFERENCES

- Booij, N., Ris R.C., and Holthuijsen, L.H. (1999). A third-generation wave model for coastal regions, Part I, Model description and validation. *J. Geophys. Res.*, **104**: 7649-7666.
- Lesser, G., J. Roelvink, J. van Kester, and Stelling, G. (2004). Development and validation of a three-dimensional morphological model, *Coastal Eng.*, **51**, 883-915.
- Luettich, R., Carr, S., Reynolds-Fleming, J., Fulcher, C., McNinch, J. (2002). Semi-diurnal seiching in a shallow, micro-tidal lagoonal estuary. *Continental Shelf Res.*, **22**, 1669-1681.
- Miller, R.L. and B.A. McKee. (2004). Using MODIS Terra 250 m Imagery to Map Concentrations of Total Suspended Matter in Coastal Waters. *Remote Sensing of Environment*, **93**(1-2), 259-266.
- Wells, J.T., Kim, S.-Y. (1989). Sedimentation in the Albemarle-Pamlico lagoonal system: Synthesis and hypotheses. *Mar. Geol.* **88**, 263-284.

Mixing of stratified waters by *Daphnia magna*

C. Noß^{1*} and A. Lorke¹

¹ Institute for Environmental Sciences, University of Koblenz-Landau, 76829 Landau, Germany

*Corresponding author, e-mail noss@uni-landau.de

ABSTRACT

This paper presents experimental results for the fluid transport induced by tethered as well as by freely swimming zooplankton organism (*Daphnia*) in a density-stratified water column. Particle image velocimetry (PIV) and planar laser induced fluorescence (PLIF) were used to measure the instantaneous velocity and density distributions and to estimate the kinetic energy, dissipation rates, vertical mass fluxes, and apparent diffusion coefficients around individual organisms. We found diffusivities of $1 \cdot 10^{-4} \text{ m}^2 \cdot \text{s}^{-1}$ in the vicinity of the tethered and $1 \cdot 10^{-5} \text{ m}^2 \cdot \text{s}^{-1}$ around the freely swimming organisms. These diffusivities are valid within a volume of influence, which can exceed the volume of the organism by two orders of magnitude. The results firstly indicate that biologically-induced fluid and mass transport by swimming zooplankton can significantly contribute to transport processes in stratified water bodies at sites and during time periods when background turbulence is weak and/or zooplankton abundance is high.

KEYWORDS

Fluid transport; *Daphnia*; PIV; PLIF; Diffusion; Dissipation.

INTRODUCTION

Turbulent vertical mixing in stratified water bodies, such as oceans, lakes and reservoirs, determines the vertical distribution of heat and density-relevant dissolved substances (Boehrer and Schultze 2008; Munk 1966). Besides current shear generated by tides, wind, internal waves, or buoyancy-driven currents, also biomixing, i.e. turbulence and vertical mixing induced by the movement of aquatic animals, has been proposed to contribute to vertical mixing with significant magnitude. Huntley and Zhou (2004) used scaling arguments to analyze the production rate of (turbulent) kinetic energy by 100 marine species, ranging in size from bacteria to whales. The result of this analysis was that at scales of typical social aggregations, each species generates kinetic energy at a rate of about $10^{-5} \text{ W} \cdot \text{kg}^{-1}$ (per kilogram of water). They concluded that animal-induced turbulence is comparable in magnitude to rates of turbulent energy dissipation that result from major storms. Based on metabolic and productivity arguments, Dewar et al. (2006) estimated the total biosphere contribution to the aphotic ocean mechanical energy in a bottom-up approach to be about 1 TW, again comparable in magnitude to that of wind and tides. Experimental evidence for biomixing, however, is very limited. Kunze et al. (2006) observed strongly increased levels of turbulence during the ascent of dense swarms of krill performing diel vertical migration in the coastal ocean. Gregg and Horne (2009) observed similarly enhanced turbulent dissipation rates within patches of enhanced acoustic backscatter, most likely caused by small fish, in Monterey Bay, and Lorke and Probst (2010) found a correlation between measured rates of turbulent kinetic energy dissipation and the abundance of small, young-of-the-year fish

around an artificial reef in Lake Constance. Common to these observations, however, is that they document the existence of biologically-generated velocity fluctuations, i.e. the stirring of the stratified water column, but do not allow for quantifying the associated rate of fluid and mass transport directly. For biologically-generated turbulence the length scale at which velocity fluctuations are generated is assumed to correspond to the size of the swimming organism, leading to the conclusion that biomixing is insignificant for most of the small and very abundant aquatic animals, like zooplankton (Visser 2007). Zooplankton, however, is of particular interest with respect to its potential contribution to vertical mixing because many species perform a diel vertical migration and thereby crossing the thermocline, a region where vertical gradients of dissolved substances are particularly strong, on a regular basis.

Very recently, Katija and Dabiri (2009) have estimated that an amount of energy, which again is comparable in magnitude to major winds and tides, can be provided by fluid transport within the viscous boundary layer surrounding swimming animals, even in a laminar flow regime. Numerical simulations (Dabiri 2010) showed that the successive interaction of zooplankton organisms with parcels of fluid lead, under certain conditions, to vertical displacement of the fluid parcels over distances much larger than the individual body size. These regions of displaced fluid are unstably stratified and, hence, amenable to large-scale overturning and efficient mixing. Laboratory investigations of the flow field generated by swimming copepods (van Duren et al. 2003; Jiang and Osborn 2004) were, so far, mainly obtained for tethered organisms and very small sample containers. All of these studies were conducted in non-stratified environments and none of them quantified fluid transport.

In this paper we quantify for the first time the small-scale fluid transport associated with tethered and freely swimming millimeter-sized zooplankton in laboratory experiments under the effect of stable density stratification. We combined particle image velocimetry (Stamhuis 2006) with laser-induced fluorescence (Crimaldi 2008) measurements to characterize the velocity field, kinetic energy, rates of viscous energy dissipation, as well as the vertical fluxes and apparent diffusion coefficients associated with the movement of individual organisms (*Daphnia magna*).

METHODS

Experiments were conducted in a linear vertical density gradient with a buoyancy frequency N ($N = (-g/\rho \cdot d\rho/dz)^{1/2}$, ρ - density, z - depth, g - gravitational acceleration) of 0.07 s^{-1} . The gradient was established in a 17.3 cm tall glass tank (9 l volume) with a maximum salt (NaCl) concentration $c_{\text{NaCl}} = 0.17 \text{ ‰}$ at the bottom and 0.0 ‰ at the top using the Oster-method (Zurigat et al. 1990). The tank was filled from the bottom to the top at a constant rate and with a linearly increasing salt concentration in the inflow. The resulting density gradient corresponds to a temperature gradient of approximately 3 °C m^{-1} at 24 °C . The fluorescent tracer Rhodamin 6G was added during the filling process at a rate proportional to that of salt, resulting in a concentration of $c_{\text{Rh}} = 0.02 \text{ mg l}^{-1}$ at the bottom and 0.0 mg l^{-1} at the surface. The intensity of fluorescence measured at a wavelength of 555 nm after excitation with laser light (532 nm) was used as a proxy to quantify the density distribution and to observe small-scale density disturbances within a 2 mm thick light sheet. The light sheet was arranged vertically and fluorescence intensity was recorded using a 4 megapixel CCD camera synchronized with laser-pulses at a rate of 7 Hz (images per second) within a 17 cm by 17 cm field of view near the centre of the tank. Raw images of the fluorescence distribution were corrected for inhomogeneous illumination due to light absorption and reflections and for fluctuations in laser power following Shan et al. (2004). The flow field was visualized using $20 \text{ }\mu\text{m}$ sized seeding particles, evenly distributed throughout the tank, and observed by a second CCD camera. Two-dimensional particle velocities within the laser light sheet were estimated by

correlating two subsequently captured image frames, each synchronized with a separate laser pulse and with a time lag of 35 ms between both exposures. These double-frame images were recorded at 7 Hz. Instantaneous velocities were analyzed by adaptive correlation and mean velocities were analyzed by the average correlation procedure of the DynamicStudio software (Dantec Dynamics) in 2.65×2.65 mm subareas, i.e., within 64×64 pixel interrogation areas with 50% overlap. The regions around swimming *Daphnia* were discarded and remaining outliers, exceeding a velocity threshold of $v = 1 \text{ cm}\cdot\text{s}^{-1}$, were replaced by mean values of the surrounding velocities. The analysis of the flow and the dispersion around zooplankton organisms was performed under two different conditions: First a single *Daphnia* was tethered with glue on the tip of a fine nylon filament and fixed within the laser light sheet. In the second set-up *Daphnia* were swimming freely through the tank and passed randomly through the light sheet and the field of view. Within the entire tank no advective (background) currents were present during the measurements and any current and density displacement in the aquarium was entirely related to the flow generated by the *Daphnia*.

RESULTS

Results obtained for tethered *Daphnia*

The organism was aligned directly in the laser sheet at the centre of the tank, in a way that its second antennae movement accelerated the fluid mainly in parallel to the light sheet (Fig.1a). The tetherline fixing did not affect the movement of the second antennae and most of the mechanical energy introduced by their steady motion resulted in the displacement of the surrounding fluid, instead of propulsion of the *Daphnia*. An individual of about 4.2 mm length caused a persistent and nearly steady fluid jet. The jet had a longitudinal extension of approx. $r = 60$ mm, where the first 32 mm had a strong downward velocity component before it turned into the horizontal direction and faded away (Fig.2a). The transversal extension of the fully developed jet was approx. 12 mm and, assuming spherical symmetry, the jet encompassed a total volume of 6.8 cm^3 , which is about 175 times the volume of the tethered organism (approximated as a sphere). The spatially averaged velocity in the jet was $\langle \vec{v} \rangle = 1.8 \text{ mm}\cdot\text{s}^{-1}$, where $\langle \rangle$ denotes spatial averaging, and the maximum velocity was $\vec{v}_{\text{max}} = 7.6 \text{ mm}\cdot\text{s}^{-1}$.

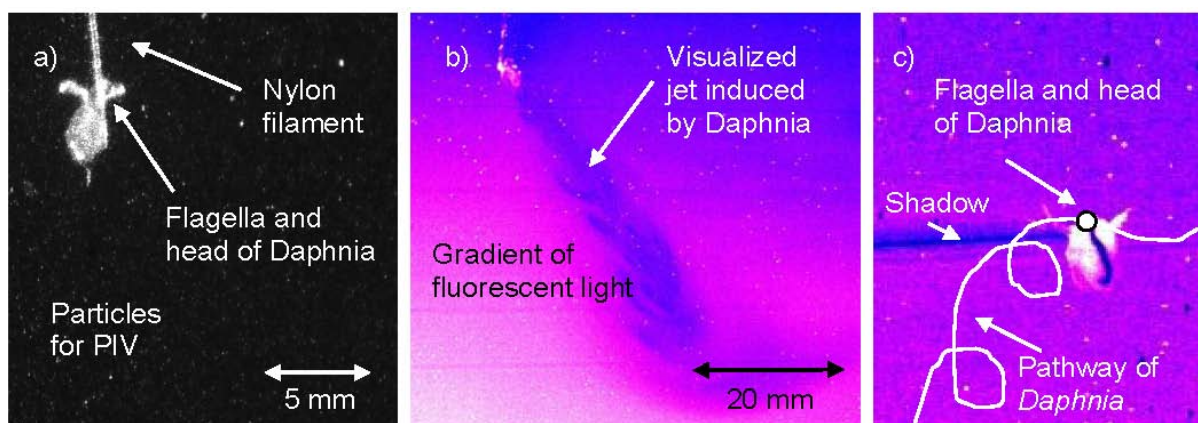


Figure 1 Raw images a) of the tethered *Daphnia* for particle image velocimetry, b) of the tethered *Daphnia* for laser-induced fluorescence and c) of the freely swimming *Daphnia* (Full video of the freely swimming *Daphnia* in auxiliary material). Explanations are provided in the images, the color in b) and c) visualizes the density distribution, which initially had a linear vertical gradient

The kinetic energy $E = 0.5 \cdot \bar{v}^2$ reached a maximum value of $10^{-5} \text{ J} \cdot \text{kg}^{-1}$ in the centre of the jet (Fig. 2b). The rate of viscous energy dissipation ε was estimated from observed velocity gradients following van Duren et al. (1998) and reached values of $10^{-6} \text{ W} \cdot \text{kg}^{-1}$ (Fig.2c). The total dissipated power P_{diss} in the fluid volume V affected by the *Daphnia* was $P_{diss} = \rho \cdot \int \varepsilon dV = 5.8 \cdot 10^{-8} \text{ W}$. V was assumed to be equal to a cylindrical volume with a diameter of dx over which $\varepsilon > 10^{-7.5} \text{ W} \cdot \text{kg}^{-1}$. Based on the observed magnitudes, the longitudinal extension of the jet r_{max} can be estimated by balancing the observed decay of kinetic energy with its rate of viscous dissipation along the jet by $r_{max} = E \cdot |\bar{v}_{max}| / \varepsilon \approx 76 \text{ mm}$, which is in reasonable agreement with the observed longitudinal extension of 60 mm. These estimates indicate that most of the kinetic energy is dissipated in the nearly vertically directed

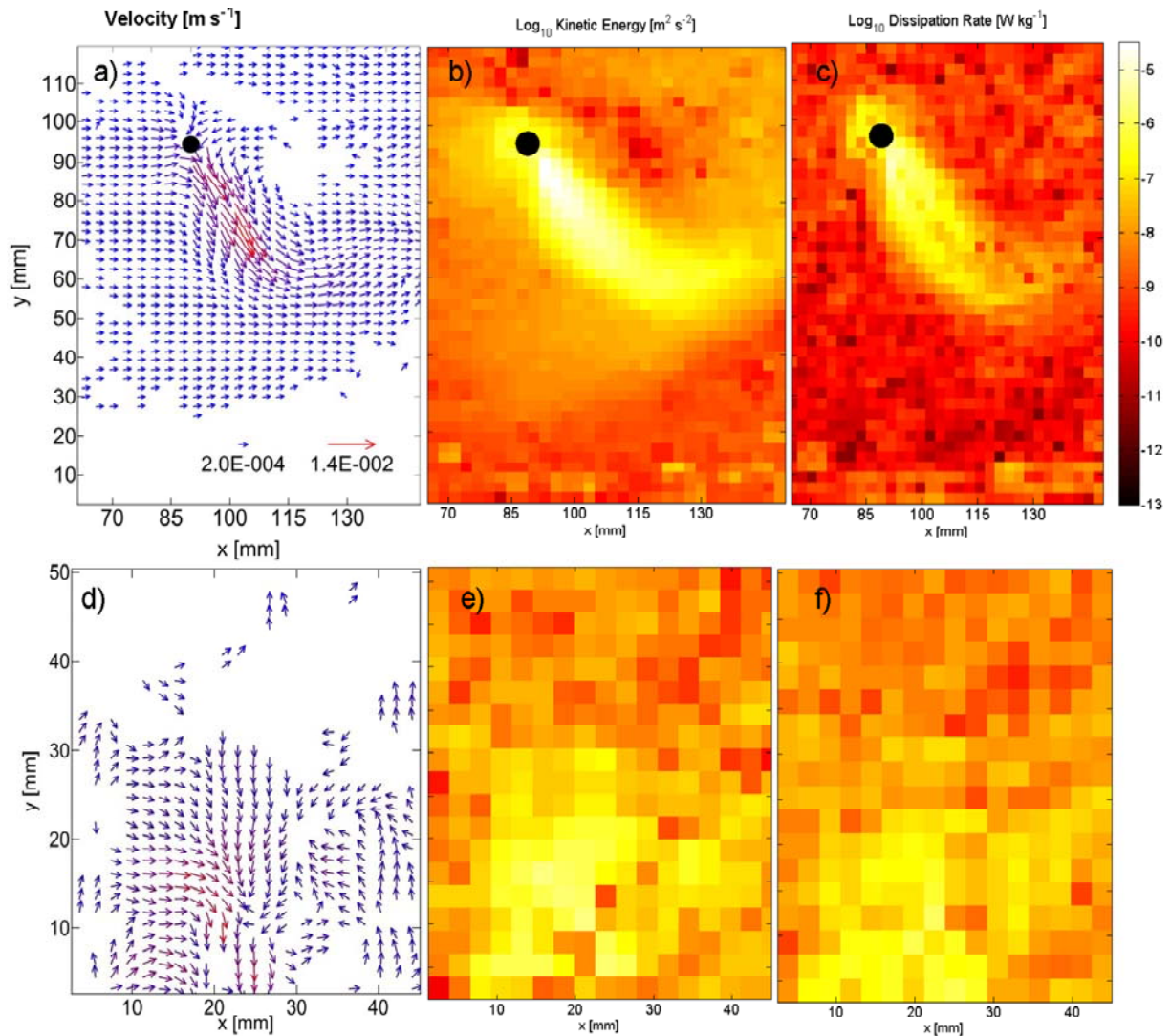


Figure 2 Vector plot of a) temporal mean velocity vectors \bar{v} (interpolated with Radial Basis Function (RBF), $\bar{v} < 2 \cdot 10^{-4} \text{ m s}^{-1}$ are blanked) of the flow field, b) kinetic energy E and c) energy dissipation rate ε induced by a tethered *Daphnia* (black dot). Vector plot of d) instantaneous velocity vectors \bar{v} of the current velocity (interpolated with RBF, $\bar{v} < 2 \cdot 10^{-4} \text{ m s}^{-1}$ are blanked), e) kinetic energy E and f) energy dissipation rate ε in the wake of a freely swimming *Daphnia* directly after it had passed through the field of view (Full videos of instantaneous velocity vectors, kinetic energy and dissipation rate of freely swimming *Daphnia* in auxiliary material). The axes are spatial coordinates in mm, in b), c), e) and f). The color coding for $\text{log}_{10}(E)$ and $\text{log}_{10}(\varepsilon)$ is identical for all panels.

jet and that the recirculating flow occurred at smaller velocities distributed over a much larger area in the far field of the jet, i.e. that the tethered *Daphnia* did not generate a circulating eddy. The fluid mixing associated with the *Daphnia*-induced flow was quantified by estimating an apparent diffusion coefficient, based on fluid displacement. 50 virtual particles were placed along a straight line perpendicular to the jet directly behind the *Daphnia* and their pathways have been followed numerically based on the observed mean velocity field in 10^{-3} s time steps. The corresponding diffusion coefficient k_{Daph} was estimated from the mean two-dimensional displacement $r = \sqrt{\Delta x^2 + \Delta y^2}$ of the particles within time Δt after release as $k_{Daph} = 0.25 \cdot \langle r^2 \rangle / \Delta t$. k_{Daph} increases with increasing Δt to $5 \cdot 10^{-5} \text{ m}^2 \cdot \text{s}^{-1}$ until the particles leave the high velocity region of the jet, which approximately corresponded to the first 32 mm of displacement. For greater Δt , k_{Daph} decreased slightly until the particles reached the end of the jet. In an independent approach, the small-scale mixing induced by the tethered *Daphnia* was estimated from the observed density fluctuations (Fig.1b) by evaluating the vertical mass flux through a horizontal plane, perpendicular to the laser light sheet. In analogy to turbulent transport, the flux J can be estimated as $J = \overline{w'c'}$, with w' denoting the fluctuation of vertical velocity, c' the fluctuation of concentration observed by laser-induced fluorescence, and the overbar denotes temporal averaging. Based on the observed nearly stationary flow field and by neglecting vertical transport outside of the cross-sectional area of the jet, the total flux induced by the jet can be estimated as the mean vertical velocity $\langle w \rangle_{Jet} \approx 1.4 \text{ mm} \cdot \text{s}^{-1}$ multiplied by the mean salt concentration $\langle c \rangle_{Jet} = 0.05 \text{ kg} \cdot \text{m}^{-3}$ within the jet, resulting in a value of $J = 7 \cdot 10^{-5} \text{ kg} \cdot \text{m}^{-2} \cdot \text{s}^{-1}$. An alternative estimate of the diffusion coefficient can be obtained from Fick's law as $k_{Daph} = -J / \langle \partial c / \partial z \rangle$, resulting in $k_{Daph} = 9.7 \cdot 10^{-5} \text{ m}^2 \cdot \text{s}^{-1}$ ($\langle \partial c / \partial z \rangle = 0.72 \text{ kg} \cdot \text{m}^{-4}$).

Results obtained for freely-swimming *Daphnia*

Although fixation within the light sheet and the nearly stationary flow field generated by the tethered *Daphnia* provide ideal experimental conditions for the development and testing of observation and analysis procedures, the resulting mixing coefficients are certainly overestimated because the mechanical energy introduced by the organism goes entirely into acceleration of surrounding water, instead of propulsion. Additional and more realistic measurements have therefore been conducted with a number of freely swimming *Daphnia* using an identical experimental setup. *Daphnia* passed through the light sheet and the field of view of the cameras randomly and for short time periods (max. 5.8 s) only (Fig.1c and see [Movie 1](#) provided in the auxiliary material). Velocity, kinetic energy, energy dissipation rate, dissipated power and the apparent diffusion coefficient have been evaluated using the procedures described above. Because of the highly unsteady character of the flow associated with the passage of a zooplankton organism, all parameters have been evaluated for each individual image, except for the dissipated power and the diffusion coefficient, which were averaged over the recorded sequence. Fig.2d-f exemplify the results showing the velocity field, kinetic energy and dissipation rate around a freely swimming *Daphnia*. Movie files of the entire movement and its hydraulic characterization are enclosed to this paper ([Movie 2](#) for velocity, [Movie 3](#) for kinetic energy and [Movie 4](#) for dissipation rate provided in the auxiliary material). Although the highest rate of viscous energy dissipation $\varepsilon = 1.3 \cdot 10^{-5} \text{ W} \cdot \text{kg}^{-1}$ induced by the freely swimming *Daphnia* is an order of magnitude higher in comparison to the maximal dissipation rate caused by the tethered *Daphnia*, the total amount of dissipated energy (dissipated power) was an order of magnitude lower, i.e. $P_{diss} = 4.4 \cdot 10^{-9} \text{ W}$, due to a smaller volume affected by the moving *Daphnia*. Virtual particle displacements within the

observed dynamic flow revealed apparent diffusivities of $k_{Daph} = 1.15 \cdot 10^{-5} \text{ m}^2 \cdot \text{s}^{-1}$ within the wake of the organism. As long as particles have been released along a line (representing a plane), which was crossed perpendicularly by the *Daphnia*, every run of computation yielded similar results (see later). The diffusion coefficient varies, however, with the degree of spatial averaging, i.e. with the length of the line along which the particles are released. k_{Daph} decreases from $1.15 \cdot 10^{-5} \text{ m}^2 \cdot \text{s}^{-1}$ to $0.3 \cdot 10^{-5} \text{ m}^2 \cdot \text{s}^{-1}$ if the width of released particles increases from the width of one *Daphnia* $D \approx 2.5 \text{ mm}$ to $10 \cdot D$. In contrast to the experiment with the tethered *Daphnia*, it is not possible to assume quasi-stationary conditions and therefore it is not possible to use mean values for evaluating the vertical mass flux from concentration fluctuations. However, it is still reasonable to consider the entire disturbance by a swimming *Daphnia* as the only source of mass transport and therefore as fluctuations with respect to zero velocities and a linear background density gradient. Hence, the vertical salt flux through a horizontal cross-section at height z which is associated with the vertical passage of a swimming *Daphnia* can be estimated as the temporal covariance of vertical velocity $w(t)$ and concentration fluctuation $\Delta c(t)$, with $\Delta c(t) = c(t) - \langle c \rangle_z$. The mean flux over D for the example with the mainly vertically swimming *Daphnia* illustrated in Fig. 1c was $J = 0.6 \cdot 10^{-5} \text{ kg} \cdot \text{s}^{-1} \cdot \text{m}^{-2}$, with a maximum value of $1.3 \cdot 10^{-5} \text{ kg} \cdot \text{s}^{-1} \cdot \text{m}^{-2}$. The corresponding diffusion coefficients are $0.8 \cdot 10^{-5} \text{ m}^2 \cdot \text{s}^{-1}$ and $1.8 \cdot 10^{-5} \text{ m}^2 \cdot \text{s}^{-1}$, respectively. Although the agreement between the diffusivity estimates from particle displacement and from the salt flux is reasonable, it has to be noticed, that both results depend strongly on the cross-sectional width, where particles have been released and over which the velocity and concentration fluctuations have been evaluated. Differences between both estimates can result from the unsteady motion of the *Daphnia*, which was integrated by the displacement method along the pathways (space) and by the flux method over time. Therefore both methods were repeated, i.e., the estimation of the diffusion via displacements starting from three additional lines of particle release and the estimation of the flux for four additional cross-sections at different heights z , each of width D , crossed by the swimming *Daphnia*. We achieved nearly identical results with $1.14 \cdot 10^{-5} \text{ m}^2 \cdot \text{s}^{-1}$ for the mean diffusion coefficient computed from the pathways (with $\pm 0.35 \cdot 10^{-5} \text{ m}^2 \cdot \text{s}^{-1}$ standard deviation) and $1.64 \cdot 10^{-5} \text{ m}^2 \cdot \text{s}^{-1}$ ($\pm 0.6 \cdot 10^{-5} \text{ m}^2 \cdot \text{s}^{-1}$) for the mean of the maximal diffusion coefficient from flux estimations. The mean diffusion coefficients from flux estimations averaged across the entire cross-section of width D was again $0.8 \cdot 10^{-5} \text{ m}^2 \cdot \text{s}^{-1}$ ($\pm 0.4 \cdot 10^{-5} \text{ m}^2 \cdot \text{s}^{-1}$).

DISCUSSION

As analyzed for copepods by Catton et al. (2007) at greater detail, these differences in the results between tethered and freely swimming organisms can be attributed to an unbalanced force, which the tethered organism can impart on the fluid by pushing against the tether. While Catton et al. (2007) observed differences in viscous energy dissipation of a factor of two to four, we found a more severe impact on diffusion coefficients k_{Daph} , which is nearly $1.0 \cdot 10^{-4} \text{ m}^2 \cdot \text{s}^{-1}$ for the tethered and one order of magnitude less for the freely swimming organisms. This difference becomes even more pronounced when the volume of influence, i.e. the volume of water for which the diffusion coefficients were estimated, are taken into account. In the experiment with the tethered *Daphnia*, a quasi-stationary jet with a total volume of approximately 7 cm^3 was observed through the continuous movement of the *Daphnia*, while in case of the freely swimming *Daphnia*, a volume of approximately 0.1 cm^3 was affected over the recorded sequence. By further taking fluid velocity and the movement of the organisms into account, the volume of water affected per unit time interval was approximately $204 \text{ mm}^3 \cdot \text{s}^{-1}$ in the tethered experiment and $31 \text{ mm}^3 \cdot \text{s}^{-1}$ for the freely swimming organism. These findings clearly demonstrate the necessity for using freely

swimming organisms for quantitative and qualitative analyses of the flow fields and fluid transport generated by swimming zooplankton. In the present study, the well-defined experimental conditions in the tethered setup have been used to validate the methods for estimating apparent diffusivities resulting from small-scale and low Reynolds number flows generated by swimming *Daphnia*. The two independent methods are based on virtual particle tracking in the observed flow field, and on direct flux measurements, respectively, and showed a remarkably good agreement in both experiments. Because of the higher degree of temporal averaging, enabled by the stationary flow field in the tethered setup, these diffusivity estimates can be considered as robust and their close agreement thus provides proof of the applicability of both methods and underlying measurements. The dissipation rates of kinetic energy, vertical fluxes and apparent diffusivities observed in the vicinity of swimming *Daphnia* are high in comparison to corresponding values found in typical environmental flows (Ivey et al. 2008; Wüest and Lorke 2003). The ratio of the energy dissipation of the freely swimming *Daphnia* to the tethered *Daphnia* was approximately 8 %. Assuming that energy dissipation equals energy production within the volume of influence, and neglecting the negative drag force of the returning of the second antennae (flagella) to its initial position (Morris et al. 1985), this ratio provides a bulk estimate of the mechanical efficiency of propulsion, which is comparable to estimates of zooplankton of similar sizes (Huntley and Zhou 2004). The total energy dissipation within the volume of influence of the freely swimming *Daphnia* is one order of magnitude and in case of the tethered *Daphnia* two orders of magnitude larger than the energy dissipation induced by tethered copepods with a body length of about 1 mm (van Duren et al. 2003). However, the energy dissipation rate of the freely swimming *Daphnia* is nearly identical to the rate of kinetic energy production of schooling animals ($10^{-5} \text{ W}\cdot\text{kg}^{-1}$) estimated by Huntley and Zhou (2004). The effect of density stratification on the observed flow fields and fluxes can be estimated by comparing the kinetic energy in the animal-induced flow with the potential energy of stratification. Such comparison is provided by the Ozmidov length scale L_O ($L_O = (\varepsilon / N^3)^{0.5}$), which is usually applied to turbulent flows (Lorke and Wüest 2002) and describes the maximum size of vertical fluid motions, before they become damped by buoyancy forces. Using $\varepsilon = 1 \cdot 10^{-6} \text{ W}\cdot\text{kg}^{-1}$ and $N = 0.07 \text{ s}^{-1}$ yields $L_O = 5.4 \text{ cm}$, which is in close agreement with the observed vertical dimension of the steady fluid jet produced by the tethered *Daphnia*. The flow field and fluid transport generated by the freely swimming *Daphnia*, however, is not much affected by density stratification, which is in accordance with the numerical simulations of Dabiri (2010). Applying the universal relationship between body mass and typical packing density of organisms provided by Huntley and Zhou (2004) to a typical mass of adult *Daphnia magna* of $\approx 0.2 \text{ mg}$ (Porter et al. 1982) yields a packing density of $7 \cdot 10^7 \text{ m}^{-3}$ in animal aggregations. This value corresponds to more than one individual within the volume of influence of 0.1 cm^3 observed in our experiments with freely swimming *Daphnia*, and indicates that the corresponding diffusivity of $1 \cdot 10^{-5} \text{ m}^2 \cdot \text{s}^{-1}$ could even be exceeded on scales of animal aggregations. This diffusivity is comparable in magnitude to turbulent diffusivities typically observed in the interior of stratified lakes (Wüest and Lorke 2003) or of the ocean (Wunsch and Ferrari 2004). Net hauls over vertical distances of a few meters, however, reveal much lower abundances of adult *Daphnia* in lakes with typical values of 10^4 m^{-3} (Huber et al. 2010) and corresponding volume-averaged diffusivities caused by freely swimming individuals of $1 \cdot 10^{-8} \text{ m}^2 \cdot \text{s}^{-1}$. Although this diffusivity is one order of magnitude smaller than the molecular diffusion coefficients of heat ($\approx 10^{-7} \text{ m}^2 \cdot \text{s}^{-1}$), it still exceeds the molecular diffusivity of dissolved substances and gases ($\approx 10^{-9} \text{ m}^2 \cdot \text{s}^{-1}$). Within and below the seasonal thermocline, vertical mass transport was shown to be close to molecular levels using tracer experiments in small lakes (von Rohden and Ilmberger 2007), or by revealing the existence of double-diffusive transport phenomena (Boehrer et al. 2009; Schmid et al. 2004). Our results thus

indicate that biologically-induced fluid transport by zooplankton may be important for vertical mixing in stratified water bodies at sites and during time periods when background mixing is weak and/or zooplankton abundance is high. Although these results are limited to observations of two individuals, the principal analysis using PIV/PLIF measurements provide a helpful method for further investigations of the vertical mixing by swimming organisms.

List of references

- Boehrer B, Dietz S, Von Rohden C, Kiwel U, Jöhnk K, Naujoks S, Ilmberger J, Lessmann D (2009) Double-diffusive deep water circulation in an iron-meromictic lake. *Geochemistry Geophysics Geosystems* 10:Q06006. doi:10.1029/2009GC002389
- Boehrer B, Schultze M (2008) Stratification of lakes. *Rev Geophys* 46:RG2005. doi:2006RG000210
- Catton KB, Webster DR, Brown J, Yen J (2007) Quantitative analysis of tethered and free-swimming copepodid flow fields. *J Exp Biol* 210 (2):299-310. doi:10.1242/jeb.02633
- Crimaldi JP (2008) Planar laser induced fluorescence in aqueous flows. *Experiments in Fluids* 44 (6):851-863. doi:10.1007/s00348-008-0496-2
- Dabiri JO (2010) Role of vertical migration in biogenic ocean mixing. *Geophys Res Lett* 37:L11602. doi:10.1029/2010GL043556
- Dewar WK, Bingham RJ, Iverson RL, Nowacek DP, St. Laurent LC, Wiebe PH (2006) Does the marine biosphere mix the ocean? *J Mar Res* 64:541-561
- Gregg MC, Horne JK (2009) Turbulence, acoustic backscatter, and pelagic nekton in Monterey Bay. *J Phys Oceanogr* 39:1077-1096
- Huber A, Peeters F, Lorke A (2010) Active and passive vertical motion of zooplankton in a lake. *Limnol Oceanogr*:conditionally accepted
- Huntley ME, Zhou M (2004) Influence of animals on turbulence in the sea. *Mar Ecol Prog Ser* 273:65-79
- Ivey GN, Winters KB, Koseff JR (2008) Density stratification, turbulence, but how much mixing? *Ann Rev Fluid Mech* 40:169-184
- Jiang HS, Osborn TR (2004) Hydrodynamics of copepods: A review. *Surv Geophys* 25 (3-4):339-370
- Katija K, Dabiri JO (2009) A viscosity-enhanced mechanism for biogenic ocean mixing. *Nature* 460:624-627
- Kunze E, Dower JF, Beveridge I, Dewey RK, Bartlett KP (2006) Observations of biologically generated turbulence in a coastal inlet. *Science* 313:1768-1770
- Lorke A, Probst WN (2010) In situ measurements of turbulence in fish shoals. *Limnol Oceanogr* 55:354-364
- Lorke A, Wüest A (2002) Probability density of displacement and overturning length scales under diverse stratification. *J Geophys Res* 107 (C12):1-11
- Morris MJ, Gust G, Torres JJ (1985) Propulsion efficiency and cost of transport for copepods: a hydromechanical model of crustacean swimming. *Mar Bio* 86 (3):283-295. doi:10.1007/bf00397515
- Munk W (1966) Abyssal recipes. *Deep-Sea Res* 13:707-730
- Porter KG, Gerritsen J, Orcutt Jr. JD (1982) The effect of food concentration on swimming patterns, feeding behavior, ingestion, assimilation, and respiration by *Daphnia*. *Limnol Oceanogr* 27:935-949
- Schmid M, Lorke A, Dinkel C, Tanyileke GZ, Wüest A (2004) Double-diffusive convection in Lake Nyos, Cameroon. *Deep-Sea Research I* 51:1097-1111
- Shan J, Lang D, Dimotakis P (2004) Scalar concentration measurements in liquid-phase flows with pulsed lasers. *Experiments in Fluids* 36 (2):268-273
- Stamhuis EJ (2006) Basics and principles of particle image velocimetry (PIV) for mapping biogenic and biologically relevant flows. *Aquatic Ecology* 40:463-479
- van Duren LA, Stamhuis EJ, Videler JJ (1998) Reading the copepod personal ads: increasing encounter probability with hydromechanical signals. *Philosophical Transactions of the Royal Society of London Series B-Biological Sciences* 353 (1369):691-700
- van Duren LA, Stamhuis EJ, Videler JJ (2003) Copepod feeding currents: flow patterns, filtration rates and energetics. *J Exp Biol* 206 (2):255-267. doi:10.1242/jeb.00078
- Visser AW (2007) Biomixing of the oceans? *Science* 316:838-839
- von Rohden C, Ilmberger J (2007) Tracer experiment with sulfur hexafluoride to quantify the vertical transport in a meromictic pit lake. *Aquat Sci* 63:417-431
- Wüest A, Lorke A (2003) Small-scale hydrodynamics in lakes. *Ann Rev Fluid Mech* 35:373-412
- Wunsch C, Ferrari R (2004) Vertical mixing, energy, and the general circulation of the oceans. *Ann Rev Fluid Mech* 36:281-314

Three-dimensional modeling of nutrient transport in the Bay of Quinte

A. Oveisy^{1*}, L. Boegman¹, Yerubandi, R. Rao²

¹*Environmental Fluid Dynamics Laboratory, Department of Civil Engineering, Queen's University, Kingston, Ontario, Canada*

²*Environnement Canada, Water Sciences & Technology, National Water Research Institute, Canada Centre for Inland Waters, Burlington, Ontario, Canada*

*Corresponding author, e-mail a_oveisy@ce.queensu.ca

KEYWORDS

Bay of Quinte; water quality modelling; nutrient transport

EXTENDED ABSTRACT

Introduction

The Bay of Quinte suffers from eutrophication resulting from excessive nutrient loads. Horizontal transport and flushing through water exchange with Lake Ontario, to dilute the loads, is limited because of the 70 km long Z-shape of the bay. Since 1986 the Bay of Quinte has been considered as an Area of Concern in the Great Lakes basin by the International Joint Commission (IJC) and recommended a Remedial Action Plan (RAP). Several studies have been conducted by the RAP including observations and applying simple input-output models. Minns et al. (1986) divided the bay into three sections and computed whole bay and sectional budgets for phosphorous, nitrogen, and chloride. Moin and Thompson (2006) modeled the Bay of Quinte for prediction of water temperature. They used a hydraulic-temperature coupled model with a one-dimensional hydrodynamic model. Because horizontal transport and mixing is important in dilution of nutrients and it determines limiting nutrient concentrations for algal growth. The small rate of mixing in the Bay of Quinte results in long persistence of nutrients, which adversely affect lake biology. A high resolution three-dimensional hydrodynamic model is used in this research to study spatial and temporal variability in hydrodynamic conditions and horizontal dispersion of nutrients in the bay.

Methods

Previous studies have not applied a three-dimensional hydrodynamic model to account for the complexity of the flow in the bay. Here, ELCOM (a three-dimensional Estuary and Lake Computer Model) is applied to the bay in order to estimate horizontal advection and mixing using the release of passive tracers. The governing equations in ELCOM are the Reynolds-averaged Navier-Stokes with the assumption of hydrostatic pressure. It solves scalar transport equations to model temperature, and salinity distributions in space and time. Details of ELCOM can be found in the Hodges and Dallimore (2006).

The model was setup and run for ice free conditions of the year 2004 from day 133 to 303. The input data for the simulation were wind velocity, air temperature, relative humidity, precipitation from the Trenton Weather Station and solar radiation from the Integrated Learning Center, Queen's University. The model was initialized from rest with initial temperatures taken from three in-water measurement stations at Hay Bay (HB), Belleville (BV) and Napanee (N). The open boundary of the bay to the Lake Ontario was forced with

water level measured at the Kingston gauge station and simulated temperature profiles (Huang et al 2010). The horizontal grid spacing was 150 m by 150 m and the model had 39 vertical layers 0.65 m thick. The main tributaries (Trent River (TR), Moira River (MR), Salmon River (SR), Napanee River (NR) and Wilton Greek (WG)) have been included in the model. Tracers were released from the main tributaries to study horizontal mixing and advection in the bay. The modeling domain is depicted in Figure 1a.

Results and Discussion

The model was validated against moored temperature timeseries profiles at Big Bay (BB), and CTD temperature profiles at BV, HB, and N. Figure 1b, 1c shows comparison of the model vs. measurement at BB. The model result follows the measurement closely and no stratification is recognizable due to shallow depth at this location. Figure 2 compares the release of passive conservative tracers from TR, SR and NR after 170 days of simulation. At TR the water shed is about 12 times larger than NR or SR, which is about 900 km². Because the flow from TR is significantly higher than to other rivers and there is no significant exchange between the Lake Ontario and the water body at the very end of the bay, the concentration is high. Comparison of Figures 2b and 2c indicates that although the watersheds, for both of these rivers, are the same; because NR is under greater influence of flushing from Lake Ontario, lower concentrations are observed. This study showed that complex shape of the bay generates spatially varied hydrodynamic conditions, which result in low horizontal transport and high retention time in some parts of the bay. Nutrient load reductions, to improve water quality, should be directed at tributaries discharging to these regions. Future work will include full simulation of Bay of Quinte biogeochemistry.

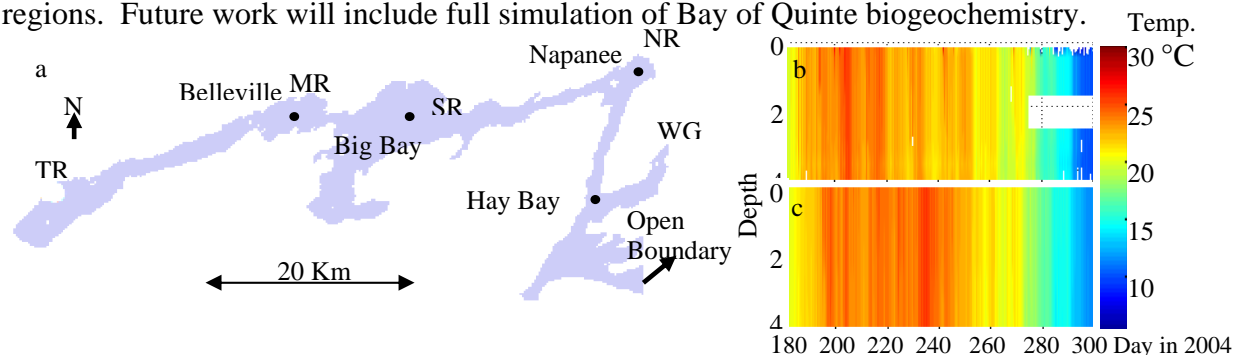


Figure 1. a, Model domain and measurement stations; Temperature profile at BB; b, measurement; c, model.

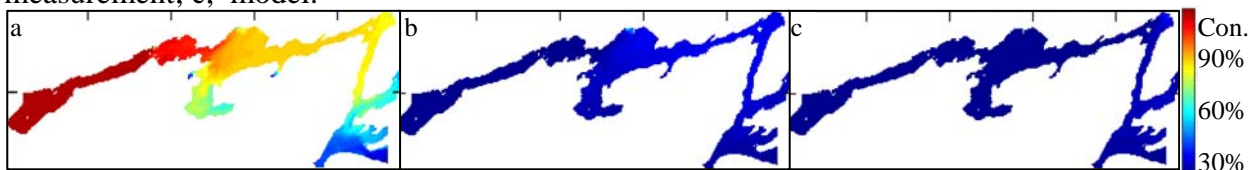


Figure 2. Concentration of passive conservative tracers released from: a, TR; b, SR; c, NR.

REFERENCES

- Hodges B. and Dallimore C. (2006), Estuary, Lake and Coastal Ocean Model: ELCOM Science Manual, Report, Centre for Water Research University of Western Australia.
- Huang, A., Rao Y.R. and Lu Y. (2010). Evaluation of a 3-D hydrodynamic model and atmospheric forecast forcing using observations in Lake Ontario. *J. Geophys. Res.* 115, CO2004.
- Minns C.K., Hurley D.A. and Nicholls, K.H. (1986). Project Quinte: point-source phosphorus control and ecosystem response in the Bay of Quinte, Lake Ontario. *Can. Spec. Publ. Fish. Aquat. Sci.* **86**: 270p
- Moin Syed M. A. and Thompson A. (2006). Long Term Water Temperature Modeling of the Bay of Quinte, Ontario. Proceedings of the 7th The International Conference on HydroScience and Engineering Philadelphia.

Modelling the transport of municipal, industrial and tributary discharges in eastern Lake Ontario and upper St. Lawrence River

Shastri Paturi¹, Leon Boegman¹, Sean Watt², Yerubandi R. Rao³

¹Department of Civil Engineering, Queen's University, Kingston, Ontario

²Cataraqui Region Conservation Authority, Glenburnie, Ontario

³National water Research Institute, Burlington, Ontario

Lake Ontario serves as a drinking water source and a sink for industrial, municipal and tributary discharges. In order to make optimum use of the water resource, the advection and mixing pathways of these wastes relative to the municipal drinking water intakes, needs to be understood, so the impact of the wastes can ultimately be minimised. In this study, the Estuary and Lake Computer Model (ELCOM) is applied to model the transport of passive tracers, as surrogates for waste discharges, surrounding the eight drinking water intakes in eastern Lake Ontario and upper St. Lawrence River. The model is validated against temperature and current profiler moorings, as well as satellite tracked drifters. To determine the impacts of physical forcing processes on contaminant transport, individual processes were switched off for model runs and results were compared to the original setup through flow visualization and cross-correlation. Mean cross-correlation coefficients of 0.67, 0.99, 0.91, 0.90, 0.98, 0.96 were calculated for no wind, no rotation, no hydraulic flow, no surface thermodynamics, and daily and 2 week averaged open-boundary water levels (removing forcing from surface seiches and storm surges, respectively), respectively. Surface wind forcing is, therefore, the dominant physical process driving contaminant transport in the region, followed by hydraulic flow through the St Lawrence River.

Chemical composition and conductivity/temperature/salinity/density relationships in freshwaters and seawaters

R. Pawlowicz^{1*}

¹*Dept. of Earth and Ocean Sciences, University of British Columbia, Vancouver, Canada, V6T 1Z4*

**Corresponding author: email rpawlowicz@eos.ubc.ca*

KEYWORDS

Aqueous solutions, Density, Electrical conductivity, TEOS-10

EXTENDED ABSTRACT

Recently, a new standard for the thermodynamic properties of seawater has been developed, the Thermodynamic Equation of Seawater 2010 (TEOS-10; IOC et al., 2010). This new standard provides thermodynamically consistent highest-quality estimates of all thermodynamic properties of seawater, including density, sound speed, heat capacity, enthalpy, chemical potential, and many others, and has many other advantages. TEOS-10 is also valid for very dilute seawaters, with mass fraction salinities typical of freshwaters, and thus should be useful in limnological situations. Here simple procedures are described which allow full chemical composition analyses and/or conductivity measurements obtained by conductivity-temperature-depth (CTD) probes to be used in conjunction with TEOS-10 to provide estimates of the salinity and of thermodynamic properties in the majority of limnological waters. This requires the definition of a useful salinity argument S_a into TEOS-10 functions, so that, e.g., $\rho = f_{TEOS10}(S_a, t, p)$.

METHODS

“True” densities and electrical conductivities are calculated for chemical compositions spanning a variety of limnological waters, over a range of temperatures, using the LIMBETA density model (Pawlowicz et al., 2010) and the LIMCOND electrical conductivity model (Pawlowicz, 2008). These estimates are then compared to densities calculated by using S_a as the salinity argument in TEOS-10, where various simple formulas are used to estimate S_a from either full chemical composition data, and/or measurements of electrical conductivity and a partial knowledge of the composition.

RESULTS AND DISCUSSION

Define the solution salinity $S_a^{\text{soln}} = \sum_i^N M_i c_i$ in which the c_i represent the actual measured concentrations (moles per kilogram of solution) of dissolved constituents and M_i their molar masses. Also define an ionic solution salinity S_a^{ionic} where the sum neglects $\text{Si}(\text{OH})_4$.

Physical properties from full chemical composition

In limnological waters in which the dominant anion is HCO_3^- or Cl^- (the vast majority of limnological waters), simply take $S_a \equiv S_a^{\text{soln}}$. If the dominant anion is HCO_3^- or Cl^- , but the mass of $\text{Si}(\text{OH})_4$ is greater than 10% of S_a^{soln} , then better results can be obtained by defining a density salinity S_a^{dens} as

$$S_a^{\text{dens}}/(\text{g/kg}) = 1.15 \times (S_a^{\text{ionic}}/(\text{g/kg})) + 50.6 \times ([\text{Si}(\text{OH})_4]/(\text{mol/kg})) \quad (1)$$

and taking $S_a \equiv S_a^{\text{dens}}$.

Physical properties from electrical conductivity measurements

Measurements of electrical conductivity should first be converted into TEOS-10 Reference Salinity S_R . This involves dividing the conductivity by 42914.0 $\mu\text{S}/\text{cm}$ to create a ratio R , calculating the Practical Salinity S_P using the Practical Salinity Scale 1978 (UNESCO, 1981) with the addition of a low-salinity correction (Hill et al., 1986) which extends its validity to dilute seawaters, and scaling this value (IOC et al., 2010):

$$S_R/(\text{g}/\text{kg}) = (35.16504/35) \times S_P \quad (2)$$

Then, in freshwaters whose dominant anion is HCO_3^- , the relationship

$$S_a^{\text{soln}}/(\text{g}/\text{kg}) = 1.6 \times (S_R/(\text{g}/\text{kg})) + 96 \times ([\text{Si}(\text{OH})_4]/(\text{mol}/\text{kg})) \quad (3)$$

can be used to estimate the solution salinity of the limnological water with an composition-dependent error of less than $\pm 20\%$. The scale factor of 1.6 will be somewhere between 1 and 1.6 if the dominant anion is SO_4^{2-} or Cl^- .

In order to obtain density and other thermodynamic properties using TEOS-10 in water whose dominant anion is HCO_3^- , calculate the conductivity-density salinity S_a^{CD} :

$$S_a^{\text{CD}}/(\text{g}/\text{kg}) = 1.8 \times (S_R/(\text{g}/\text{kg})) + 50.6 \times ([\text{Si}(\text{OH})_4]/(\text{mol}/\text{kg})) \quad (4)$$

Then, take $S_a \equiv S_a^{\text{CD}}$. The resulting density error is less than $\pm 0.1 \times (\rho - \rho_0)$ where ρ_0 is the density of pure water.

These relationships will be less valid for saline lakes which are high in Cl^- or SO_4^{2-} , and in dilute coastal lakes greatly affected by rainfall of marine origin (also often high in Cl^-). In these cases the properties must be either directly measured, or more detailed numerical modelling carried out.

References

- Hill, K. D., T. M. Dauphinee, and D. J. Woods (1986). The extension of the Practical Salinity Scale 1978 to low salinities. *IEEE J. Oceanic Eng. OE-11*(1), 109–112.
- IOC, SCOR, and IAPSO (2010). *The international thermodynamic equation of seawater - 2010: Calculation and use of thermodynamic properties*. Manual and Guides No. 56. Intergovernmental Oceanographic Commission, UNESCO (English). Available from <http://www.TEOS-10.org>.
- Pawlowicz, R. (2008). Calculating the conductivity of natural waters. *Limnol. Oceanogr. Methods* 6, 489–501.
- Pawlowicz, R., D. G. Wright, and F. J. Millero (2010). The effects of biogeochemical processes on oceanic conductivity/salinity/density relationships and the characterization of real seawater. *Ocean Sci. Discuss.* 7, 773–836.
- UNESCO (1981). Background papers and supporting data on the Practical Salinity Scale 1978. Unesco Technical Papers in Marine Science 37, Paris.

Internal wave activity and the distribution of plankton in the epilimnion Lake Opeongo, Canada.

P. Pernica^{1*}, M.G.Wells¹, W.G.Sprules²

¹ Department of Physical and Environmental Sciences, University of Toronto Scarborough,
1265 Military Trail, Toronto, ON, Canada, M1C 1A4

² Department of Ecology and Evolutionary Biology, University of Toronto Mississauga, 3359
Mississauga Rd, Mississauga, ON, Canada L5L 1C6

*Corresponding author, e-mail ppernica@physics.utoronto.ca

KEYWORDS

Internal waves; turbulence; Richardson number

EXTENDED ABSTRACT

In a lake, the epilimnion is the layer directly below the free surface that extends downwards to the strongly stratified seasonal thermocline region. In contact with the atmosphere, the epilimnion responds strongly to wind stresses and heat fluxes and due to its weak thermal stratification, it has been assumed to be homogeneously turbulent. However, numerous studies have shown that while the epilimnion is influenced by local meteorology, it does not necessarily have uniform properties, and often displays intermittent mixing and weak temperature gradients. Field data from Lake Opeongo (Ontario, Canada) demonstrate that the epilimnion was isothermal for only 34% of the 2009 summer, while for 28% of July and August there was a temperature difference over the depth of the epilimnion of $\Delta T \geq 2^\circ\text{C}$. During these periods of weak stratification within the epilimnion we observe evidence of internal waves in the temperature time series data. In this paper we investigate the occurrence of these waves, their relationship with values of gradient Richardson number Ri_g and the effect of these waves on the distribution of plankton in the epilimnion.

Blukacz et al. (2009) demonstrated a correlation between the patchiness of zooplankton in the epilimnion and wind speed in Lake Opeongo with a maximum patchiness observed to occur for wind speeds between 3-6 ms^{-1} . Previous studies have also shown that zooplankton and phytoplankton patchiness can result from the movement of internal waves due to the expanding and contracting layers and by causing aggregation above wave troughs and below wave crests (e.g Lennert-Cody and Franks (2002)). Analysis of mixing processes in Lake Opeongo indicates active mixing at $Ri_g < 0.25$ and a sharp decrease in mixing for $Ri_g \sim O(1)$. We suggest that for intermediate values of $Ri_g \sim 0.5$ we observe higher than basin scale frequency internal waves in the epilimnion.

The study was conducted during July and August 2009 in Lake Opeongo, a freshwater, dimictic lake located in Algonquin Provincial Park, Ontario, Canada. A string of 16 fast response thermistors, with one meter spacing in the first 7 m was placed adjacent to a moored ADCP recording every 2 seconds in 60 cm bins. The wind was predominantly from the west and the depth of the epilimnion was at 5–7.5 m during this study. Plankton sampling using an Optical Plankton Counter (OPC) was performed along 3 transects that intersected the location of the thermistor string and ADCP. The OPC was towed at a depth of 2.2 m below the surface. Coefficients of variation of zooplankton abundance were compared with values of Ri_g for intersection times.

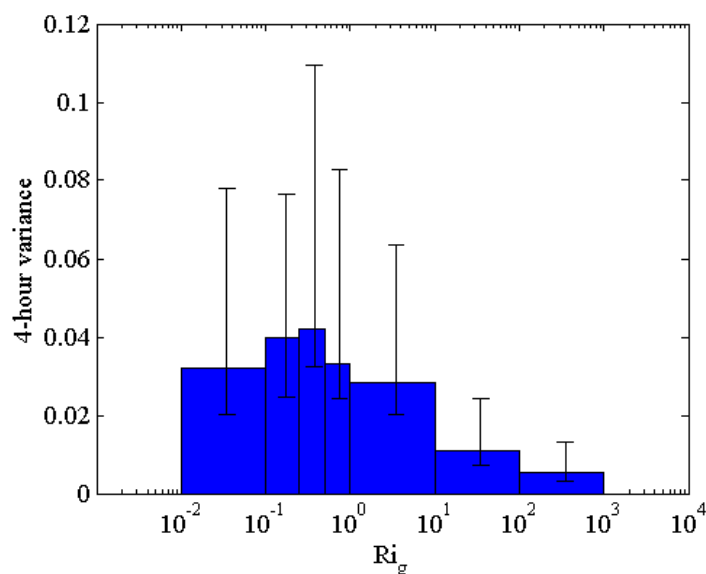


Figure 1: 4-hour variance of isotherm displacement as a function of Ri_g . The binned values of variance were averaged with error bars as the 25th and 75th quartile. The highest variance occurs for values of $Ri_g \sim 0.25-0.5$.

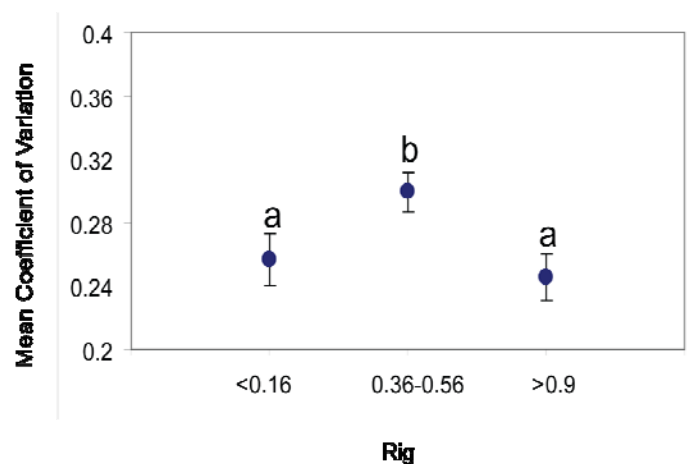


Figure 2: Mean coefficient of variation for small-bodied zooplankton as a function of Ri_g . Highest coefficients of variation occur for values of $Ri_g \sim 0.36-0.56$.

To quantify the effect of shorter than basin scale wave periods we remove wave periods longer than 4 hours from the specific isotherm. A four hour variance of these displacements is calculated. The resulting variances are compared to binned values of Ri_g . The binned values of variance were averaged with error bars as the 25th and 75th quartile (Fig.1). Highest values of variance occur for values of Ri_g between 0.25 - 0.5. Statistical analysis of zooplankton distribution show that small scale spatial variability of small zooplankton (268-450 μm) are greatest at intermediate $Ri_g \sim 0.36-0.56$ (Fig.2). We suggest that increased variance of isotherm displacement at moderate Ri_g values is linked to the increased variation of zooplankton at those values of Ri_g .

Blukacz E.A., Shuter, B.J. and Sprules, W.G. 2009. Towards understanding the relationship between wind conditions and plankton patchiness. *Limnology and Oceanography*, **54**(5): 2009, 1530–1540.

Lennert-Cody, C.E., and Franks, P.J.S. 2002. Fluorescence patches in high-frequency internal waves. *Marine Ecology-Progress Series*, **235**: 29-42.

A simplified model for deep water renewal in Lake Baikal

S. Piccolroaz^{1*}, M. Toffolon¹

¹ *Department of Civil and Environmental Engineering, University of Trento,
via Mesiano 77, 38123, Trento, Italy*

**Corresponding author, e-mail sebastiano.piccolroaz@ing.unitn.it*

ABSTRACT

In deep temperate lakes, thermobaricity (i.e. the decrease in the temperature of maximum density of fresh water with increasing depth) is the crucial physical property governing deep ventilation. If an external forcing is strong enough to mix and move the surface layers downward to a critical depth, thermobaric downwelling could be initiated and a portion of cold and oxygenated surface water freely sinks. The renewal of deep water determines significant effects on the ecobiology of the whole lake. Estimates of the sinking volume extension from the observations are often uncertain, suggesting that developing a modelling tool may be a challenging and worthwhile task.

A simplified one-dimensional numerical model has been developed to analyze the deep downwelling mechanism. Given a profile of the vertical diffusivity, the numerical model solves the reaction-diffusion equation for temperature and any other generic tracer C (e.g. dissolved oxygen, passive tracers, biological tracers). The pressure is assumed as hydrostatic, and a non-linear equation of state is used, which takes into account the effects of both pressure and temperature on water density. The downwelling occurrences (volume, arrival depth) are simulated given the seasonal cycle of surface layer temperature and a stochastic model for external forcing. Hence, variable volumes of surface water are forced to sink down to a given depth, depending on the available external energy input and the instantaneous temperature profile. These intrusions may determine an instability in the density profile that is handled by means of a Lagrangian algorithm, which at every temporal step checks the stability of the water column. Such a model, thanks to its simplicity, requires few input data and low computational efforts that make it suitable to perform long term simulations. Therefore, secular trends could be observed analyzing the numerical results obtained using different climate change scenarios.

The model has been calibrated and validated on the South Basin of Lake Baikal obtaining a good agreement between the numerical results and the temperature.

KEYWORDS

Deep ventilation; Downwelling; Lake Baikal; Thermobaricity; Numerical model.

INTRODUCTION

Deep ventilation in lakes is the renewal of hypolimnetic deep-water by mixing and/or replacement with surface water. This phenomenon shows important effects on the ecobiology of the whole lake since it is capable to enrich the hypolimnetic waters in dissolved oxygen and enhance the nutrients exchange along the entire water column.

Temperate lakes (i.e. lakes in which the surface water temperature passes through the temperature of maximum density $T_{\rho \max}$ twice a year) show two typical thermal stratification profiles: (a) an inverse, stable profile in the uppermost strata of the basin overlying warmer, stratified water during the cold season and (b) a regular stratified profile with temperatures decreasing with depth and always above $T_{\rho \max}$ during the warm season. Shallow lakes are mostly dimictic, that is they are characterized by two periods of global circulation of their water (once in autumn and the other in spring, when the surface water temperature approaches $T_{\rho \max}$). On the contrary, in the deepest temperate lakes typically only the surface layer turns over twice a year, while the deep-water is just occasionally and partially renewed.

In this work, the focus is on deep-water renewal mechanism that occurs in profound, temperate lakes. Lake Baikal (Siberia), the deepest and largest lake in the world in terms of volume, has been assumed as reference basin due to its importance and the dataset available. Observing Lake Baikal, Weiss et al. (1991) explained the deep-water renewal as a consequence of thermobaric instability, that is the property for which $T_{\rho \max}$ of freshwater (nearly 4°C at the atmospheric pressure) decreases with increasing depth. Therefore, if a volume of surface water (colder than the deep water) is pushed sufficiently in depth by an external forcing, beneath a certain depth it results denser than the surrounding water. Thus, it starts to sink freely until it reaches deep water having the same temperature (i.e. density) or until the very bottom of the lake. The depth at which the sinking surface water and the in situ water show the same density is known as compensation depth h_c (Weiss et al., 1991). For typical deep intrusions in Lake Baikal, h_c can be localized at about 250 m depth. For a detailed description of deep ventilation mechanism, see Weiss et al. (1991), Watts and Walker (1995) and Wüest et al. (2005).

Downwellings are likely to happen on occasion of the transition between the two seasonal stratification profiles, when the temperature gradient of the uppermost layer is small, and the energy required to mix and move the surface water volume until h_c is lower. The physical process responsible to provide the energy necessary to initiate deep downwellings has not been clarified completely, and several theories have been proposed: cabbeling instability of thermal bars (Shimaraev et al., 1993), dense water river inflow (Homann et al., 1997) and wind energy input (Weiss et al., 1991; Killworth et al., 1996; Botte and Kay, 2002; Wüest et al., 2005; Schmid et al., 2008).

In order to investigate the deep-water renewal mechanism and evaluate the extension and frequency of the sinking volumes, many data analyses have been conducted (Hohmann et al., 1997; Ravens et al., 2000; Peeters et al., 2000; Wüest et al., 2005; Schmid et al., 2008) and some numerical simulation adopting 2D or 3D models have been performed (Akitomo et al., 1995; Watts and Walker, 1995; Botte and Kay, 2002). Due to the big extension of Lake Baikal and the complexity of the physical phenomena taking place in its waters, the available data are usually not sufficient to apply complex statistical tools or use sophisticated thermo-hydrodynamic models. As a matter of fact, the main numerical works adopting 2D or 3D models have been performed referring to very schematic and/or partial domains and adopting simplified boundary conditions (in particular with respect to the wind forcing). Under these conditions, it is often difficult and uncertain to obtain a rigorous representation of the processes occurring in the real basin, suggesting the development of simplified numerical models as an interesting alternative that, besides, is perhaps more coherent with the few available data.

Therefore, a simplified one-dimensional model has been developed, which simulates deep ventilation triggered by thermobaricity occurring in profound lakes. The model requires a few data in input that, together with its simplified structure, permits both to reduce the need of

artificial parameterizations and to ensure a fast computational speed. The accuracy in the results is consistent with that of the input data.

In order to verify the consistency of the model, it has been applied to the case of the South Basin of Lake Baikal. The model has been calibrated by comparing numerical results with the available observation data of temperature (by courtesy of Prof. Alfred Wüest and his research team, EAWAG) and other tracers. Successively, the model has been validated through long-term (i.e. centuries) simulations, and the main variables (e.g. mean annual downwelling volume, typical downwelling temperature) have been estimated and compared to literature.

METHODS

A time-dependent, one-dimensional numerical model has been developed in order to study deep-water renewal occurring in profound, temperate lakes. The model solves a reaction-diffusion equation for the temperature by means of the usual backward Euler implicit finite difference scheme. Convection contribute is introduced by using two algorithms handling (a) the convection due to buoyancy within the unstable regions ($N^2 < 0$, where N^2 is the Brunt-Väisälä frequency) of the water column, and (b) the deep convection due to downwelling occurrences.

For the generic tracer C , the reaction-diffusion equation solved by the model is

$$\frac{\partial C}{\partial t} = -\frac{1}{S} \frac{\partial(S\phi)}{\partial z} + R, \quad (1)$$

$$\phi = -\left(D_z \frac{\partial C}{\partial z}\right), \quad (2)$$

where t is the temporal variable, z is the vertical coordinate defined positive downward (i.e. z is the depth), S is the horizontal surface at a fixed depth, ϕ is the vertical tracer flux, D_z is the diffusion coefficient, and R is the reaction term describing sources and sinks. In general all the parameters are dependent on the depth.

The non-linear Chen and Millero (1986) equation of state for freshwater has been used, in order to evaluate to high precision (better than 10^{-6} g/cm³) the main thermophysical properties of lake water required by the model (e.g. density ρ , specific heat capacity c_p , thermal expansibility α etc.):

$$\rho = \rho(T, P) = \rho_0 \left(1 - \frac{P}{K}\right)^{-1}, \quad (3)$$

where T is the water temperature, P is the pressure, $\rho_0 = \rho_0(T)$ is the reference density at the atmospheric pressure, and K is a function of T and P . Following Killworth et al. (1996) and Wüest et al. (2005), water salinity has been assumed to contribute little to the stratification of Lake Baikal, thus its contribution has been neglected in evaluating the thermophysical properties.

The pressure P has been assumed as hydrostatic:

$$\frac{dP}{dz} = \rho g, \quad (4)$$

where g is the gravitational acceleration. Hydrostatic approximation is convenient and justified to simulate long term dynamics (i.e. longer than the time scale of the single process) in which the instantaneous behavior is not of main interest.

Hereafter, the vertical displacement of water volumes (due to downwelling events and/or to water column stabilization) is assumed to follow an adiabatic path (i.e. the moving volumes do not exchange heat with the surrounding water) according to

$$\left. \frac{dT}{dz} \right|_{ad} = \frac{g\alpha(T + 273.15)}{c_p} = \Gamma, \quad (5)$$

where Γ is the adiabatic temperature gradient, which is known to be small, especially near $T_{\rho, max}$, where it vanishes. However, if stratification is weak Γ could assume values close to the real temperature gradient, gaining in importance for the thermal stability of the water column (for further details see Landau and Lifshitz, 1987; Osborn and LeBlond, 1974).

The numerical discretization of the physical domain follows a finite volume scheme which divides the water body into n sub-volumes having the same volume (thereby, in the most general case, having different vertical extension according to the hypsometric curve of the basin). The extent (thus, the number) of the sub-volumes is decided *a priori* trying to find an acceptable compromise between a good resolution of the results and a sufficiently high computational speed. In this work, the South Basin of Lake Baikal (having a depth of 1,461 m and a volume of about 6,300 km³) has been discretized into 159 sub-volumes that have a volume of 40 km³ and are characterized by a minimum, maximum and mean vertical extension of 5 m, 66 m and 9 m, respectively. A staggered grid has been used for the numerical solution of equation (1), in which the variable of the model (the generic tracer C) and the main thermophysical variables (α , ρ and c_p) are defined at the center of each sub-volume, while the diffusion parameter D_z is defined at the sub-volume interfaces. This approach allows one to calculate the fluxes at the sub-volumes' boundaries, thus implementing a mass-conservative scheme.

The model consists of three main components: (a) an algorithm handling the vertical stabilization in the case of buoyancy instability, (b) a Lagrangian-based algorithm handling the deep downwelling mechanism, and (c) the reaction-diffusion equation solver. Aimed at guaranteeing both little computational cost and good temporal resolution of the results, a time step Δt of half a day has been chosen ($\Delta t = 12$ h). Both the reaction-diffusion solver and the stability algorithm handling buoyant mixing are solved with this temporal step. On the contrary, the algorithm handling the deep ventilation mechanism uses a different time step, Δt_{down} , a multiple of Δt , which represents the temporal scale of the downwellings. At each time step Δt , the model follows the sequence of operations shown in Figure 1.

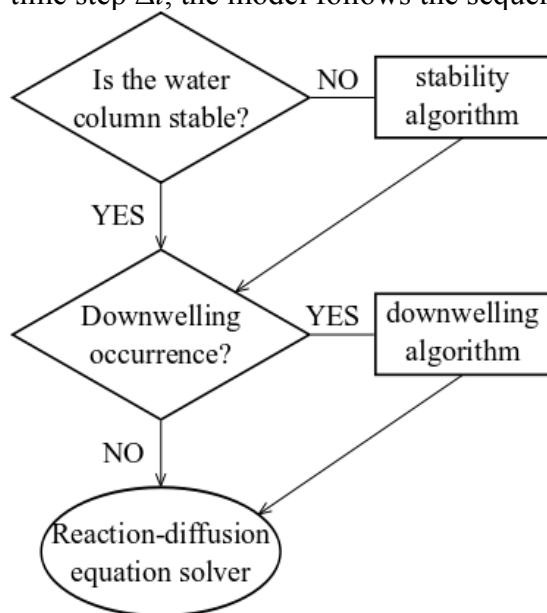


Figure 1. Block diagram of the model representing the sequence of the operations solved at each time step.

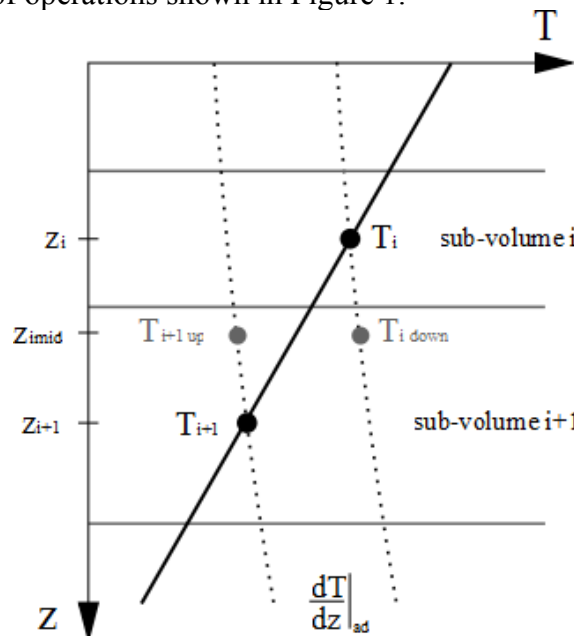


Figure 2. Sketch for the stability evaluation procedure: stable profile for $\alpha > 0$, $\Delta\rho(T, P)|_{z_{imid}} = \rho(T_{i+1 up}, P|_{z_{imid}}) - \rho(T_{i down}, P|_{z_{imid}}) > 0$.

Stability algorithm

At each time step Δt , the entire water column is tested for static stability by evaluating the density difference $\Delta\rho$ of each couple of neighbor sub-volumes i and $i+1$ (respectively centered in z_i and z_{i+1}) at their midpoint ($z_{i\ mid}$). The sub-volumes are ideally shifted towards $z_{i\ mid}$ following the adiabatic transformation Γ , and two new values of temperature are computed (see Figure 2): the temperature $T_{i+1\ up}$ of the lower sub-volume ($i+1$) displaced upward, and the temperature $T_{i\ down}$ of the upper sub-volume (i) displaced downward. Therefore, the density of each displaced sub-volume is computed with respect to the new temperature and pressure at $z_{i\ mid}$, and the local stability is evaluated according to the condition

$$\begin{cases} \Delta\rho(T, P)|_{z_{i\ mid}} > 0 \rightarrow \text{stable} \\ \Delta\rho(T, P)|_{z_{i\ mid}} = 0 \rightarrow \text{neutral} , \\ \Delta\rho(T, P)|_{z_{i\ mid}} < 0 \rightarrow \text{unstable} \end{cases} \quad (6)$$

where

$$\Delta\rho(T, P)|_{z_{i\ mid}} = \rho(T_{i+1\ up}, P(z_{i\ mid})) - \rho(T_{i\ down}, P(z_{i\ mid})) \quad (7)$$

Starting from the couple showing the higher instability, the whole water column is progressively stabilized by simply inverting the position of the unstable sub-volumes.

The rearrangement of the unstable regions is instantaneously performed at each time step. In this way, the vertical convection due to buoyancy is not represented exactly with its actual physical temporal scale (i.e. hours to days). Nevertheless, the overall vertical convection mechanism is suitably reproduced for long term analyses (i.e. weeks to years, the temporal scale investigated in this work) .

Downwelling algorithm

To handle the deep downwelling process, a Lagrangian-based algorithm is performed at each downwelling time step Δt_{down} . Each sub-volume is temporarily discretized in m homogeneous, smaller parts (hereafter sub-volume parts) having the same value of C as that of the initial sub-volume (in this work each sub-volume, $40\ km^3$, has been divided in 8 parts having a volume of $5\ km^3$). This allows one to model deep ventilation using a finer computational grid, with negligible increase of the computational cost. At each downwelling time step, probabilistic values of the external specific energy input, e_I , and the descending volume extension, V_{down} , are assigned by means of a stochastic approach. e_I and V_{down} are calculated from the wind speed and duration, which are randomly extracted from seasonal (i.e. winter and summer) probabilistic curves that can be constructed on the basis of large datasets. Given the temperature profile at that time, the downwelling temperature T_d and the compensation depth h_c are calculated respectively as: (i) the mean temperature within the active layer (corresponding to V_{down}), and (ii) the depth at which the sinking volume (that follows the adiabatic transformation Γ during its descent) shows the same density as the surrounding water. Note that, because of the typical thermal profile and the thermobaric effect, they usually have different temperatures (being the local and the descending water above and below the $T_{p\ max}$, respectively). Once T_d and h_c have been computed, the model calculates the energy per unit volume e_R that the descending water volume should have to overcome the buoyancy force and reach h_c . A number p of sub-volumes parts having a cumulative volume that matches V_{down} are displaced downward until a certain depth depending on the comparison between e_R and e_I . In case $e_I < e_R$ a shallow downwelling occurs and the p sub-volumes parts are displaced downward to a depth $h_s < h_c$. In this case the sinking water is lighter than the surrounding water and generates an unstable profile that is stabilized by the stability

algorithm at the beginning of the following time step. On the contrary, if $e_I > e_R$ a deep event occur and the p sub-volumes parts are displaced beneath h_c until local water having the same temperature of the sinking volume is reached or, when the intrusion is heavier than the deep water, until the very bottom of the lake. Once the downwelling is performed, the previous discretization is reestablished, re-combining together the sub-volumes parts in groups of m elements and computing the mean value of the generic tracer C for each group.

Heat equation solver

The last step is the solution of the reaction-diffusion equation (1) for the temperature and the other tracers (e.g. dissolved oxygen and CFC concentration). The backward Euler implicit scheme has been used, obtaining an unconditionally stable numerical solution. As a consequence, no restriction are needed for Δt . In order to guarantee both little computational efforts and good temporal resolution of the results, a Δt of half a day has been chosen.

The boundary conditions at the surface and at the bottom are respectively fixed (a) through the assignment of the superficial value of the tracer C according to measures (for the temperature) or analytical relationships (for the dissolved oxygen or the CFC's concentration), and (b) by the imposition of a Neumann condition at the bottom of the lake (geothermal heat flux for T , areal consumption rate for the dissolved oxygen, and no flux condition for CFC). Concerning the reaction term R in each vertical layer, this is has been calculated differently for each type of tracer: assuming the geothermal heat flux contribution at the sediment-water interface for T , estimating the volumetric and areal consumption rate for the oxygen along the water column, and assuming $R=0$ for the CFC.

RESULTS AND DISCUSSION

To apply the model to any particular case, it is necessary to first calibrate the main parameters: the seasonal probabilistic curves of wind speed and duration and the diapycnal diffusivity profile. Lake Baikal, the world's deepest and largest freshwater basin in terms of volume, has been assumed as case study. The model has been applied to the South Basin of the lake, where deep ventilation has been observed and studied during the last decades. The calibration has been performed comparing numerical simulations with measured profiles of temperature and a passive tracer (CFC₁₂) (data from Killworth et al. 1996; Peeters et al., 2000). Successively, the diapycnal diffusivity profile and the stochastic model for the wind forcing have been validated through a long-term (8 centuries) simulation. An additional validation of the model has been obtained by comparing the values of the calibrated parameters (i.e. diapycnal diffusivity profile) and the characteristic variables (i.e. mean annual downwelling volume, typical downwelling temperature) with estimates from literature. The calibration and validation procedures are discussed in detail in Piccolroaz and Toffolon (2011), while in this article the main results of a medium-term simulation are presented. The calibrated model has been applied to simulate a 50 years period, assuming the external conditions to remain the same (i.e. no climate change scenarios). The seasonal probabilistic curves of wind speed and duration have been built from the long-term observation dataset available in Rzhaplinsky and Sorokina (1977), while the surface temperature cycle has been obtained on the basis of a 9-year measurements dataset (2000-2009, courtesy of Prof. A. Wüest and his research team). In Figure 3, simulated temperature profiles are compared with measurements (from the available dataset, 2000-2009) in two typical winter and summer periods. Due to the stochastic approach used to model the external forcing, numerical results have been averaged over the last 10 years of simulation. The model allows for a quantitative estimate of the main characteristics of the deep ventilation mechanisms. The range of

temperature and volumes of deep downwelling events in Lake Baikal are reported in Table 1, where results from model are presented together with literature estimations. As a whole, the results are coherent with the existing measurements, which are however affected by non-negligible uncertainties. Finally, it is worth noting that the present model can be used to derive complete statistics of the downwelling events, which are not reported here for lack of space but will be examined in detail in Piccolroaz and Toffolon (2011).

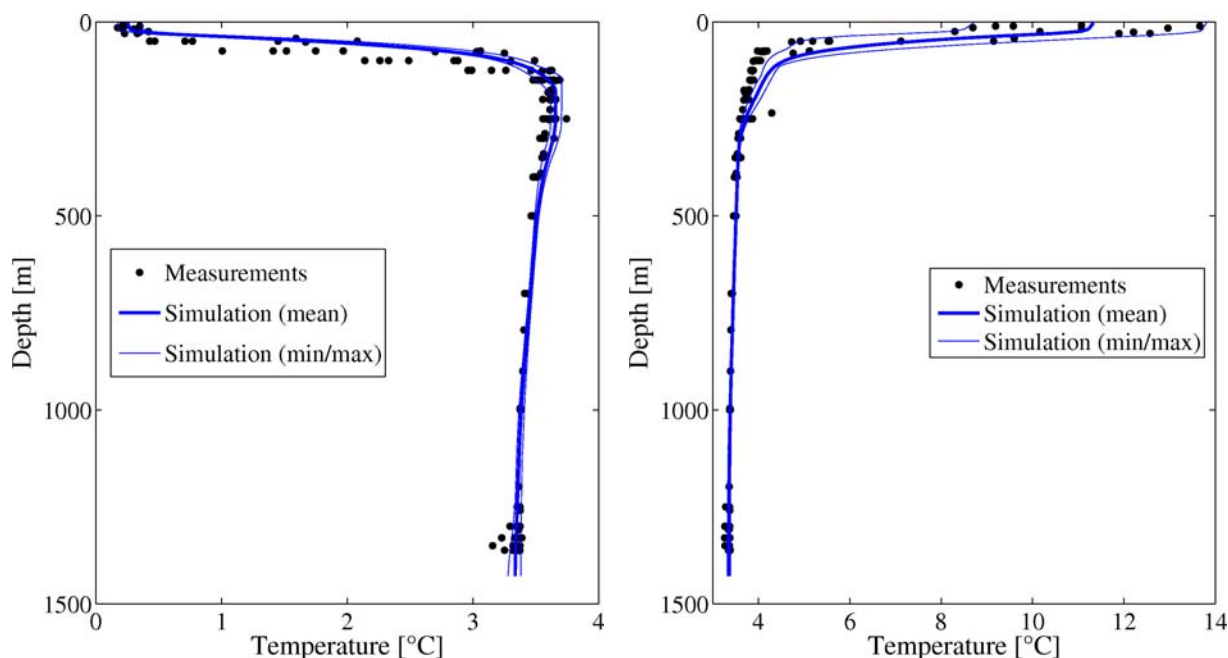


figure 3. Comparison between simulated and measured temperature profiles in winter (15 February 2000-2009, left) and summer (15 September 2000-2009, right). Numerical results have been averaged over the last 10 years of simulation.

Table 1. Comparison between numerical results and literature estimations of the main variables characterizing deep ventilation in Lake Baikal (all the variables refer to downwellings beneath 1400 m depth): mean annual downwelling volume \bar{V}_{down} and typical downwelling temperature T_{down} .

	T_{down} (°C)	\bar{V}_{down} (km ³)
Present model	3.17±0.11	80±30
Peeters et al., 2000	-	110
Wüest et al., 2005	3.15÷3.27	10÷30
Schmid et al., 2008	3.03÷3.28	50÷100 (winter season)

CONCLUSIONS

A simplified, one-dimensional numerical model has been presented that is suitable to analyze deep ventilation occurring in profound lakes. The model numerically computes the evolution of the vertical temperature profiles (and any other tracer) taking into account the stability of the water column and the occurrences of deep water intrusions. The model handles a few data in input (according to the reduced information often available for large basins) and shows a simplified structure. Together these features ensure a significant computational time saving, while the accuracy of the results is consistent with that of the input data.

In order to face the lack of wind data, a stochastic approach has been developed for the wind forcing, that is based on seasonal probabilistic curves for wind speed and duration. Long-term observational datasets are required to construct such probabilistic distribution.

The model has been calibrated and validated performing medium- and long-term simulations (from decades to centuries) over the South Basin of Lake Baikal. The numerical results show good agreement with measurements and literature estimates, and the model seems to simulate the deep ventilation phenomenon accurately.

Due to the considerable computational speed, the model is suitable to analyze the future behavior of the lake and its response to climate change scenarios, by performing long time simulations (i.e. hundreds of years). Moreover, further analysis could be focused on characterizing the implications of deep ventilation for the vertical distribution of dissolved oxygen, nutrients, biological components and other tracers.

ACKNOWLEDGEMENT

The authors would like to thank the research group headed by Prof. Alfred Wüest at EAWAG (Switzerland) for providing the temperature data used for the model calibration and for the stimulating discussions about the model. The work of the second author has been supported by the project DEWAX, cofunded by Provincia Autonoma di Trento and European Commission (Marie Curie actions, project Trentino - PCOFUND-GA-2008-226070, Researcher 2010 outgoing - Call 4).

REFERENCES

- Akitomo N., Tanaka K., Awaji K. and Imasato T. (1995). Deep convection in a lake triggered by wind: Two-dimensional numerical experiments with a nonhydrostatic model. *J. Oceanogr.*, **51**(2), 171-185.
- Chen C. and Millero F. (1986). Precise thermodynamic properties for natural-waters covering only the limnological range. *Limnol. Oceanogr.*, **31**(3), 657-662.
- Botte V. and Kay A. (2002). A model of the wind-driven circulation in Lake Baikal. *Dynam. Atmos. Oceans*, **35**(2), 131-152.
- Homann R., Kipfer R., Peeters F., Piepke G., Imboden D. and Shimaraev M. (1997). Deep-water renewal in Lake Baikal. *Limnol. Oceanogr.*, **42**(5), 841-855.
- Killworth P., Carmack E., Weiss R. and Matear R. (1996). Modeling deep-water renewal in Lake Baikal. *Limnol. Oceanogr.*, **41**(7), 1521-1538.
- Landau L.D. and Lifshitz L.M. (1987). *Fluid Mechanics*. Pergamon Press, New York.
- Osborn T.R. and LeBlond P.H. (1974). Comments on "static stability in freshwater lakes". *Limnol. Oceanogr.*, **19**(3), 544-545.
- Peeters F., Kipfer R., Hofer M., Imboden D. and Domysheva V. (2000). Vertical turbulent diffusion and upwelling in Lake Baikal estimated by inverse modelling of transient tracers. *J. Geophys. Res.*, **105**(C6), 3451-3464.
- Piccolroaz S. and Toffolon M. (2011). Deep ventilation in Lake Baikal: a simplified model for long-term simulations. In preparation for *Journal of Geophysical Research - Oceans*.
- Ravens T., Kocsis O., Wüest A. and Granin N. G. (2000). Small-scale turbulence and vertical mixing in Lake Baikal. *Limnol. Oceanogr.*, **45**(1), 159-173.
- Rzheplinsky G. and Sorokina A. (1977). Atlas of wave and wind action in Lake Baikal. Gidrometeoizdat (in Russian).
- Schmid M., Budnev N.M., Granin N.G., Sturm M., Schurter M. and Wüest A. (2008). Lake Baikal deepwater renewal mystery solved. *Geophys. Res. Lett.*, **35**(9).
- Shimaraev M.N., Granin N.G. and Zhdanov A. (1993). Deep ventilation of Lake Baikal waters due to spring thermal bars. *Limnol. Oceanogr.*, **38**(5), 1068-1072.
- Shimaraev M.N., Verbolov V.I., Granin N.G. and Sherstyankin P.P. (1994). Physical Limnology of Lake Baikal: A Review. Baikal International Center for Ecological Research, Irkutsk-Okayama.
- Watts S. and Walker R. (1995). A three-dimensional numerical model of deep ventilation in temperate lakes. *J. Geophys. Res.*, **100**(C11), 22,711-22,731.

- Weiss R., Carmack E. and Koropalov V. (1991). Deep-water renewal and biological production in Lake Baikal. *Nature*, **349**(6311), 665-669.
- Wüest A., Ravens T., Granin N., Kocsis O., Schurter M. and Sturm M. (2005). Cold intrusions in Lake Baikal: Direct observational evidence for deep-water renewal. *Limnol. Oceanogr.*, **50**(1), 184-196.

Plunging inflows and the summer photic zone, Kinbasket and Revelstoke reservoirs

Roger Pieters^{1,2*}, and Greg Lawrence²

¹ *Earth and Ocean Sciences, University of British Columbia, 6339 Stores Road,
Vancouver, BC, Canada V6T 1Z4*

² *Civil Engineering, University of British Columbia, 2002 - 6250 Applied Science Lane,
Vancouver, BC, Canada V6T 1Z4*

**Corresponding author, e-mail rpieters@eos.ubc.ca*

ABSTRACT

Kinbasket and Revelstoke reservoirs are part of the Columbia River in eastern British Columbia, Canada. Hydroelectricity from these large reservoirs represents about 30% of the province's generation capacity. Of interest to water use planning is the effect of reservoir operation on pelagic productivity. We address one part of this question, the resupply of nutrients carried by inflows that plunge below the photic zone during the summer. Using a water balance for the photic zone, three cases are considered: (1) a shallow outlet, (2) a deep outlet, and (3) a filling reservoir (no outlet). For (2) and (3), entrainment of surface water by the plunging inflow is important. With entrainment, inflows are made available to the photic zone; without entrainment nutrients remain in the deep water or short circuit to the deep outlets.

KEYWORDS

Reservoir, inflow, entrainment, photic zone, interflow, nutrients, productivity

INTRODUCTION

The operation of hydroelectric reservoirs, which were designed for power generation and flood control, is under increasing constraint for other concerns such as water supply, recreation and, the focus here, fisheries. At the same time, the flexibility of hydroelectric reservoirs is being recognized as a complement to other, less flexible, renewable energy sources such as wind and solar. Balancing these many concerns requires an understanding of the effect of reservoir operation on fisheries productivity. Here we tackle one small part of this complex question, by examining the supply of nutrients carried by tributary inflow to the photic zone during the summer. We examine tributary and reservoir temperature data for Kinbasket and Revelstoke reservoirs, which suggest that, in many cases, inflows plunge below the photic zone in summer. We then use a simple balance to determine the fraction of this inflow that ultimately enters the photic zone, and briefly sketch the implications for Kinbasket and Revelstoke reservoirs.

METHODS

Multidisciplinary surveys of Kinbasket and Revelstoke reservoirs were conducted from May to October in 2008-2010; see BC Hydro (2010, 2011) for further detail. Included were monthly

profiles of temperature, conductivity, PAR and other parameters using a Sea-Bird SBE19plus with a Biospherical QSP-2300L PAR sensor. Tributary temperature measurements were made with an Onset Tidbit or Hobo (± 0.25 °C), while spot measurements were made during tributary sampling (± 0.5 °C).

SITE DESCRIPTION

Kinbasket and Revelstoke Reservoirs are part of the Columbia River (Figure 1). The Columbia River begins near Columbia Lake, flows north, entering the Columbia Reach of Kinbasket Reservoir, and continues north to the main pool where it is joined by the Canoe Reach (Figure 1). At this point the Columbia River turns south, through Mica Dam and into Revelstoke Reservoir. Both reservoirs are long and narrow with steep sides, and fill former river valleys with the exception of a small pre-impoundment lake on the Columbia Reach. Both reservoirs have deep outlets. Characteristics of the reservoirs are given in Table 1.

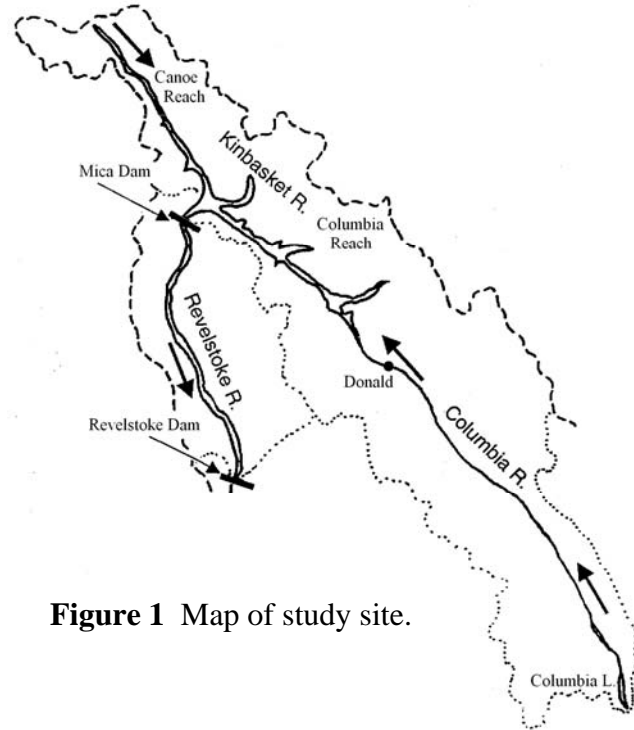


Figure 1 Map of study site.

The Columbia River at Donald, the largest inflow to Kinbasket Reservoir, provides only 31% of the inflow to Kinbasket, the remainder is provided by local tributaries. The flow of the Columbia at Donald is typical of natural flows in the region, with a large freshet peak of snow melt in spring that tails off gradually through summer (Figure 2c).

Table 1 Characteristics of the reservoirs

	Max. Depth (m)	Area (km ²)	Mean Outflow (m ³ /s)	Drawdown (m)	Drawdown Area (km ²)	Outlet Depth (m)
Kinbasket R. Mica Dam	~170	425	590	47	220	65
Revelstoke R. Revelstoke Dam	~120	115	750	1.5	2.4	28

The water level in Kinbasket Reservoir is drawn down in winter for hydroelectric generation (Figure 2a). From May to July, the water level rises as freshet inflow is stored to provide flood control downstream; during this time the outflow from Kinbasket Reservoir is low (Figure 2c). Once Kinbasket Reservoir has filled, the tail of the freshet is released, with increased outflow during August and September.

For Revelstoke Reservoir, the outflow from Kinbasket Reservoir provides the majority (71%) of the annual inflow. However, from May to July, when Kinbasket Reservoir is filling and outflow

from Kinbasket is low, the inflow to Revelstoke Reservoir is dominated by local inflows. Revelstoke Reservoir is operated run-of-the-river with little change in water level (Figure 2b).

The depth of the photic zone, determined from the 1% light level, varies from 15 to 25 m in Kinbasket and 10 to 20 m in Revelstoke (Figure 3a,b). The temperature at the 1% light level is shown in Figure 3c,d, along with the temperature at the surface and available tributary temperatures. As density is controlled primarily by temperature, tributary temperature sets the maximum depth to which the tributary can plunge in the reservoir. During plunging, entrainment of surface water would reduce the depth of neutral buoyancy, as discussed further below.

For Kinbasket, the temperature of the main inflow, the Columbia River at Donald, is relatively warm and would enter as a surface overflow or plunge within the photic zone until September when it cools more rapidly than the reservoir. In contrast, the local tributary inflows are quite cold, with the glacial fed Sullivan River averaging 5 °C through the summer. While not all of the tributaries are as cold as this, the available data, while limited, suggests that most inflows would plunge below the photic zone in the absence of significant entrainment.

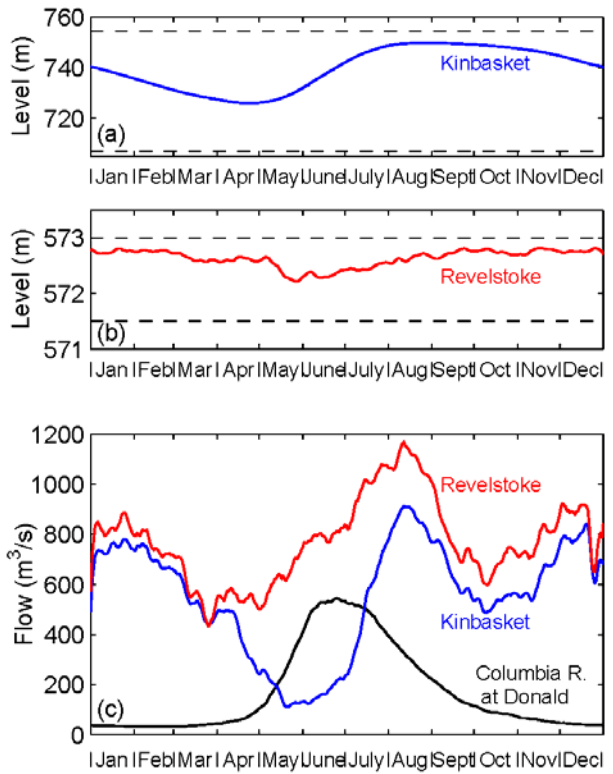


Figure 2 Average (a,b) level and (c) outflow for Kinbasket and Revelstoke reservoirs.

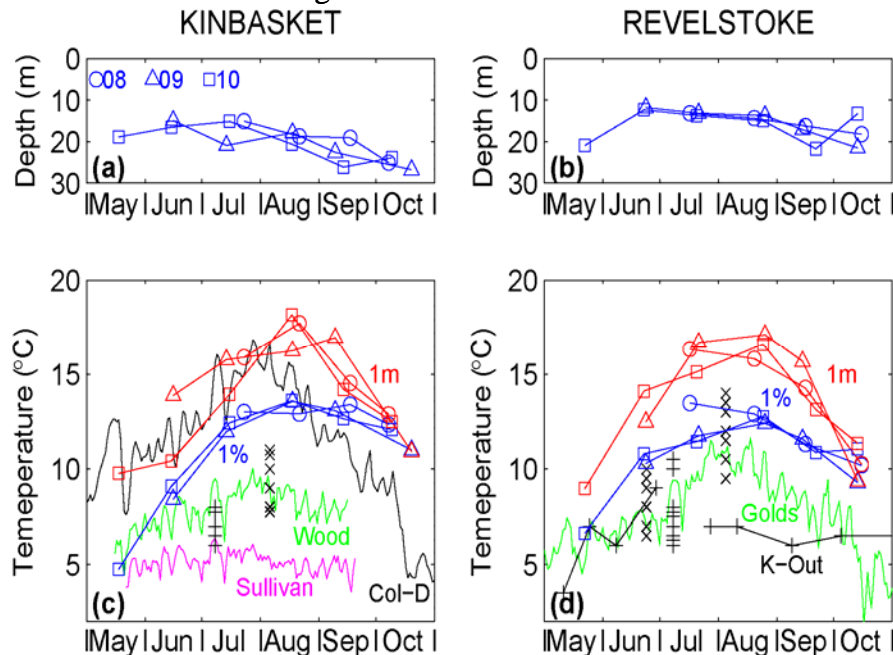
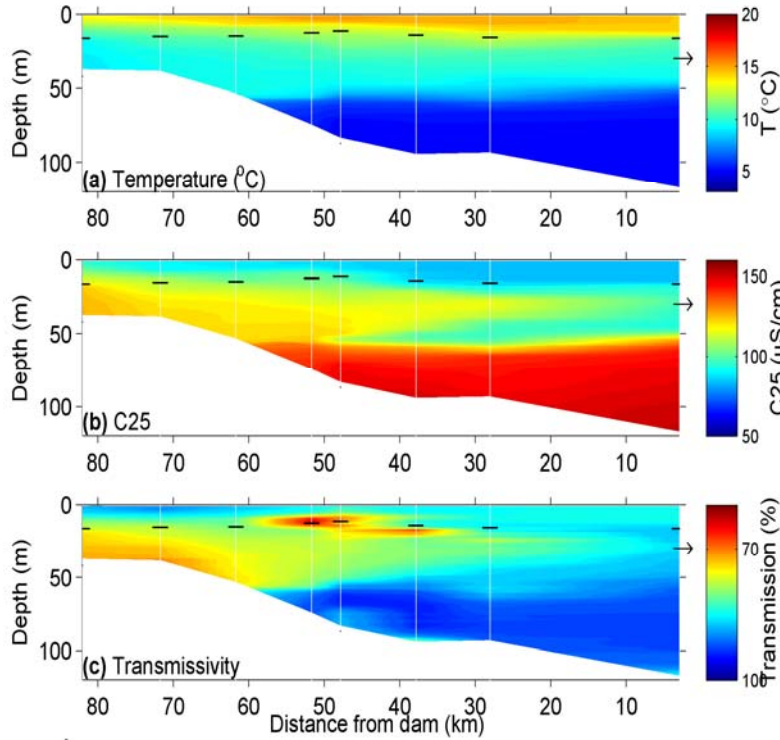


Figure 3 (a,b) Depth of the 1% light level, 2008-2010. (c,d) Temperature at (RED) 1 m, and (BLU) 1% light level, 2008-2010. Included are the daily average temperatures for the (c) Wood R., Sullivan R., Columbia R. at Donald, (d) Goldstream R. and Kinbasket outflow, 2010. Other tributaries (x) 2008, and (+) 2009.



For Revelstoke, the deep outflow from Kinbasket is cold (Figure 3d). Once outflow from Kinbasket increases in mid July, this cold inflow forms an interflow below the photic zone (Figure 4). Tributaries to Revelstoke Reservoir are warmer than those to Kinbasket; about half of the Revelstoke tributaries remained colder than the temperature of the 1% light level through summer (Figure 3d).

Figure 4 Interflow through Revelstoke Reservoir, 8-9 Sep 2008. The interflow between 15 and 60 m depth exits through the outlet marked at 28 m on the right. Dashes mark the base of the photic zone.

FATE OF INFLOW PLUNGING BELOW THE PHOTIC ZONE

Not including the Columbia River at Donald, many of the inflows to Kinbasket and Revelstoke Reservoirs are cooler than the temperature of the 1% light level and, neglecting entrainment, would plunge below the depth of the photic zone. Here we examine the fate of these inflows for a reservoir with (1) a shallow outlet, (2) a deep outlet, and (3) no outlet (reservoir filling).

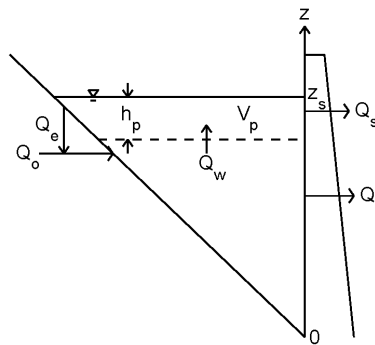


Figure 5 Reservoir schematic. Dashed line marks bottom of the photic zone. Q_w is the flow of water into the photic zone from below.

Figure 5 gives a schematic of a reservoir with inflow (Q_o), and outflow (shallow, Q_s , and deep, Q_d). The change in surface level, z_s , is given by,

$$\frac{dz_s}{dt} = \frac{1}{A(z_s)}(Q_o - Q_s - Q_d), \tag{1}$$

where $A(z)$ is the area, z is elevation, and t is time. The surface level rises when $Q_o > Q_s + Q_d$ and falls when $Q_o < Q_s + Q_d$.

Next, consider the volume of the photic zone,

$$\frac{dV_p}{dt} = Q_w - Q_s - Q_e, \quad (2)$$

where Q_w is the flux of water into the photic zone from below, and Q_e is the flow of shallow water entrained by the plunging inflow (Figure 5). The volume of the photic zone is given by,

$$V_p = \int_{z_s(t)-h_p(t)}^{z_s(t)} A(z) dz, \quad (3)$$

where $h_p(t)$ is the depth of the photic zone from the water surface. Differentiating (3) gives

$$\frac{dV_p}{dt} = A_s \frac{dz_s}{dt} - A_p \left(\frac{dz_s}{dt} - \frac{dh_p}{dt} \right),$$

where $A_s \equiv A(z_s)$ is the surface area, and $A_p \equiv A(z_s - h_p)$ is the area at the bottom of the photic zone. Using this and equation (1) we solve for the flux of new water into the photic zone, Q_w ,

$$Q_w = Q_s + Q_e + \left(1 - \frac{A_p}{A_s} \right) (Q_o - Q_s - Q_d) + A_p \frac{dh_p}{dt}. \quad (4)$$

The flux into the photic zone increases with shallow outflow, Q_s , and entrainment of water from the surface layer into the inflow, Q_e . The third term results from the bathymetry; as the reservoir fills, the original volume is spread shallower over a wider area; volume is added from below to maintain the photic zone at a given depth. This term goes to zero when the water level does not change, $Q_o - Q_s - Q_d = 0$, and for a reservoir with vertical walls, $A_p = A_s$. The fourth term gives the apparent flow into the photic zone as the depth of the photic zone, h_p , increases.

For Kinbasket Reservoir, the surface area for the region of active storage is can be approximated as $A = A_o - mh$, where $A_o = 425 \times 10^6 \text{ m}^2$ is the surface area at full pool, $m = 4.7 \times 10^6 \text{ m}$, and h is the draw down from full pool. The bathymetric factor, $(1 - A_p/A_s)$, then becomes $h_p/(A_o/m - h)$. For Kinbasket Reservoir with a photic zone depth of $h_p = 20 \text{ m}$, the bathymetric factor varies from 0.2 at full pool ($h = 0$), to 0.5 at minimum pool ($h = 47$).

Three cases For the first case, consider a shallow outflow, constant h_p , and constant water level; namely the reservoir is operated run-of-the-river with shallow outflow balancing inflow, $Q_o = Q_s$. In this case,

$$Q_w = Q_s + Q_e = (1 + E)Q_o, \quad \text{Case 1 (5)}$$

where the entrainment has been written in terms of an entrainment factor or dilution, $E = Q_e/Q_o$. This case is similar to a lake, where all of the inflow enters the photic zone as it upwells toward the shallow outlet.

In the second case for a deep outlet and constant water level,

$$Q_w = Q_e + A_p \frac{dh_p}{dt} = \left(E + \left(\frac{A_p}{Q_o} \right) \frac{dh_p}{dt} \right) Q_o. \quad \text{Case 2 (6)}$$

For h_p constant, the flow depends only on the entrainment, E . For $E = 0$, none of the inflow enters the photic zone, with all inflow passing directly to the deep outlet.

In the third case, consider no outflow and reservoir filling. In this case,

$$Q_w = \left(E + \left(1 - \frac{A_p}{A_s} \right) + \left(\frac{A_p}{Q_o} \right) \frac{dh_p}{dt} \right) Q_o. \quad \text{Case 3 (7)}$$

which is the same as Case 2, with the added bathymetric term.

Flux of nutrients To explore the flux of nutrients into the photic zone, we define the concentration of limiting nutrients in the inflow, C_o ; the concentration in the photic zone, C_p , which, for simplicity, we assume is depleted $C_p = 0$; and the concentration of the combined entrainment and inflow,

$$C_{in} = \frac{C_o Q_o + C_p Q_e}{Q_o + Q_e} = \frac{C_o}{1 + E}. \quad (8)$$

We assume that the depth of neutral buoyancy for this combined inflow is just below the depth of the photic zone, or, more reasonably, that the combined inflow plunges to any depth below the photic zone and that the concentration of nutrients in the deep water, $C_d \approx C_{in}$. In either case, the concentration of nutrients in the upwelling, $C_w \approx C_o / (1 + E)$.

Table 2 Flux from below, J_w , for 3 cases

Case	$J_w = C_w Q_w$
1. surface outflow, $dh_p / dt = 0$	$C_o Q_o$
2. deep outflow	$\left(\frac{E + \left(\frac{A_p}{Q_o} \right) \frac{dh_p}{dt}}{1 + E} \right) C_o Q_o$
3. no outflow, reservoir filling	$\left(\frac{E + \left(1 - \frac{A_p}{A_s} \right) + \left(\frac{A_p}{Q_o} \right) \frac{dh_p}{dt}}{1 + E} \right) C_o Q_o$

In the first case for a surface outlet, the flux of nutrients from below is, $J_w = C_o Q_o$ (Table 2), and, as expected, all nutrients pass into the photic zone. For the second case with a deep outlet, the flux depends only on the entrainment, E , when $dh_p / dt = 0$ (Table 2). As will be discussed further below, values of E range from 0 to 5. As E increases, more water is entrained, and upwelling increases; however, the water entrained from the photic zone is depleted in nutrients and dilutes the tributary inflow. The fraction of inflow nutrients entering the photic zone, $J_w / C_o Q_o = E / (1 + E)$ is only 0.5 at $E = 1$ (Figure 6). The third case, with a filling reservoir, has the added bathymetric term (Table 2). For Kinbasket Reservoir, consider $(1 - A_p / A_s) = 0.4$ and $dh_p / dt = 0$; this increases the fraction of inflow nutrients entering the photic zone especially at low E (Figure 6).

Up to now, we have neglected changes in the depth of the photic zone, h_p . In both Kinbasket and Revelstoke reservoirs, the depth of the photic zone increased over summer (Figure 3a,b). Consider Kinbasket at constant water level (Case 2), with $A_p \sim 300 \text{ km}^2$, $Q_o \sim 1,100 \text{ m}^3/\text{s}$ (freshet inflow), and $\Delta h_p \sim 10 \text{ m}$ over 3 months, which gives $(A_p/Q_o)dh_p/dt \sim 0.4$. The effect of this is like that of the bathymetric term in a filling reservoir, Figure 6. If both the photic zone was deepening and the reservoir was filling, then both terms would play a role.

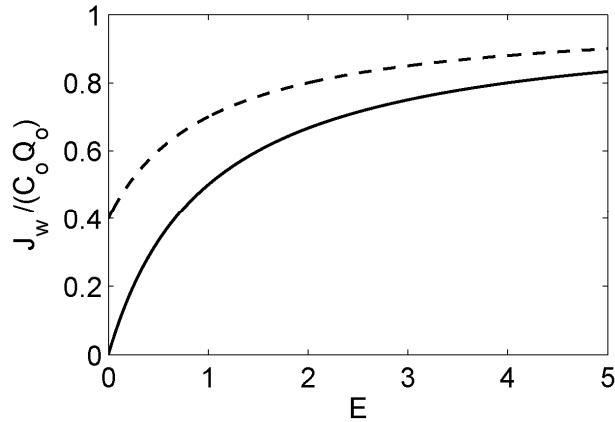


Figure 6 Fraction of total inflow nutrients reaching the photic zone as a function of the entrainment, E . **(solid)** Case 2 for a deep outlet and h_p constant. **(dash)** Case 3 for filling with h_p constant and $(1 - A_p/A_s) = 0.4$; or Case 2 with a deep outlet and increasing depth of the photic zone $(A_p/Q_o)dh_p/dt = 0.4$.

DISCUSSION

We consider the period mid-June to September when most tributary temperatures suggest plunging below the photic zone. Both reservoirs are temperature stratified during this time (Figure 3c,d) and, even though some cooling occurs in September, cooling does not deepen the photic zone until October. From mid-June to early July there is little release from Kinbasket, the reservoir fills, and Case 3 applies. During August and September, when the reservoir is near full pool, and the tail of the freshet is released from the deep outlet, Case 2 applies. For Revelstoke Reservoir, there is little change in the water level, outflow occurs from a deep outlet, and Case 2 also applies.

In both Case 2 and 3 the entrainment, E , is important to the upwelling of inflow nutrients. For the main inflow to reservoirs, the entrainment is typically small, $E < 0.3$ (Johnson et al. 1989). However, for tributary inflow to natural lakes, where the inflow is not constrained by the original river bed, the entrainment can be larger, and ranged, for example, from 0.4 to 5.1 in Fleenor and Schladow (2000).

For Kinbasket, 55% of the annual inflow occurs from mid-June to September. Of this 40% of inflow comes from Columbia at Donald, most of which will enter the photic zone except in September when a small fraction may go below the photic zone if entrainment is low. The remaining 60% of the inflow to Kinbasket is from local tributaries. For Revelstoke only 35% of the inflow occurs during this period, as the annual inflow is dominated by Kinbasket outflow during winter. However, from mid-June to September, 64% of the inflow to Revelstoke is from local tributaries. The dominance by local inflow during the summer in both Kinbasket and Revelstoke highlights the importance of characterizing tributary temperature and entrainment.

Of course, entrainment of surface water will increase the temperature of the net inflow and result in a shallower depth of neutral buoyancy. For example, Wood River with a summer mean temperature of 8 °C plunging through surface water of 16 °C, will reach the temperature at the base of the photic zone, 13 °C, with $E = 1.7$. For $E \geq 1.7$, Wood River would plunge into the photic zone. For E just below 1.7 the fraction of nutrients entering the photic zone would be 0.6 (Case 2, h_p constant). As a result, the fraction of nutrients entering the photic zone could increase suddenly with sufficient entrainment.

There are a number of other factors which could complicate the simple picture developed here. There is significant diurnal variation in stream temperature, typically several degrees, and stream inflows could plunge to varying depths over the course of a day. Other potential factors include diapycnal mixing and internal waves.

CONCLUSIONS

For a reservoir with a deep outlet (Case 2), inflow that plunges below the photic zone will short circuit the photic zone unless entrainment drives sufficient upwelling. For a reservoir that is filling (Case 3), inflow that plunges below the photic zone raises the elevation of the photic zone, and while there is a bathymetric effect due to the spreading of the photic zone, much of the inflow is stored in the deep water for release in winter.

ACKNOWLEDGMENTS

We are grateful to K. Bray for management of this project, and to B. Manson and P. Bourget for sample collection. We thank A. Akkerman, H. Keller and T. Moser for assistance with data processing. We gratefully acknowledge funding provided by B.C. Hydro.

REFERENCES

- BC Hydro. 2010. Kinbasket and Revelstoke Reservoirs Ecological Productivity Monitoring. Progress Report Year 1 (2008). BC Hydro, Water Licence Requirements. Study No. CLBMON-3. 140pp.
- BC Hydro. 2011. Kinbasket and Revelstoke Reservoirs Ecological Productivity Monitoring. Progress Report Year 2 (2009). BC Hydro, Water Licence Requirements. Study No. CLBMON-3. 266pp.
- Fleenor, W.E. and S.G. Schladow. 2000. Mixing in the plunge zone of lake inflows. Proceedings of the Fifth International Symposium on Stratified Flows, Vancouver, Canada, July 10-13, 2000, pp 307-312.
- Johnson, T.R., Ellis, C.R. and H.G. Stefan. 1989. Negatively buoyant flow in diverging channel, IV: entrainment and dilution. J. Hydraulic Engineering, 115(4), 437-456.

Seasonal variation of solitary wave properties

M. Preusse^{1,2*}, H. Freistuehler¹ and F. Peeters²

¹ Department of Mathematics and Statistics, University of Konstanz, Universitätsstraße 10, 78457 Konstanz, Germany (heinrich.freistuehler@uni-konstanz.de)

² Limnological Institute, University of Konstanz, Mainastr. 252, 78464 Konstanz, Germany (frank.peeters@uni-konstanz.de).

*Corresponding author, e-mail martina.preusse@uni-konstanz.de

KEYWORDS

DJL; instabilities; KdV; nonlinearity; solitary waves.

EXTENDED ABSTRACT

Introduction

Internal solitary waves (SW) propagating in association with a basin-scale seiche are a common phenomenon in many long lakes. Since the properties of SW such as phase velocity, wave length, energy, propagation depth, and nonlinearity depend on stratification, these waves change their typical appearance over the seasons. Nonlinearity is a particularly interesting wave property: From a modelling perspective, the degree of nonlinearity of SW is crucial to determine, whether the waves can be simulated reasonably well by the KdV equation or need to be simulated by a nonlinear approach, e.g. the DJL equation (given the waves are stationary). In particular a KdV model can only be applied to develop a closure scheme for hydrostatic water quality models in a lake, if the degree of nonlinearity of SW occurring in the field is small. From an ecological point of view, highly nonlinear waves with unstable shape, either breaking or carrying trapped cores, are an important phenomenon. E.g. the breaking of SW results in sporadic mixing events. Mixing will have prominent consequences during seasons, where nutrients are depleted in the upper layers of the water body and may initiate plankton patchiness. We analyse the variation of SW properties with special emphasis on seasonality. Especially the frequency of nonlinear processes is investigated. Seasonal prototypes of the measured waves are simulated using both the DJL and the stratified KdV equation in order to obtain a tool to differentiate between weakly and fully nonlinear waves and to demonstrate the influence of seasonal varying stratification.

Methods

In order to derive the seasonal varying wave characteristics we rely on a long-term temperature time series recorded in a subbasin of Lake Constance over a period of 6 years at a water depth of 145 m. A total of 219 wave trains were automatically extracted from the time series together with the wave properties of the leading soliton of each wave train (for details see Preusse *et al.*, in preparation). The nonlinearity index of a wave, which is defined as $nl=a/h$, where a is amplitude and h is a relevant depth scale, was estimated by applying the propagation depth as relevant depth. Here, propagation depth is defined as depth z , where isopycnal displacement, of the isopycne which is in rest at z , is maximal. Seasonal prototypes of measured solitons were simulated by the DJL equation (the code was generously provided by M. Stastna, see Stastna and Lamb, 2002) and the stratified KdV equation (as in Ostrovsky

and Stepanyants, 2005) for typical measured seasonal stratifications, assuming a zero background current.

Results and discussion

In Lake Constance, SW occur between April and November. The properties of these waves have a large variety (Figure 1). Observed amplitudes range between 2 and 30 m, wave trains contain between 1 and 25 SW, propagation depths vary between 1 and 50 m, nonlinearity indices between 0 and 10. In the case of propagation depths and nonlinearity indices the variation could partly be explained by the propagation direction. Another part of the variation could be attributed to season: Propagation depths significantly increase over the year, whereas waves are especially nonlinear in spring. These observations were confirmed by the simulated seasonal prototypes independently of the chosen model. This demonstrates that the seasonality of propagation depth and nonlinearity is triggered by stratification.

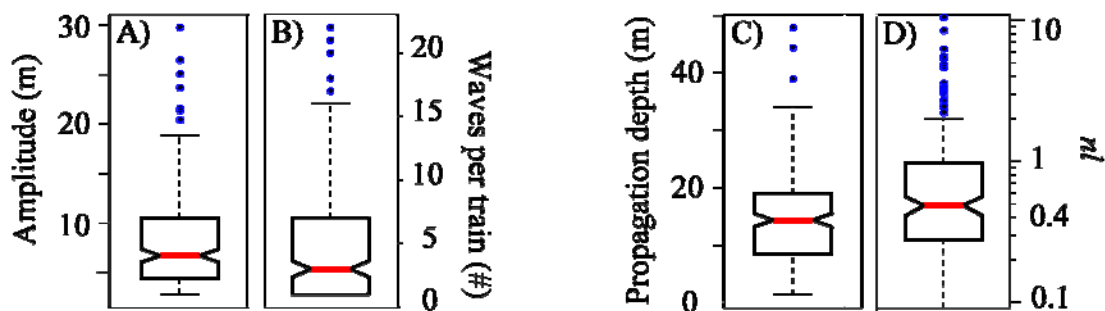


Figure 1. Boxplots of observed (A) amplitudes, (B) numbers of waves per train, (C) propagation depths and (D) nonlinearity indices. Note the lognormal scale in D.

However, the vertical profiles of DJL- und KdV- simulated solitons differ from each other, suggesting that the simulated wave prototypes are fully nonlinear. The corresponding measured seasonal mean and median nonlinearity indices lie between 0.4 and 0.5, indicating that a boundary of $nl = 0.4$ for weakly nonlinear waves, as obtained by Grue *et al.* (1999) in laboratory experiments, is rather generous in our case and probably leads to an underestimation of the amount of fully nonlinear waves in Lake Constance. Nevertheless a proportion of 60% of all SW has to be considered fully nonlinear according to this boundary. Moreover about 25% of wave trains and 15% of the leading waves were associated with density inversions, indicating either shear instabilities or trapped cores. An inspection of the corresponding solitons revealed that both phenomena occurred. The nonlinearity index corresponding to the leading wave turned out to be a good estimate of the probability of the occurrence of overturns associated with the leading wave or even the wave train: 99% of the leading waves with a nonlinearity index below 0.8 were stable with a growing probability of observing inversions above this value.

REFERENCES

- Grue, J., *et al.* (1999), Properties of large-amplitude internal waves, *J. Fluid Mech.*, 380, 257-278.
 Ostrovsky, L.A. & Stepanyants, Y.A. (2005), Internal solitons in laboratory experiments: Comparison with theoretical models., *Chaos*, **15** (3).
 Preusse, M, Freistuehler, H. & Peeters, F (in preparation), Seasonal variation of solitary wave properties.
 Stastna, M. & Lamb, K.G. (2002), Large fully nonlinear internal solitary waves: The effect of background current., *Physics of fluids*, **14** (9).

Relevance of inflow temperature variations over the daily cycle on tropical reservoirs physical limnology.

Ricardo Román-Botero¹, Andrés Gómez-Giraldo² y Mauricio Toro Botero³
Posgrado en Aprovechamiento de Recursos Hidráulicos - Universidad Nacional de Colombia
¹rroman@unal.edu.co; ²eagomezgi@unal.edu.co; ³fjmtoro@unal.edu.co

Measurements of temperature, salinity and suspended solids concentration of the inflows of tropical reservoirs located around 2100 meters above sea level reveals that the inflow density changes are dominated by the temperature changes, which were as high as 6°C over a 6-hour period. Temperature profiles measured through the water column during the field campaigns show surface-to-bottom temperature variations close to 6°C too, with the minimum and maximum temperatures in the profile being close to the minimum and maximum temperatures in the inflows. We also observed that in tropical reservoirs it is difficult to identify a well defined epilimnion, metalimnion and hypolimnion vertical structure. Instead, relatively similar vertical temperature gradients are observed over most of the water column with somehow larger buoyancy frequency values at particular depths. Although some changes are observed in the surface temperature through the year, this continuous stratification pattern was always observed. Because the similarity between the temperature range in the water column and the temperature range of the inflows over the daily cycle, and the gradual vertical variation of temperature in the reservoir, the density current changes its level of intrusion over most of the depth range over a daily cycle. As this may have an important effect over water quality, we suggest that recording the inflow temperature continuously is very important in order to address properly the functioning of tropical ecosystems. This issue, which usually does not have a big relevance on temperate lakes, as well as the particular stratification pattern, is some of the elements that must be addressed when studying tropical physical limnology.

Impact of climate change on Cannonsville reservoir thermal structure in the New York City Water Supply

Nihar R. Samal¹, Don Pierson², Yongtai Huang¹, Jordan S. Read³, Aavudai Anandhi¹, and Emmet M. Owens⁴

¹*CUNY Institute for Sustainable Cities, Hunter College, City University of New York,
695 Park Ave. New York, NY 10065, USA*

²*New York City Dept. Environmental Protection, 71 Smith Ave, Kingston, N.Y. 12401 USA*

³*University of Wisconsin-Madison, Civil and Environmental Engineering, Environmental Fluid Mechanics
1415 Engineering Dr Rm 1261, Madison, WI 53706, USA*

⁴*Upstate Freshwater Institute, P.O. Box 506, Syracuse, NY 13214 and Adjunct Professor, Dept. of Civil and
Environmental Engineering, Syracuse University, Syracuse, NY 13244, USA*

KEYWORDS

Thermal structure, mixing, 1-D hydrodynamic model, New York City Water Supply, climate change

EXTENDED ABSTRACT

The thermal structure of lakes and reservoirs is an important regulator of biogeochemical processes, and a property that is well simulated using mechanistic hydrodynamic models. A one-dimensional reservoir model is applied to examine the thermal structure in a deep reservoir that is located, approximately more than 100 miles northwest of New York City, and is an important part of the New York City water supply. Other studies have used a variety of one dimensional models to explore the potential impact of climate change on lakes and reservoirs, including studies undertaken by Arvola et al. (2009), Jones et al. (2009), MacKay, et al. (2009), Borowiak et al. (2008), Markensten and Pierson (2007), Hondzo and Stefan (1991). These studies mainly involved sensitivity analyses run time over long scales. Few studies have been carried out using climate change scenarios obtained from General Circulation Models (GCMs).

In the present investigation, data from three GCMs (CGCM3, ECHAM & GISS) were run for each of three emission scenarios (A1B, A2 and B1) for the 2081-2100 future period. Using a monthly change factor methodology (as described in Anandhi et al., 2011), GCM simulated values of mean daily air temperature, wind speed and solar radiation were used to produce change factors that were applied to a 39 year record of local meteorological data to produce future scenarios to drive the reservoir models. Future climate scenarios derived from the same GCMs and using the same change factor methodology were also used to drive the Generalized Watershed Loading Functions-Variable Source Area Model (GWLF-VSA Schneiderman et al., 2007) in order to simulate reservoir tributary inflow. GWLF-VSA is a lumped parameter model based on the original GWLF model (Haith and Schoemaker, 1987) that simulates daily stream flow discharge and monthly sediment and nutrient loads at a watershed scale. The one-dimensional reservoir model consists of three components: (1) a hydrothermal sub-model, (2) nutrient sub-models, and (3) a phytoplankton sub-model based on the PROTECH model (as described in Reynolds et al., 2001).

This paper deals mainly with the output of the hydrothermal sub-model which simulates the vertical dynamics of reservoir thermal stratification and related transport regimes, based on changes in such

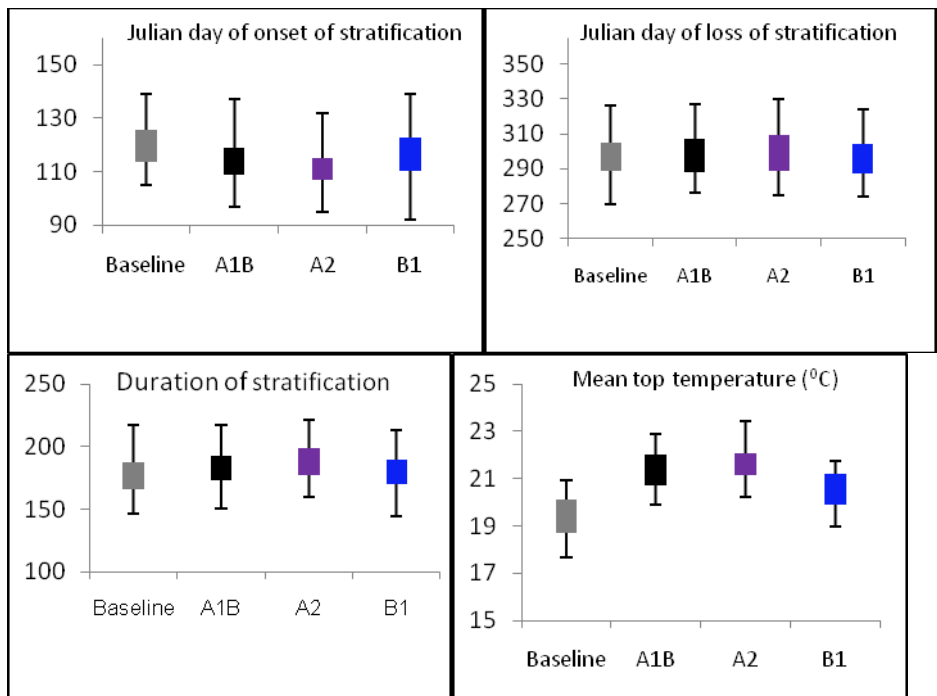
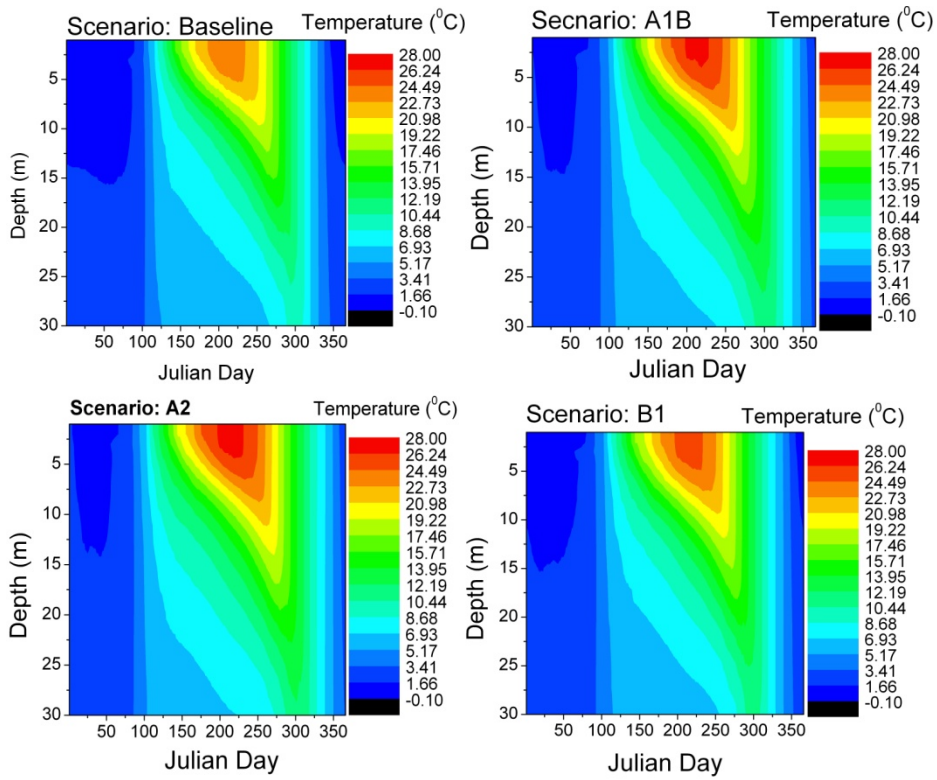
critical (state) variables as meteorological, hydrological and operational conditions. Comparisons between simulations based on present day climate data (baseline conditions) and future simulations (change factor adjusted baseline conditions) are used to evaluate the development and breakdown of thermal stratification, as well as a number of metrics that describe reservoir thermal structure, stability and mixing. General features of the simulated changes in thermal structure are evident in the isopleths diagrams in Figure 1. These are constructed for each future scenario from a yearly matrix (day 1-365) of mean daily (n=39) temperature profiles. These temperature isopleths, based on average scenario conditions, suggest that in the future the onset of stratification will begin earlier and end later resulting in a longer period of stratification, particularly under the A1B and A2 emission scenarios that predict greater increases in atmospheric CO₂. The vertical extent of stratification is deeper, and epilimnetic temperatures are also warmer during the future scenarios and again these changes are more pronounced for the A1B and A2 scenarios. Comparing all climate scenarios shows that between 32%-80% of a year undergoes stronger and deeper stratification, as defined by the temperature difference between surface and bottom ($\Delta T = T_s - T_b$) that ranged between 9 to 22 °C. There is a substantial increase in both surface and bottom temperatures under different future climate scenarios.

The daily vertical temperature profiles output from the model and the daily wind speed over the simulation time period was further processed using the Lake Analyzer program (described and developed by Read, J.S., et al., (2011) to calculate Schmidt stability, Lake number and buoyancy frequency on daily basis. The Schmidt stability (St), which is the resistance to mechanical mixing due to the potential energy in the stratification of the water column was first defined by Schmidt (1928) and later modified by Hutchinson (1957), describes the strength of density stratification. Here the mean Schmidt stability is maximum for A1B and A2 scenarios. As the stability increases due to gradual warming of the surface waters, and the so called centre of gravity of the system moves deeper into the water column as a result of vertical differences in density. The Lake number (Ln), defined by Imberger and Patterson (1990) is a quantitative index of the dynamical stability of the water column and shows the extent of deep turbulent mixing. A higher lake number indicates that the deep turbulent mixing is minimal. The extent deep turbulent mixing is reduced during A1B and A2 scenarios as compared the present climate conditions, which is in agreement with the higher Schmidt stability - the stronger stratification dominates the forces introduced by the surface wind energy. The buoyancy frequency (N^2), which represents the local stability of the water column based on the density gradient is given by $N^2 = (g/\rho) (\partial\rho/\partial z)$. The stable and the stronger stratification for the A1B and A2 scenarios reduces vertical mixing, and the mixing at the surface is of limited vertical extent. These projections of warmer water temperature and longer duration of stratification under future conditions, as indicated by these metrics, could potentially result in an increase in the net heat flux to the hypolimnion and reduced availability of dissolved oxygen.

References

1. Anandhi A, Frei A, Pierson DC, Schneiderman EM, Zion MS, Lounsbury D, Matonse AH. 2011. Examination of change factor methodologies for climate change impact assessment. *Water Resources Research* **47**: W03501, DOI:10. 1029/2010WR009104.
2. Arvola, L., George, G., Livingstone, D.M., Jarvinen, M., Blenckner, T., Dokulil, M.T., Jennings, E., Aongusa, C.N., Noges, P., Noges, T. and Weyhenmeyer, G.A. 2009. The impact of changing climate on the thermal characteristics of lakes, D.G. George (ed.) *The impact of climate change on European lakes*, Aquatic Ecology series 4, DOI 10.1007/978-90-481-2945-4_6, Springer, pp. 85-101.
3. Borowiak, D., Baranczuk, J. and Nowinski, K. 2008. The directions of the thermal stratifications of upper Radunskie lake as a result of observed climatic changes., Balwois 2008-Ochrid, Republic of Macedonia-27, 31 May 2008.

4. Hondzo, M. and Stefan, H.G. 1991. Three case studies of lake temperature and stratification response to warmer climate, *Water Resources Research*, Vol. 27, No. 8, pp-1837-1846.
5. Jones, I, Sahlberg, J. and Persson, I. 2009. Modelling the impact of climate change on the thermal characteristics of lakes, D.G. George (ed.) *The impact of climate change on European lakes*, Aquatic Ecology series 4, DOI 10.1007/978-90-481-2945-4_6, Springer, pp. 103-120.
6. Markensten, H. and Pierson, D. (2007). Weather driven influences on phytoplankton succession in a shallow lake during contrasting years: application of PROTBAS. *Ecological Modelling* 207, 128-136.
7. MacKay, M. D., Neale, P. J., Arp, C. D., Senerpont Domis, L. N. De., Fang, X., Gal, G., Johnk, K. D. G. Kirillin, Lenters, J. D., Litchman, E., MacIntyre, S., Marsh, P., Melack, J., Mooij, W. M., Peeters, F., Quesada, A., Schladow, S. G., Schmid, M., Spence, C. and Stokes, S. L. Modeling lakes and reservoirs in the climate system *Limnol. Oceanogr.*, 54(6, part 2), 2009, 2315–2329.
8. Read, J.S., et al., Derivation of lake mixing and stratification indices from high-resolution lake buoy data, *Environmental Modelling & Software* (2011), doi:10.1016/j.envsoft.2011.05.006
9. Reynolds, C.S., Irish, A.E. and Elliott, J.A. (2001). The ecological basis for simulating phytoplankton responses to environmental change (PROTECH). *Ecological Modelling* 140, 271-291.
10. Schneiderman EM, Steenhuis TS, Thongs DJ, Easton ZM, Zion MS, Neal AL, Mendoza GF, Walter MT. 2007. Incorporating variable source area hydrology into the curve number based Generalized Watershed Loading Function model. *Hydrological Processes* **21**:3420–3430.



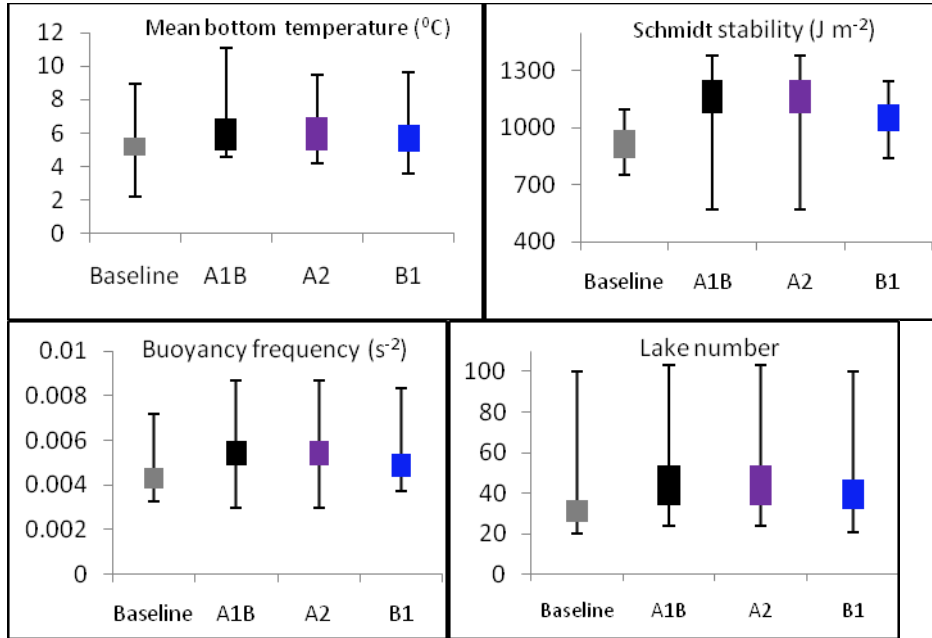


Figure 1 . The top row shows average temperature isopleths diagrams for each baseline and future climate scenario. These are created by averaging the daily profile data associated with the baseline simulation and daily pooled data associated with the GCM scenarios. Box plots are likewise created using daily data from the baseline scenario and pooled daily data from all GCM derived scenarios

A study of sedimentary oxygen demand with large-eddy simulation: from large-scale hydrodynamics to small-scale mixing processes

Carlo Scalò¹, Ugo Piomelli¹ and Leon Boegman²

Department of Mechanical and Materials Engineering, Queen's University, McLaughlin Hall, 130 Stuart Street, Kingston K7L3N6, Ontario, Canada¹

Department of Civil Engineering, Queen's University, Ellis Hall, 58 University Avenue, Kingston K7L3N6, Ontario, Canada²

We implemented a bio-geochemical model for dissolved oxygen (DO) transfer from water to underlying organic sediment beds coupled with Large-Eddy Simulation (LES) of turbulent transport on the water side. In this technique the larger turbulent eddies, that are dependent on the initial and boundary conditions, are directly resolved by the grid, whereas, the mixing due to the smaller (sub-grid) scales, whose evolution is believed to be universal, is modeled. The oxygen concentration field is modeled as a high-Schmidt-number ($Sc \gg 1$) passive scalar which is absorbed across the sediment-water interface (SWI) by an organic sediment layer. The complete model has been validated by reproducing fluid dynamic conditions for different flow rates and temperatures tested in a laboratory recirculating flume where complete (water and sediment) DO measurements were obtained from micro-sensor data [O'Connor et al. *Limnol. Oceanogr.* 53(2), 2008]. The numerical predictions show good agreement with the observations, especially at low/intermediate Reynolds numbers [Scalò et al. Submitted to *JGR-Oceans*]. The model relies on a new numerical strategy for the coupling of the discretized governing equations across the SWI which allowed its extension to a well-established eddy-resolving numerical technique such as LES. The mathematical and numerical setup so obtained helped us define the limitations of present oxygen transfer models and the sensitivity of the results to difficult-to-measure model parameters. Also, there is the need to develop a process-oriented parameterization of the sedimentary oxygen demand (SOD) based on resolvable flow features in the near-wall region. At the moment, there is no mechanistic model for SOD based on parameters resolved in currently adopted RANS models used for water-quality monitoring and management; SOD is set (to a fixed value) such that modeled DO concentration matches in-situ observations. These models would considerably benefit from this parameterization, which is only possible by accurately capturing the (turbulent) transport dynamics on the water-side.

Following the aforementioned validation phase, we performed a preliminary parametric study by looking at oxygen absorption dynamics in a statistically steady flow in an open channel configuration. The main purpose is to highlight the role of the Schmidt number (controlling the intensity of diffusive transport across the SWI) and the Reynolds number (controlling the wall-shear stress). The main result of this analysis is shown in Figure 1 where the Sherwood number (a normalization for the SOD) is plotted against the friction Reynolds number, for different Sc . Either decreasing Sc or increasing the wall-shear stress increases the SOD. The semi-empirical mass transfer law based on the surface-renewal theory [Boudreau, B., and B. Jørgensen, Oxford University Press, USA 2001] systematically overestimates the DO absorption rate with respect to LES. Analogous effects of changes in the wall-shear stress can be observed at an instantaneous level in a statistically unsteady flow such as a regularly oscillating boundary layer. The time-series of the oxygen concentration level at the SWI and the corresponding wall-shear stress, driven by an oscillating current of a period of 10 min and intensity of 10 cm/s for $Sc = 650$, is shown in Figure 2. The low oxygen diffusivity (high Sc number) determines a time lag between the peak of the wall-shear stress and the increase in the DO flux across the SWI whose effects are evident in the (instantaneously) increased value of DO concentration at the SWI.

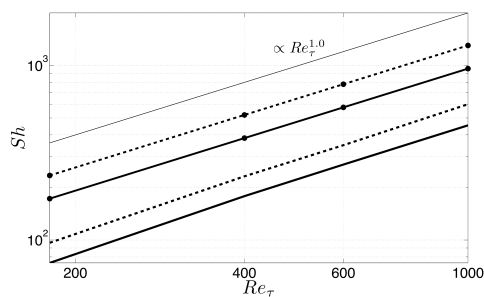


Figure 1: Sherwood number plotted against friction Reynolds number. Results are for $Sc=200$ (solid line) and $Sc=500$ (dashed line). Correspondent prediction from the surface renewal theory for $Sc=200$ (solid line with filled circles) and $Sc=500$ (dashed line with filled circles).

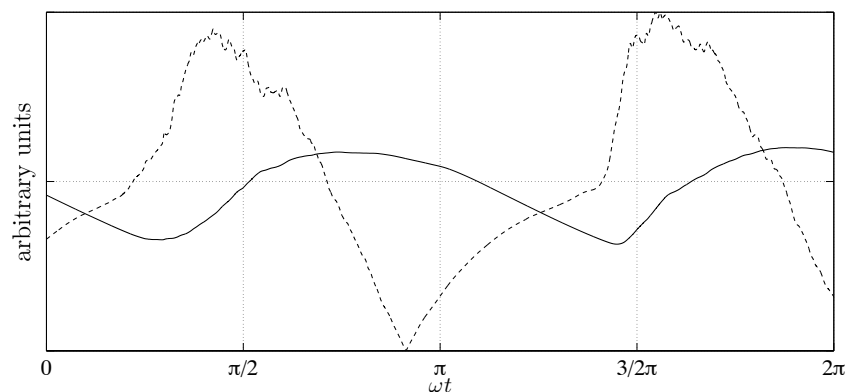


Figure 2: Time-series of wall-shear stress (dashed line) and oxygen concentration at sediment-water interface (solid line) over an oscillatory cycle period.

Some Applications of Lagrangian (Particle Tracking) Methods in Hydrodynamic Modeling

David J. Schwab

NOAA Great Lakes Environmental Research Laboratory, 4840 South State Road Ann Arbor, MI 48108

David.Schwab@noaa.gov

Lagrangian (particle tracking) methods can offer significant advantages over Eulerian (fixed frame of reference) methods for certain fluid flow problems. This presentation will discuss several applications where particle tracking has been used to provide useful results in hydrodynamic modeling problems. These include calculation of residence time in complex flow systems, simulation of material dispersion in high gradient flows, and tracking of biological organisms. Each of these problems is associated with a practical application in the Great Lakes. Possible future applications for combining particle tracking methods with agent-based models will also be discussed.

Application of a multi-nested ocean circulation model for investigating circulation, flushing time and dispersion in Halifax Harbour and adjacent waters

Shiliang Shan* and Jinyu Sheng

Department of Oceanography, Dalhousie University,
Halifax, B3H 4R2, Nova Scotia, Canada

*Corresponding author, e-mail sshan@phys.ocean.dal.ca

KEYWORDS

Multi-nested; ocean circulation model; Halifax Harbour; flushing time; dispersion.

EXTENDED ABSTRACT

Halifax Harbour is one of the world's largest ice-free natural harbours and is situated on the south coast of Nova Scotia, Canada. The Harbour is an elongated estuary which consists of the Outer Harbour, Inner Harbour, Northwest Arm, Eastern Passage, Narrows and Bedford Basin (Fig. 1). Pollution control and sustainable development of Halifax Harbour require reliable information about how material is transported and dispersed within the harbour and how the harbour is flushed through water exchanges with the open ocean (Petrie and Yeats, 1990). From the biological and chemical point of view, flushing time, dispersion and retention are important factors in determining levels of contamination and concentrations of nutrients in Halifax Harbour.

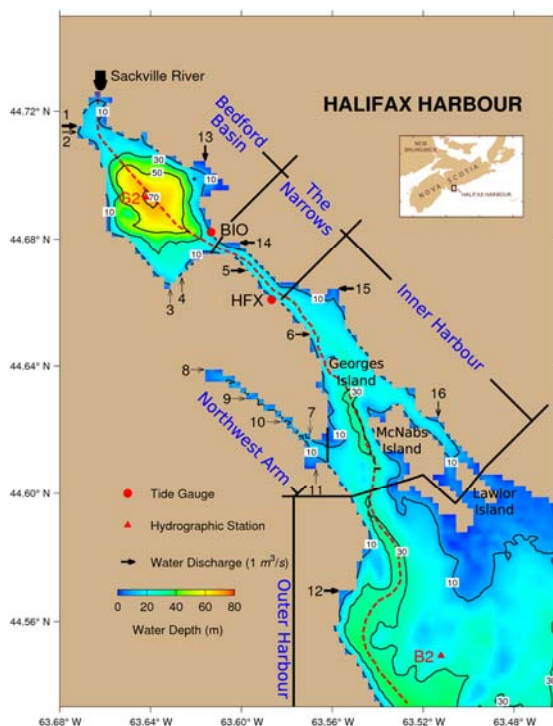


Figure 1. Gridded (~200 m) bathymetry of Halifax Harbour and adjacent waters. Five geographic divisions labelled in blue are used in this study. Red dots indicate positions of two tide gauges. Water discharge locations are numbered 1 to 16 and discharge values are indicated by scaled arrows.

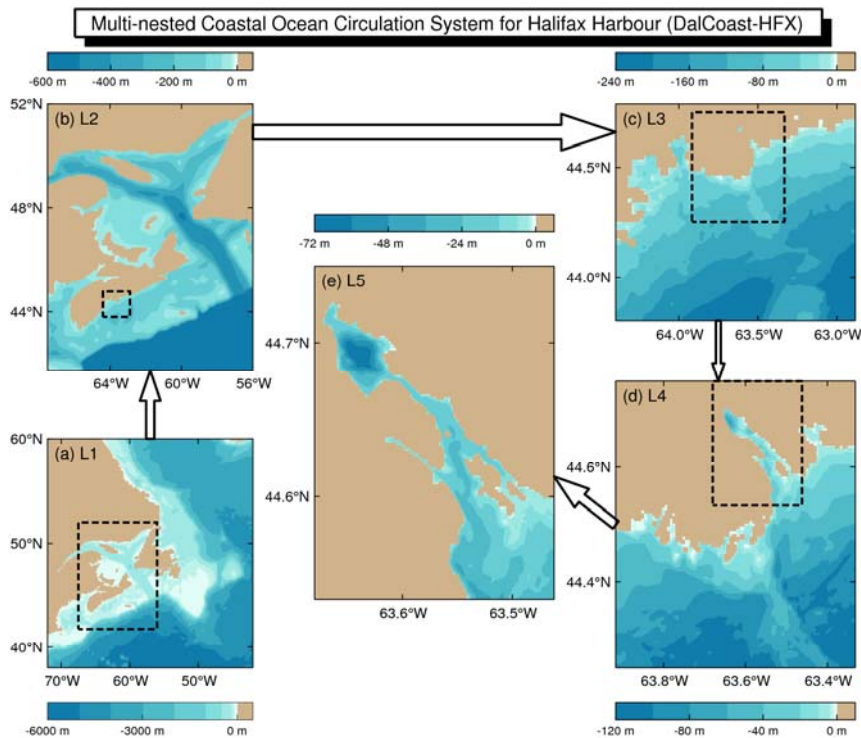


Figure 2. Domains and major bathymetric features of five submodels of the nested-grid ocean circulation model known as the NCOPS-HFX. (a) Submodel L1 (horizontal resolution of $(1/12)^\circ$, ~ 9 km) and (b) submodel L2 ($(1/16)^\circ$, ~ 7 km) are Dalcoast (Thompson et al., 2007); (c) submodel L3 (~ 2 km), (d) submodel L4 (~ 500 m) and (e) submodel L5 (~ 200 m) are based on CANDIE (Sheng et al., 1998). Land is marked by the tan color.

A multi-nested coastal ocean circulation modelling system (DalCoast-HFX) was developed recently by Shan et al., (2011) for simulating three-dimensional circulation and hydrographic distributions in Halifax Harbour. The multi-nested modelling system has a five sub-models (Fig. 2) with a coarse-resolution ($1/12^\circ$) outer-most model for the eastern Canadian shelf and a fine-resolution (~ 200 m) inner-most model for Halifax Harbour, Bedford Basin and adjacent waters based on the Princeton Ocean Model and DANDIE (Sheng et al., 1998; Thompson et al., 2007; Yang and Sheng 2008). The nested-grid modelling system is forced by tides, winds, surface heat fluxes and freshwater discharges.

Shan et al. (2011) recently assessed the performance of DalCoast-HFX by comparing model results (Fig. 3) with independent observations of sea level from coastal tide gauges and currents from moored instruments. The simulated hydrography is also compared against a new monthly climatology created from all available temperature and salinity observations made in the Harbour over the last century. They demonstrated that the modelling system reproduces accurately the main features of the observed tides and storm surge, seasonal mean circulation and hydrography, and wind driven variations.

The main objective of this paper is to quantify the flushing time, dispersion and retention in the Harbour based on the time-dependant, 3D currents produced by DalCoast-HFX. Both passive tracers and passive particles carried passively by the model currents are used in the study.

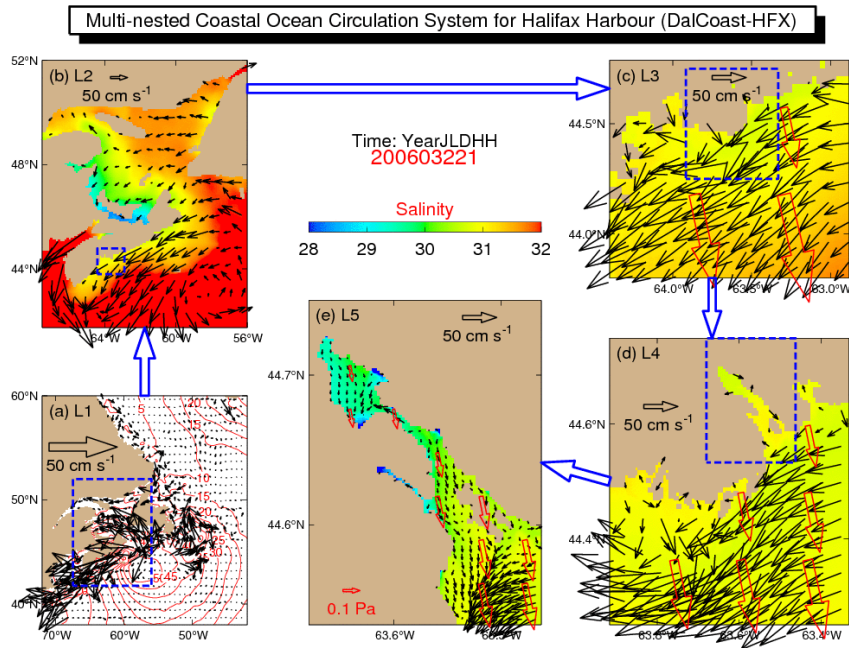


Figure 3. A snapshot of (a) depth-averaged currents (black arrows) and total surface elevations (red/blue contours for positive/negative values with the contour interval of 5 cm) produced by submodel L1; (b) surface currents (black arrows) and sea surface salinity (images) produced by submodel L2; and (c-e) near-surface (2 m) currents and salinities produced by submodels L3-L5 of the NCOPS-HFX at day 32.875 (21:00 UTC February 1) in 2006. Red open arrows are wind stress vectors. For clarity, velocity vectors are plotted at every (a) 9th, (b) 10th, (c) 5th, (d) 7th, and (e) 3rd model grid point.

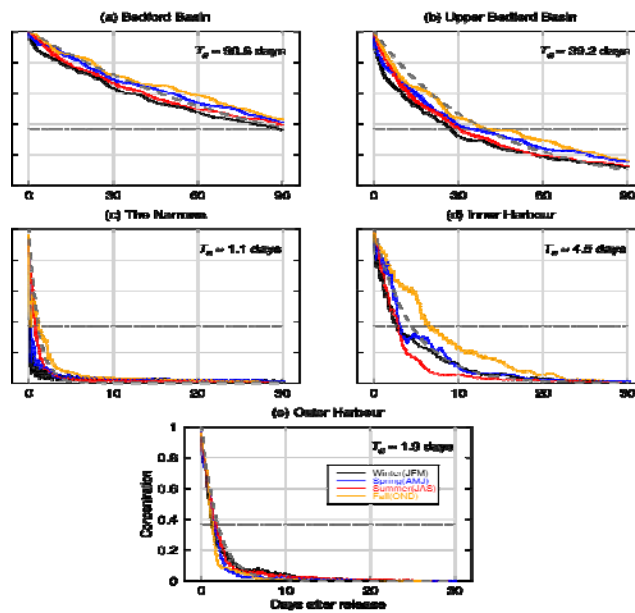


Figure 4. Time series of volume averaged concentrations (VACs) of passive tracer for five different subareas in Halifax Harbour (see Fig. 1) in four seasons in 2006.

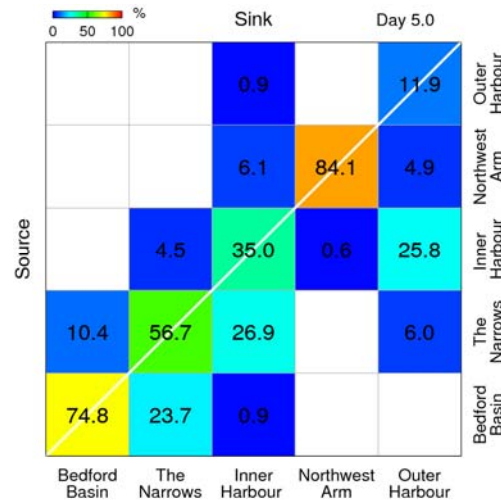


Figure 5. Connectivity matrix over five subareas in Halifax Harbour (see Fig. 1) based on passive particles carried by model-calculated annual mean currents produced by submodel L5.

The time series of passive tracer concentrations in Halifax Harbour produced by DalCoast-HFX are shown in Fig. 4, from which the flushing time is estimated to be ~90.6 days in the entire Bedford Basin, ~39.2 days in the upper Bedford Basin, and only ~1.1, 4.5 and 1.9 days in the Narrows, Inner Harbour and Outer Harbour, respectively.

Analysis of trajectories of passive particles tracked numerically based on the inner-most model current fields demonstrates movements of passive particles in Halifax Harbour strongly affected by tidal and storm-induced currents. Hydrodynamic connectivity in the study region is also examined in terms of a transition matrix (Fig. 5) calculated from the movements of particles that are carried passively by the time-independent 3D annual mean currents (TRACK-mean) produced by submodel L5 of DalCoast-HFX with an added random walk to approximate the subgrid scale dispersion. The TRACK-mean experiment shows that within five days, about 75% and 85% of particles are remain in Bedford Basin and the Northwest Arm, respectively; and nearly 90% of particles are flushed to the open sea in the Outer Harbour.

REFERENCES

- Shan S., Sheng J., Thompson K.R. and Greenberg D.A. (2011). Simulating the three-dimensional circulation and hydrography of Halifax Harbour using a multi-nested coastal ocean circulation model. *Ocean Dynamics*, DOI:10.1007/s10236-011-0398-3.
- Petrie B. and Yeats, P. (1990). Simple models of the circulation, dissolved metals, suspended solids and nutrients in Halifax Harbour. *Water Pollut. Res. J. Can.*, **25**, 325–349.
- Sheng J, Wright D.G., Greatbatch R.J., and Dietrich D.E. (1998). CANDIE: a new version of the DieCAST ocean circulation model. *J. Atmos. Ocean Technol.*, **15**, 1414–1432.
- Thompson K.R., Ohashi K., Sheng J., Bobanovic J., and Ou J. (2007). Suppressing bias and drift of coastal circulation models through the assimilation of seasonal climatologies of temperature and salinity. *Cont. Shelf Res.*, **27**, 1303–1316.
- Yang B., and Sheng J. (2008). Process study of coastal circulation over the inner Scotian Shelf using a nested-grid ocean circulation model, with a special emphasis on the storm-induced circulation during tropical storm Alberto in 2006. *Ocean Dyn.*, **58**, 375–396.

Investigating Storm-Induced Circulation and Hydrodynamic Connectivity in the Pearl River Estuary of China using a Nested-Grid Coastal Circulation Model

Jinyu Sheng* and Liqun Tang

¹*Department of Oceanography, Dalhousie University, Halifax, B3H 4R2, Nova Scotia, Canada*

²*Department of Sediment Research, China Institute of Water Resources and Hydropower Research, Beijing, China*

**Corresponding author, e-mail Jinyu.Sheng@Dal.Ca*

KEYWORDS

Coastal circulation model; Pearl River Estuary; storm-induced circulation; Typhoon Koryn.

EXTENDED ABSTRACT

The Pearl River Estuary (PRE) is a subtropical estuary on the east coast of Guangdong Province of China, connecting the Pearl River with the South China Sea in the east of the Pearl River Delta over South China's Guangdong Province (Fig. 1). The Pearl River Delta is rich in agriculture and aquaculture resources and has been in the forefront of the economic expansion in the last 25 years. Rapid urbanization and industrialization of this region with influxes of people from other parts of China in the past half century, however, makes this region notoriously polluted (Harrison et al. 2008), with sewage and industrial waste treatment facilities failing to keep pace with the growth in population and industry. Better knowledge of three-dimensional (3D) circulation and capability of predicting circulation is needed for better management of coastal resources over this region.

Circulation and hydrographic distributions in the PRE are affected by many forcing mechanisms operating over the region, including tides, wind, sea surface heat and freshwater fluxes, and buoyancy forcing associated with freshwater runoff from the Pearl River system. Significant efforts were made in the past in examining the basic hydrographic features and main physical processes in the Estuary (Wong et al., 2003a and b). Recently Tang et al. (2009) and Ji et al. (2011a and b) examined the main physical processes affecting the circulation and associated synoptic and seasonal variability of the estuarine circulation in the PRE using a nested-grid coastal ocean circulation model (DalCoast-PRE). The main objective of this study is to examine the storm-induced circulation during super typhoon Koryn and hydrodynamic connectivity in the PRE based on model results produced by DalCoast-PRE.

DalCoast-PRE has three downscaling subcomponents: an outer-most sub-model with a coarse horizontal resolution of ~7 km for simulating tidally forced and wind-driven surface elevations and depth-mean currents over China Seas from Bohai Sea to the northern South China Sea; and an inner-most sub-model with a fine resolution of ~1.2 km for simulating

three-dimensional (3D) currents and temperature/salinity fields in the PRE and adjacent waters. DalCoast-PRE is driven with time-dependent and spatially varying forcing including tidal and atmospheric forcing, and buoyancy forcing associated with river discharges.

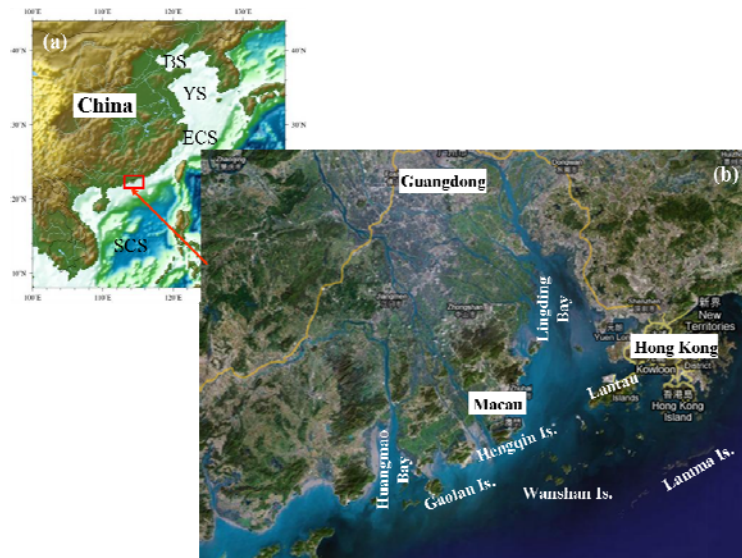


Figure 1. Satellite images of (a) China seas and (b) the Pearl River Estuary and adjacent coastal waters. Abbreviations are used for Bohai Sea (BS), the Yellow Sea (YS), the East China Sea (ECS) and the South China Sea (SCS).

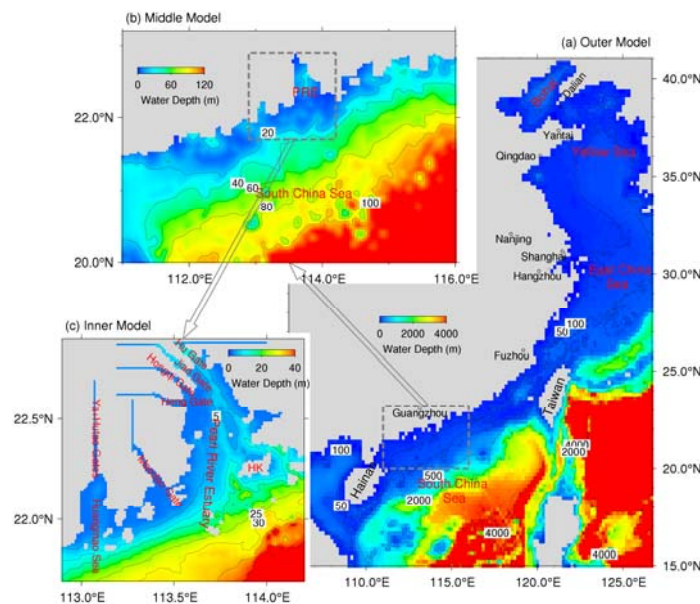


Figure 2. Major bathymetric features of the nested-grid coastal ocean circulation modelling system for the Pearl River Estuary based on the Princeton Ocean Model (POM). (a) The outer model is a coarse-resolution (~ 7 km) storm surge model; (b) the middle model is an intermediate-resolution (~ 3 km) shelf circulation baroclinic model for the inner shelf of the northern South China Sea; (c) the inner model is a fine-resolution (~ 1.2 km) coastal circulation model for the Pearl River Estuary (PRE) and adjacent waters.

Super typhoon Koryn was the first typhoon during the Pacific typhoon season in 1993 and formed near the Caroline Islands on June 15 as a low pressure system. Koryn moved northward and then westward, and became a tropical storm on June 17. Koryn reached a typhoon status on June 23 and rapidly intensified on the next day to become the first super typhoon of the season with maximum winds of 225 km h^{-1} and a minimal pressure of 910 mbar. After making landfall on the east coast of northern Luzon in the Philippines early on June 26 with winds estimated at 210 km h^{-1} , Koryn entered the South China Sea as a Category 2 typhoon around noon on June 26. It then moved rapidly west-northwest across the northern part of the South China Sea with winds of 165 km h^{-1} . Koryn made landfall near Hong Kong on June 27 and weakened into a strong tropical storm and dissipated on June 28.

To simulate the storm-induced circulation during Koryn, DalCoast-PRE was integrated from January 1, 1992 using the 3-hourly surface wind stress and atmospheric pressure fields produced by the National Marine Environmental Forecast Center (NMEFC) of China. Since the NMEFC wind and pressure fields have a relatively low horizontal resolution (0.5 degrees in both longitude and latitude), an idealized vortex suggested by Holland (1980) was added to the NMEFC atmospheric wind and pressure fields after June 23, 1993 to better represent winds and atmospheric pressures associated with Koryn.

Figure 3 represents the wind stress, surface elevations and circulation in the morning of June 26, 1993 (model day 542.4). At this time, the center of Koryn was located to the northwest of Luzon Island. The circulation and hydrographic distributions in the PRE and adjacent waters have not been affected by the storm. The surface temperatures produced by DalCoast-PRE are about 30°C in the PRE and about 28°C over the inner shelf of the southern SCS (Figs. 3b,c).

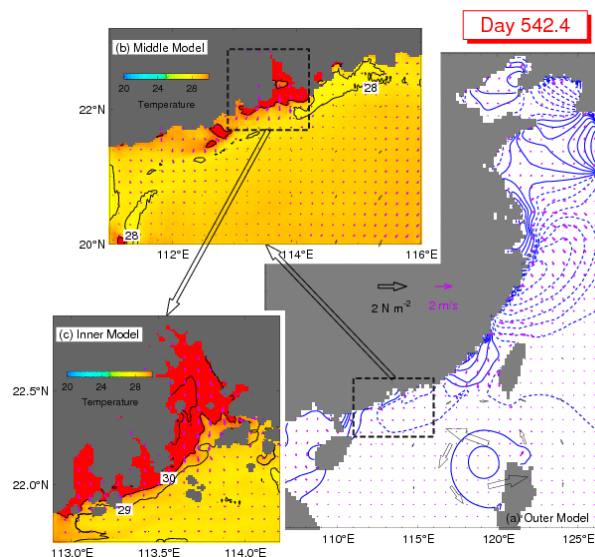


Figure 3. Circulation at model day 542.4 (09:36 June 26, 1993) produced by the DalCoast-PRE. (a) Surface elevations (blue contours, in the unit of m) and depth-mean currents (solid arrows) over China Seas produced by the outer model; (b) surface temperature (image) and surface currents (solid arrows) over the inner shelf of the northern SCS produced by the middle model; and (c) surface temperature (image) and surface currents (solid arrows) produced over the PRE produced by the inner model of the nested-grid system. Black open arrows represent wind stress vectors. Velocity vectors are plotted at every 10th grid point in (a) and every 6th grid point in (b) and (c).

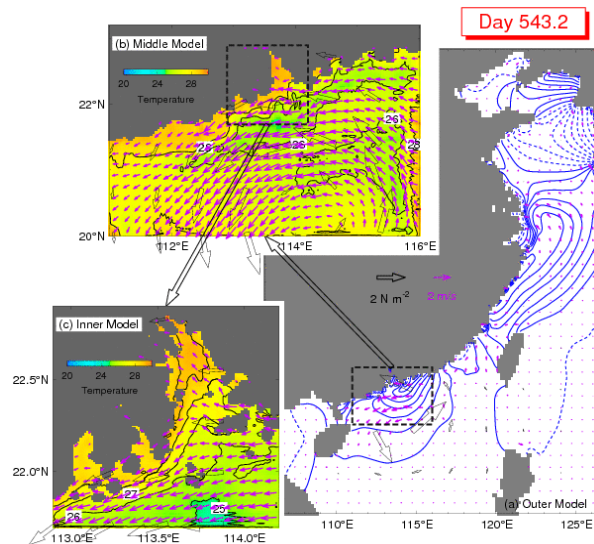


Figure 4. As in Figure 3, except at 04:48 June 27 (model day 543.2), 1993.

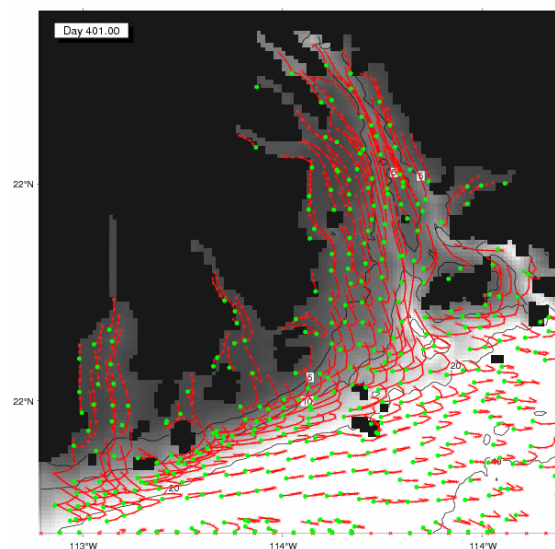


Figure 5. Lagrangian view of horizontal movements of particles carried by ocean currents produced by the middle model of DalCoast-PRE at model day 401.00.

At day 543.2 (04:48 June 27, 1993), Koryn reached the shelf waters to the south of the PRE (Fig. 4a). The surface wind stress at this time was strong (about 2 Pa) over the northern South China Sea close to the PRE and relatively weak over other regions of the China Seas. The simulated circulation at this time has large coastal setup induced by Koryn near the mouth of the PRE and is mainly tidal circulation over other regions. The surface currents at day 543.2 produced by DalCoast-PRE (Figs. 4b,c) are strong and southwestward and alongshore near the coast of the PRE due to the combination of the wind forcing and large pressure gradients near the coast. In comparison with model results before the storm, The SSTs in the PRE at day 543.2 are cooler by $\sim 2^{\circ}\text{C}$ due mainly to coastal upwelling induced by the Koryn.

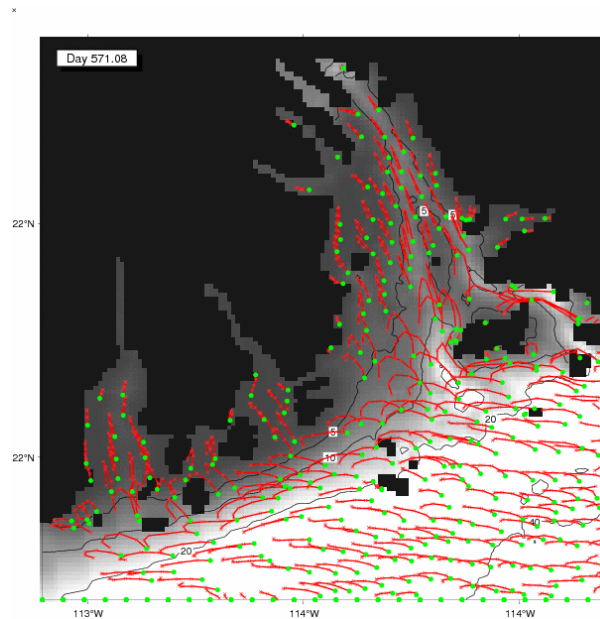


Figure 6. As in Figure 5, except at model day 571.08.

To study the hydrodynamic connectivity in the PRE and adjacent waters, horizontal movements of particles are calculated using the fourth-order Runge-Kutta method from the currents produced by the middle model of DalCoast-PRE. Random horizontal movements are included to represent the small-scale influence of physical processes that are not modeled explicitly in the study. Figures 5 and 6 present the particle movements in the view of Lagrange currents at model days 401.00 and 571.08 respectively.

REFERENCES

- Ji X., Sheng J., Tang L., Liu D. and Yang X. (2011a). Process study of circulation in the Pearl River Estuary and adjacent coastal waters in the wet season using a triply-nested coastal circulation model, *Ocean mod.*, **38**, 138-160, doi:10.1016/j.ocemod.2011.02.010.
- Ji X., Sheng J., Tang L., Liu D. and Yang X. (2011b). Process study of dry-season circulation in the Pearl River Estuary and adjacent coastal waters using a triple-nested coastal circulation model, *Atm. Ocean*, **49**, 138-162, doi:10.1080/07055900.2011.580165.
- Wong L., Chen J., Xue H., Dong L., Su J. and Heinke G. (2003a). A model study of the circulation in the Pearl River Estuary (PRE) and its adjacent coastal waters: 1. Simulations and comparison with observations. *J. Geophys. Res.*, **108**, C3156. doi: 10.1029/2002JC001451.
- Wong L., Chen J., Xue H., Dong L., Guan W. and Su J. (2003b). A model study of the circulation in the Pearl River Estuary (PRE) and its adjacent coastal waters: 2. Sensitivity experiments. *J. Geophys. Res.*, **108**, 26.1-26.12. doi: 10.1029/2002JC001451.
- Tang L., Sheng J., Ji X., Cao W. and Liu D. (2009). Investigation of circulation and hydrography over the Pearl River Estuary of China using a nested-grid coastal circulation model. *Ocean Dyn.*, **59**, 899-919, doi: 10.1007/s10236-009-0218-1.

Integration of Bayesian inference techniques with mathematical modelling

Yuko Shimoda¹, Yerubandi R. Rao², and George B. Arhonditsis^{1*}

¹ Ecological Modelling Laboratory, Department of Physical & Environmental Sciences,
University of Toronto, Toronto, Ontario, M1C 1A4, Canada

² Water Science and Technology Directorate, Environment Canada, Burlington, Ontario, L7R
4A6, Canada

*Corresponding author, e-mail georgea@utsc.utoronto.ca

Keywords: Eutrophication; risk assessment; Bayesian inference; hydrodynamic modelling.

Introduction: In the context of water quality assessment, the application of process-based models typically has a deterministic character, whereby single-value predictions at each point in time and space are derived from uniquely determined model inputs. Most of the existing calibration efforts aim at reproducing the average ecological dynamics, but fail to capture the entire range of natural conditions experienced. The credibility of these practices and their adequacy in addressing environmental management problems has recently been questioned for two main reasons. First, regardless of its complexity and supporting information, the application of any modeling construct involves substantial uncertainty contributed by model structure, parameters, and other associated inputs (e.g., boundary or initial conditions). Second, models parameterized to depict the average ecosystem behavior are inadequate in addressing the type of percentile-based standards needed to accommodate the natural spatiotemporal variability and may bias (underestimate) the predictions of the frequency of standard violations under various management options.

For better model-based decision analysis that can effectively support the development of environmental standards and the policy making process, the uncertainty in model predictions as well as the full range of the expected system responses must be rigorously quantified and reported in a straightforward way (Arhonditsis *et al.*, 2007). Model uncertainty analysis essentially aims to make inference about the joint probability distribution of model inputs, reflecting the amount of knowledge available for model parameters, initial conditions, forcing functions, and model structure. In this regard, Bayes' Theorem provides a convenient means to combine existing information (prior) with current observations (likelihood) for projecting future ecosystem response (posterior). Hence, the Bayesian techniques are more informative than the conventional model calibration practices, and can be used to refine our knowledge of model input parameters while obtaining predictions along with uncertainty bounds for output variables (Arhonditsis *et al.*, 2007).

Despite the compelling arguments for considering Bayesian inference techniques as an integral part of the model development process, their high computational demands along with the lack of analytical expressions for the posterior distributions was until recently a major impediment for their broader application. Nonetheless, the advent of fast computing has allowed the development of several methods for performing Bayesian inference and the most commonly used technique is called Markov chain Monte Carlo (MCMC); a general methodology that provides a solution to the difficult problem of sampling from high dimensional distributions for the purpose of numerical integration. In this paper, we present a modeling exercise in which Bayesian inference techniques are used to calibrate an integrated hydrodynamic-eutrophication model. Our case study is the Hamilton Harbour, a eutrophic system in the Province of Ontario, Canada, where the anticipated benefits from the Bayesian framework can be used from stakeholders and policy makers to guide the use of millions of dollars of restoration and to dictate the Best Management Practices.

Methods: We developed an ecological model that considers the interplay among the limiting nutrient (phosphate), phytoplankton, zooplankton, and particulate phosphorus. The plankton

model was forced by the local circulation patterns, as derived from the application of the Estuary and Lake Coastal Ocean Model (ELCOM) model to the Hamilton Harbour (Rao *et al.*, 2009). The Bayesian calibration was founded upon the assumption that the model is an imperfect simulator of the system and the corresponding process (structural) error σ^2 follows a Gaussian distribution that is invariant with the input conditions. In the context of the Bayesian statistical inference, the posterior probability density of the parameters and the initial conditions of the state variables, given the observed data y , is defined as:

$$p(\theta, y_0, \sigma^2 | y) = \frac{p(y|f(\theta, x, y_0, \sigma^2))p(\theta)p(y_0)p(\sigma^2)}{\iiint p(y|f(\theta, x, y_0, \sigma^2))p(\theta)p(y_0)p(\sigma^2)d\theta dy_0 d\sigma^2} \propto p(y|f(\theta, x, y_0, \sigma^2))p(\theta)p(y_0)p(\sigma^2)$$

where $f(\theta, x, y_0)$ denotes the eutrophication model, x is a vector of time dependent control variables (e.g., boundary conditions, forcing functions) describing the environmental conditions, θ is the vector of time independent calibration model parameters, y_0 corresponds to the vector of the initial conditions, $p(\theta)$, $p(y_0)$ and $p(\sigma^2)$ represent the prior probabilities of the model parameters, initial conditions, and process error, respectively. To improve the computational efficiency of the MCMC implementation, we introduced a novel one-dimensional framework, in which the eutrophication model was simultaneously calibrated at four sites, while the hydrodynamic computations were performed externally and the spatial variability in the Harbour was accommodated as follows:

$$\frac{\partial C}{\partial t} = \nabla(D\nabla C) - \bar{v} \cdot \nabla C + \varphi$$

where the term φ in the advection-diffusion equation represents a stationary, Gaussian, and Markov process, known as an Ornstein–Uhlenbeck or "mean-reverting" process. In particular, this process includes a drift coefficient β through which its (long-term) mean acts as an equilibrium level. The mean and variance of this continuous state-space process are given by:

$$E[\varphi(t) | \varphi(0)] = \varphi(0)e^{-\beta t}, \quad Var[\varphi(t) | \varphi(0)] = \omega^2 \left(\frac{1 - e^{-2\beta t}}{2\beta} \right) \text{ with } \varphi(0) \sim N\left(0, \frac{\omega^2}{2\beta}\right)$$

and ω^2 corresponds to a variance parameter, assumed proportional to the observed values.

Results and Discussion: We applied the Bayesian methodological framework to examine the likelihood of the Hamilton Harbour Area of Concern meeting the delisting objectives for the beneficial use impairment (BUI) *Eutrophication or Undesirable Algae*, if the nutrient loading reductions proposed by the Hamilton Harbour Remedial Action Plan are actually implemented. The basic lessons learned from the present analysis are as follows:

- i) The current epilimnetic total phosphorus goal of 17 $\mu\text{g/L}$ is probably too stringent and therefore a somewhat higher mean value (e.g., 20 $\mu\text{g/L}$) may provide a more realistic target. The water quality standard of mean chlorophyll *a* concentrations in the Harbour lower than 10 $\mu\text{g/L}$ is achievable.
- ii) Acknowledging the uncertainty of the contemporary nutrient loading estimates in the Harbour as well as the lurking known or unknown "ecological unknowns", the water quality setting process must be pragmatic and the natural variability should be explicitly accommodated by permitting a realistic frequency of violations, e.g., exceedences of the goal for 10-15% or less of the weekly-collected samples during the stratified period should still be considered as compliance of the system with the water quality goals.

References

- Arhonditsis, G.B., Qian, S.S., Stow, C.A., Lamon, E.C., Reckhow, K.H., 2007. Eutrophication risk assessment using Bayesian calibration of process-based models: Application to a mesotrophic lake. *Ecol. Model.* **208**, 215-229.
- Rao, Y.R., Marvin, C.H., Zhao, J., 2009. Application of a numerical model for circulation, temperature and pollutant distribution in Hamilton Harbour. *J. Great Lakes Res.* **35**, 61-73.

Sensitivity of the simulated Kingston-Basin Lake Ontario summer temperature profile from a finite volume model

Jennifer A. Shore^{1*} and Yerubandi R. Rao²

¹*Royal Military College of Canada, Kingston ON Canada*

²*National Water Research Institute, Environment Canada, Burlington, ON Canada*

**Corresponding author, e-mail jennifer.shore@rmc.ca*

Keywords

Kingston Basin, Lake Ontario, finite volume model, lake hydrodynamics

Introduction

Kingston Basin is a region of complex bathymetry at the northeastern end of Lake Ontario that includes three large islands and funnels the Great Lakes outflow through to the Saint Lawrence River. To model this complex system we employ a geometrically flexible finite volume model (FVCOM) to simulate the hydrology of Kingston Basin and the rest of Lake Ontario. FVCOM employs a triangular unstructured grid that has the flexibility needed to sufficiently resolve the bathymetry in the Basin but also uses an efficient computational scheme similar to finite difference models.

Methods

The FVCOM model is forced with surface net heat fluxes, wind, precipitation and river inflow from the Niagara River for the summer of 2006. In 2006, the National Water Research Institute (NWRI) collected atmospheric and hydrographic data at four sites in Lake Ontario and Kingston Basin. Incoming short and longwave radiation data was collected every 10 minutes and this was used to compute the net surface heat flux used to force the model. The 2006 summer circulation and temperatures were simulated by the model and validated against the observations of lake temperatures collected by NWRI. Net heat fluxes were also computed using outputs from the National Centre for Environmental Prediction's North American Regional Reanalysis (NARR). Three different schemes are used to compute the net surface heat flux forcing for the model and results are compared against observations.

Results

Figure 1 illustrates the model domain and the locations of the four NWRI stations where the 2006 atmospheric data used to force the model was collected. Model simulated temperatures are compared to temperature data collected from April 14th to Oct 9th at station 406. Net surface heat flux was computed using the short and longwave NWRI observations along with latent and sensible heatfluxes computed either from a Princeton Ocean Model³ (NWRI_POM) simulation or using the AIRSEA⁴ Matlab Package (NWRI_HB). Net surface heat fluxes were also computed from heat flux components from the NARR dataset.

Figure 2 illustrates the simulated model results for vertical temperature profile at station 403 for the NWRI_POM and NARR forced cases and their respective root mean square error (RMSE) terms computed for the summer timeseries. RMSE values produced by FVCOM were

comparable to those from a similarly forced ocean model (Nucleus for European Modelling of the Ocean - NEMO). NEMO solutions were provided by Frederic Dupont of Environment Canada.

The summer thermocline begins to set up near the end of May and stabilizes over the next month. The development of the thermocline in the simulated model and the RMSE results indicate that the vertical mixing scheme in FVCOM is adequate and similar to model results from a comparable ocean model simulation (NEMO) though it underestimates the depth of the thermocline.

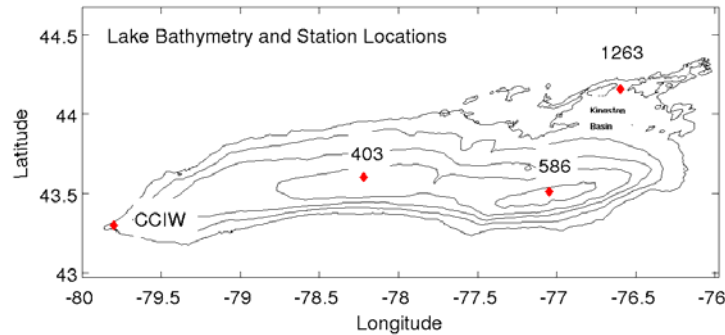


Figure 1: Lake Ontario and Kingston Basin bathymetry and station locations.

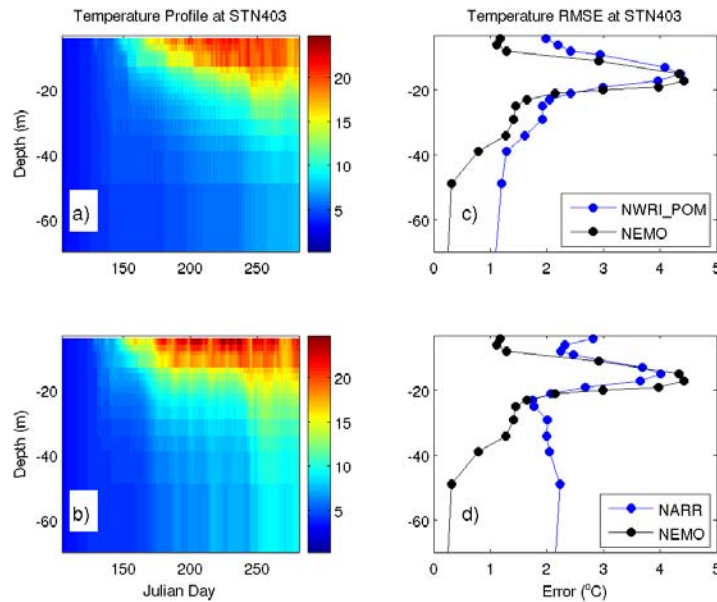


Figure 2: Simulated temperature profiles at station 403 for a) NWRI_POM and b) NARR cases. RMSE temperature errors for c) NWRI_POM and d) NARR cases at the same location. NEMO RMSE values are provided for comparison in black.

³ Courtesy Frederic Dupont, Environment Canada: frederic.dupont@ec.gc.ca.

⁴ Developed by Bob Beardsley and Rick Pawlowicz: woodshole.er.usgs.gov/operations/sea-mat.

Flow in porous sediments induced by steady and unsteady internal waves

M. Stastna^{1*}, J. Olsthoorn¹

¹ *Department of Applied Mathematics, University of Waterloo, 200 University Avenue West, Waterloo, ON, Canada, N2L 3G1.*

**Corresponding author, e-mail mmstastn@uwaterloo.ca*

KEYWORDS

internal waves; porous media; Darcy's Law; nonhydrostatic effects

EXTENDED ABSTRACT

INTRODUCTION

The interior of lakes is known to be dynamically active on many different length and time scales. For density stratified lakes, internal wave motions make up a significant part of these motions. In recent years, a fair amount of interest has been focused on how motions in the water column interact with the lake bottom, especially since this interaction could alter the biogeochemical cycles in the main water column. Particular attention has been paid to the induced flow of water in the porous lake bottom. This has been done using measurements in the field (e.g. sediment breathing, Lorke *et al.*, 2003) and laboratory studies that focused on the asymmetry of flow over ripples (Huettel *et al.*, 1996). Internal wave motions can serve as a readily accessible model of variability on intermediate scales; smaller than the basin-scale yet larger than those associated with turbulent bottom boundary layers. We have developed numerical models of flow in a porous lake bottom due to a variety of internal wave motions, ranging in scale from tens of meters to basin-scale.

Internal waves themselves can be modeled at various levels of sophistication, ranging from linear models to sophisticated numerical models that span the entire basin and require various parametrizations (e.g. the MITgcm, Adcroft *et al.*, 1997). We have chosen to use fully nonlinear internal waves, which are solutions of the Dubreil-Jacotin-Long equation (Soontiens *et al.*, 2010). While these require some numerical methods to find a solution, they are formally equivalent to the full set of inviscid governing equations. In other words they make no approximation based on amplitude, yet the flows they induce remain laminar (in the main water column).

We will begin with simple models using Darcy's law with a constant permeability, then discuss models for active remodeling of the permeability distribution. These are based on the observation that internal waves may induce significant turbulence in the bottom boundary layer, and thereby lift detritus that plugs the pore space at the fluid-porous medium interface. We will subsequently turn to time dependent motions, and discuss how the evolution, nonlinear steepening and break down into wave trains of internal seiches is expressed in the porous substrate (for reasons of space these results are discussed only briefly in the extended abstract).

METHODS

The internal wave solutions are computed using highly accurate pseudo-spectral methods (Soontiens *et al.*, 2010). The bottom pressure profile is subsequently extracted and used to force the porous medium model. This implies that the wave motion is “one-way” coupled to the porous medium. In reality the flow in the porous medium does modify the fluid motion in the boundary layer, though published results suggest that this influence is very weak, and indeed weaker than other uncertainties in the model (e.g. small scale bottom topography).

In steady state the equations governing flow in the saturated porous medium are fairly standard, with Darcy’s Law relating filtration rate to pore pressure and the conservation of mass for an incompressible saturating fluid yielding a Laplace’s equation for the pore pressure. The Laplace’s equation is solved using the same highly accurate pseudospectral method as the internal waves and the filtration rate recovered a posteriori.

The situation is far less clear for time dependent flow. There are several competing models available in the literature with various terms kept or dropped, generally with little justification. We thus adopt the simplest model (Nield and Bejan, 2006) in which the pressure is still governed by the Laplace’s equation while the filtration rate equation modifies Darcy’s Law by including the fluid acceleration term.

RESULTS AND DISCUSSION

For the case of constant permeability the results are fairly straightforward. The low pressure associated with the trapped internal wave of depression that forms over a trench topography yields a region of suction. Maximum filtration occurs along the sloping sides of the topography.

However, both the sloping topography and the wave-induced currents are expected to induce turbulence in the bottom boundary layer. This turbulence will modify the permeability distribution, especially near the fluid-porous medium interface. In turn, this will break the symmetry of the filtration rate across the wave crest, with increased pumping on the downstream side of wave.

For traveling waves such as internal solitary waves the pore pressure adjusts instantaneously (due to the incompressibility assumption). The filtration, however, is modified by the presence of the acceleration terms in the governing equations. Nevertheless, the main conclusions for trapped waves carry over to propagating waves, including wave trains resulting from the break down of basin scale internal seiches.

REFERENCES

- Lorke, A., Muller, B., Maerki, M. and Wuest, A. (2003). Breathing sediments: The control of diffusive transport across the sediment-water interface by periodic boundary-layer turbulence. *Limn. Oceanogr.*, 48, 2077-2085.
- Huettel, M., Ziebis and W., Forster, S. (1996). Flow induced uptake of particulate matter in permeable sediments. *Limn. Oceanogr.*, 41, 309-322.
- Marshall, J., Hill, C., Perelman, L. and Adcroft, A. (1997). Hydrostatic, quasi-hydrostatic and nonhydrostatic ocean modeling. *J. Geophys. Res.*, 102, 5733-5752.
- Soontiens, N., Subich, C. and Stastna, M. (2010). Numerical simulation of supercritical trapped internal waves over topography. *Phys. Fluids*, 22, 116605, doi:10.1063/1.3521532
- Nield, D. A. and Bejan, A. (2006). *Convection in porous media*. Springer, New York.

The impact of numerical method choice on solutions to a dispersive shallow water model

D. Steinmoeller^{1*}, M. Stastna¹, K. Lamb¹

¹ *Environmental and Geophysical Fluid Dynamics Group, Department of Applied Mathematics, University of Waterloo, Waterloo, ON, N2L 3G1, Canada*

*Corresponding author, e-mail dsteinmo@math.uwaterloo.ca

KEYWORDS

Shallow water equations; Wave dynamics; Dispersion; Numerical methods.

EXTENDED ABSTRACT

Introduction

The finite volume method (FVM) is by far the most widely used numerical method in physical oceanography and limnology applications. By its nature, however, it imparts large amounts of artificial dissipation to numerical solutions. In light of this, we present the discontinuous Galerkin finite element method (DG-FEM) as a high-order alternative to FVM for solutions to a Boussinesq-type weakly non-hydrostatic shallow water model in general geometries. It is shown that at high orders of accuracy and in simple geometries, DG-FEM solutions can be of comparable energy-conserving character to solutions obtained using pseudospectral methods, which offer the highest order of accuracy possible. Furthermore, for complex geometries, DG-FEM allows for high order solution of problems that are impossible to treat with comparable accuracy by other means.

Methods

We consider the simple dispersive shallow water model for a single fluid-layer used by de la Fuente *et al.* (2008) in their study of internal waves in a circular basin

$$h_t + \nabla \cdot (hu) = 0, \quad (1)$$

$$(hu)_t + \nabla \cdot ((hu)u) = -g h \eta_x + f v h + (H^2/6) (\nabla \cdot (hu))_x, \quad (2)$$

$$(\overline{h\nu})_t + \nabla \cdot ((\overline{h\nu})\mathbf{u}) = -g h \eta_y - f u h + (H^2/6) (\nabla \cdot (\mathbf{h}\mathbf{u}))_y, \quad (3)$$

where $h(x,y,t) = H(x,y) + \eta(x,y,t)$ is the total depth of the fluid column, g is the acceleration due to gravity, f is the Coriolis frequency, H is the mean depth, η is the free surface elevation, and $\mathbf{u} = (u,v)$ represents the depth-averaged horizontal velocity vector. The last terms in equations (2) and (3) represent dispersive effects due to weakly non-hydrostatic corrections to the hydrostatic pressure and do not appear in the traditional shallow water model.

In simple geometries such as periodic channels, rectangular basins, and torus-shaped basins solutions can be obtained using spectral spatial discretization methods that are known to give the most accurate numerical approximations possible (Trefethen, 2000; Boyd, 2001). These methods have the added benefit of having low amounts of inherent artificial dissipation. Given these desirable properties, we have chosen spectral methods as a benchmark for the discontinuous Galerkin finite element method (DG-FEM) that can be used in more general geometries (Hesthaven & Warburton, 2008), e.g., realistic lake geometries.

We have implemented numerical codes that use both spectral and DG-FEM methods in MATLAB and carried out a series of numerical simulations in the hopes of determining if DG-FEM can serve as a viable method for carrying out simulations of realistic lake flows.

Results and Discussion

As a first test, we have decided to compare results from the DG-FEM method to the Fourier spectral method in 1D with a flat bottom to better understand the performance of the DG-FEM method at varying orders of accuracy. To perform this comparison, we have run a simulation in which a packet of short waves of two distinct wavelengths is released from rest. Due to dispersion, we expect the longer waves to overtake and lead the shorter waves after sufficient time has passed. The number of grid points used in the spatial discretization was held fixed for all runs. Results are shown in Figure 1.

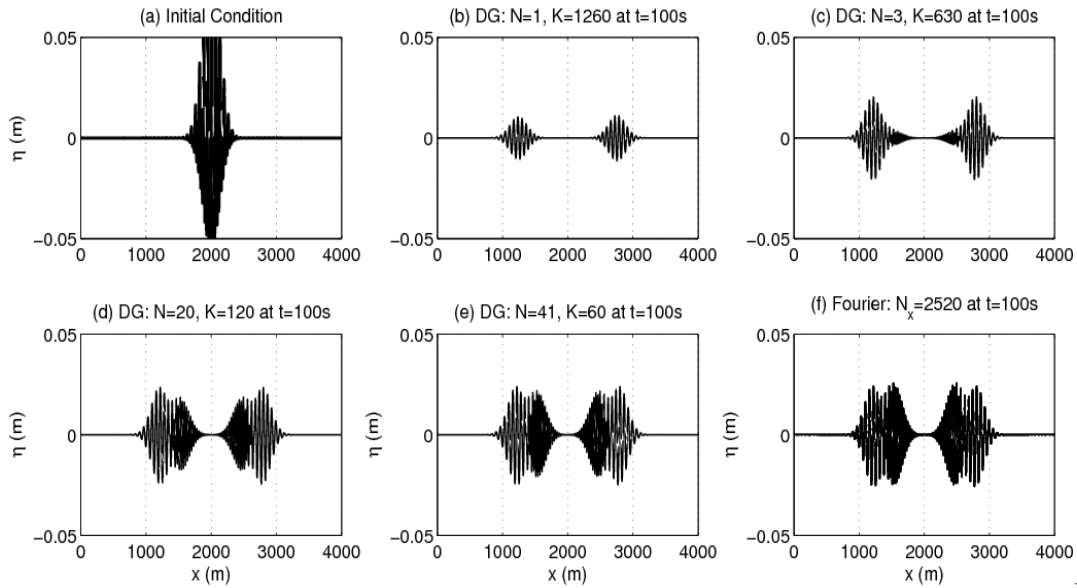


Figure 1:

Fixed time snapshots of the free-surface displacement at various orders of approximation for the 1D dispersive short-waves run. Panels (b)-(f) are all at time $t = 100\text{s}$. (a) η at $t = 0$. (b) DG-FEM $N = 1$ result. (c) DG-FEM $N = 3$ result. (d) DG-FEM $N = 20$ result. (e) DG-FEM $N = 41$ result. (f) Fourier Method with $N_x = 2520$ grid points.

A striking observation is that for the low-order runs, the shorter waves are either dissipated entirely or to a very large degree. Close inspection of the plots reveals that even at a very high order of $N = 41$, the DG-FEM method cannot match the energy-conserving qualities of the Fourier method. This behaviour is likely owed to the fact that in the vicinity of elemental interfaces, the DG-FEM method reduces to a low-order finite volume method and hence will always have some amount of inherent numerical dissipation (Hesthaven & Warburton, 2008).

To test the viability of the DG-FEM method in two-dimensions we have performed simulations of a surface seiche in Lake Pinehurst, AB. The contour of the lake boundary was inferred from 200m bathymetry data and, for simplicity, a flat bottom was assumed and the Coriolis parameter was set to zero. The resulting domain was triangulated using the `mesh2d` software package, and the simulation was carried out by initializing the $N=4$ DG-FEM method with a linear free-surface tilt and no initial velocity. Some snapshots of the seiching evolution are shown in Figure 2 along with area-integrated energy time-series to illustrate the extent of numerical dissipation in the simulation. After 50 minutes of physical time, 4% of the total energy has been artificially dissipated.

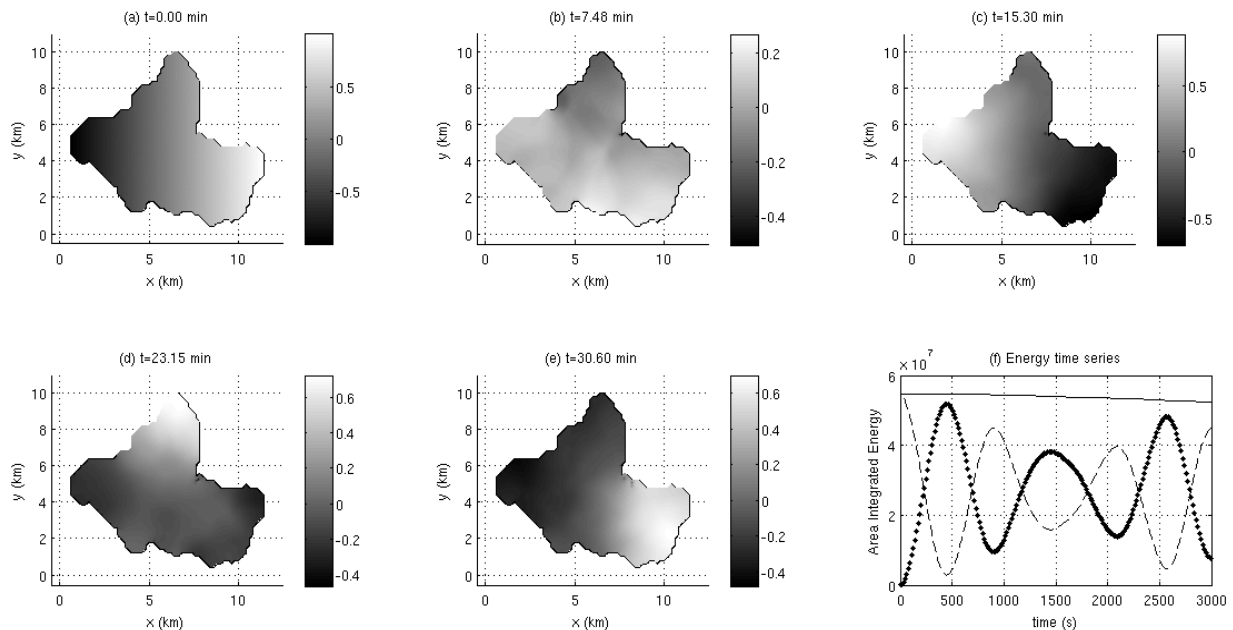


Figure 2: Panels (a)-(e) are fixed time snapshots of free surface displacement for the Lake Pinehurst, AB simulation. Panel (f) shows area-integrated energy time series. The dotted, dashed, and solid lines represent the kinetic energy, available potential energy, and the total energy, respectively.

In this talk, we will also present seiching results for Lake Opeongo, ON, and further discuss the performance of DG-FEM in two-dimensional simulations at various orders of approximation.

REFERENCES

- Hesthaven, J. & Warburton, T. (2008). *Nodal Discontinuous Galerkin Methods: Algorithms, Analysis, and Applications*. Springer. New York, USA.
- Trefethen, L. (2000). *Spectral Methods in MATLAB*. Society for Industrial and Applied Mathematics. Philadelphia, USA.
- de la Fuente, A., Shimizu, K., Imberger, J. & Nino, Y. (2008). The evolution of internal waves in a rotating, stratified, circular basin and the influence of weakly nonlinear and nonhydrostatic accelerations. *Limnol. Oceanogr.*, **53**(6), 2738-2748.
- Boyd, J. (2001). *Chebyshev and Fourier Spectral Methods*, 2nd edition. Dover Publications. Toronto, Canada.

Climate Change, does it happen as abrupt transition or as steady linear process?

A. K. Stips^{1*}, M-J. Lilover²

¹ *Global Environment Monitoring, Joint Research Centre, Via E. Fermi, TP272, I-21027 Ispra, Italy*

² *Marine Systems Institute, Akadeemia tee 15a, 12618 Tallinn, Estonia*

*Corresponding author, e-mail adolof.stips@jrc.ec.europa.eu

KEYWORDS

Breakpoints, climate change, feedback, linear process

EXTENDED ABSTRACT

INTRODUCTION

Systems that have an internal feedback mechanism are principally behaving non-linear. The climate on earth is such a complex system with internal feedback and a non-linear characteristic should therefore be expected. Abrupt shifts in climatic conditions have first been discovered at high latitudes in the Northern Hemisphere when investigating Greenland ice cores and have captured the attention of scientists since then. On very long time scales of about 100000 years the seemingly fast changing glacial – interglacial cycles and on relatively shorter time scales of about 2000 years the occurrence of Dansgaard-Oeschger events are a striking evidence for such non-linear behavior. Therefore the classical assumption of linear (slow and smooth) changes in climate and environmental conditions has been questioned recently even on very short time scales of only a few decades. A discussion on tipping points and regime shifts has started and stationarity has declared to be death (Milly *et al.*, 2008).

Nevertheless it is still common practice to calculate and publish linear trends from global data sets. The classical example is the often cited (IPCC) global warming trend of 0.05°C/decade for air temperature during the last 150 years. The inadequacy of this linear trend model over such a long period becomes obvious when looking at the difference of the observed 2009 mean temperature to that estimated from the calculated linear trend, see Figure 1. A similar inspection of several global atmospheric and oceanographic data time series provides reasonable doubt concerning the correctness of the application of linear regression analysis to century long time series. It is clear that when applying any statistical method to real world data the underlying process dynamics has to be considered, in order to avoid misinterpretations of the statistical results.

Using a structural test based on the F statistics to test for breakpoints we can show that most of the analyzed global climate time series contain statistical significant structural changes (breaks in the mean or in the slope of a linear regression). We will reveal the existence of breakpoints for most investigated parameters at the end of the 70ties beginning of the 80ties of the last century. Breakpoints detected at a comparable time in many different regional and global climate variables are a strong indication for the existence of a regime shift in the state of the climate.

DATA AND METHODS

Methodology for estimating breakpoints in time series

The first idea for estimating breakpoints in time series regression models was given by Bai (1994) and was extended to multiple breaks by Bai and Perron (1998, 2003), but several other methods have been developed since then. Basically we have to do tests for assessing deviations from the classical linear regression model. As a first guess it is reasonable to assume that a time series has b breakpoints, where the coefficients shift from one stable regression relationship to another one. Consequently there must exist $b+1$ segments with constant regression coefficients. These optimal segments have then to be found by a dynamic programming approach, minimizing the residual sum of squares for certain observation intervals. The F statistics can be used to estimate the optimal number of breakpoints and it is possible to construct confidence intervals. The application of the procedure with instructive examples is given by Zeilies *et al.* (2003). The test has to be done respectively for a change in the mean and for a change in the trend. In case of testing for breakpoints in the mean value the time series has to be first detrended.

Significance tests are all made respectively to a 5% error probability threshold.

Data used for estimating breakpoints in time series

Our study is based on time series of Global surface temperatures, a number of climate indices and external forcing data, but the focus of the abstract is on the temperature data only.

The temperature data are from the Climatic Research Unit of the University of East Anglia <http://www.cru.uea.ac.uk/cru/data/temperature>. As we investigate global-scale time series, we process the variance unadjusted versions of the data (Brohan *et al.*, 2006). We show two series of annual surface temperature anomalies. The first is the CRUTEM3 (Brohan *et al.*, 2006) series of land air data and the third series is HADSST2 (Rayner *et al.*, 2006) for marine data. The anomalies are against the 1961–1990 climatology and span the 1850–2009 period.

RESULTS AND DISCUSSION

The time series of global land air temperature anomalies is plotted in Fig.1 together with the calculated linear trend of $\sim 0.05\text{K/decade}$ (black solid straight line) which is statistically significant. The inadequacy of this linear trend model over such a long period becomes obvious when we look at the difference of the observed 2009 mean temperature to that estimated from the calculated linear trend over the full period, which gives an underestimation of about 48% ($\sim 0.36^\circ\text{C}$ to low, compared to a total change of 0.75°C , see Figure 1.)

Using the objective method for estimating breakpoints in the linear trend we find the most significant breakpoint in 1976. The high statistical significance is further supported by the small confidence interval of only 4 years. The two trends calculated separately for both segments before and after the breakpoint in 1976 are extremely different by a factor of 10. The trend is 0.024K/decade before 1976 and 0.218K/decade thereafter, which is actually 4 times the mentioned overall IPCC trend. This confirms that the time series of global air temperature exhibits a statistically significant structural change.

We extend the test by estimating breakpoints in the time series mean, after removing the significant overall trend. The result of this calculation is presented in Figure 2. This time we find 2 very significant breakpoints, one in 1889 and one in 1986. The respective sub-period mean values are significant different. In summary the different statistical tests reveal a significant linear trend and significant breakpoints in the mean as well as in the trend of the

temperature data. Therefore we cannot decide if the analyzed data represent a linear or non-linear process based only on the statistical results.

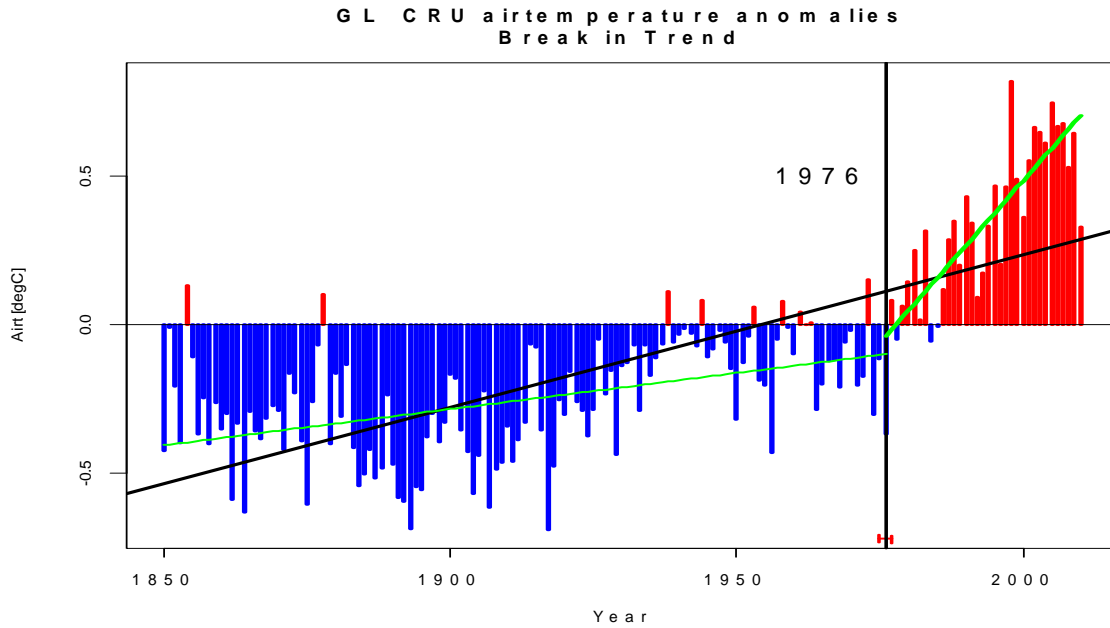


Figure 1. Breakpoint in the trend of the global annual air temperature anomalies over land. The straight black line is the significant linear trend calculated over the full period. The most significant breakpoint (see small confidence interval) occurs 1976. The two green lines are the respective significant linear trends before and after the breakpoint.

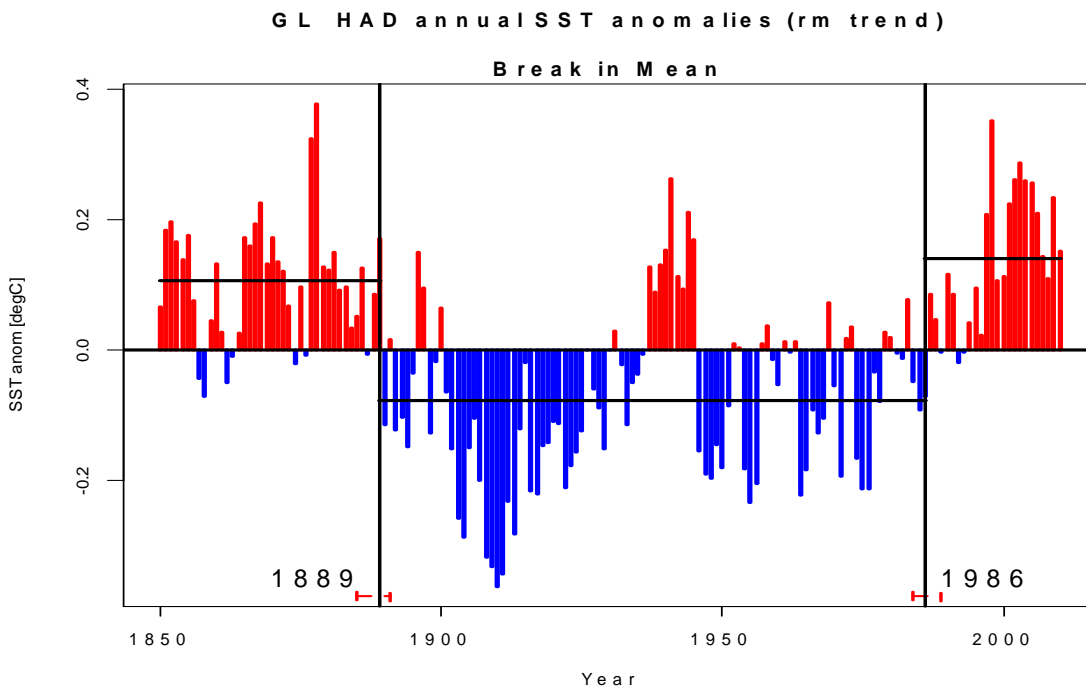


Figure 2. Breakpoint in the mean (trend removed) of the global annual air temperature anomalies over land. Two significant breakpoints occur in 1889 and 1986. The mean of the respective sub-period is indicated by the black vertical lines.

Any projection of the future global air temperature from past records will depend strongly on our decision of the underlying process model, specifically if we are using the linear trend from the full time series or only from the last strong increasing period. The existence of a breakpoint around 1980 could also be considered as sign for a state change in global air temperature pointing to a change in the climate system.

An attempt was made to reinvestigate some well known global climate time series. A more thorough inspection of the available data provides some reasonable doubt concerning the uncritical application of least square regression analysis to the available time series. Indeed based on the F statistics most of the analyzed time series cannot be considered as stationary and therefore the usefulness of linear regression might be questioned. Testing for structural breakpoints in these time series reveals for most investigated variables and also most tested climate indices the existence of breakpoints in the 70-80ties of the last century

The enormous difference between trends calculated with and without consideration of breakpoints has significant implications for any predictions based on the calculated trends. Reconstructed prehistoric climate indices provide clear evidence for the non-linear behavior of the climate system and for the existence of abrupt changes (tipping points). Therefore the calculation of linear trends can only be justified for sufficient short time intervals. The results of any statistical investigation cannot provide a decisive conclusion about the underlying process dynamics, but can be only used to question or support our assumptions. The final confirmation for the real process dynamics has to come from an accurate and complete geophysical description of the climate system, a difficult and complex task still to be accomplished.

REFERENCES

- Bai J., 1994, "Least Squares Estimation of a Shift in Linear Processes", *Journal of Time Series Analysis*, 15, 453-472.
- Bai J. and P. Perron, 1998, "Estimating and Testing Linear Models With Multiple Structural Changes", *Econometrica*, 66, 47-78.
- Bai J. and P. Perron, 2003, "Computation and Analysis of Multiple Structural Change Models", *Journal of Applied Econometrics*, 18, 1-22.
- Brohan P., J.J. Kennedy, I. Harris, S.F.B. Tett, P.D. Jones. 2006. Uncertainty estimates in regional and global observed temperature changes: a new dataset from 1850. *Journal of Geophysical Research* 111(D12): D12106.1–D12106.21.
- Milly P. C. D., J. Betancourt, M. Falkenmark, R. M. Hirsch, Z. W. Kundzewicz, D. P. Lettenmaier, R. J. Stouffer, 2008. Stationarity Is Dead: Whither Water Management?, *Science*, 319, 573-574
- Rayner NA., P. Brohan, D.E. Parker, C.K. Folland, J.J. Kennedy, M. Vanicek, T.J. Ansell, S.F.B. Tett, 2006. Improved analyses of changes and uncertainties in sea surface temperature measured in situ since the mid-nineteenth century: The HadSST2 dataset. *Journal of Climate*, 19(3): 446–469, DOI: 10.1175/JCLI3637.1.
- Zeileis A., C. Kleiber, W. Krämer, K. Hornik, 2003, "Testing and Dating of Structural Changes in Practice", *Computational Statistics and Data Analysis*, 44, 109-123. doi:10.1016/S0167-9473(03)00030-6.

Shear instabilities in internal solitary waves

C. Subich^{1*} and K. Lamb²

¹ *csubich@math.uwaterloo.ca*

² *kglamb@math.uwaterloo.ca*

Department of Applied Mathematics

University of Waterloo

200 University Avenue West

Waterloo, Ontario, Canada N2L 3G1

Keywords

Internal wave dynamics; Shear instability; Spectral methods

EXTENDED ABSTRACT

Recent observations and simulations of internal solitary-like waves on the Oregon Shelf (Lamb and Farmer, 2011) have shown that these waves can form with shear-unstable regions near the wave crest. These shear-unstable regions can amplify small perturbations upstream of the wave into Kelvin-Helmholtz billows at the back of the wave, slowly extracting energy from the internal wave and mixing fluid near the pycnocline. These instabilities provide a potential mechanism for dissipation of large internal waves without shoaling or breaking effects.

This work presents the results of numerical simulations of these waves conducted with a three-dimensional, pseudospectral method. Both narrow waves with a low minimum Richardson number and broad waves with higher minimum Richardson numbers are considered, and simulations have been conducted in both two and three dimensions. The three-dimensional simulations show that the generated billows undergo three-dimensional motion in the tail of the internal waves (in a reference frame propagating with the wave crest), potentially affecting their mixing efficiency.

Internal wave generation

For this study, internal waves were generated by taking an initial two-layer stratification of the form:

$$\bar{\rho}(z) = 1 - 10^{-3} \tanh\left(m \frac{z - z_0}{d}\right)$$

where $-100\text{m} < z < 0$ is the vertical coordinate of the domain, z_0 is the location of the centre of the pycnocline, and $m = 2 \tanh^{-1}(0.99)$, such that d is the length scale over which 99% of the density transition occurs. This basic stratification was used as the boundary condition for a numerical solution of the Dubreil-Jacotin-Long equation (Lamb, 2002), which computes solitary waves as a nonlinear eigenvalue problem in terms of the isopycnal displacement $\eta(x, z)$:

$$\nabla^2 \eta - \frac{N^2(z-\eta)}{c^2} \eta = 0,$$

where the eigenvalue c is the resulting phase speed of the wave. The equation is solved iteratively with a continuation method to increase the wave size, measured by its Available Potential Energy (Lamb, 2002).

The resulting waves have an extended region of low Richardson number (< 0.125), and the Taylor-Goldstein equation is solved with the profile at the wave crest to determine the temporal frequency of the perturbation that gives the largest spatial growth rate. This frequency is used to perturb the vertical momentum equation upstream of the wave

Simulation

These waves are imported into a three-dimensional, pseudospectral solver (Subich, 2011) that expands the momentum and density equations with Fourier modes in the (periodic) streamwise and spanwise directions and sine/cosine modes in the vertical direction, as appropriate for no-normal-flow boundary conditions. The computational domain is 1 km long and 100 m deep, with a sponge layer occupying the last 5% of the domain to damp out billows before they exit the domain. For three-dimensional simulations, the spanwise extent was chosen based on the average separation between billows in the wave-tail of the corresponding two-dimensional simulation. The simulation is conducted in a reference frame moving with the internal wave's phase speed, so that the wave profile remains fixed within the domain.

Upstream of the wave, the vertical momentum equation is perturbed with a small ($O(10^{-4})$) forcing in the centre of the pycnocline. These perturbations propagate into the wave, are amplified in the unstable region, and exit at the tail of the wave, carrying some of the wave's energy. For larger waves, these perturbations grow into full Kelvin-Helmholtz billows with statically-unstable regions, where denser fluid overlies lighter fluid. This process is illustrated in Figures 1 and 2.

Development of spanwise structure and motion in these billows generally happens after they have propagated out of the wave crest, consistent with the results of (Barad and Fringer, 2010) for a similar setup involving the free evolution of a density disturbance.

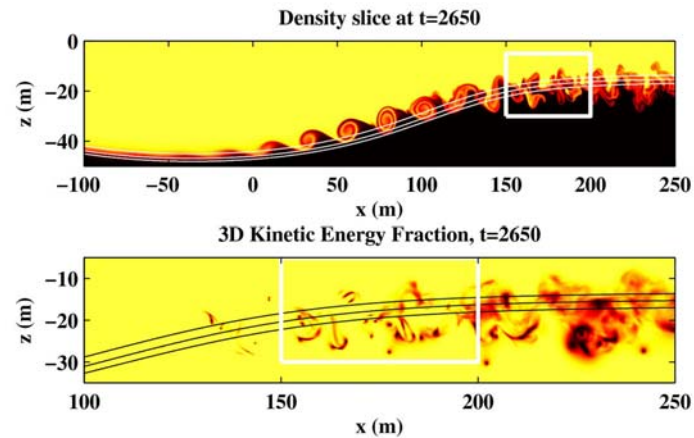


Figure 1: Profile of billow generation in a typical case (darker is denser), along with three-dimensionalization in the wave tail (darker is more three-dimensional). The highlighted region is shown in full profile in Fig. 2.

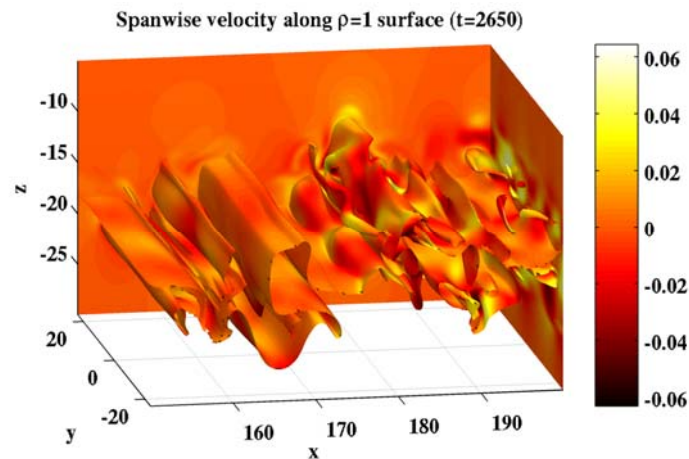


Figure 2: Three-dimensional isosurface of the centre of the pycnocline, of the region highlighted in Fig. 1. The isosurface shading corresponds to spanwise velocity.

References

- Barad, M. F. and Fringer, O. B. (2010). Simulations of shear instabilities in interfacial gravity waves. *Journal of Fluid Mechanics*, **644**:61.
- Lamb, K. G. (2002). A numerical investigation of solitary internal waves with trapped cores formed via shoaling. *Journal of Fluid Mechanics*, **451**:109–144.
- Lamb, K. G. and Farmer, D. (2011). Instabilities in an Internal Solitary-like Wave on the Oregon Shelf. *Journal of Physical Oceanography*, **41**(1):67–87.
- Subich, C. (2011). *Simulation of the Navier-Stokes Equations in Three Dimensions with a Spectral Collocation Method*. PhD thesis, University of Waterloo.

Study on the Physical Mixing Patterns in the St. Clair River by Dye Release

Y. Sun^{1*}, M. Wells¹, S. Bailey², E.J. Anderson³ and D.J. Schwab⁴

¹ Department of Physical and Environmental Sciences, University of Toronto Scarborough, Toronto, Ontario, MIC 1A4, Canada

² Great Lakes Laboratory for Fisheries and Aquatic Sciences, Fisheries and Oceans Canada, 867 Lakeshore Road, Box 5050, Burlington, Ontario, L7R 4A6, Canada

³ Cooperative Institute for Limnology and Ecosystems Research, University of Michigan, Ann Arbor, MI, 48108, USA

⁴ Great Lakes Environmental Research Laboratory, National Oceanic and Atmospheric Administration, Ann Arbor, MI, 48108, USA

*Corresponding author, e-mail yajun.sun@utoronto.ca

KEYWORDS

Aquatic biological invasion; ballast water discharge; dye release; river dispersion;

Summary

Physical dilution patterns of discharged ballast water highly influence the establishment and spread of biological invasions introduced by ballast water discharge. In order to understand the impacts of the dispersion of ballast water in the Great Lakes, we conducted several dye release experiments in 2009. In two trials dye was discharged by ships and in three trials dye was directly released. Observations confirm that ship jets rapidly diluted the solution by a hundred fold due to the high jets' momentum. Three approaches were used to estimate the longitudinal diffusivity K_x and transverse diffusivity K_y . Our results found that K_x was $O(10 \text{ m}^2\text{s}^{-1})$ while K_y was $O(0.1 \text{ m}^2\text{s}^{-1})$ in most regions of the St. Clair River. Analyses also confirm that peak concentration decayed inversely with time.

Introduction

Mixing patterns in rivers are often viewed as two dimensional due to high width/depth ratios (Fischer *et al.*, 1979). With respect to the St. Clair River (width/depth ≈ 80), the mixing pattern is also manipulated by longitudinal mixing (x -direction) and transverse mixing (y -direction), which are determined by longitudinal diffusivity (K_x) and transverse diffusivity (K_y) respectively. Previous research confirms positive relationships between river diffusivities and channel scales, l as: $K = \kappa l u^*$ (u^* is the shear velocity; κ is a dimensionless scale coefficient). With respect to K_x , l refers to the river width, w and κ ranges 2~50; with respect to K_y , l refers to the river depth, d and κ ranges 0.3~3 (Rutherford, 1994). Estimates of diffusivities in rivers based on proposed empirical formulae often come with errors as high as one order of magnitude (Rutherford, 1994). Therefore field work is often desirable to obtain diffusivities in natural rivers, either indirectly by sampling on channel velocities and bathymetry or directly by tracer releases (Carr *et al.*, 2007). In this study we estimated diffusivities in the St. Clair River by dye releases.

Method

Five trials of dye (21% rhodamine) releases were conducted in the St. Clair River in 2009 (Fig. 1). In two trials (Release I & II) rhodamine solutions (3.81 kg and 7.62 kg of net mass, respectively) were added into the ballast water tanks of freighted ships in advance. Dye-mixed ballast water was then discharged from ships and time series were recorded at 32.4 km

downstream by a Turner fluorometer. In three trials (GLOS releases) conducted by the Great Lakes Observing System (GLOS), rhodamine solutions (7.04 kg of net mass in each trial) were directly released in the river. Three release sites were chosen at the centre, east and west side of the river (Centre, East and West Release). For each release, 7~9 transects were monitored at various downstream locations by fluorometers on moving boats. Position of observation was interpreted under the local frame, which sets the x axis along the Canadian-U.S. international boundary line (see the yellow line in Fig. 1) in the middle of the river and the y axis along the transverse direction, increasing from the U.S. to Canadian side. Hence each pair of (x, y) means the downstream distance and transverse distance of each observation. Under the assumption of “frozen cloud” during the measuring periods, each transect was transformed into a 2D spatial profile by linear interpolation. Three approaches were applied to estimate diffusivities in the St. Clair River: (i) both K_x and K_y were estimated on three 2D spatial profiles from transect A, B and C (See Fig. 1) based on the definition of diffusivity, i.e. increase of tracer variances over time; (ii) longitudinal diffusivity was estimated based on downstream observed time series whose time span was proportional to the root of K_x ; (iii) a composite diffusivity $K_{xy} = (K_x K_y)^{1/2}$ was estimated based on log-regression of peak concentration to time (by all the transects: 7~9 for each GLOS release).



Figure 1. This shows the field area where dye solutions were released and measured. The yellow line in the middle of the river is the international boundary between Canada and U.S.

Results and discussion

The observed peak concentration of Release I and II at the downstream measuring location were about 0.8 and 1 ppb, which were decreased by four orders of magnitude from the initial concentration. The interpolated 2D spatial profiles of GLOS releases confirmed that tracer clouds increased in size and decreased in concentration over time. All of the spatial profiles were transversely limited to a high extent. The log regression of peak concentration C_{max} to time confirmed that the peak concentration decreased inversely over time since release: $\log(C_{max}) = -1.23\log(t) + 12.74$ ($R^2=0.93$), where t is time since release. The obtained slope is

close to -1, consistent with the 2D mixing model. One difference between the Release I & II and GLOS releases was on the total dilution ratios, about 10,000 for the former and 100 for the latter, measured ten hours after release. The additional 100-fold dilution in Release I & II was attributed to the jet mixing associated with the ship discharging. Another difference between the two sets of trials was the observed advection velocities: about 1 ms^{-1} for GLOS releases while about 0.5 ms^{-1} for Release I & II. This difference could be attributed to the transverse velocity shear, because there was lower flow velocity near the river banks where the two time series were measured for Release I & II.

Estimates of diffusivities were summarized in Table. 1. Despite the wide range of diffusivities, estimates are fairly consistent among the different approaches and different trials: the longitudinal diffusivity K_x was $O(10 \text{ m}^2\text{s}^{-1})$ and the transverse diffusivity K_y was $O(0.1 \text{ m}^2\text{s}^{-1})$ in most regions of the St. Clair River. Estimates of K_x were on the same order of magnitude with the estimates by numerical modeling (Shen et al., 2010). Composite diffusivity K_{xy} was $O(1 \text{ m}^2\text{s}^{-1})$, consistent with the result of log regression. The scale coefficients were obtained as $\kappa_x = K_x/(wu^*) \approx 1$ and $\kappa_y = K_y/(du^*) \approx 0.6$ in the St. Clair River. The κ_y was well within the reported range while κ_x was lower than those of many other rivers (Rutherford, 1994). The low κ_x might partly be attributed to the transversely limited tracer clouds, which were less subject to the transverse shear effects that often contribute to additional mixing. The high difference between K_x and K_y accounts for the transversely limited mixing in the St. Clair River. Therefore discharged solution (e.g., ships' ballast water) near either side of the river will stay close to that side. According to the reaction-diffusion model, the downstream lake (Lake St. Clair) could be more vulnerable to biological invasions introduced by ballast water discharge due to relatively weak mixing in lakes ($0.02 \text{ m}^2\text{s}^{-1}$ to $0.3 \text{ m}^2\text{s}^{-1}$) (Drake et al, 2005).

Table 1. This lists the experimental results. C_0 refers to initial concentration. Estimates of K are categorized into two groups: two releases by ships (Release I & II) and three GLOS releases. Estimates are given in the form as mean (low, high).

Release	Date (dd/mm)	River flow (m^3s^{-1})	C_0 (ppb)	K_x (m^2s^{-1})	K_y (m^2s^{-1})	K_{xy} (m^2s^{-1})
I	16/07	5120	11,700	34	-	-
II	18/07	5050	17,000	(6, 81)		
GLOS (centre)	18/08			30	0.17	0.21
GLOS (east)	19/08	4900	110	(16, >100)	(<0.1, 4)	(<0.1, 15)
GLOS (west)	20/08					

REFERENCES

- Carr, M.L. and Rehmann, C.R. (2007). Measuring the dispersion coefficient with Acoustic Doppler Current Profilers. *Journal of Hydraulic Engineering* 133(8): 977-982.
- Drake, J.M., Lodge, D.M. and Lewis, M. (2005). Theory and preliminary analysis of species invasions from ballast water: controlling discharge volume and location. *American Midland Naturalist* 154(2): 459-470.
- Fischer, H.B., List, E.J., Koh, R.C.Y., Imberger, J., and Brooks, N.H. (1979). *Mixing in Inland and Coastal Waters*, Academic, New York.
- Rutherford, J.C. (1994). *River Mixing*. West Sussex, England.
- Shen, C., Niu, J., Anderson, E.J. and Phanikumar, M.S. (2010). Estimating longitudinal dispersion in rivers using Acoustic Doppler Current Profilers. *Advances in Water Resources* 33: 615-623.

Near Inertial Poincaré Waves in Lake Michigan

C. Troy^{1*}, S. Ahmed¹, T.C. Hsieh¹, J. Chen¹, and N. Hawley²

¹ *Hydraulics and Hydrology Group, School of Civil Engineering, Purdue University, West Lafayette, IN, USA*

² *NOAA Great Lakes Environmental Research Laboratory, Ann Arbor, MI, USA*

*Corresponding author, e-mail troy@purdue.edu

KEYWORDS

Internal waves; Great Lakes; physical limnology; Poincaré waves; thermal stratification

EXTENDED ABSTRACT

INTRODUCTION

Near-inertial internal Poincaré waves dominate the internal wave field in Lake Michigan, having an ubiquitous signature on offshore currents (Mortimer, e.g. Mortimer 2004). As such, we hypothesize that they may govern the lateral dispersion of substances in the lake's interior, control cross-thermocline mixing away from the shore, and may regulate bottom boundary layer turbulence and exchange in the deeper locations of the lake. The degrees to which Poincaré waves locally impact each of these processes are largely governed by the spatial structure of the dominant modes excited by the wind, which is what this study seeks to elucidate.

Because of Lake Michigan's large size (approximately 500km by 135km), the associated Burger number is consistently $O(10^{-1})$ or less, rendering all of the primary Poincaré modes to be of near-inertial period (Csanady 1967; Antenucci and Imberger 2001). In addition, the near-inertial period of these waves means that they are better classified as rotational waves weakly modified by gravity (and not vice-versa), with most energy portioned as kinetic. The waves effect only very moderate thermocline displacements of several meters or less, even near the shore where amplitudes should be largest; in this way these waves are quite different than the large amplitude shoaling internal waves seen in the coastal ocean and smaller lakes. For this reason, the role of these seiches in basin-scale mixing is unknown, and likely different than our growing understanding of the role of oceanic internal waves in basin-scale mixing (boundaries + internal waves = mixing).

METHODS

In this work we examine several data sets in order to better characterize Lake Michigan's Poincaré wave structure as it relates to vertical mixing, horizontal dispersion, and other issues of interest. Two data sets (and ongoing measurements), from 2009 and 2010, characterize the nearshore cross-shelf structure of Poincaré wave-induced thermocline motions and currents. Additional NOAA-GLERL data sets from a deep location (160m) in the southern basin of Lake Michigan are used to characterize the deepwater influence of these waves, where thermocline displacements are negligible but near-inertial currents are strong (e.g. 50cm/s).

RESULTS AND DISCUSSION

Nearshore Poincaré wave structure

From two 20km-long cross-shelf transects near Michigan City, IN and Muskegon, MI (south and eastern Lake Michigan coasts, respectively), the cross-shelf distributions of Poincaré wave-induced (near-inertial) thermocline displacements have been determined (Figure 1). These data, averaged over a two month period during summer stratification, demonstrate the very modest thermocline displacements associated with the dominant Lake Michigan seiche as well as the subtle cross-shelf structure for actual bathymetry.

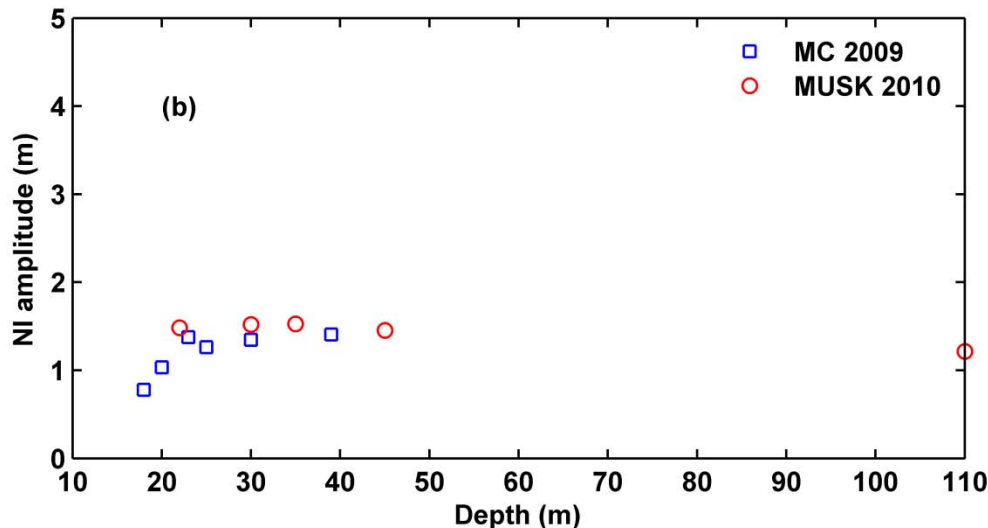


Figure 1. Cross-shelf structure of near-inertial Poincaré wave-induced thermocline displacements from two transects (Michigan City and Muskegon). Wave amplitudes – expected to be largest near the shore - are very modest because of the near-inertial period of the seiche.

Deepwater influence of Poincaré waves in Lake Michigan

A two-year ADCP record from the southern basin of Lake Michigan (1999-2001; and a single-point current meter) shows the profound influence of the dominant near-inertial internal seiche on mid-lake currents. In brief, two findings are notable: (1) the magnitude of near-inertial surface currents is extraordinarily large, sometimes approaching 50cm/s, and persistently more than 20cm/s for the entirety of the “stratified period”; (2) the “stratified period” as it pertains to near-inertial Poincaré waves appears to span the majority of the calendar year, roughly from early spring through late December, suggesting that even several degrees of top-to-bottom thermal difference is enough to support these waves. The latter result suggests that the influence of these waves is temporally much more extensive than the conventional wisdom that internal waves are restricted to the strongly-stratified summer period.

REFERENCES

- Antenucci, J.P., and J. Imberger (2001). Energetics of long internal gravity waves in large lakes, *Limnol. Oceanogr.*, 46(7), 1760-1773.
- Csanady, G.T. (1967). Large scale motion in the Great Lakes, *J. Geophys. Res.*, 72(16), 4151- 4162.
- Mortimer, C. H. (2004). Lake Michigan in Motion-Responses of an Inland Sea to Weather, Earth-Spin, and Human Activities. University of Wisconsin Press.

Poincaré Waves in the Central Basin of Lake Erie

Reza Valipour,¹ * Leon Boegman,¹ Damien Bouffard,¹ and Yerubandi R. Rao²

¹*Environmental Fluid Dynamics Laboratory, Department of Civil Engineering, Queen's University, Kingston, Ontario, K7L 3N6, Canada*

²*Environment Canada, Water Science & Technology, National Water Research Institute, Canada Centre for Inland Waters, Burlington, Ontario L7R 4A6, Canada*

*Corresponding author, e-mail: Reza.Valipour@ce.queensu.ca

KEYWORDS

ELCOM; horizontal modes; Lake Erie; Poincaré wave; vertical modes.

EXTENDED ABSTRACT

Poincaré waves are the dominant wind induced large scale internal waves in the central basin of Lake Erie. They play a crucial role in driving physical processes, such as vertical mixing, which influence biogeochemistry. Apart from the well-known near inertial period of these waves (~17 h), the vertical and horizontal modal structure and of the waves are poorly understood (e.g. Rao et al. 2008).

To clarify the Poincaré wave modal structure in central Lake Erie, extensive field measurements, including high resolution temperature, and velocity were collected during the summers of 2008-2009 in the central basin of Lake Erie. The data set is part of a larger project to investigate the lakes hypoxia problem (e.g. Boegman et al. 2008). Water temperatures were recorded at stations 341, 1227, 1228, and 1231 (these stations are located between the central and western basins of the lake) using temperature loggers (TR-1050/ TR-1060, RBR Ltd., Canada) sampling at an interval of 10 s with an accuracy of $\pm 0.002^\circ\text{C}$. The moorings were operated continuously from May 2008 to October 2008 and similarly in 2009. A 1.8 m-tripod was also deployed at a depth of 17.5 m on the bottom of Lake Erie at station 341. The tripod was equipped with an upward looking acoustic Doppler current profiler (ADCP, Nortek AS, Norway) at height 1.8 meter above the bottom with the accuracy of 1% of measured value. It recorded velocity with sampling period of 1 second every 15 minutes in separate 1 m cells with burst (average) interval of 180 second to the surface. Meteorological data were obtained from a metrological buoy at station 341 that recorded average wind speed and direction every 10 min. It should be noted that the stations are located 10 km apart.

The vertical mode-one Poincaré wave was found to be dominant during the seasonal stratified period (Figure 1). After a wind event, there is first an increase in barotropic energy followed by vertical mode one and vertical mode-two Poincaré waves, as dominant baroclinic components. The horizontal modal structure was investigated in a sensitivity analysis, using idealized wind forcing to drive a three-dimensional hydrodynamic transport model. The model revealed a horizontal mode-two structure consisting of cells in both the central and eastern basins. In each cell, the Poincaré wave travels in a clockwise direction, in agreement with linear wave theory. Progressive vector diagrams and velocity data are employed to show the role of Poincaré waves in local movement of water particles and residual circulation in the central basin of the lake.

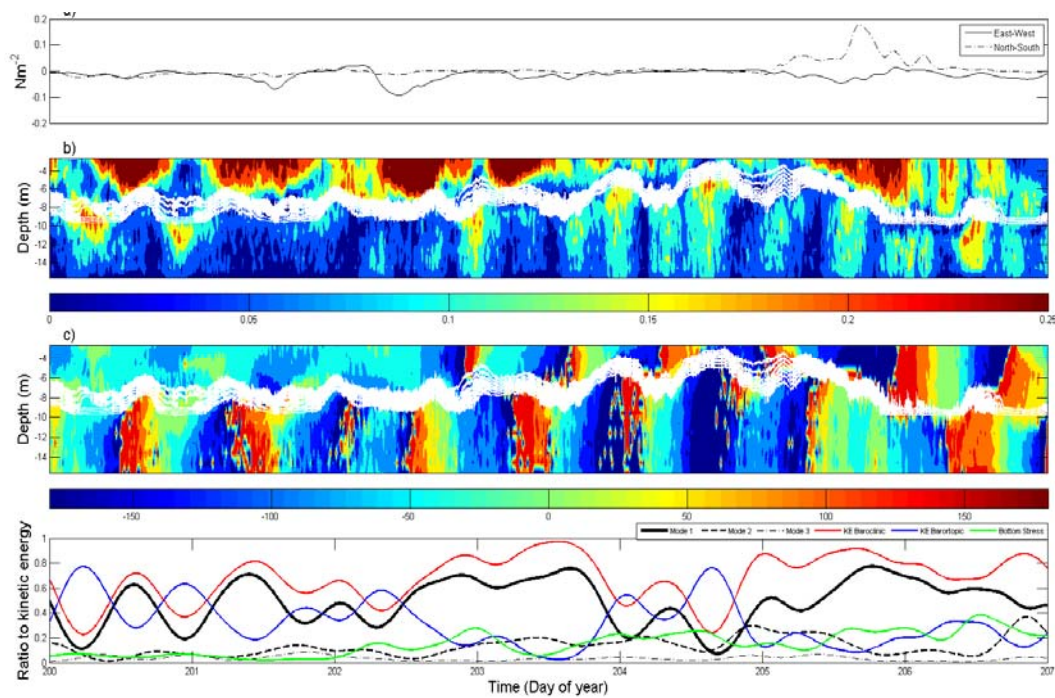


Figure 1. Time series of wind stress obtained from the quadratic law (Rao et al. 2008) and velocity structure at station 341 for the summer 2009. [a] The time series of wind stress. [b] Background plots are observed absolute velocity structures, the white lines showing the 10 second isotherms of 12, 13, 14, 15, 16, 17 and 18 °C. [c] Background plots are observed phase velocity structures, 0 and -180 is direction from west to east, +180 is direction from east to west, the white lines showing the 10 second isotherms of 12, 13, 14, 15, 16, 17 and 18 °C. [d] The low passed filtered (15h<) of normalized energy distribution of total baroclinic (baroclinic energy/total energy, total energy=baroclinic+barotropic), barotropic (barotropic energy/total energy), bottom stress, bottom stress/ (maximum observed bottom stress), time series of vertical energy for different modes. The normalized energy of different vertical mode means that the time series values are divided by the total kinetic energy (barotropic energy and baroclinic energy) at station 341 for a particular time.

REFERENCES

- Boegman, L., Loewen M.R., Culver, D.A., Hamblin, P.F. and Charlton, M.N. (2008). Spatial-dynamic modeling of algal biomass in Lake Erie: Relative impacts of Dreissenid mussels and nutrient loads. *J. Environmental Eng. - ASCE*. 134(6): 456-468.
- Rao, Y. R., Nathan Hawley, Murray N. Charlton and Schertzer W. M. (2008). Physical processes and hypoxia in the central basin of Lake Erie. *Limnol. Oceanogr.*, 53(5).

Thermal Variability within a Complex Branching Estuarine System

R.W. Wagner^{1*} and M. Stacey¹

¹ 665 Davis Hall, University of California, Berkeley, Department of Civil and Environmental Engineering, 94720-1710

*Corresponding author, e-mail wagnerw@berkeley.edu

KEYWORDS

Conference; conference paper; thermal variability; branching estuary.

EXTENDED ABSTRACT

Branching tidal channel systems confound simple modeling efforts for resolving small-scale advection and mixing processes within them. These processes determine the creation and breakdown of gradients of ecologically important scalars (e.g. salt or temperature). In light of this, field measurements and work is necessary to inform the effects of within channel transport and mixing on the region's thermal environment, including the effects of exchanges between intersecting channels or between channels and shallow habitats.

We present results of two field campaigns to assess thermal mixing processes in the Cache Slough/Liberty Island (CSLI) complex within California's Sacramento-San Joaquin Delta (the Delta). The Delta is an inland estuary at the upstream end of the San Francisco Bay Estuary with waters from the Sacramento and San Joaquin Rivers, primarily, mixing with salt water from San Francisco Bay. The CSLI complex is singled out because it is "typical" within the Delta, containing tidal sloughs, flooded "islands," and the input of fresh water from the nearby Sacramento River, but also because it has been identified as a model for future restoration efforts in the Delta due to discovery of important species using the flooded island as habitat.

For both field campaigns, we deployed thermistors; conductivity, temperature, and depth (CTD) sensors; and an acoustic Doppler current profiler (ADCP) within a cross section of Cache Slough. We observed the creation and breakdown of large thermal gradients within the cross section, both vertically and horizontally, on a variety of time scales. Principal component analysis (Figure 1) indicates that although much of the vertical gradients are due to local heating and cooling, fluxes of thermal gradients from adjoining channels and from shallow habitats nearby are likely also important.

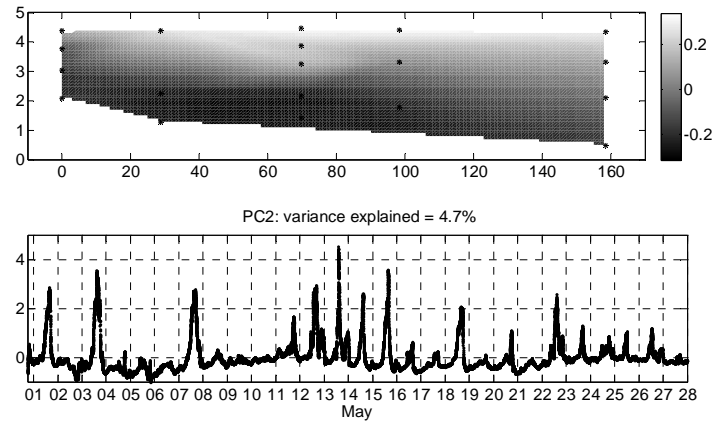


Figure 1: Principal component (PC) analysis of the cross sectional temperature: PC2. The upper panel shows the eigenvector of PC2 with the x-axis representing lateral distance within the cross section and the y-axis representing vertical distance within the cross section; the lower panel displays the time series of PC2. Stars represent thermistor locations. The upper panel shows that this PC represents the vertical stratification within the cross section. The lower panel shows that this stratification is largely varying on diurnal time scales.

Further, we analyze the interaction between density gradients resulting from these thermal gradients and the transport within the cross section (Figure 2). Lateral overturning within the cross section serves to mix out thermal (and other) gradients, while vertical stratification serves to limit mixing within the cross-section. Scaling analyses of the cross channel momentum budget indicates temporally-varying controls on mixing in the cross section.

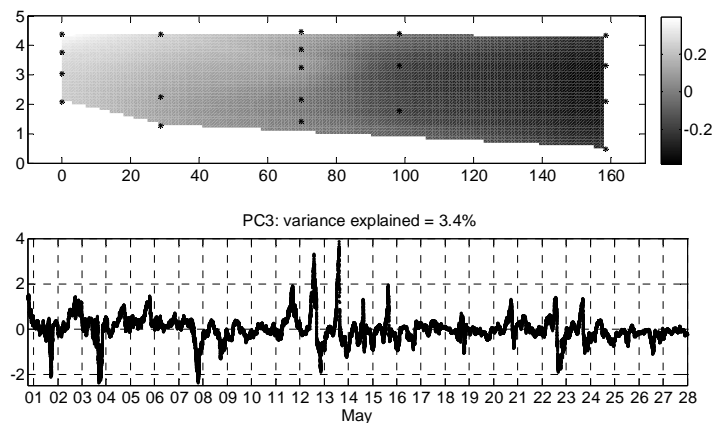


Figure 2: Principal component (PC) analysis of the cross sectional temperature: PC3. The upper panel shows that this PC represents the lateral temperature gradients within the cross section. The lower panel shows the complexity of the time variance of this PC, varying on both diurnal and tidal time scales.

Atmospheric conditions appear to dominate the thermal dynamics within this system; however, lateral temperature gradients are variable on what appears to be both the tidal and diurnal timescales and that lateral circulation appears to be tied to lateral density (temperature) forcing, although the effects of wind and channel curvature may contribute. This work leads to an improved understanding of transport and mixing in branching deltaic channels near channel junctions and adjacent to channel/island intersections.

Internal wave driven transport of fluid away from the boundary of a lake

D.J. Wain^{1*}, M.S. Kohn², J.A. Scanlon², and C.R. Rehmann²

¹ Applied Physics Laboratory, University of Washington, Henderson Hall, Seattle, WA 98105

² Department of Civil, Construction, and Environmental Engineering, Iowa State University, Town Engineering Building, Ames, IA 50011

*Corresponding author, e-mail wain@apl.washington.edu

KEYWORDS

Internal waves, turbulence, mixing, tracer studies, boundary-interior communication

Stratification in lakes inhibits the transport of nutrients, gases, and other dissolved substances. As a result, mixing induced from wind disturbances may play a vital role in transporting dissolved and suspended substances. When a lake is stratified, mixing can originate from wind induced internal waves interacting with the boundaries of basins (e.g., MacIntyre *et al.* 1999). Along with mixing caused by internal waves, intrusive layers have been observed transporting mixed boundary fluid offshore (Gloor *et al.* 2000, Marti and Imberger 2008, Wain and Rehmann 2010).

To investigate offshore transport of fluid from a lake boundary into the interior, an experiment that combined measurements of meteorological forcing and profiles of temperature and temperature microstructure with a dye release was performed in West Okoboji Lake in northwest Iowa (Fig. 1). The lake has a surface area of 15.6 km², a length of about 9 km, a mean depth of 12 m, and a maximum depth of 41 m. During the experiment, meteorological conditions were measured every 15 s by a Lake Diagnostic System located in the south end of the lake (Fig. 1), water temperature profiles were measured at the LDS and at another thermistor chain located at the north end of the lake, and turbulence was measured with a temperature microstructure instrument. Rhodamine WT was injected in the metalimnion to track fluid from the slope moving into the interior. The dye was tracked using a tow-yo

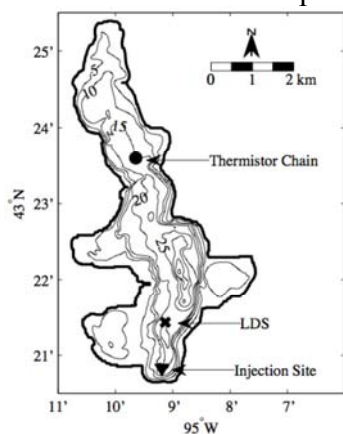


Figure 1. Bathymetric map of West Okoboji Lake with depth contours marked every 5 m.

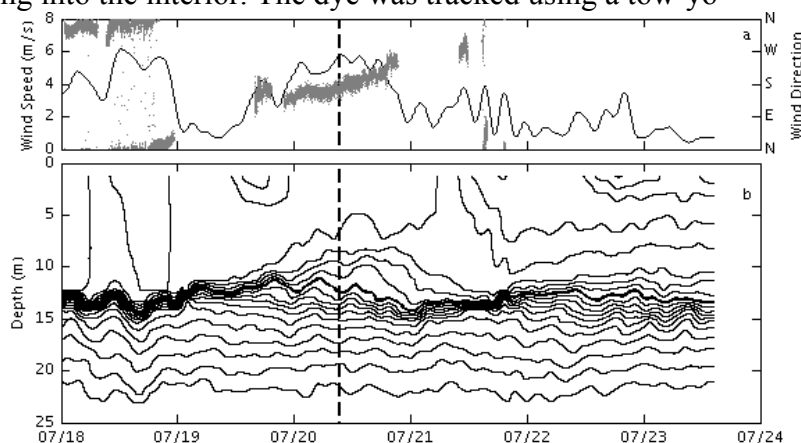


Figure 2. (a) Filtered wind speed (along with the wind direction when the Lake number was below 10). (b) Depths at the LDS of the 14°C-22.5°C isotherms (spaced at 0.5°C) before and during the tracer study. The thick line denotes the injection isotherm (19°C) and the dashed line marks the injection time.

method with a fluorometer that was integrated with a global positioning system and conductivity, temperature, and depth (CTD) profiler so that concentration, temperature, depth, and position could be sampled simultaneously.

The ability of the stable stratification to resist the overturning moment caused by the wind was quantified with the Lake number. The vertical eddy diffusivity was estimated from a heat budget, temperature microstructure, and vertical spreading of the dye. Temperature profiles from the LDS and the thermistor chain were used to compute the diffusivity with the heat budget method of Jassby and Powell (1975). Temperature microstructure was used to compute the dissipation of temperature variance χ_T and then the vertical eddy diffusivity. The vertical eddy diffusivity was also estimated from moments of the dye concentration distribution. The horizontal eddy diffusivity K was computed from the horizontal spreading of the dye.

Isotherm depths were computed by interpolating between temperatures measured by the LDS. Fig. 2 provides the depths of all the isotherms during the study period along with the wind forcing. The changes in metalimnetic thickness indicate a vertical mode two -2 response to the wind forcing. As the natural period of the V2H1 wave is over 40 hours, the 16 hours between the wind events on 7/18 and 7/19-20 did not allow for free oscillation of the metalimnion. Instead, the second wind event enhanced the metalimnetic compression at the north end and expansion of the metalimnion on the south end. This wind event lasted for approximately 29 hours; it was during this time the dye was injected.

Vertical eddy diffusivity K_{zm} from temperature microstructure measurements provided no clear evidence for boundary mixing. At both the LDS and thermistor chain, the vertical eddy diffusivity K_{zt} computed with the heat budget method decreased to a local minimum on the order of 10^{-5} m^2/s at a depth of 15 m and increased again. The dye cloud, as indicated by the horizontally averaged concentration profiles, extended approximately 2.1 m from 12.2 m to 14.3 m depth during the dye survey centered at 10.5 h after the injection. The survey centered at 29.2 h after the injection showed that the cloud spread and sank; it extended 3.5 m from 12.3 m to 15.8 m depth. The vertical eddy diffusivity K_{zd} calculated with from the moments was 4×10^{-6} m^2/s .

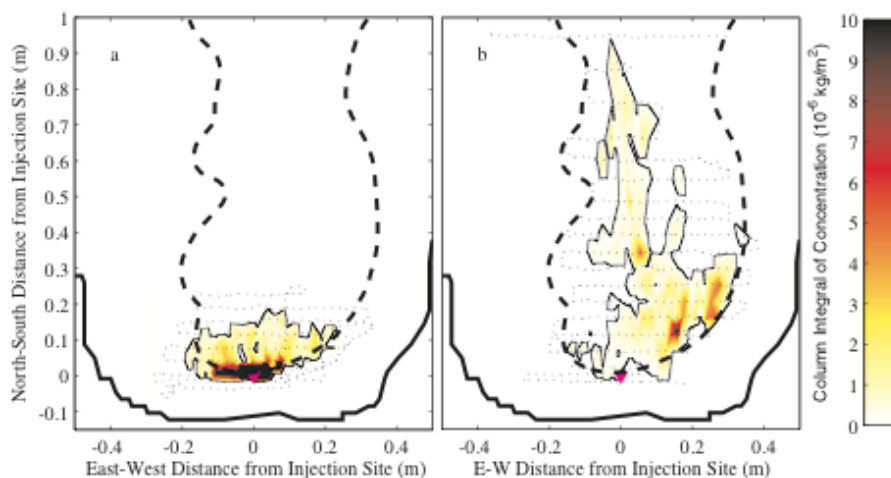


Figure 3. The dye map surveys centered at (a) 10.5 h after injection (9.3-11.8 h) and (b) 29.2 h after injection (25.8-32.6 h), with the lake perimeter (heavy black line), the injection isobath of 13.25 m (dashed black line), boat track (dotted line), and injection site (magenta triangle).

The horizontal dispersion of the dye was investigated with the surveys at 10.5 and 29.2 h after the injection (Fig. 3). At 29.2 h after the injection, the dye spread about 950 m into the lake. Assuming no advection, a modified moment analysis (to account for the wall) yielded $K = 0.6 \text{ m}^2/\text{s}$. But while there is no mean advection in the lake, the observed V2H1 motions can generate a metalimnetic jet, which may transport fluid into the interior (Marti and Imberger 2008). After frequencies at which displacements are not coherent between the thermistor chains were eliminated with a low pass filter, a first horizontal mode seiche structure was assumed and the velocity field was estimated from the isotherm displacements. To investigate the spreading due to advection along the lake axis, we integrated the dye concentration across the lake and vertically through the dye cloud to construct a 1-D model of the dye cloud and applied the estimated velocity field to the dye cloud measured at 10.5 h (Fig. 4); 80% of the along-lake variance of the dye cloud at 29.2 h could be attributed to the advective field. To explain the remaining variance, $K = 0.1 \text{ m}^2/\text{s}$ is required. The effective horizontal diffusivity estimated from shear dispersion from the internal wave field (Young *et al.* 1982) varies between 0 (at the walls) and $10 \text{ m}^2/\text{s}$ (at the center of the lake). For each time step in Fig. 4, we can compute a concentration-weighted average K over the dye cloud (Fig. 5), showing that shear dispersion from the internal wave field might be sufficient to explain the remaining spreading. Both the velocity and the horizontal diffusivity at the wall are zero, but if mixed fluid moves off the boundary by some other mechanism, the internal wave driven advection and diffusion can draw fluid away into the interior. We continue to investigate other mechanisms that might contribute to the spreading of the dye cloud.

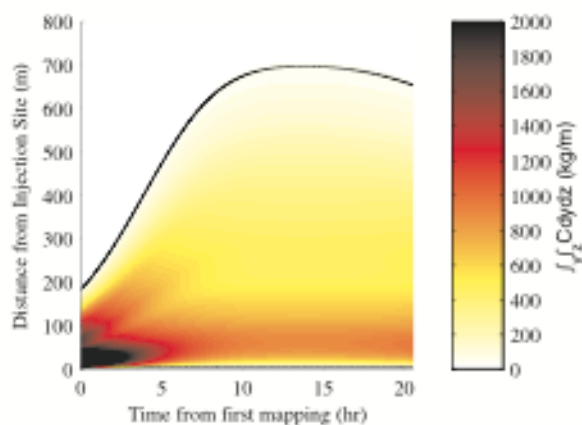


Figure 4. Model prediction of spreading of dye cloud due to horizontal velocity gradients.

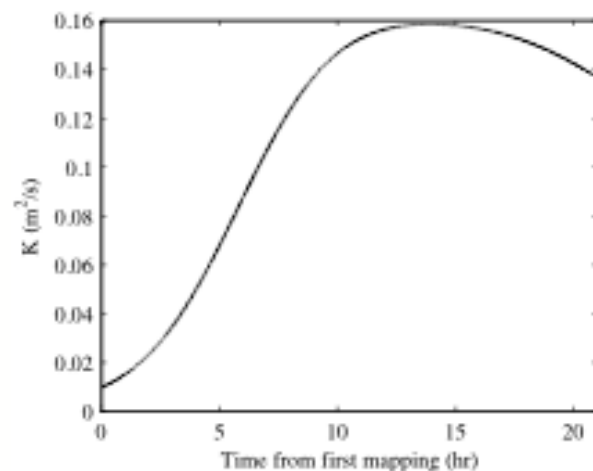


Figure 5. Mass-weighted horizontal dispersion as a function of time.

- Gloor, M., Wüest, A., and Imboden, D.M. 2000. Dynamics of mixed bottom boundary layers and its implications for diapycnal transport in a stratified, natural water basin, *J. Geophys. Res.*, 105: 8629-8646.
- MacIntyre, S., Flynn, K.M., Jellison, R., and Romero, J.R. 1999. Boundary mixing and nutrient fluxes in Mono Lake, California, *Limnol. Oceanogr.*, 44:512-529.
- Marti, C.L., and Imberger, J. 2008. Exchange between littoral and pelagic waters in a stratified lake due to wind-induced motions: Lake Kinneret, Israel. *Hydrobiologia*, 603: 25-51.
- Wain, D.J., and Rehmann, C.R., 2010. Transport by an intrusion generated by boundary mixing, *Water Resour. Res.*, 46: W08517, doi:10.1029/2009WR008391.
- Young, W.R., Rhines, P.B., and Garrett, C.J.R., 1982. Shear flow dispersion, internal waves and horizontal mixing in the ocean, *J. Phys. Oceanogr.*, 12: 515-527.

Great Lakes Climate and Ice Research: Diagnosis and Modeling

Jia Wang

NOAA Great Lakes Environmental Research Laboratory, Ann Arbor, MI 48108 USA

Jia.wang@noaa.gov

The impacts of ENSO (El Nino and South Oscillation) and Arctic Oscillation (AO) on the Great Lakes ice cover were investigated using ice observations for winters 1963-2010, and NCEP reanalysis data. Signatures of ENSO and AO were found in the Great Lakes ice cover. However, the impacts are nonlinear and asymmetric. Strong El Nino events are often associated with least ice cover on the Great Lakes, while the impacts of weak El Nino and La Nina events on the Great Lakes are marginally significant. Negative AO events are often associated with severe ice cover, while positive AO event has smaller impact. The strong El Nino and negative AO events explained about 50% severe and least ice cover winters on the Great Lakes, respectively. The interference of the effects of ENSO and AO over the Great Lakes makes the relationships complicated. This may be an important cause of nonlinear and asymmetric responses of the regional climate including lake ice in the Great Lakes to ENSO and AO. In addition, case-to-case investigations of lake ice cover in response to extremely anomalous weather/climate events are conducted.

A coupled Great Lakes Ice-circulation Model (GLIM) was implemented in Lake Erie to investigate synoptic variations and seasonal cycle of lake ice and circulation under daily and hourly atmospheric forcing. The model has been validated using satellite and in situ measurements. Furthermore, a 5-lake unstructured grid model is also implemented for regional climate change (ice, hydrodynamics, and ecosystems) studies in response to large-scale climate change.

The dilution and dispersion of ballast water discharged into harbours of the Great Lakes.

M. Wells¹, S.A. Bailey^{2,3} and B. Ruddick⁴.

¹ *1 Department of Physical and Environmental Sciences, University of Toronto Scarborough, Toronto, Ontario, M1C1A4.*

² *Great Lakes Laboratory for Fisheries and Aquatic Sciences, Fisheries and Oceans Canada, 867 Lakeshore Road, Box 5050, Burlington, Ontario, L7R 4A6.*

³ *Great Lakes Institute for Environmental Research, University of Windsor, 401 Sunset Avenue, Windsor, Ontario, N9B 3P4*

⁴ *Department of Oceanography, Dalhousie University, Halifax, Nova Scotia,*

*Corresponding author, e-mail wells@utsc.utoronto.ca

KEYWORDS

Biological Invasions, Great lakes, Harbors.

EXTENDED ABSTRACT

Observations are presented on dilution and dispersion rates of ballast water discharged under normal operational conditions at the semi-enclosed port of Goderich, Ontario. The ballast water was tagged with Rhodamine-WT dye and microscopic magnetically-attractive tracer particles. Maximum concentrations of dye immediately after discharge were diluted to 1-5% of initial ballast tank concentrations, and within 3 days had decreased to less than 0.1 % of initial concentrations. Inside the harbor, there was 10-20% of the ballast water still present after 2 days, consistent with a flushing rate of 0.8-1.15 day⁻¹. Magnetic particles were collected up to 7.5 km outside the harbor after one day, consistent with a dilution factor of order 10⁵ outside the harbor. The results of this study are discussed in the context of ballast water discharge standards proposed by the International Maritime Organization to minimize the introduction of aquatic nonindigenous species through ships' ballast water and sediments.

Ballast water carried by commercial ships is presumed responsible for 55-70% of aquatic nonindigenous species' (ANS) introductions to the Great Lakes since 1959 (Ricciardi, 2006). Beginning in 1989, various voluntary and mandatory ballast water management practices have been introduced to ameliorate the risk of ship-mediated introductions to the Great Lakes. An international convention to regulate ballast water discharges was also adopted to reduce ballast-mediated introductions globally, primarily through the use of physical and/or chemical treatment systems (IMO, 2004). The international convention, once ratified, will set density-based discharge standards, including a standard applicable to zooplankton (<10 individuals greater than 50 µm in minimum dimension per m³, summed over all species; IMO, 2004).

The theoretical efficacy of the proposed standard is based on 'propagule pressure theory', wherein establishment success is positively related to characteristics of the propagule supply (i.e., the total number of propagules released and frequency of inoculation events. For sexually-reproducing taxa, this relationship can be understood in terms of basic population demographics, such as birth and death rates, immigration events and Allee effects. The expectation is, that if the number of propagules in ballast water can be reduced below some threshold inoculum size, then the population growth rate becomes negative and the

probability of successful establishment will be zero. Empirical evaluation of the proposed ballast water discharge standards is extremely difficult because threshold densities for successful establishment are unknown, and are likely species- and system-specific (see Bailey et al., 2009).

Understanding the spatial dispersion of propagules post-discharge further complicates estimates of establishment probability. After the initial release of ballast water, the growth of introduced populations will depend upon how rapidly the population can increase through reproduction, compared to the rate at which the density decreases due to losses, such as through physical dispersion of aquatic organisms. If a population is dispersed faster than it can reproduce, then the population density will decrease until extinction. Conversely, a population discharged into a habitat that supports a reproduction rate which is greater than the rate of loss can increase in density and establish a local foothold. Introductions into sheltered areas may increase establishment probabilities of low-density inocula if the inoculum is maintained within a cohesive unit of water. As an example, in the Great Lakes, ballast water is almost exclusively discharged while ships are at port— often sheltered areas with limited rates of water exchange.

In our presentation we will describe the spatial dispersion of ballast water after discharge into a semi-enclosed port, with a view to improve understanding of the dispersal of released propagules. While there have been numerical simulations of the spread of ballast water after release and some technical literature is available on the short-range dilution of ballast water the work described in Wells et al (2011) is the first study to empirically examine dilution and dispersion of ballast water in the context of species' introductions. Results are presented from an experiment in 2008 designed to measure and quantify a) the dilution rate of ballast water post-discharge; b) the residence time of ballast water in Goderich Harbor; and c) the transport of propagules over large distances outside the harbor. Dye and magnetically-attractive particles were used to track discharged ballast water and to estimate residence time of water in Goderich Harbor. The residence time in the harbor is then compared to biological growth rates of zooplankton species, and a discussion is presented of the impact of dilution rates as a potentially important factor in determining the risk of ANS establishment.

Bailey, S.A., Velez-Espino, L.A., Johannsson, O.E., Koops, M.A., and Wiley C.J., (2009). Estimating establishment probabilities of Cladocera introduced at low density, an evaluation of the proposed ballast water discharge standards. *Can. J. Fish. Aquat. Sci.* 66(2), 261-276.

IMO (International Maritime Organization), (2004). The International Convention for the control and management of ships ballast water and sediments, adopted 13 February, 2004.

Ricciardi, A., (2006). Patterns of invasion in the Laurentian Great Lakes in relation to changes in vector activity. *Diversity Distrib.* 12, 425-433.

Wells, M.G., Bailey, S.A., and Ruddick, B. (2011) The dilution and dispersion of ballast water discharged into Goderich Harbor. *Mar. Poll. Bull.* (in press) doi: 10.1016/j.marpolbul.2011.03.005

Particle- and temperature-related effects by a possible extension of the Grimsel pump-storage scheme on downstream Lake Brienz

Alfred Wüest^{1,2}, Stefan Hunziker¹, Matteo Bonalumi^{1,2}, Martin Schmid¹

¹Eawag: Swiss Federal Institute of Aquatic Science and Technology, Seestrasse 79, CH-6047 Kastanienbaum, Switzerland, alfred.wueest@eawag.ch

²Institute of Biogeochemistry and Pollutant Dynamics, ETH Zurich, CH-8092 Zurich, Switzerland

Due to the uneven demand for power, the retail prices for electricity in the European grid vary by an order of magnitude over the scales of a day and a week. As the electricity production is also irregular (especially the “new-renewable” wind and photovoltaics), and as there is no efficient storage technology available, the water-based pump-storage schemes are used for turning surplus electric energy into potential energy for later peak-demand production. The European Alps are currently the host of various such pump-storage project ideas.

In this presentation, an example of such a possible project is discussed for feasibility. As shown in Figure 1, the already existing three upstream (artificial) reservoirs would be connected among each other and finally connected to the downstream natural Lake Brienz. Currently, the waters from the reservoirs have high suspended inorganic particle concentrations due to the upstream glaciers and are very cold, as the sunlight is hardly entering the turbid water. Although the particle flux scheme would basically remain the same - the sources being the glaciers and the sink being Lake Brienz - the coupling would substantially reduce the reservoir turbidities and thereby increase the water temperatures. Results from a 3-box model analysis are presented and possible effects are discussed.

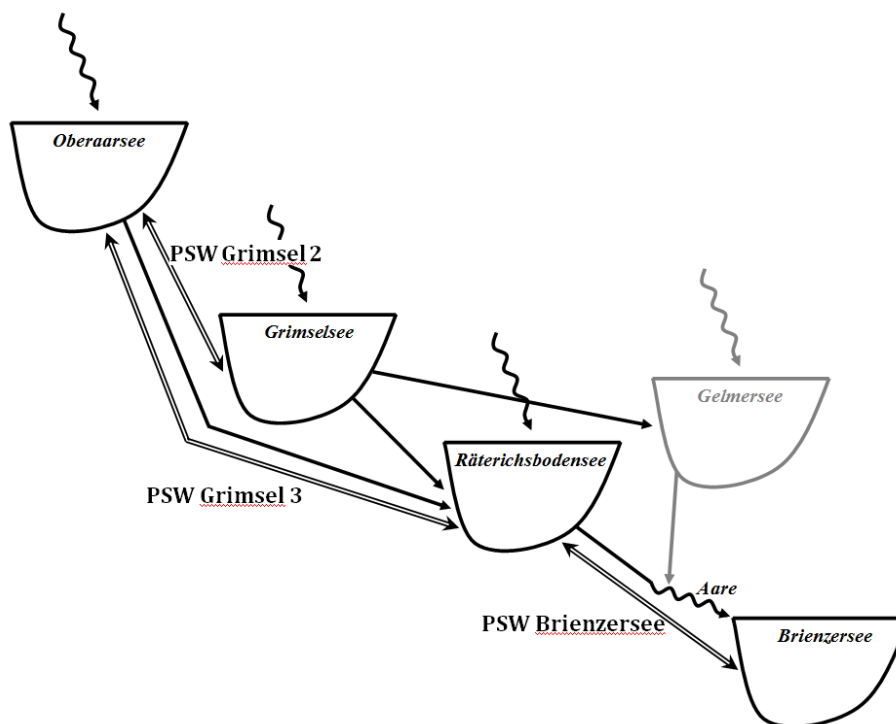


Figure 1. The three upper basins (O, G and R) are artificial dams withholding the water from their catchments for hydropower production. The connections among the basins by the three indicated PSWs, would allow storing water on a higher elevation during periods of low electricity consumption (night, weekends). Critical is the inclusion of a natural lake (Brienzensee) as the lower basin of such a PSW scheme.

Numerical Study of Dispersion and Hydrodynamic Connectivity of Near-Surface Waters in Lake Huron

J. Zhao¹, Y.R. Rao¹, and J. Sheng²

¹National Water Research Institute, Environment Canada, 867 Lakeshore Rd., Burlington, ON, L7R 4A6, Canada

²Department of Oceanography, Dalhousie University, Halifax, NS, B3H 4J1, Canada

Keywords

Numerical model; dispersion; hydrodynamic connectivity; Lake Huron

1. Introduction

Lake Huron is the second largest Laurentian Great Lake and the fifth largest freshwater lake in the world. It contains a volume of 3,540 km³, and a shoreline length of 6,157 km. The Lake has a horizontal dimension of about 330 km east to west and 290 km north to south with a maximum water depth of 230 m and an average water depth of about 60 m. For Lake Huron, habitat is a primary concern. Many nearshore areas of the Lake have been altered due to human influences. To understand the chemical and biological processes that occur in the Lake, and the pathway and destination of the contaminants, we employed a three-dimensional (3D) primitive equation z-level ocean circulation model known as CANDIE (Canadian version of DieCAST, Sheng et al., 1998) to simulate the circulation and dispersion patterns in the Lake.

2. The nested-grid circulation modeling system and particle tracking

The nested-grid modeling system of Lake Huron has two sub-components: a coarse-resolution outer model (2.5 × 2.5 km) covering Lake Huron (LH) and Georgian Bay (GB); and a fine-resolution inner model (0.9 × 0.9 km) covering southeastern of the Lake (Fig. 1). Both the inner and outer models have the same 30 unevenly spaced z-levels in the vertical. The model is forced with monthly mean net heat flux and 12 hourly wind stress calculated from the wind speeds extracted from the NCEP/NCAR reanalysis data with amplitudes modified based on the observed wind in the Lake (Sheng and Rao, 2006).

For tracking movements of passive particles in the surface layer, the particles are assumed to be non-reactive and neutrally buoyant and carried by the monthly mean horizontal currents of the nested-grid modeling system using the following fourth-order Runge-Kutta scheme (Press et al., 1989):

$$\vec{x}(t) = \vec{x}(t_0) + \int_{t_0}^t \vec{u}(\vec{x}, t) dt + \vec{\delta} \quad (1)$$

where $\vec{x}(t)$ and $\vec{x}(t_0)$ are horizontal position vectors of a passive particle at time t and initial time t_0 respectively, $\vec{u}(\vec{x}, t)$ is the horizontal velocity vector of model currents, and $\vec{\delta}$ is additional random horizontal displacements used to represent the influence of physical processes that are not

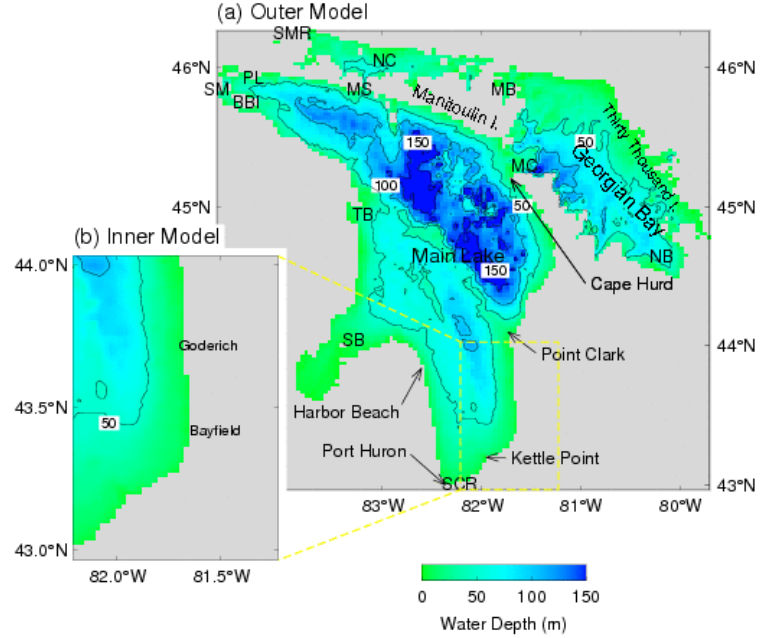


Fig.1 Major bathymetric features for the nested grid modeling system, which consists of (a) the coarse-resolution outer model covering Lake Huron and Georgian Bay, and (b) the fine-resolution inner model covering the southeast shoreline of Lake Huron. Abbreviations are used for St. Mary's River (SMR), St. Clair River (SCR), straits of Macinac (SM), Patrick Landing (PL), Bois Blanc Island (BBI), Mississagi Strait (MS), Main Channel (MC), North Channel (NC), Thunder Bay (TB), Saginaw Bay (SB), Nottawasaga Bay (NB), and Manitowaning Bay (MB).

modeled explicitly in this study. We follow Hannah et al. (1998) and express $\vec{\delta}$ as

$$\vec{\delta} = (\xi\sqrt{2\kappa\Delta t}, \zeta\sqrt{2\kappa\Delta t}) \quad (2)$$

Where ξ and ζ are random deviates from a Gaussian distribution of zero mean and unit variance respectively, Δt is the time step used in the numerical integration of (1), and κ is a horizontal eddy diffusivity set to $2 \text{ m}^2 \text{ s}^{-1}$ (Rao and Murthy, 2001).

To quantify retention and dispersion of passive particles, we follow Cong et al. (1996) and Sheng et al. (2007) and define the retention index as

$$R(\vec{x}, t) = \frac{N(\vec{x}, t)}{N(\vec{x}, t_0)} \quad (3)$$

where $N(\vec{x}, t_0)$ is the number of particles released initially in a sub-area of a given size centered at \vec{x} at initial time t_0 , and $N(\vec{x}, t)$ is the number of original particles remaining within the sub-area at some later time t . The retention index defined above represents the proportion of particles released in a given sub-area at t_0 remaining inside the sub-area at a later time t . The value of R is between 0 and 1, with higher values corresponding to higher retention of particles.

3. Model Results

Figure 2 shows the monthly mean near-surface (1.5 m) circulation in June. The circulation pattern in Lake Huron is dominated by a strong cyclonic coastal jet along the shoreline and relatively

weak southeastward currents over the central region of the main lake. This current field is responsible for the dispersal of the passive particles released in the whole lake.

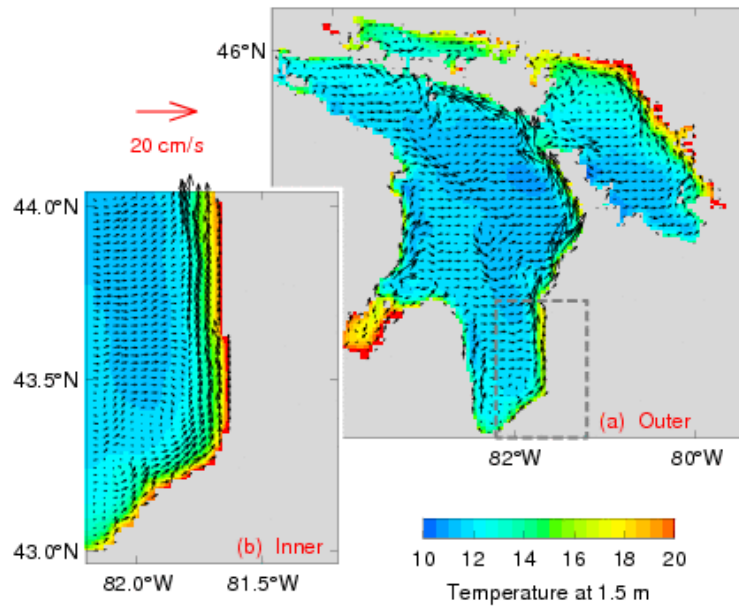


Figure 2 Monthly mean near-surface (1.5 m) currents and temperature distribution in June calculated from 3D model results produced by (a) the outer model and (b) inner model of the nested-grid system. Velocity vectors are plotted at every third model grid point in (a) and every fourth grid point in (b) respectively.

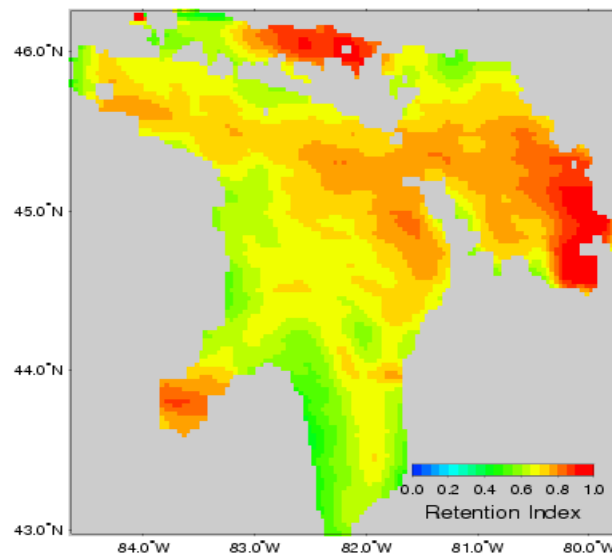


Figure 3 Distribution of retention indices in Lake Huron based on horizontal movements of near-surface particles advected by monthly mean near-surface currents in June calculated from model results produced by the outer model at day 9.

To investigate the hydrodynamic connectivity of surface waters in the Lake, the outer model domain is divided into 9 sub-regions (with names and boundaries of the sub-regions indicated in Figure 4). The exchanges of near-surface particles between different sub-regions are estimated based on particle trajectories calculated from model currents.

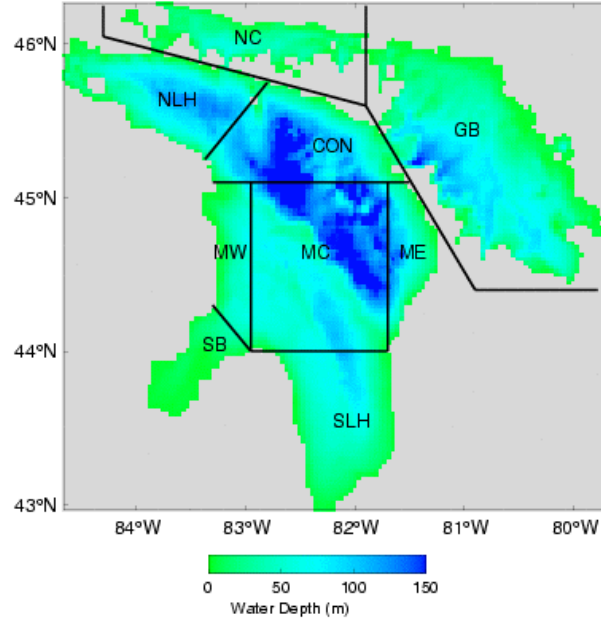


Figure 4 Names and boundaries of 9 sub-regions used in the calculation of transition matrix of passive particles in the surface waters.

Table 1: Transition matrix of near-surface waters over 9 sub-regions of the outer model domain during a 9-day period calculated from outer model currents. All the values are multiplied by 100 and those less than 0.005 are not shown.

	NC	GB	NLH	CON	MW	MC	ME	SB	SLH
SLH	—	—	—	—	—	5.3	2.8	—	91.4
SB	—	—	—	—	7.1	2.4	—	87.8	2.7
ME	—	—	—	7.5	—	2.6	89.8	—	—
MC	—	—	—	—	—	79.8	11.6	—	8.6
MW	—	—	—	—	68.7	21.9	—	2.9	6.5
CON	—	3.7	—	80.0	5.0	11.2	—	—	—
NLH	—	—	83.7	15.3	—	—	—	—	—
GB	—	99.0	—	0.9	—	—	—	—	—
NC	97.0	2.2	0.7	—	—	—	—	—	—

Figure 5 shows the retention indices of near-surface water calculated from the monthly mean near-surface currents in June, July, and August, which are produced by the fine-resolution inner model. The sub-area used in the calculation of the retention index is a square box with the horizontal dimension of 20 x 20 km. Within each box, near-surface passive particles are released uniformly with 100 particles per square km. The horizontal distribution of retention indices for near-surface particles advected by model currents for 3 days in each of the three months have similar large-scale features, characterized by relatively high retention indices of about 60-80% over the deep area, and lower retention indices of about 40% over the coastal region. The retention indices for 6 and 9 days have similar pattern as those for 3 days, but with reduced magnitude. The calculated retention indices also exhibit month-to-month variability.

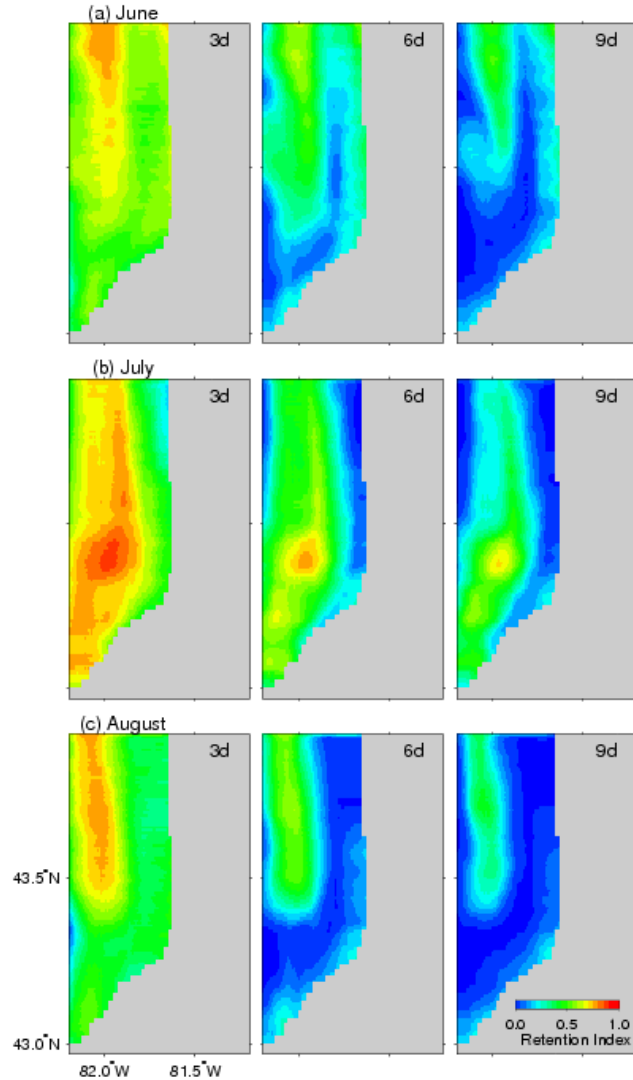


Figure 5 Distribution of retention indices over the inner model domain based on horizontal movements of near-surface particles advected passively by monthly mean near-surface currents in (a) June, (b) July, and (c) August.

Reference:

- Cong, L., Sheng, J. and Thompson, K.T., 1996. A retrospective study of particle retention on the outer banks of the Scotian Shelf 1956-1993. *Canadian Technical Report of Hydrography and Ocean Sciences*, 170, 132 pp.
- Hannah, C.G., Naimie, C.E. and Loder, J.W., 1998. Upper-ocean transport mechanisms from the Gulf of Maine to Georges Bank, with implications for Calanus supply. *Continental Shelf Res.*, 17: 1887-1911.
- Rao, Y.R., Murthy, C.R., 2001. Coastal boundary layer characteristics during summer stratification in Lake Ontario. *J. Phys. Oceanogr.*, 31, 1088-1104.
- Sheng, J. and Rao, Y.R., 2006. Circulation and thermal structure in Lake Huron and Georgian Bay: Application of a nested-grid hydrodynamic model. *Continental Shelf Res.*, 26: 1496-1518.
- Sheng, J., Wright, D.G., Greatbatch, R.J., Dietrich, D., 1998. CANDIE: A new version of the DieCAST ocean circulation model. *J. Atm. and Oceanic Tech.*, 15, 1414-1432.

Participants List

1	George Arhonditsis	University of Toronto	georgea@utsc.utoronto.ca
2	Anton Baglaenko	University of Waterloo	abaglaen@uwaterloo.ca
3	Leon Boegman	Queen's University	leon.boegman@civil.queensu.ca
4	Bertram Boehrer	Helmholtz Centre for Environmental Research	bertram.boehrer@ufz.de
5	Myriam Bormans	CNRS/University of Rennes	myriam.bormans@univ-rennes1.fr
6	Damien Bouffard	Queen's University	damien.bouffard@queensu.ca
7	Melissa Coman	University of Toronto	melissa.coman@utoronto.ca
8	Remo Cossu	University of Toronto	remo.cossu@utoronto.ca
9	Natalia Demchenko	Russian Academy of Sciences	ndemchenko@mail.ru
10	Maureen Downing-Kunz	University of California, Berkeley	mokunz@berkeley.edu
11	Michael Dunphy	University of Waterloo	mdunphy@math.uwaterloo.ca
12	Frederic Dupont	Environment Canada	frederic.dupont@ec.gc.ca
13	Xing Fang	Auburn University	xing.fang@auburn.edu
14	Marco Ghisalberti	University of Western Australia	ghisalbe@sese.uwa.edu.au
15	Andres Gomez Giraldo	Universidad Nacional de Colombia	eagomezqi@unal.edu.co
16	Kate Hayes	Credit Valley Conservation	khayes@creditvalleyca.ca
17	Bogdan Hlevca	University of Toronto	bogdan@hlevca.com
18	Yongtai Huang	Hunter College of CUNY	hyongtai@dep.nyc.gov
19	Janos Jozsa	Budapest University of Technology and Economics	jozsa@vit.bme.hu
20	Homa Kheyrollah Pour	University of Waterloo	h2kheyro@uwaterloo.ca
21	Alexandra King	Cornell University	atk6@cornell.edu
22	Julika Kreling	University of Koblenz-Landau	j.kreling@gmx.de
23	Jessica Lacy	US Geological Survey	jlacy@usgs.gov
24	Charles Lemckert	Griffith University	c.lemckert@griffith.edu.au
25	Matti Leppäranta	University of Helsinki	matti.lepparanta@helsinki.fi
26	Madis-Jaak Lilover	Marine Systems Institute	madis@phys.sea.ee
27	Wentao Liu	University of Waterloo	w13liu@math.uwaterloo.ca
28	Andreas Lorke	University of Koblenz-Landau	lorke@uni-landau.de
29	Youyu Lu	Bedford Institute of Oceanography	Youyu.Lu@dfo-mpo.gc.ca
30	Andreas Maeck	University of Koblenz-Landau	maeck@uni-landau.de
31	Andrey Martynov	Université du Québec à Montréal (UQAM)	a.martynov@gmail.com
32	Santiago Moreira	Institute of Hydrobiology	santiago.moreira_martinez@tu-dresden.de
33	Ryan Mulligan	Queen's University	mulliganr@civil.queensu.ca
34	Christian Noß	University of Koblenz-Landau	noss@uni-landau.de
35	Ali Oveisy	Queen's University	a_oveisy@ce.queensu.ca
36	Shastri Paturi	Queen's University	shastri.paturi@ce.queensu.ca
37	Rich Pawlowicz	University of British Columbia	rpawlowicz@eos.ubc.ca
38	Patricia Pernica	University of Toronto	ppernica@physics.utoronto.ca
39	Sebastiano Piccolroaz	University of Trento	sebastiano.piccolroaz@ing.unitn.it
40	Roger Pieters	University of British Columbia	rpieters@eos.ubc.ca
41	Martina Preusse	University of Konstanz	martina.preusse@uni-konstanz.de
42	Nihar Ranjan Samal	City University of New York	NSamal@dep.nyc.gov
43	Carlo Scalo	Queen's University	cscalo.ca@gmail.com
44	Shiliang Shan	Dalhousie University	sshan@phys.ocean.dal.ca

45	Jinyu Sheng	Dalhousie University	Jinyu.Sheng@Dal.Ca
46	Jennifer Shore	Royal Military College of Canada	jennifer.shore@rmc.ca
47	Eleanor Stainsby	Ontario Ministry of the Environment	eleanor.stainsby@ontario.ca
48	Marek Stastna	Univeristy of Waterloo	mmstastn@uwaterloo.ca
49	Derek Steinmoeller	University of Waterloo	dsteinmo@math.uwaterloo.ca
50	Adolf Konrad Stips	CEC Joint Research Centre	adolf.stips@jrc.ec.europa.eu
51	Christopher Subich	University of Waterloo	csubich@math.uwaterloo.ca
52	Yajun Sun	University of Toronto	sunyajun_syj@yahoo.com
53	Aaron Thompson	Environment Canada	Aaron.Thompson@ec.gc.ca
54	Marco Toffolon	University of Trento	marco.toffolon@ing.unitn.it
55	Cary Troy	Purdue University	troy@purdue.edu
56	Reza Valipour	Queen's University	valipour.r@gmail.com
57	R. Wayne Wagner	University of California, Berkeley	wagnerw@berkeley.edu
58	Danielle Wain	University of Washington	wain@apl.washington.edu
59	Jia Wang	Great Lakes Environmental Research Laboratory	jia.wang@noaa.gov
60	Mathew Wells	University of Toronto	wells@utsc.utoronto.ca
61	Miles Wilson	Royal Military College	miles.c.wilson@gmail.com
62	Alfred Wuest	EAWAG	alfred.wueest@eawag.ch
63	Ram Yerubandi	Environment Canada	Ram.Yerubandi@ec.gc.ca
64	Jun Zhao	Environment Canada	J.Zhao@ec.gc.ca
65	Luis Leon	Environment Canada	Luis.Leon@ec.gc.ca
66	Weitao Zhang	Environment Canada	tonyzhang_ca@yahoo.com
67	Padala Chittibabu	Environment Canada	padala.chittibabu@ec.gc.ca
68	Josef Ackerman	University of Guelph	ackerman@uoguelph.ca
69	Steven Monismith	Stanford University	monismith@stanford.edu
70	Sally MacIntyre	University of California, Santa Barbara	sally@icess.ic.ucsb.edu
71	Kevin Lamb	University of Waterloo	kglamb@math.uwaterloo.ca
72	David Schwab	Great Lakes Environmental Laboratory	David.Schwab@noaa.gov
73	Eric Segal	Nortek	eric@nortekusa.com
74	Fabian Wolk	Rockland Scientific	fabian@rocklandscientific.com
75	Jennifer Gouthro	Hoskin Scietific	jgouthro@hoskinscientific.com
76	Micheal Head	PME Inc.	mhead@pme.com
77	Mark Visit	RBR Limited	info@rbr-global.com
78	Murray Mackay	Environment Canada, Downsview	Murray.mackay@ec.gc.ca
79	Alexander Forrest	UC-Davis	alforrest@ucdavis.edu